STUDIES ON PHOTOPHYSICAL AND CHARGE CARRIER DYNAMICS OF GRAPHENE OXIDE AND TERNARY BLEND BASED POLYMER SOLAR CELLS

LALSINGH GUGULOTH

DEPARTMENT OF PHYSICS

NATIONAL INSTITUTE OF TECHNOLOGY, WARANGAL

JUNE, 2021

STUDIES ON PHOTOPHYSICAL AND CHARGE CARRIER DYNAMICS OF GRAPHENE OXIDE AND TERNARY BLEND BASED POLYMER SOLAR CELLS

A thesis submitted in partial fulfillment of the requirements for the award of the degree of

DOCTOR OF PHILOSOPHY

in

PHYSICS

by

LALSINGH GUGULOTH

(Roll No: 715084)

Supervisor:

Dr. KUSUM KUMARI

DEPARTMENT OF PHYSICS,

NATIONAL INSTITUTE OF TECHNOLOGY, WARANGAL

WARANGAL-506004, TELANGANA, INDIA.

JUNE, 2021

DEDICATED

TO

MY PARENTS & TEACHERS

DECLARATION

This is to declare that the work presented in the thesis entitled "**Studies on Photophysical and Charge Carrier Dynamics of Graphene Oxide and Ternary Blend based Polymer Solar Cells**" is a bonafide work done by me under the supervision of **Dr. Kusum Kumari**, Assistant Professor in the Department of Physics and was not submitted elsewhere for the award of any degree.

I declare that this written submission represents my ideas in my own words and where others ideas or words have been included; I have adequately cited and referenced the original sources. I also declare that I have adhered to all principles of academic honesty and integrity and have not misrepresented or fabricated or falsified any idea/data/fact/source in my submission. I understand that any violation of the above will be a cause for disciplinary action by the Institute and can also evoke penal action from the sources which have thus not been properly cited or from whom proper permission has not been taken when needed.

Date: 03-June-2021 (Lalsingh Guguloth)

Place: NIT Warangal Roll Number: 715084

NATIONAL INSTITUTE OF TECHNOLOGY, WARANGAL

CERTIFICATE

This is to certify that the work presented in the thesis entitled "**Studies on Photophysical and Charge Carrier Dynamics of Graphene Oxide and Ternary Blend based Polymer Solar Cells**" is a bonafide work carried out by **Mr. Lalsingh Guguloth** under my supervision and was not submitted elsewhere for the award of any degree.

3/6/2021

Date: 03-June-2021
Place: NIT Warangal

Dr. Kusum Kumari
Assistant Professor
Research Supervisor

ACKNOWLEDGEMENT

I would like to express my sincere heartfelt gratitude to my research supervisor, **Dr. Kusum Kumari**, Assistant Professor, Department of Physics, NIT Warangal for her constructive guidance, relentless encouragement, and her love of research motivated me throughout my research life. I very much appreciate the freedom to pursue my research interests that she has given for completion of this research work. Moreover, she inspired to ensure the completion of this work. Her expertise, availability to discuss ideas and willingness to share her knowledge were instrumental. For this, I will be eternally grateful.

I express my sincere thanks to Prof. D. Dinakar, Head, Department of Physics, NITW, for his valuable suggestions and support. I express my sincere thanks to Former Heads of Department of Physics for their valuable help and support.

I sincerely thank the members of the Doctorial scrutiny committee (DSC), Prof. R. L. N. Sai Prasad, Dr. P. Abdul Azeem, Dr. Vishnu Shanker, for their valuable suggestions at every stage of my research.

I express my sincere thanks to the Director, National Institute of Technology, Warangal, for having given me the opportunity to carry out the work and allowing me to submit the work in the form of thesis. I express my sincere thanks to MHRD, New Delhi for the financial support in the form of fellowship.

This thesis work was supported by Empowerment and Equity Opportunities for Excellence in Science program, Science and Engineering Research Board, Department of Science & Technology, Government of India (project no. EEQ/2016/000723), and Technology Mission Division, Department of Science & Technology, Government of India (project no. DST/TMD/SERI/S56(C)).

I am thankful to senior faculty members of our department, Prof. S.V.S. Ramana Reddy, Prof. Sai Sankar, Prof. L. Ramgopal Reddy, Prof. R. L. N. Sai Prasad, and Prof. K. Venugopal Reddy for their encouragement and support.

I take this opportunity to express my gratitude to Dr. B. Sobha, Dr. T. Venkatappa Rao, Dr. P. Abdul Azeem, Dr. P. Syam Prasad, Dr. Sourabh Roy, Dr. Thangaraju, Dr. D.

Haranath, Dr. D. Paul Joseph, Dr. V. Jayalakshmi, Dr. R. Rakesh Kumar, Dr. K. Uday Kumar, Dr. Vijay Kumar, Dr. Surya K. Ghosh, Dr. Hitesh Borkar, Dr. Aalu Boda, Department of Physics, National Institute of Technology, Warangal for their valuable advice, encouragement and moral support in my career.

I am very much thankful to Dr. Satyender Singh, Associate professor, JNU University, New Delhi, for Raman spectroscopy.

I express my sincere thanks to my friends and colleagues Dr. Ashish kumar, Dr. P. M. Pratheeksha, Dr. K. Uma Devi, Dr. T. Ramesh, Ms. Sravanthi, Mr. M. Nagaraju, Mr. Srinath, Mr. VDR Pavan, Ms. Manjula, Mr. N. PurusothamReddy, Mr. Buchaiah, Mr. Ramesh.B, Mrs. V.P.Madhurima, Mr. Koustav Dey, Mr. Akshaykanth. A, Mr. Krishnamraju, Mr. A. Prasad Babu, Mr. Sushil Patel.A, Mr. Vishnu Jaiswal, Mr. Sathaiah, Mr. Jayaram Babu, Mr. Siju Mishra, Mr. Nikhel.V, Ms. Mahalakshmi. A, Ms. Lavanya.T, Mrs. Ramadevi. S p, Mr. Muniramaiah. R, Ms. Supraja. P, Mr. Partha Pratim Das, Ms. N Anitha, Ms. Pooja Yadav, Mr. Badavath Purnesh Singh , Ms. Anjaly babu, Mr. Gouranga Maharana, Mr. Naveen kumar Kurapati, Ms. Muddamalla Rakshita, and other co-research scholars for their munificent support.

With all happiness I acknowledge the cheerful assistance rendered by all my senior research colleagues Mr. D. Gnyaneshwar, Dr. R. Ramarajan, Dr. S. Rajkumar, Dr. V. Himamaheswara Rao, Dr. P.V.N. Kishore, Dr. M. Mohan babu, Dr. Hari Krishna for their encouragement thoughout the period of my research.

I would like to thanks to Non-Teaching members of our department Mr. Jaisingh. A, Mr. Krisnaswamy. N, Mr. Veerah. K, Mr. Pratap. G, Mr. Srinivas. B, Mrs. Kamala. K, Mrs. Krishnaveni. P, Mr. Serihari and Mrs. Husna for their encouragement and support.

It would not have been possible for me to enter my research journey without their motivation, cooperation and encouragement. Heart goes to my beloved Family Members who with all their patience, prayers and faith in the Almighty, waited all these long years to see me reaching this stage. Their blessings and care always gave me new favour to do something more with perfection. I always remember and cherish the encouragement and inspiration provided by my mother and father during the course of my research work.

LALSINGH GUGULOTH

ABSTRACT

One of the renewable energy technologies is Photovoltaics (PV), the technology that directly converts daylight into electricity. Organic solar cells (OSCs) have been showing promise as a way of producing renewable energy with the help of effective organic materials. The efficiencies and lifetimes reached in organic solar cells have steadily been increasing over the years as more research in the field is being conducted. OSCs are one of the emerging photovoltaic technologies and are classified as third-generation solar cells with organic material as the light absorbing photoactive layer. In recent years, OSCs have shown a great promise of delivering cost effective, flexible, light weight, large area and easy processable solar cells. Power conversion efficiency (PCE) ~ 14-15% have already been realized in polymer solar cells based on donor-acceptor interpenetrating bulk heterojunction. More recently international R & D efforts are focused towards the development of ternary blend based polymer solar cells (TPSCs) employing a blend of two or three absorption complementary components, comprising of either two-electron donors and one electron acceptor (D_1:D_2:A) or one electron donor and two-electron acceptors (D:A_1:A_2) systems, offering not only enhanced light-harvesting ability of the photoactive layer but also enhanced exciton dissociation and charge transfer. The state-of-the-art PCE of approx. 16-17% have been realized in TPSCs. However, both high PCE and good stability are simultaneously required for commercial applications. Accordingly, several efforts have been devoted to the development of TPSCs, especially the proper selection of both the photoactive layer and charge transport layers are notably crucial. So far, different hole transport materials (HTLs) such as poly(3,4-ethylenedioxythiophene) doped with poly(styrene sulfonate) (PEDOT:PSS), MoO_3, V_2O_5, WO_3, NiO etc. However, instability of TPSCs using these HTLs has been still a serious isssue. In this direction, more recently, TPSCs using 2D materials such as graphene and graphene oxide have gained much attention as it holds a further promise due to high carrier mobilities (due to inorganic nature), better charge transport, better physical and chemical stability, cost effectiveness etc.

There is wide scope in this field of ternary blend especially using 2D Materials for further improvement. Hence, the present work is focused on achieving simultaneously good efficiency and stability in the ternary solar cell devices. The present thesis addresses the main scientific issues in improving the performance of such 2D materials and ternary-blend based solar cells is, (i) Optimization the Morphology of the active layer for better charge dissociation, carrier mobilities, and charge transport , (ii) Recombination in the active layer and at the HTL/Active layer interface need to be controlled for enhanced carrier collection, and (iii) improving the device stability. Therefore, the thesis work probes and broadens the understanding of the fundamental photovoltaic properties of both binary and ternary blended organic solar cells. Also, carbon based 2D Materials have been explored and investigate how they can be successfully incorporated into the TPSCs to enhance their performances. The studies related to photophysics and charge carrier dynamics have been investigated in-depth.

This thesis mainly comprises of synthesis of Graphene Oxide(GO) and Fluorinated Graphene Oxide(FGO) by modified Hummer's method. Here, GO and F-rGO nanosheets have been successfully utilized for improving the properties of HTL and active layer, respectively. Subsequently, preparation of HTLs [PEDOT:PSS, GO, and PEDOT:PSS -GO composite films] have been carried out and optimized their thin films by spin coating technique. It is found that, PEDOT:PSS-GO(1:1) composite provides beneficial hole transport properties over PEDOT:PSS. Hence, it is an potential alternative HTL. On the other hand, preparation of ternary blend active layers [(P3HT (D_1): PTB7-th (D_1): PCBM(A_1), and [PTB7-th (D): PCBM (A_1): F-rGO (A_2)], and (P3HT:PTB7-th:PCBM) Ternary Blends have been optimized for solar cell applications. After systematic structural and optical investigations, it is established that (P3HT:PTB7-th:PCBM) (0.3:0.7:1) composition offer sensitized emission, and strong PL quenching via FRET/charge transfer. Hence, enhanced exciton dissociation occur within the ternary blend ensuring good photovoltaic properties, and hence, showed potential to use as active layer. Further, TPSCs were fabricated using the ternary blends and different PEDOT:PSS /GO/PEDOT:PSS -GO composite films HTLs, in typical device configuration, *ITO*(ϕ ~ 4.8eV)*/ HTL(~40nm) / ternary blend (~180nm) / LiF/Al* (ϕ ~4.3eV). Ternary solar cells, ITO/ PEDOT:PSS-GO (1:1) / P3HT:PTB7-th:PCBM (0.3:0.7:1)/ LiF/Al, have showed

the best and enhanced performance (PCE ~7.1% and stability~only10% loss after 500 hours) compared to other binary blend and other HTLs based devices.

In addition, The utilization of F-rGO as the electron acceptor material in PTB7-th:PCBM bulk heterojunction photovoltaic devices has been demonstrated. The TPSC, ITO / PEDOT:PSS / PTB7-th:PCBM + F-rGO(5wt.%)/ LiF / Al, yield a PCE enhancement (~7.36%) compared to PTB7-th:PCBM (~3.54%) based devices. F-rGO nanosheets not only enhance the charge dissociation by promoting the electron extraction from PTB7-th polymer to PCBM, but also support charge transport by providing conducting pathways. This results in improved PCE of (PTB7-th:PCBM:F-rGO) based ternary devices. Also, good photo-stability of F-rGO significantly improved the overall air-stability of [PTB7-th:PCBM + F-rGO] compared to binary [PTB7-th:PCBM] blend devices

These in-depth studies open a new avenue for the potential commercialization of low-cost and solution-processed TSCs.

TABLE OF CONTENTS

LIST OF FIGURES

CHAPTER 1

CHAPTER 3

CHAPTER 5

CHAPTER 6

LIST OF TABLES

CHAPTER 6

CHAPTER 7

LIST OF ABBREVIATIONS AND SYMBOLS

α	Absorption Coefficient
T	Absolute Temperature
Δ	Activation Energy
AM	Air mass
Al	Aluminium
A1, A2, A3	Amplitude constants
a-Si	amorphous Silicon
V_{app}	Applied Voltage
I	applied current
F	Applied Electric Field
NA	Avogadro's number
τ_{avg}	Average Life time
Ar	Argon gas
AFM	Atomic Force Microscopy
P_o	Back ground carrier concentration
K_B	Boltzmann's Constant
C_{60}	Buckminsterfullerene
BHJ	Bulk Heterojunction
V_{bi}	Built-in-Potential
CdSe	Cadmium Selenide
CdTe	Cadmium Telluride
Ca	Calcium
CNT	Carbon Nanotubes
Nc	Carrier concentration
P_x	Carrier concentration
μ	Carrier mobility
T_c	Characteristic Temperature for Trap Distribution
E_t	Characteristic Trap Energy

CT	Charge Transfer
e	Charge of the electron
CL	Chlorobenzene
σ	Conductivity
CuI	Copper Iodide
CuPc	Copper Pthalocyanine
CuSCN	Copper Thiocyanate
J_D	Current densities in dark
J_L	Current densities in illumination
J-V	Current Density-Voltage
I-V	Current-Voltage
N	Defects density
DI	Deionized water
H_b	Density of traps
ε_r	Dielectric constant
θ	Diffraction Angle
DMSO	Dimethyl Sulfoxide
D:A	Donor:Acceptor
D_1:D_2:A	$Donor_1$:$Donor_2$:Acceptor
D:A_1:A_2	Donor:$Acceptor_1$:$Acceptor_2$
Nv	Effective density of states
V_{eff}	Effective Voltage
μe	Electron mobility
ETL	Electron Transport Layer
ETM	Electron Transport Material
E_g	Energy Band Gap
Et	Energy of trap
E_m	Emission
λ_{em}	Emission wavelength
EG	Ethylene Glycol
E_x	Excitation

λ_{exc}	Excitation wavelength
G_{max}	Excition generation rate
EQE	External quantum efficiency
τ_1	Fast component
FESEM	Field emission scanning electron microscope
FF	Fill Factor
t	Film thickness
FRET	Förster Resonance Energy Transfer
EFRET	Förster Resonance Energy Transfer Efficiency
R_o	Förster radius
FTO	Fluorine Doped Tin Oxide
Au	Gold
GO	Graphene Oxide
HOMO	Highest Occupied Molecular Orbital
EHOMO	Highest Occupied Molecular Orbital Energy Level
HRTEM	High Resolution Transmission Electron Microscopy
μ_h	Hole mobility
HTL	Hole Transport Layer
HTL	Hole Transport Material
HRS	Hours
HCl	Hydrochloric Acid
H_2O_2	Hydrogen Peroxide
ITO	Indium Tin Oxide
ICBA	Indene-C60 bisadduct
P_i	Injected carrier concentration
d	Inter-planar spacing
ISC	Inverted Solar Cell
‘a,’ ‘b,’ ‘c,’	Lattice constants
$\tau1, \tau2, \tau3$	Life times
LiF	Lithium Fluoride
ELUMO	Lowest Unoccupied Molecular Orbital Energy Level

LUMO	Lowest unoccupied Molecular Orbital
Mg	Magnesium
J_{max}	Maximum Current Density
P_{max}	Maximum Power
MPP	Maximum Power Point
V_{max}	Maximum Voltage
V	Measured Voltage
$\tau 2$	Medium component
μm	micrometer
hkl	Miller indecis values
mA	milli Ampere
mg	milli grams
mL	milli Liter
Min	Minutes
MoO_3	Molybdenum Oxide
NC	Nanocrystal
NP	Nanoparticle
NiO	Nickel Oxide
DMF	N-N-Dimethylformamide
I_{hkl}	Observed peak intensity
V_{oc}	Open Circuit Voltage
λ	Optical Wavelength
OSC	Organic Solar Cells
OPV	Organic Photovoltaics
O_2	Oxygen
ε_o	Permittivity of free space
$PC_{61}BM$	Phenyl-C61-butyric Acid Methyl Ester
$PC_{71}BM$	Phenyl-C71-butyric Acid Methyl Ester
hν	Photon Energy
J_{ph}	Photo current density
PL	Photoluminescence

PV	Photovoltaics
h	Planck's constant
PSC	Polymer Solar Cells
PEDOT:PSS	Poly(3, 4-ethylenedioxythiophene):Poly(styrenesulfonate)
P3HT	Poly(3-hexylthiophene)
PCPDTBT	Poly[2,6-(4,4-bis-(2-ethylhexyl)-4H-cyclopenta[2,1-b;3,4-b']dithiophene)-alt-4,7-(2,1,3 benzothiadiazole)]
PTB7	Poly[(ethylhexyloxy)-benzodithiophene-(ethylhexyl)-thienothiophene]
PTB7-th	Poly[4,8-bis(5-(2-ethylhexyl)thiophen-2-yl)benzo[1,2-b;4,5-b']dithiophene-2,6-diyl-alt-(4-(2-ethylhexyl)-3-fluorothieno[3,4-b]thiophene-)-2-carboxylate-2-6-diyl)]
PBDTTT-C	Poly[(4,8-bis-(2-ethylhexyloxy)-benzo(1,2-b:4,5- b') dithiophene)-2,6-diyl-alt-(4-(2-ethylhexanoyl) -thieno[3,4-b]thiophene-)-2-6-diyl)]
PBDTTPD	Poly[(5,6-dihydro-5-octyl-4,6-dioxo-4H-thieno[3,4-c]pyrrole-1,3-diyl) [4,8-bis[(2-ethylhexyl)oxy] benzo[1,2-b:4,5-b']dithiophene-2,6 diyl]
MDMO-PPV	Poly[2-methoxy-5-(3,7-dimethyloctyloxy)-1,4-phenylene vinylene]
MEH-PPV	Poly[2-methoxy-5-(2′-ethylhexyoxy)-1,4-phenylene vinylene]
PCPDTBT	Poly[2,6-(4,4-bis-(2-ethylhexyl)-4H-cyclopenta[2,1-b;3,4-b′]dithiophene)- alt-4,7- (2,1,3 benzothiadiazole)]
PPV	Poly-phenylene vinylene
$KMnO_4$	Potassium Permanganate
PCE (or) ηˌ	Power Conversion Efficiency
Q_D	Quantum efficiency donor
K	Relative orientation
ρ	Resistivity
RPM	Rotation per Minutes
RT	Room Temperature

RMS	Root Mean Square
J_{sat}	Saturation current density
V_{sat}	Saturation Voltage
SEM	Scanning Electron Microscopy
SAED	Selected Area Electron Diffraction
Ag	Silver
Rs	Sheet resistance
SC	Short Circuit
Isc	Short-Circuit Current
J_{sc}	Short–Circuit Current Density
τ_3	Slowest component
SMU	Sourse Measurement Unit
SCLC	Space charge Limited current
SCLC	Space-Charge-Limited Conduction
cm^2	square centimeter
H_2SO_4	Sulfuric Acid
TPSC	Ternary Polymer Solar Cells
TCSPC	Time-correlated single photon count
TRPL	Time Resolved Photoluminescence
TiO_2	Titanium Dioxide
Tc	Trap distribution of Temperature
V_{TFL}	Trap filled limit voltage
TEM	Transmission Electron Microscopy
TCO	Transparent Conductive Oxide
WO_3	Tungsten Oxide
UVO	Ultra-Violet Ozone
UPS	Ultra Violet Photo electron spectroscopy
UV-Vis	Ultraviolet-Visible
UV-Vis-NIR	Ultraviolet-Visible-Near infrared spectroscopy
VCU	Vacuum Coating Unit
V_2O_5	Vanadium Pent oxide

H_2O	Water
Φ	Work Function
XRD	X-ray Diffraction
XPS	X-ray Photoelectron spectroscopy
Δ_o	Zero field Activation Energy
ZnO	Zinc Oxide
ZuPc	Zinc Pthalocyanine
DIO	1, 8-Diiodoctane
PFN	[(9, 9- bis(3'-(N,N-dimethylamino)propyl)-2,7-fluorene)-alt-2,7-(9,9- dioctylfluorene)]

CHAPTER 1

INTRODUCTION

1.1 General Background and Motivation

The use of nonrenewable energy has caused serious environmental problems on the earth. The amount of greenhouse gases produced going faster as the amount of fossil fuels burned grew. As a result, the Earth is becoming increasingly hotter, and sea levels are steadily rising. Renewable energy resources have been extensively investigated in order to solve the problem. The sources of renewable energy such as biomass, hydro-power, wind, geothermal and solar, play a significant role in world's energy supply. The percentage of all the energy sources contributing to the total world's energy is revealed in the pie chart shown below in Fig. 1.1.

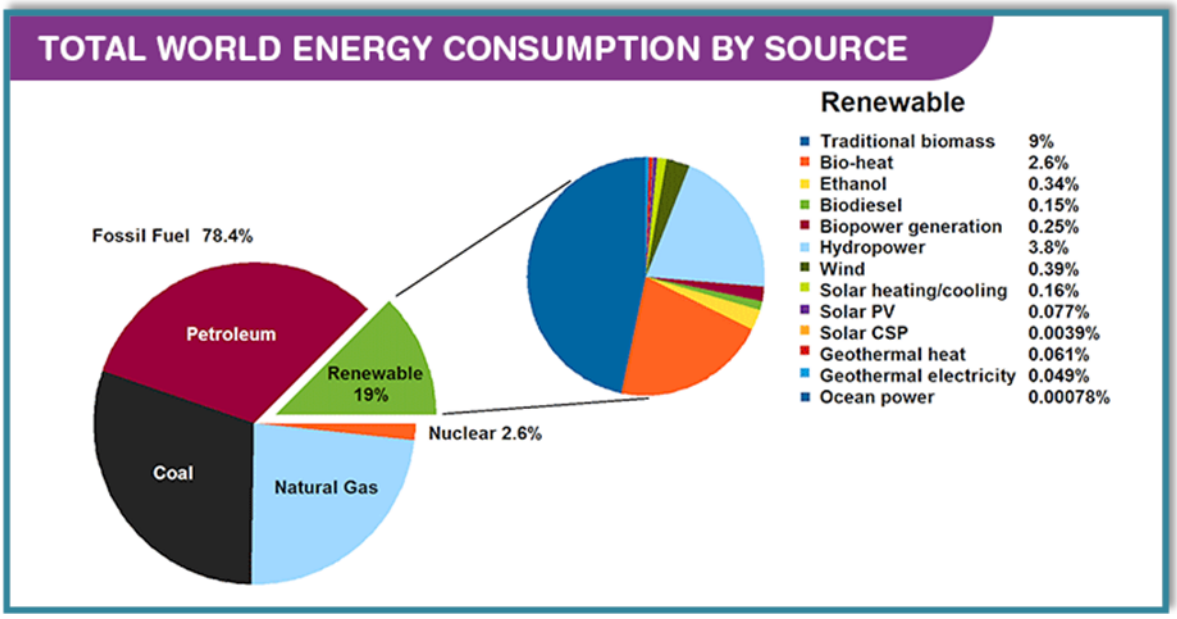

Figure 1.1 *Renewable Energy Consumption in the World's Energy Supply, 2020.*

Fortunately, we have renewable energy sources that will not run out and will not have substantial negative environmental consequences. Solar photovoltaic (PV), onshore wind, hydro, and offshore wind power facilities will produce 85 percent of global

electricity in 2050, and renewable energy will account for about half of the world's energy mix. The increased world consumption of marketed energy from all fuel sources over the 2006 to 2050 projection period is shown in Fig. 1.2.

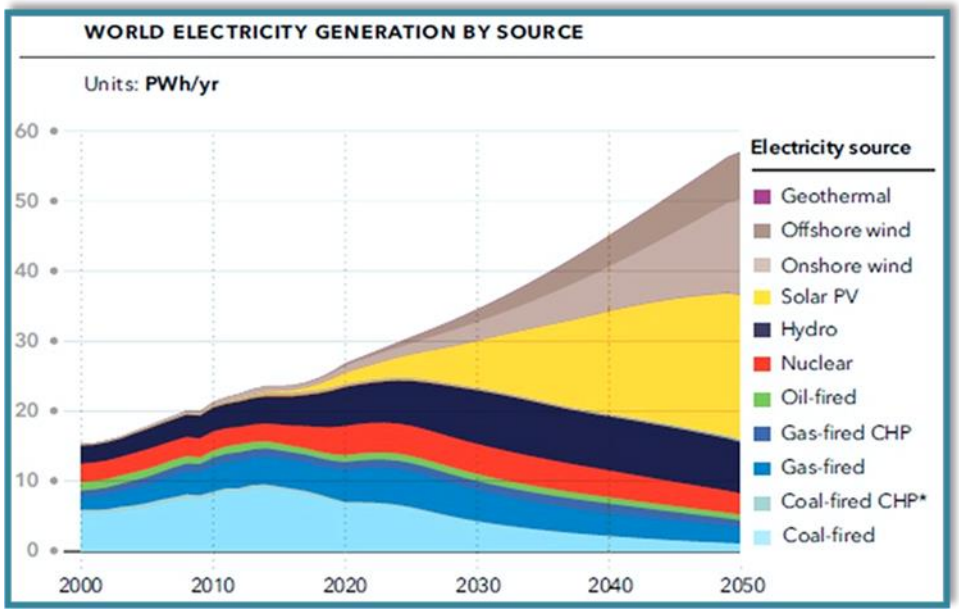

Figure 1.2. *The increased world consumption of marketed energy from all fuel sources over the 2006 to 2050 projection period.*

Photovoltaic (PV) technology, which harvests energy directly from the sun, is widely acknowledged as a critical component of future global energy generation [63]. PV technology, or solar cells that convert sunlight directly into electricity, is one of the most rapidly increasing renewable energy technologies, if not the fastest expanding industry at the moment. These PV devices are mainly fabricated from semiconductor materials PVs can be made out of a number of semiconductor materials, such as silicon, copper indium gallium diselenide (CIGS), cadmium telluride (CdTe), and sometimes even organic semiconductors (OPV). Although PV conversion efficiency is crucial, for most applications, cost efficiency—the cost per watt of power—is more significant. The main advantage of solar cells involves their graceful procedure: just converting daylight into electricity. No requirement of water and fuels, maintenance requirements is very less, no by-product, no sound pollution or no requirement of transferring from one location to other after installation. Although the initial cost is very high yet operation and

maintenance cost is very low [1-6]. A great deal of research has gone into lowering the initial cost, increasing efficiency, extending the longevity, and simplifying the manufacturing process. As a result, continual research has been conducted in this field, resulting in three generations of PV technology.

First generation solar cells were based on silicon (*Si*) which possess good efficiency (>15%) and durability (>20 years). Si based solar cells are available in the market but because of their high cost they are away from the reach of a common man of the country. Therefore efforts are being made to reduce the cost and improve further the performance of Si based solar cells or find out new materials to replace Si.

An alternative progress towards solar cells, presently intensive work is being performed on organic solar cells (OSCs) using small molecules and polymers as active layers which can be processed over large areas at relatively low temperatures, either through thermal deposition of small molecules or by spin coating of solution processable polymers. The energy consumption for fabrication of polymer solar cells (PSCs) are very less compared to inorganic solar cells due to high throughput and low temperature process which permits preparation through roll-to-roll printing technology. Due to inexpensive and high absorption coefficients, these materials are allowed to make thin film of thickness in nanometer order. Furthermore, because PSC construction works well with flexible substrates, it has the potential to become the next generation of light weight and low cost renewable energy resource. As a result, PSCs have grabbed the curiosity of academia and industry researchers all around the globe. The state-of-the-art power conversion efficiencies (PCE) of approx. 14-15% have been realized in single-junction polymer bulk heterojunction (BHJ) in binary blend configurations which consist of one electron-donor and one electron-acceptor **[7-14]**. However, both high PCE and good stability are simultaneously required for commercial applications. As a result, new electron-accepting and electron-donating organic materials, blend morphological management, interface engineering, and the innovation of current device designs have now been given priority **[15-18]**. Despite major attempts to develop binary blend polymer BHJs based PSC devices, the fundamental restriction is the small absorption window (100–200 nm) of polymer thin films (usually 100nm) compared to inorganic semiconductors like silicon **[19-21]**. To overcome these limitations tandem PSCs have

emerged, where multiple active layers with complementary absorption are stacked vertically connected together by an interfacial buffer layer. Such a tandem configuration not only improves the light-harvesting due to complementary absorption but also reduces the thermalization losses as each active layer independently absorbs a specific segment of the solar range. However, the complication of the fabrication process involved in tandem PSC significantly increases its manufacturing cost **[20, 21]**. On the other hand, recently, ternary blend based PSCs have attracted tremendous interest employing a blend of two/three absorption complementary components, comprising of either two-electron donors and one electron acceptor (D_1:D_2:A) or one electron donor and two-electron acceptors (D:A_1:A_2) systems, offering enhanced light-harvesting ability of the photoactive layer **[22-24]**. The ternary blend's distinct benefit is due to the simplicity of the production methods used, which makes them more appealing than the sophisticated tandem cells. Also, the third ternary additive in ternary blend acting either as a secondary donor or acceptor material forms a charge cascade structure offering an extra interface for exciton dissociation and charge transfer **[25-28]**. As a result, ternary blend PSCs have demonstrated better performances with the state-of-the-art PCE ~16-17% **[20-28]**. Several groups have reported ternary blend active layers employing various electron donor polymer materials such as "poly(3-hexyl-thiophene) (P3HT), poly[N-9′ -heptadecanyl-2,7-carbazole-alt-5,5-(4′ ,7′ -di-2-thienyl-2′ ,1′ ,3′ -benzothiadiazole)] (PCDTBT), poly[2,6-(4,4-bis(2-ethylhexyl)-4H-cyclopenta [2,1-b;3,4-b′]dithiophene)-alt-4,7(2,1,3-benzothiadiazole)] (PCPDTBT), poly[(ethylhexyloxy)-benzodithiophene-(ethylhexyl)-thienothiophene] (PTB7), and poly[(5,6-dihydro-5-octyl-4,6-dioxo-4H-thieno[3,4-c]pyrrole-1,3-diyl)[4,8-bis[(2 ethylhexyl)oxy]benzo[1,2-b:4,5-b′]dithiophene-2,6-diyl] (PBDTTPD) blended with electron acceptors such as [6,6]-phenyl C_{71}-butyric acid methyl ester ($PC_{71}BM$), and Indene-C_{60} bisadduct (ICBA)". However, TPSCs show relatively poor device stability to replace conventional thin film and *Si* solar cells which are known to be high temperature and high cost photovoltaic technologies. Hence, there remains a great challenge for further optimization and development of TPSCs for their commercialization. This could be achieved by exploring their photo-physical activities in detail through extensive studies. Furthermore, the charge transport layers between the photoactive layer and electrodes, such as the hole transport layer (HTL) and electron

transport layer (ETL), as well as the interfaces produced between the electrodes and charge transport layers, as well as between charge transport layers and the photoactive layer, play an important role in increasing the overall performance of TPSCs. Hence, the proper selection of both the photoactive layer and charge transport layers is notably crucial. So far, "poly(3,4-ethylenedioxythiophene) doped with poly(styrene sulfonate) (PEDOT:PSS)" is the present major materials employed as HTL in conventional devices which facilitate the hole extraction and significantly improve the surface morphology of the interface between active layer/ITO anode **[29-32]**. It also offers high optical transparency in the solar region, high electrical conductivity, and high work function along with easy solution processing in an aqueous medium. However, PEDOT:PSS is not an ideal HTL as it exhibits inefficient electron blocking capability and high hygroscopicity which results in instability of the PSC devices. Transition-metal-oxides such as MoO_3, V_2O_5, WO_3, NiO etc. are as a substitute for PEDOT:PSS by numerous organizations, based on favorable energy matching and increased device stability **[29-32]**. But, depositing these materials via the expensive high-temperature vacuum deposition brings not only complicity, but also not suitable for large area roll to roll production.

As a cost-effective and easy processing alternative, recently, 2D carbon materials such as graphene oxide (GO) and GO derivatives, have gained much attention for their application not only in HTL but also in active layer, owing to their attractive optical and electronic properties like excellent optical transparency (>97%), high conductivity, ultrahigh carrier mobilities, and excellent thermal and chemical stability **[33, 34]**. Their ability to deposit on flexible substrates via a roll-to-roll process using the simple solution and room temperature processing has also been very impressive. Therefore, GO and GO derivatives are regarded as promising candidates and reported to grantee high efficient and high stable PSCs.

1.2 Basics of Solar Cells

Solar cells are essentially semiconductor junctions under illumination. A traditional silicon solar cell, as shown in Fig.1.3, is made up of P- type and N-type semiconductors forming a P-N junction, an anti-reflective coating, and metal electrodes for collecting photo-generated charge carriers from the n-type and p-type layers **[35-40].**

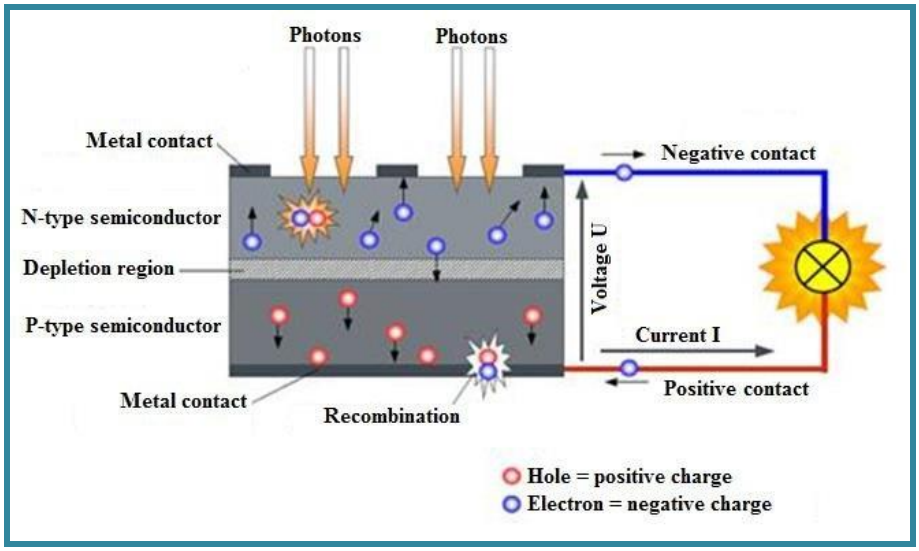

Figure 1.3 *Schematic of a typical p-n junction solar cell.*

When an N-type and P-type semiconductor are brought into contact, electrons and holes are transported across the P-N junction until equilibrium is attained. When solar radiation is incident, photons are absorbed leading to generation of electron-hole pairs in both N-type and P-type semiconductor regions. The photo-generated electrons and holes diffuse to the P-N junction and are transported by the built-in internal electric field, resulting in electric current flowing across it. Hence, photocurrent is produced by a solar cell. In fact, the operation of a PV cell can be generally divided into three basic steps:

1. Absorption of photons
2. Generation of carriers
3. Collection of carriers

Various types of solar cells and photovoltaic materials have different physical or chemical mechanisms behind these key steps. The energy conversion efficiency cell is determined by the efficiency of all the steps involved, and is optimized by selection of materials, cell-design, and several other factors.

1.3 Different Generations of Solar Cells

In 1839, Alexander Edmond Becquerel (French physicist) discovered the solar cells effects during analyzing with a solid electrode in an electrolyte solution [**41**]. The first solar cell, however, was created in 1883 by an American inventor "Charles Edgar Fritts", who used selenium to cover a huge plate of copper and then capped it with an extraordinarily thin film of gold leaf [**42]**. In 1954, Chaplin developed the first inorganic solar cell based on crystalline silicon, with a PCE of roughly 6%, six years since Walther H. Brattain, William B. Shockley, and John Bardeen, who were awarded the Nobel Prize for the transistor, discovered the p-n junction [**43]**. Oil embargoes in the 1970s prompted a surge in interest in alternative energies, and the first practical solar modules for global use were built in 1976 **[44]**. The development of solar cells can be considered to be in three generations. Figure 1.4 depicts the year-by-year evolution of the PCE of several solar cell systems.

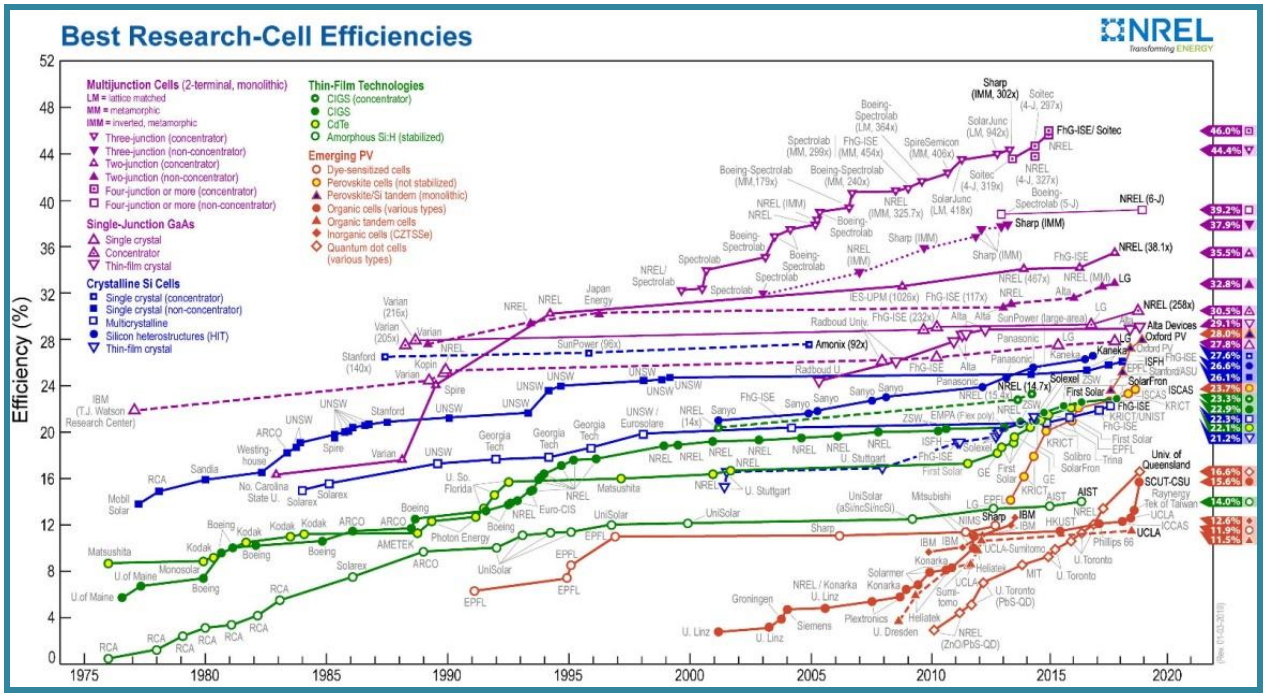

Figure 1.4 *Evolution of record cell efficiencies of various solar cell technologies. This graph is provided by the NREL.*

1.3.1 First Generation Solar Cells

Ist generation solar cells are fabricated from crystalline *Si*. This is most advanced technology for the production of solar cells at industrial scale and has a share of more than 90% in solar energy market **[45]**.

These cells are single layer p-n junction diode with large-area and are capable of generating functional electricity from solar radiation. The PCE of commercially available *Si* solar cell is about 20% **[46]**. Although the efficiency achieved at laboratory is 25% which is just closer to the theoretical efficiency of about 33% **[47]**. The main advantages of c-Si solar cells are high carrier mobility, broad spectral absorption range, and high efficiency **[48,49]**. The main drawback of crystalline *Si* solar cell is expensive production cost **[50]**. Electricity production costs are often ten times greater than fossil fuel generation costs.

1.3.2 Second Generation Solar Cells

The IInd generation solar cells include thin film semiconductors which solar cell composed of amorphous-*Si*, polycrystalline-*Si*, *CdTe*, *CIGS etc*. They are much efficient compared to Ist generation crystalline *Si* based solar cells. Amorphous *Si* solar cells have an optical band gap of 1.1-1.5 eV and perform similarly to crystalline *Si* solar cells. Polycrystalline *Si* is made up of pure Si grains and, due to its mobility, performs better than earlier designs. *CdTe* cells are less expensive than silicon, however it is not as efficient. *CIGS* cells are deposited on "glass" or "stainless steel" using complicated techniques. This generation comprises all thin-film solar cell technologies and accounts for 10 % of total solar cell manufacturing. The PCE of solar cells made from these materials is around 15-20% **[51-54].**

1.3.3 Third Generation Photovoltaic Cells

To boost the performance of IInd generation solar cells and to reduce the cost of production, IIIrd generation solar cells were introduced. A lot of research has been approved internationally to develop organic materials based solar cells which come under this generation of solar cells **[55-70]**. The main advantages of such technology are low production cost, flexible devices, light weight, large area devices, and easy fabrication

process which can be done either by spin coating or by printing technology of solution processable polymers. PCEs for single, double, and triple junction based cells have been reported in the scientific literature at roughly 12 percent [**71]**, 14 percent [72], and 17 percent [72,7], respectively. PCE of devices, on the other hand, clearly lag behind those of their inorganic first and second generation counterparts, restricting their practical applicability. In order to consistently increase the performance of PSC devices, more effort should be put into developing unique material systems, creative device structures, and standardizing production procedures.

Table 1.1 *shows the obtained conversion efficiencies[2] of single cell and module for various types of solar cells.*

PV Technology		Cell Conversion Efficiency	Module Conversion Efficiency
Crystalline	Monocrystalline silicon (Si)	27.6%	24.4%
	Multicrystalline Si	23.3%	20.4%
	Multi-junction Gallium arsenide (GaAs)	47.1%	38.9%
Thin film	Cadmium telluride (CdTe)	22.1%	19.0%
	CIGS	23.4%	19.2%
Emerging	Perovskite	25.2%	17.9%
	Organic	17.4%	11.7%

1.4 Polymer Solar Cells

Organic Solar Cells (OSCs) have emerged as a promising candidate for photovoltaic technology and have shown significant progress in the past few years. Among the OSCs, especially polymer solar cells (PSCs) have shown great potential owing to their low-cost, easy solution processing, flexible, lightweight, and ability for bandgap engineering **[1-7]**. The state-of-the-art PCE of approx. 14-15% have been realized in single-junction polymer bulk-heterojunction (BHJ) in binary blend configurations which consist of one electron-donor and one electron-acceptor **[7-14]**. However, both high PCE and good stability are simultaneously required for commercial applications. As a result, new electron-accepting and electron-donating organic materials,

optimization of blend morphologies, interface engineering, and the improvement of new device topologies have all been emphasized **[136-139]**.

1.4.1 Organic semiconductors

All organic semiconductors are comprised of alternated single and double carbon bonds having a conjugated pi-electrons electrical structure. The conjugated organic polymers or small molecules contain σ-bond and π-bond along the length of molecular structure. The π-electrons of all the carbon atoms overlap and form π-band [referred as Lowest Unoccupied Molecular Orbital (LUMO)] and π*-band [referred as Highest Occupied Molecular Orbital (HOMO)] along the conjugation path which causes the wave functions to delocalize over the conjugated backbone. The energy band gap of these conjugated organic materials fall in range 1-4 eV. The chemical structures. Of some of the typical conjugated polymers are listed below in Figure 1.5. These π-electron system posses all the crucial electronic features for solar light conversion into electricity: light absorption, carrier generation and transport.

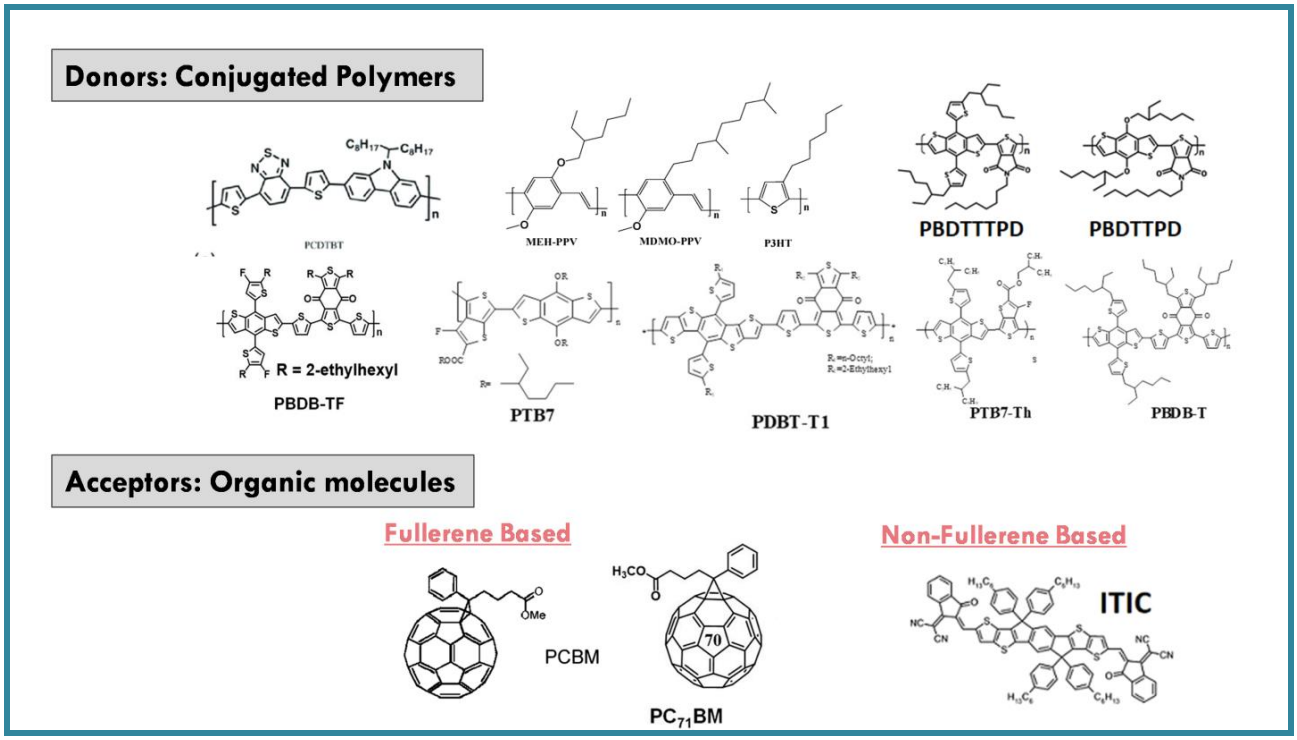

Figure 1.5 *Typical conjugated polymers and their chemical structure used in preparation of polymer solar cells.*

1.4.2 Applications of Organic semiconductors

- ❖ Appreciably lower production costs by deposition techniques under low temperature compared to conventional inorganic technologies
- ❖ Modules of OPV devices have low weight and mechanically flexible, that's why these devices can be used in mobile devices.
- ❖ Manufacturing of OPV in a continuous process using state of the art printing tools.
- ❖ New market opportunities, e.g. wearable PV.
- ❖ Wide range of applications due to semi-transparent nature of devices.
- ❖ Non-toxicity and low consumption of abundant absorbing materials.
- ❖ Due to light weight, these devices can be easy integrated into other products.

1.4.3 Device Architecture of Polymer Solar Cells

The typical diagram of PSCs is illustrated in Figure 1.6, in which active materials, hole transport layer (HTL) and electron transport layer (ETL) are sandwiched systematically between indium tin oxide (ITO) acting as an anode and aluminium metal (low work function) that acts as a cathode in conventional structure. Although there has been a lot of research into polymer-based solar cells, these cells are not commercially viable due to their low efficiency and short life span when compared to *Si*-based solar cells. Investigating new donor and accepter materials, alternative HTL and ETL, altering device architecture, new fabrication and processing methods, and seeking for optimal encapsulation materials are the key challenges for PSCs.

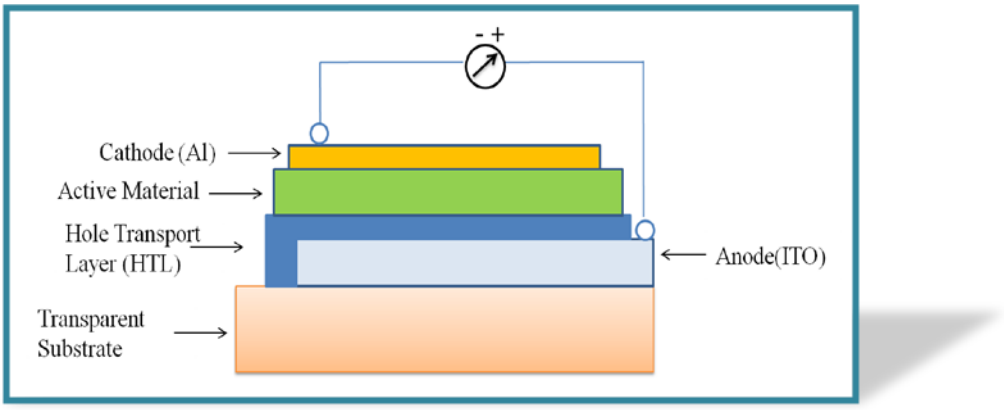

Figure 1.6 *Schematic diagram of polymer solar cells in which HTL and active material is sandwich in between ITO coated anode and aluminium cathode.*

The device architecture of PSCs reported in the literature can be classified as single layer, bilayer and bulk-heterojunction. The development of different configurations be motivated by the desire to improve PCE by improving the PV processes in conjugated polymer materials.

1.4.3.1 Single Layer Solar Cells

The first PSC was very simple where a single layer of polymer active layer is sandwiched between two electrodes, usually a transparent conductive oxide (TCO) anode and a metal cathode. Figure 1.7 illustrates the typical structure of single layer solar cell. For example, a solution of P3HT polymer was inserted in between ITO electrode and aluminium electrode. The efficiency was very less about only 0.1% which is the main limitation of single layer solar cells. The electrical field generated at active material is due to the difference in work function of two electrodes which is very less for efficient exciton dissociation in polymers **[73, 74].** Moreover, recombination losses are very high due to movement of holes and electrons in the same material **[75].**

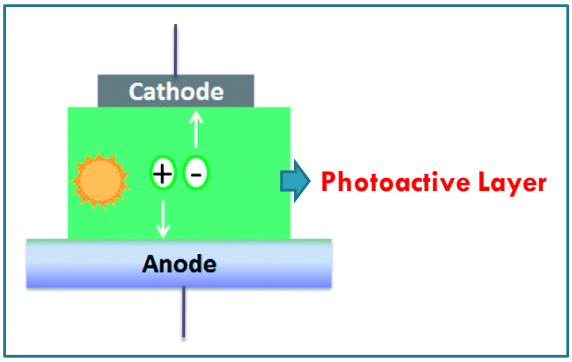

Figure 1.7 *Schematic diagrams of single layer solar cell device **[76].***

1.4.3.2 Bilayer Solar Cells

The development in PSC took place further on by making the active layer via depositing two semiconducting layer one composed of electron donor (D) and the other one as electron acceptor (A). The energy level structure for this donor-acceptor (D-A) bilayer device is depicted in Fig. 1.8. These bilayer devices showed improvement in the exciton dissociation/separation process [**76-87**].

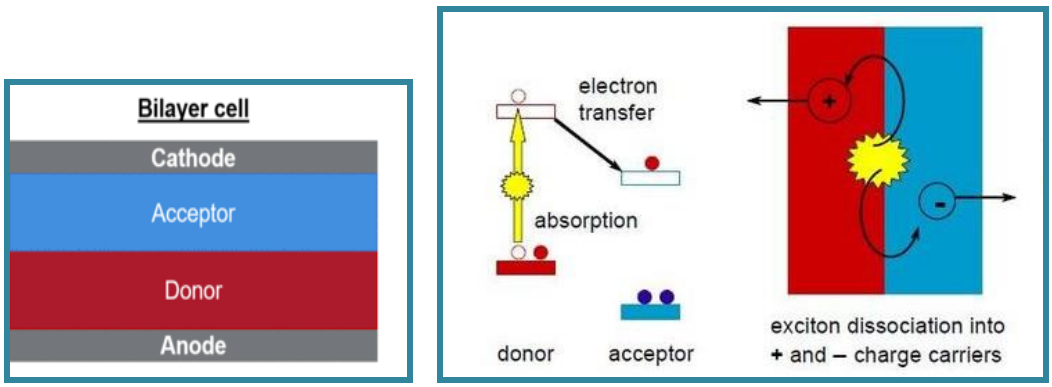

Figure 1.8 *Schematic diagrams of bilayer hetero junction solar cell devices and its energy level diagram* **[76]**.

Charge transfer at a donor–acceptor interface is used to photogenerate charge carriers in such devices. For an example this charge transfer process **[76, 77]** from a PPV polymer (D) to PCBM (A) molecules has been represented in Fig. 1.9 shown below. Because the donor and acceptor components have different relative energy levels, the excitons can be separated at the D-A contact (shown in Fig. 1.8). The materials for the donor and acceptor were previously stated in Fig.1.5. Charge generation occurs with close efficiency 1% PCE if the exciton diffusion length is greater than the length to the D-A contact interface.

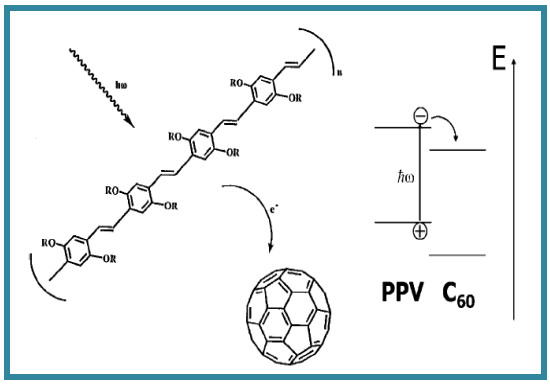

Figure 1.9 *Photograph of the photo-induced charge transfer in the PPV polymer to the C_{60} or PCBM.*

For numerous reasons, the bilayer configuration is preferable to the single layer structure: The D-A interface improves exciton splitting, the active zone is expanded to both the D and A portions of the junction, almost doubling its dimension to around 20

nm, and electron & hole transport is divided into different materials, which substantially lower the recombination-losses **[76].** Furthermore, the band gap can theoretically modified to match well with the solar radiation by employing two distinct semiconductors. For such bilayer devices, PCE of 1.5 % to 4 % were being observed **[88-90].**

The disadvantage of both single and bi-layer architecture **[77, 91]** is that the exciton dissociation occurs far from the collecting electrodes. Only excitons produced within 10 - 20 nm of the electrodes (single-layer devices) and the DA interface (bi-layer devices) can reach the electrodes and be collected in these devices. This results in low quantum efficiencies. The notion of an inter penetrating network of donor and acceptor was devised to solve this difficulty. Better efficiencies have been demonstrated in PSC employing bulk-heterojunction (BHJ).

1.4.3.3 Polymer-Fullerene Bulk-heterojunction Devices

In BHJ devices, the photoactive layer comprise of interpenetrating phase separated BHJ **[92-99]** blend of donor and acceptor where both the phases are intimately intermixed such that the interface lie within the diffusion length of the photogenerated excitons. The BHJ approach has significantly enlarged the interfacial region between the D and A, resulting in higher efficiency **[92-99].** Schematic representation of such a bulk-heterojunction solar cell is shown in Fig.1.10.

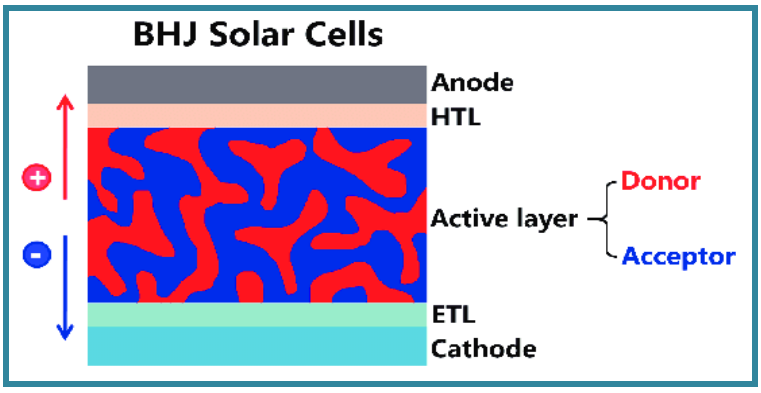

Figure 1.10 *Bulk-heterojunction configuration in PSC along with donor(D)-acceptor(A) and schematic representation of phase separated interpenetrating polymer: fullerene bulk heterojunction* ***[76].***

The efficiency of charge transfer in a D-A bulk heterojunction **[77, 100, 101, 76]** is ultra fast because the separation time of the charge carriers at the D-A interface is in femto-second range whereas their recombination time is in milli-seconds. Therefore, it leads to almost 100% exciton dissociation efficiency. These charge carriers must now be transferred to the appropriate electrodes. For this, the conception of phase separated interpenetrating network of D-A components has shown promising results and efficiency of polymer solar cells as high as ~ 10-12% have been reported **[102].** However, still a lot is desired to be done in these bulk heterojunction based polymer solar cells for improving their efficiency and stability before one can think of commercializing this cost effective technology.

1.4.4 Polymer Solar Cell: Working Principle

The typical device structures of PSC are schematically revealed in Fig. 1.8 and Fig. 1.10. The photoactive layer consists of two organic semiconductor materials, one serving as an electron donor and one serving as an electron acceptor. Light excites an electron from the HOMO level of the donor materials to its LUMO level. After excitation, electrons leave behind a positively charged hole. An exciton is a quasi-particle made up of an electron and a hole that is bound together by Coulomb interactions. By choosing materials with suitable work functions, one can create a driving force for the exciton to split up and its components to drift towards each electrode. The principle is illustrated in Figure 1.11.

The photovoltaic processes that occur in PSCs can be broken down into five steps, Absorption of photons, Exciton generation, Diffusion and dissociation of exciton into free charges, Transport of charge carriers to the electrodes and collection, as represented in an energy diagram shown in Fig. 1.11.

Here, the processes of conversion of light into electricity by an organic solar cell can be schematically described with the following steps:

1. Light absorption and Exciton Generation: Absorption of a photon leading to the formation of an excited state, that is, the bound electron hole pair (exciton) creation.
2. Exciton Dissociation and Separation: Exciton diffusion to a region where exciton dissociation, i.e., charge separation occurs.

3. Charge Collection: Charge transport within the organic semiconductor to the respective electrodes.

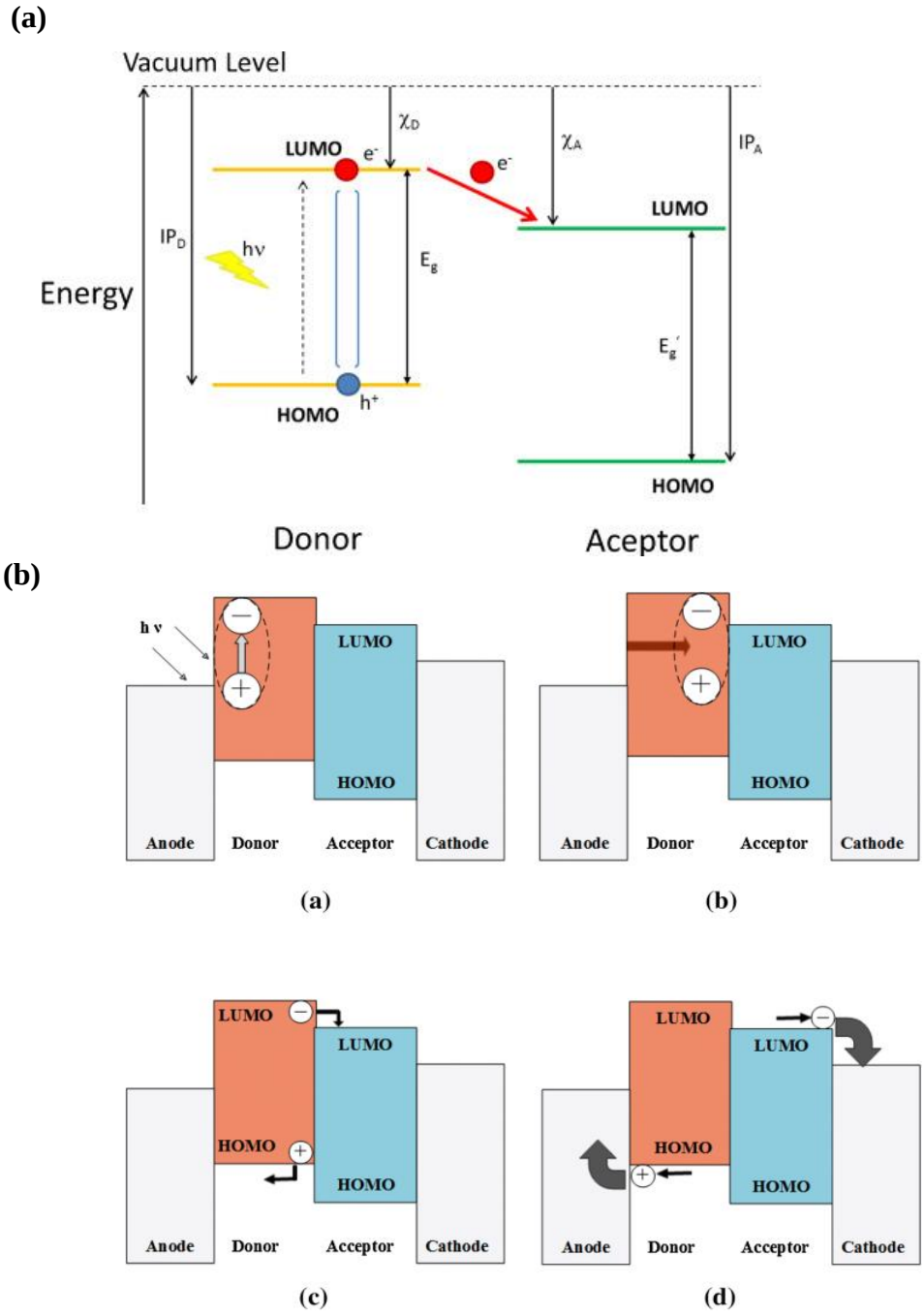

Figure 1.11 *(a) Energy level diagram, (b) Scheme of all the elementary physical processes occurring in PSC* ***[103].***

1.4.5 Solar Cell Performance

A solar cell is a semiconductor device that turns light into electrical energy directly. A solar cell's equivalent circuit in terms of a current generator and a diode can be drawn. This is equivalent circuit and current-voltage (*I-V*) characteristic of a solar cell under illumination is shown in Fig. 1.12 (a and b) **[112]**. At the maximum power point (MPP), the current is I_{MPP} and voltage is V_{MPP}. It should be noted that at open cuiruit voltage, V_{OC}, the photo-current is zero, whereas at short-circuit current J_{SC} the photo-voltage is zero.

A further significant feature of the solar cell characteristic is the "fill factor (*FF*)" described as,

$$FF = \frac{V_{MPP} \times I_{MPP}}{V_{OC} \times I_{SC}}, \tag{1}$$

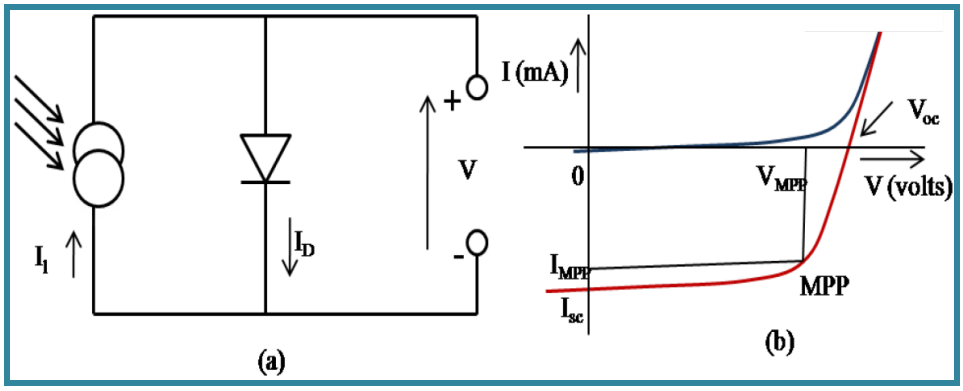

Figure 1.12 (a) *Equivalent circuit diagram of solar cell, and (b) I-V characteristic of solar cell* V_{OC}, I_{SC}, *and* I_{MPP}, V_{MPP} *at MPP point* ***[111].***

Thus, the "maximum output power of the solar cell" is mentioned as,

$$P_{\max} = V_{MPP} \times I_{MPP} = J_{SC} \times V_{OC} \times FF, \tag{2}$$

At last, the PCE (η) of the solar cell is defined as "power produced by the cell (P_{max}) divided by the power incident (P_{light}) on the cell":

$$\eta = \frac{P_{\max}}{P_{Light}}, \tag{3}$$

Different solar cells compared with each other in terms of *FF*, V_{OC}, and I_{SC}. The PEC of different solar cells is affected by the cell's temperature and, more crucially, the quality of solar illumination, which includes total light intensity and spectral distribution

[112]. As a result, a standard measuring condition has been established to make solar cell assessment more similar across labs.

The standard condition used for characterizing the solar cells:

(i) light intensity : 1000 W/m^2

(ii) spectral distribution of the light source should match with AM1.5 global standard solar spectrum. For standard measurements, specific solar simulator light sources are employed in practice.

(iii) temperature of the cell: 25 ^{0}C.

1.4.6 Literature review of BHJ polymer solar cells

The reported values of PCE for different combinations of donor polymers and acceptor in single junction or multiple junction architecture are presented in Table 1.2.

Table 1.2 *Summary of recently reported efficiencies of different polymer BHJ solar cells [113].*

S.No	Donor polymer/ acceptor material	Architecture	Bandgap (eV)	Efficiency (%)	Year	References
1	PTPTB:$PC_{61}BM$	Single junction	1.7-2.1	1	2004	Winder and Sariciftci, 2004
2	PEOPT:$PC_{61}BM$	Single junction	1.75	0.02	2004	Winder and Sariciftci, 2004
3	PFDTBT:$PC_{61}BM$	Single junction	1.9	2	2004	Winder and Sariciftci, 2004
4	P3HT:$PC_{61}BM$	Single junction	2.1	2.8	2006	Vanlaeke et al., 2006
5	PCPDTBT:$PC_{71}BM$	Single junction	1.70	3.2	2006	Muhlbacher et al., 2006
6	PCPDTBT:$PC_{70}BM$	Single junction	1.70	5.1	2008	Hou et al., 2008
7	PCDTBT:$PC_{70}BM$	Single junction	1.8	6.1	2009	Park et al., 2009
8	P3HT:$PC_{61}BM$	Single junction	2.1	4.4	2010	Tsai et al., 2010
9	PCDTBT:$PC_{70}BM$	Single junction	1.8	7.1	2011	Chu et al., 2011
10	P3HT:$PC_{61}BM$	Single junction	2.1	3.37	2012	Albrecht et al., 2012
11	P3HT:$PC_{61}BM$	Single junction	2.1	3.68	2012	Li et al., 2012
12	P3HT:$PC_{61}BM$	Single junction	2.1	3.9	2012	Albrecht et al., 2012
13	PCPDTBT:$PC_{70}BM$	Single junction	1.70	6.16	2012	Albrecht et al., 2012
14	P3HT:$PC_{61}BM$	Single junction	2.1	4.24	2013	Zhou et al., 2013
15	PTB7:$PC_{70}BM$	Single junction	1.6	7.9	2013	Zhou et al.,

						2013
16	**PBDTP-DTBT:$PC_{71}BM$**	**Single junction**	**1.70**	**8.07**	**2013**	**Zhang et al., 2013**
17	**PTB7:$PC_{70}BM$**	**Single junction**	**1.6**	**8.67**	**2013**	**Lu et al., 2013**
18	**P3HT:ICBA/PDTP-DFBT:$PC_{61}BM$**	**Tandem junction**	**1.24**	**10.6**	**2013**	**You et al., 2013**
19	**P3HT:$PC_{61}BM$**	**Single junction**	**2.1**	**4.24**	**2014**	**Chi et al., 2014**
20	**PCDTBT:$PC_{70}BM$**	**Single junction**	**1.8**	**7.20**	**2014**	**Liu et al., 2014b**
21	**PDVT-10/PBDTTT-EFT:$PC_{71}BM$**	**Single junction**	**1.84**	**10.08**	**2015**	**Liu S. et al., 2015**
22	**PTB7-th/ZnO/CPEs:$PC_{71}BM$**	**Tandem junction**	**1.6**	**11.3**	**2015**	**Zhou et al., 2015**
23	**PBDB-TF:IT-4F**	**Single junction**	**1.89**	**13.7**	**2018**	**Li et al., 2018**
24	**PFN-Br/PBDB-T:FM/PTB7-th:O6T-4F:$PC_{71}BM$**	**Tandem junction**	**1.25**	**17.3**	**2018**	**Meng et al., 2018**

1.4.7 Strategies to boost the performance of Solar Cells

In BHJs, even with properly chosen photoactive layer material i.e, polymer donors and acceptors, electrons and holes may still diffuse randomly within the material and end up at the wrong electrode, where it will recombine with its counterpart and thereby constitute an energy loss. It is to prevent such losses, and to promote transport of charges, a HTL and an ETL have been integrated into the device structure. Such HTL and ETL are called as interface transport layers (shown in Fig.1.13) .

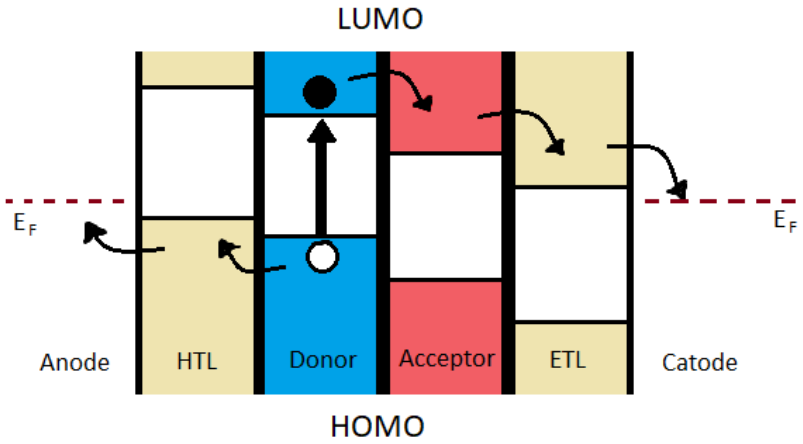

Figure 1.13 *Electrons moving downwards energy bands and holes moving upwards energy bands via ETL and HTL, respectively.*

Hence, it is concluded that a proper choice of photoactive layer and interface transport layers are crucial to achieve good performance of PSCs.

1.4.7.1 Tandem solar cells

The device architecture of the PSCs documented in the literature can be classified as single layer, bilayer, or bulk. The development of these structures is motivated by the desire to improve the PCE by improving the exciton dissociation and carrier collection processes in the active layer **[126,127]**.

One technique to improve the PCE is by stacking two or more "sub-cells" which show complementary absorption to harvest low and high energy photons in the different "sub-cells", called as tandem solar cells. This architecture enhance the absorption of light as well as reduce the thermalization loss as compared to single-junction PSCs **[114-120],** as depicted in Fig. 1.14 (b).

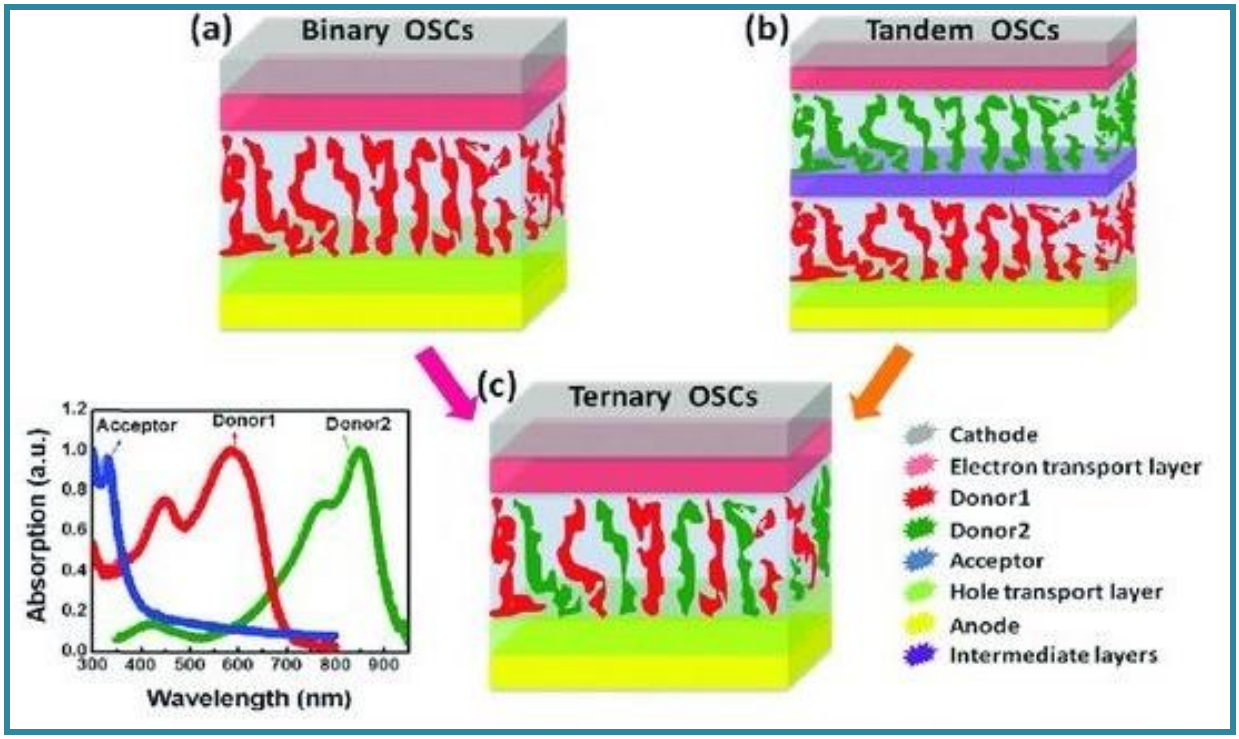

Figure 1.14 *Schematic representation of configuration, (a) binary PSCs, (b) tandem PSCs, and (c) ternary OSCs* ***[114].***

1.4.7.2 Ternary blend based polymer solar cells

However, due to the complexity of tandem solar cell technology, Recently, ternary polymer solar cells (TPSCs) have emerged as one of the most promising candidates for achieving high performance which utilizes the concept of solar absorption in complimentary parts of the solar spectrum. The schematic of TPSCs are shown in Fig. 1.14 (c) where a ternary blend is used as photoactive-layer. Here, ternary blends can be made by blending two donors and one acceptor, resulting in (D_1:D_2:A)-type; or two acceptors in one single donor materials, resulting in (D_1:A_1:A_2)-type ternary blends **[18-20].** In general, the active layers of TPSCs comprise three elements: the dominant D:A system and a third-component, which can be a polymer, a small molecule, a dye, or a nanoparticle **[128-135].**

Ternary Solar Cells: Architectures and Working Mechanism

TPSCs have drawn interest because they not only give a substantial light harvesting advantage through complementary-absorption, but they also increase charge generation and carrier collecting features **[136-146].** The TPSC using D_1:D_2:A blend, in particular, demonstrate the benefits of broad solar absorption and simple design.

Furthermore, in these ternary blends based on the HOMO and LUMO energy levels of the respective D and A, "cascade-energy alignment" is documented. The creation of three different cascade structures has been acknowledged in the literature, depending on their distinct band-gaps, is depicted in Fig.1.16.

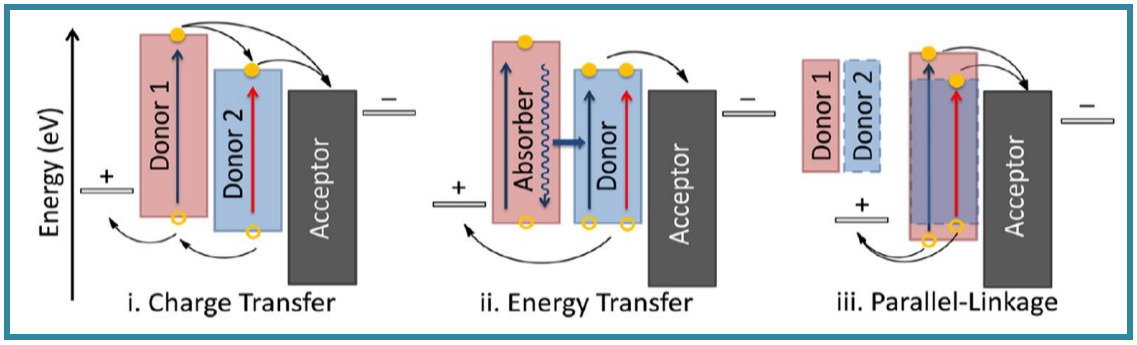

Figure 1.15 *Schematic of three fundamental mechanisms (charge transfer, energy transfer, and parallel linkage) in ternary solar cells to boost the performance of TSCs.*

Many ternary blend reports show increased exciton dissociation probability in diverse ternary blend systems via two know fundamental phenomenon such as "Förster resonance

energy transfer (FRET)" between D-D and "charge transfer (CT)" at the D-A interface owing to "cascade energy alignment" **[141,146,147].** As seen in Fig. 1.16 (a-c), the first category is A-Type [D_1: D_2 (low E_g): A] blend system wherein both FRET & CT is possible. B-type [D_1: D_2 (low E_g): A] blend also represents the same yet with different energy alignment. However, the third category, C-Type [D_1: D_2 (high E_g): A] blend system, demonstrate that only CT with no possibility of FRET **[137, 148].**

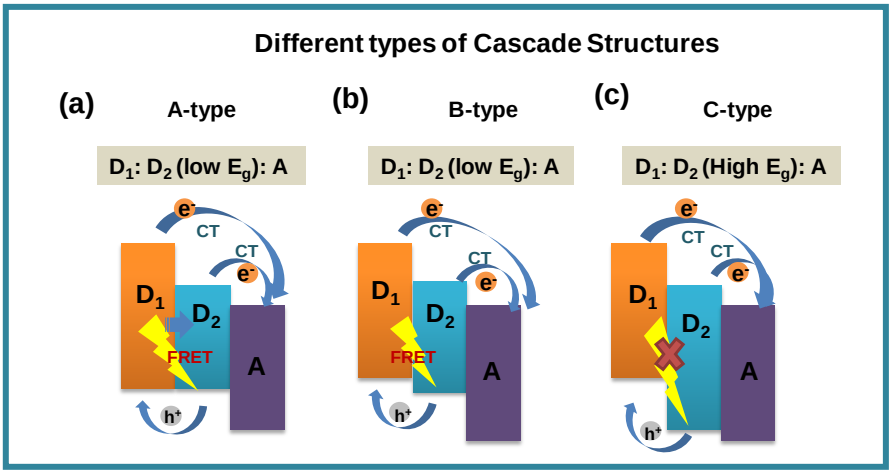

Figure 1.16. *Schematic energy diagrams of different cascades of dual donor and acceptor interfaces in ternary blends.*

All three types of cascading ternary blends have been reported for TPSCs in the literature, with PCEs increasing by 30-50 percent due to sensitization emission and significant PL reduction owing to FRET/CT induced increased exciton separation in the ternary blend **[137, 149].** However, there are few information on the dynamics of excitons dissociation and its impact on device performance in these (D_1:D_2:A) systems.

Literature Review of Ternary Solar Cells:

Inspiringly, the PCEs of TPSCs have exceeded 10%, showing great potential for obtaining high performance TPSCs **[150, 151],** as summarized in Table 1.3. For further enhancement, several elementary physical issues are required to be elucidated, hence, needed further exploration.

Table 1.3 *Summary of the PV performance of ternary and binary solar cells* ***[114]*** *under the AM 1.5G illumination at 100 mW cm^{-2}.*

	Photovoltaic parameters (binary)						**Photovoltaic parameters(ternary)**				
Binary blend [D:A]	**Jsc [mA cm^{-2}]**	**Voc [V]**	**FF [%]**	**PCE [%]**	**The third component (TC)**	**Ratio [D:TC:A]**	**Jsc [mA cm^{-2}]**	**Voc [V]**	**FF [%]**	**PCE [%]**	**Ref.**
PTB7-th:PC$_{71}$BM	**17.53**	**0.805**	**65.26**	**9.2**	**P-DTS (FBTTH$_2$)$_2$**	**0.85:0.15:1.1**	**18.44**	**0.755**	**75.27**	**10.5**	**150**
P-DTS(FBTTH$_2$)$_2$:PC$_{71}$BM	**12.63**	**0.711**	**59.74**	**5.40**							
PTB7-EFT:PC$_{71}$BM	**17.11**	**0.786**	**65.1**	**8.75**	**PDVT-10**	**1:0.005:1.5**	**18.73**	**0.78**	**69.0**	**10.08**	**151**
PTB7-th:PC$_{71}$BM	**14.92**	**0.75**	**70.3**	**7.88**	**PID2**	**0.8:0.2:1.5**	**16.68**	**0.78**	**70.8**	**9.20**	**159**
PID2:PC$_{71}$BM	**5.29**	**0.86**	**44.3**	**2.01**							
PTB7:PC$_{71}$BM	**14.7**	**0.731**	**63.5**	**6.8**	**PCDTBT**	**0.7:0.3:2**	**17.1**	**0.795**	**65.4**	**8.9**	**160**
PTB7:PC$_{71}$BM	**14.99**	**0.701**	**68.8**	**7.35**	**ICBA**	**1:0.225:1.275**	**16.68**	**0.735**	**71.2**	**8.88**	**161**
PTB7:ICBA	**10.84**	**0.873**	**50.1**	**4.83**							
PTB7:PC$_{71}$BM	**15.1**	**0.72**	**66.3**	**7.2**	**PBDTT-SeDPP**	**0.5:0.5:2**	**18.7**	**0.69**	**67.4**	**8.7**	**162**
PBDTT-SeTDP:PC$_{71}$BM	**16.9**	**0.68**	**62.9**	**7.2**							
α-6T/SubPc	**7.46**	**1.09**	**57.9**	**4.69**	**SubNc**		**14.55**	**0.96**	**61.0**	**8.40**	**158**
α-6T/SubNc	**12.04**	**0.94**	**53.9**	**6.02**							
PBDTTPD-HT:PC$_{71}$BM	**11.79**	**0.99**	**58.14**	**6.85**	**BDT-3TCNCOO**	**0.6:0.4:1**	**12.17**	**0.969**	**71.23**	**8.40**	**163**
BDT-3TCNCOO:PC$_{71}$BM	**10.11**	**0.968**	**72.63**	**7.48**							
PTB7:PC$_{71}$BM	**15.0**	**0.72**	**67.1**	**7.25**	**PID2**	**0.9:0.1:1.5**	**16.8**	**0.72**	**68.7**	**8.22**	**164**
PID2:PC$_{71}$BM	**5.27**	**0.86**	**44.4**	**2.01**							
LP2:PC$_{71}$BM	**11.80**	**0.97**	**64.0**	**7.32**	**LP4**	**0.5:0.5:3**	**13.88**	**0.94**	**62.0**	**8.09**	**165**
LP4:PC$_{71}$BM	**13.15**	**0.90**	**56.0**	**6.63**							
SMPV:PC$_{71}$BM	**9.22**	**0.92**	**69**	**5.85**	**SQ**	**0.9:0.1:1**	**11.18**	**0.92**	**72**	**7.40**	**166**

SQ:$PC_{71}BM$	**4.50**	**0.90**	**28**	**1.13**							
DTffBT:PCBM	**12.2**	**0.91**	**56.5**	**6.26**	**DTPyT**	**0.5:0.5:1**	**13.7**	**0.87**	**58.9**	**7.02**	**167**
DTPyT:PCBM	**12.8**	**0.85**	**58.1**	**6.30**							
ASSQ/C_{60}	**7.46**	**0.97**	**58.3**	**4.22**	**SQ**	**1:2/C60**	**10.05**	**0.87**	**70.3**	**6.15**	**168**
SQ/C_{60}	**9.05**	**0.81**	**63.5**	**4.65**							
P3HT75-co-EHT25:PCBM	**7.96**	**0.675**	**59**	**3.16**	**P3HTT-DPP-10%**	**0.9:0.1:1.1**	**15.05**	**0.603**	**61**	**5.51**	**169**
P3HTT-DPP-10%:PCBM	**14.38**	**0.57**	**62**	**5.07**							
PBTADN:$PC_{71}BM$	**6.9**	**0.83**	**53.1**	**3.0**	**BantHBT**	**1:0.2:4**	**11**	**0.91**	**56.4**	**5.6**	**170**
P3HT:PCBM	**7.1**	**0.57**	**63**	**2.5**	**PCPDTBT**	**0.8:0.2:1**	**8.02**	**0.62**	**55.4**	**2.8**	**171**
P3HT:PCBM	**8.6**	**0.57**	**63.6**	**3.1**	**Si-PCPDTBT**	**0.6:0.4:1**	**11**	**0.59**	**62.1**	**4.0**	**172**
P3HT:ICBA	**7.9**	**0.82**	**60.1**	**3.9**	**Si-PCPDTBT**	**0.8:0.2:1**	**10**	**0.79**	**64.9**	**5.1**	**173**
P3HT:PCBM	**10.3**	**0.59**	**53**	**3.27**	**SQ**	**1:0.01:1**	**11.6**	**0.60**	**64.8**	**4.51**	**174**
P3HT:PCBM	**9.69**	**0.55**	**66**	**3.5**	**SiPc**	**1:0.048:1**	**11.1**	**0.58**	**65**	**4.2**	**175**
PCDTBT:$PC_{71}BM$	**10.79**	**0.86**	**68**	**6.3**	**Ag NPs (40nm)**	**1:0.01:4**	**11.61**	**0.88**	**69**	**7.1**	**176**
PTB7:$PC_{71}BM$	**16.71**	**0.732**	**68.03**	**8.31**	**Au:BCNT**	**-**	**18.50**	**0.743**	**72.61**	**9.98**	**177**
$CH_3NH_3Pb_{3-x}Cl_x$	**19.3**	**0.98**	**72.9**	**13.8**	**DOR3T-TBDT:$PC_{71}BM$**	**-**	**21.2**	**0.99**	**67.9**	**14.3**	**178**
$CH_3NH_3Pb_{3-x}Cl_x$	**18.1**	**0.89**	**60.4**	**9.7**	**PBDTT-SeDPP:$PC_{71}BM$**	**-**	**20.6**	**0.94**	**62.0**	**12.0**	
$CH_3NH_3PbI_3$	**13.09**	**0.90**	**80.33**	**9.46**	**PDPP3T:PCBM**	**-**	**13.93**	**0.88**	**71.78**	**8.80**	**179**
PDPP3T:PCBM	**8.82**	**0.67**	**67.07**	**3.96**		**-**					

1.4.7.3 Hole Transport Layers (HTL)

The introduction of an interlayer between the photoactive material and the anode, referred to as HTL is one technique to improve the PCE. The HTL material is chosen based on a number of criteria. In order to create the driving force for holes to move towards the anode of the device, the HTL should have a high enough work function to

match the HOMO of the donor. To prevent the drift of electrons towards the anode, the HTL should have its conduction band (CB) above the LUMO of the material. These criteria makes for good ohmic contact between the anode and the photoactive layer, since holes move upwards energy bands, while simultaneously shielding the anode from electrons, whom are moving downwards energy bands.

Apart from these energy band properties, there are a few more criteria that need to be met for a material to be suitable for use as a HTL in solar cells. In the conventional device structure, the material used as a HTL must be transparent enough to allow for light to pass through into the photoactive layer, and it needs to be cost effective in production. The material should also have a high hole mobility, and be stable enough to prevent degradation of the cell.

PEDOT:PSS which is normally used as HTL offers various desired properties such as "optical transparency, simple processing and good ohmic contact between anode and photoactive material". However, PEDOT:PSS is highly degrading which leads to reduced stability of these PEDOT:PSS based devices. In view of this, investigations into other materials to serve as a substitute for PEDOT:PSS are being done. Alternately, transition metal oxides such as MoO_3, V_2O_5, WO_3, NiO etc. have been employed based on favorable energy alignment, and the increased device stability has been reported by several groups **[180-183]**. But, depositing these materials via the expensive high-temperature vacuum deposition brings not only complicity, but also not suitable for large area roll to roll production.

1.4.7.4 Engineering PEDOT:PSS HTL using 2D Materials

PEDOT:PSS is an inefficient electron-blocking material compared to other promising hole transport layers by reducing device current efficiency due to electron leakage to the anode. To overcome these limitations, currently, several 2D nanosheets such as "Graphene Oxide (GO), molybdenum disulfide (MoS_2), tungsten disulfide (WS_2), tungsten diselenide (WSe_2)" were investigated to replace PEDOT:PSS **[184]**. 2D materials such as are added in active layer, hole transport layer, and electron transport layer to improve their properties. Among these, Graphene Oxide (GO) is one of the most interesting materials, because unique opto-electronic properties. It also prove to offer long-term stability to the solar cells. Their ability to deposit on flexible substrates via a

roll-to-roll process using the simple solution and room temperature processing has also been very impressive. Therefore, GO and GO derivatives are regarded as promising candidates and reported to grantee high efficient and high stable PSCs.

Generally, despite possessing the favorable high work-function match well with the HOMO of the respective donor polymers, but the insulating property of GO limits its use as HTL in enhancing the device performances of PSCs. Their application for scalable and reproducible manufacturing of PSCs becomes difficult. Nevertheless, integrating GO with PEDOT:PSS i.e., building the hybrid PEDOT:PSS-GO composite HTL is also a promising strategy with can complement the drawbacks of single GO and conventional PEDOT:PSS **[185-187]**. Since past few years, both GO and hybrid PEDOT:PSS-GO in the bilayer and composite form has been widely used as HTLS and have shown encouraging results in achieving good interfacial hole extraction properties, high electron blocking, high film optical transparency, surface morphology, and high conductivity, which have significantly improved the PCE and stability of the PSCs devices.

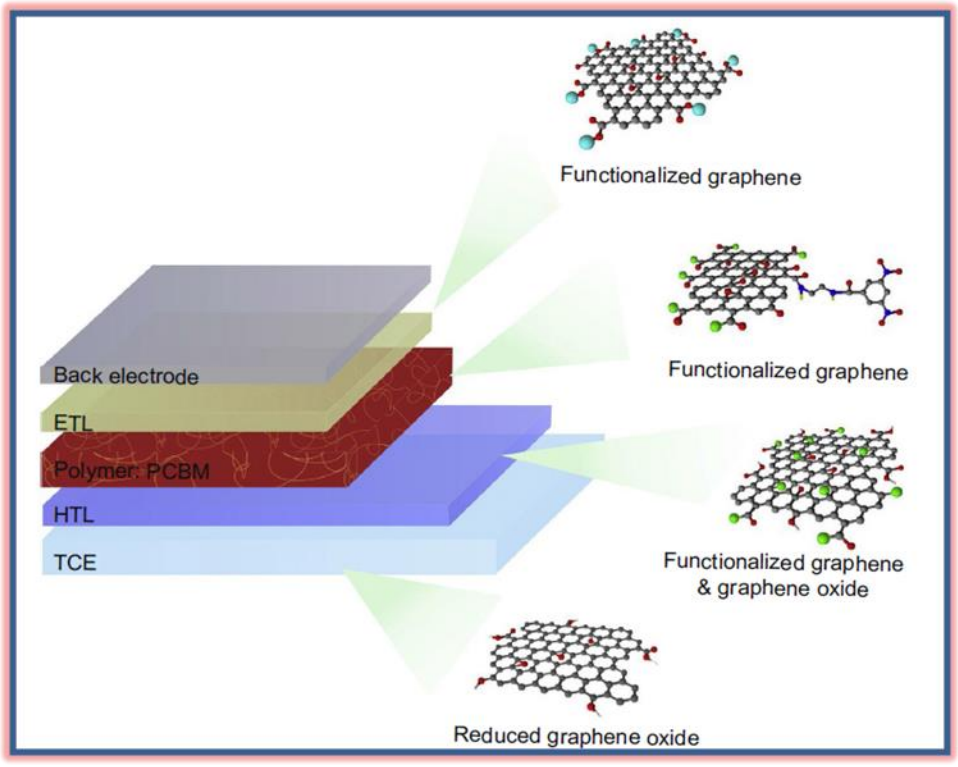

Figure 1.17 *Graphene, Graphene Oxide and its derivatives are used in ETL and HTL, respectively.*

There are numerous articles signifying the utilization of different 2D materials as ternary additive component into the photoactive layer of TPSC, summarized in Table 1.4 **[188,189].**

Table 1.4. *A summary of the key photovoltaic parameters of the optimum ratios of BHJ ternary OSCs incorporating 2D materials* ***[202].***

Donor	Acceptor	Third Component		Jsc (mA/ cm^{-2})	Voc (V)	FF (%)	η(%)	Ref
		Name	Ratio (%)					
P3HT	$PC_{61}BM$	SPF Graphene	10	5.30	0.64	41.0	1.40	191
P3HT	$PC_{61}BM$	Pristine Graphene	1	3.60	0.52	36.0	0.70	192
P3HT	$PC_{61}BM$	Graphene	0	7.25	0.60	65.0	2.79	193
			2	7.91	0.60	66.0	3.17	
P3HT	$PC_{61}BM$	N-rGO	0	10.65	0.59	52.0	3.19	194
			0.5	14.95	0.59	51.0	4.48	
PCDTBT	$PC_{71}BM$	GNF-EDNB	0	11.58	0.89	54.6	5.59	195
			0.05	12.91	0.90	57.6	6.59	
PCDTBT	$PC_{71}BM$	GO-TPP	0	11.49	0.88	57.1	5.80	196
			0.3	13.61	0.89	58.9	7.13	
PTB7	$PC_{71}BM$	GO-TPP	0	16.50	0.76	60.4	7.60	196
			0.3	18.27	0.77	62.7	8.81	
PCDTBT	$PC_{71}BM$	rGO-Sb_2S_3	0	11.60	0.90	54.6	5.58	197
			0.25	13.80	0.93	55.5	7.00	
PTB7	$PC_{71}BM$	GOQD	0	15.20	0.74	59.7	6.70	198
			0.2	16.10	0.73	60.4	7.11	
PTB7	$PC_{71}BM$	GQD5	0	15.20	0.74	59.7	6.70	198
			0.5	15.20	0.74	67.6	7.60	

PTB7	**$PC_{71}BM$**	**GQD 10**	**0**	**15.20**	**0.74**	**59.7**	**6.70**	**198**
			0.02	**15.30**	**0.74**	**63.6**	**7.21**	
P3HT	**$PC_{61}BM$**	**GQD**	**0**	**14.27**	**0.59**	**31.0**	**2.91**	**199**
			0.6	**26.46**	**0.60**	**33.0**	**5.64**	
PCDTBT	**$PC_{71}BM$**	**WS_2**	**0**	**10.70**	**0.90**	**60.5**	**5.7**	**200**
			1.5	**12.10**	**0.88**	**59.3**	**6.2**	
PCDTBT	**$PC_{71}BM$**	**WS_2-Au**	**0**	**10.70**	**0.90**	**60.5**	**5.7**	**200**
			1.5	**12.50**	**0.90**	**58.6**	**6.4**	
PTB7	**$PC_{71}BM$**	**S-WSe_2**	**0**	**15.12**	**0.73**	**67.5**	**7.54**	**201**
			2	**15.28**	**0.72**	**69.0**	**7.86**	
PTB7	**$PC_{71}BM$**	**M-WSe_2**	**0**	**15.12**	**0.73**	**67.5**	**7.54**	**201**
			2	**17.04**	**0.72**	**69.5**	**8.78**	
PTB7	**$PC_{71}BM$**	**L-WSe_2**	**0**	**15.12**	**0.73**	**67.5**	**7.54**	**201**
			2	**16.24**	**0.72**	**68.7**	**8.16**	

1.5 Motivation and scope of the current work

Significant progress has been made in TPSCs to demonstrate the PCE reaching ~10-12%, however, fundamental working principle in these TPSCs are still under investigations. Furthermore, it is necessary to manage the blend-morphology and optimize PV activities like "exciton formation, dissociation, carrier generation, charge transfer, and collection" in order to advance the performance of TPSCs. However, identifying the underlying mechanisms was not simple and necessitated substantial research. A detailed and in-depth studies on the morphology and photo charge carrier dynamics in the ternary system are very limited.

Also, despite possessing the favorable high work-function match well with the HOMO of the respective donor polymers, but the insulating property of GO limits its use as HTL in enhancing the device performances of PSCs. Their application for scalable and reproducible manufacturing of PSCs becomes difficult. Nevertheless, integrating GO with PEDOT:PSS i.e., building the hybrid PEDOT:PSS-GO composite HTL is also a

promising strategy which can complement the drawbacks of single GO and conventional PEDOT:PSS [203, 204]. Since past few years, both GO and hybrid PEDOT:PSS-GO in the bilayer and composite form has been widely used as HTLs and have shown encouraging results in achieving good interfacial hole extraction properties, high electron blocking, high film optical transparency, surface morphology, and high conductivity, which have significantly improved the PCE and stability of the PSCs devices. However, several groups have reported the use of PEDOT:PSS-GO as HTLs mostly with binary blend BHJ system combinations and reported enhanced PCE as high as 10% [204]. This provides a motivational platform to explore the potential use of PEDOT:PSS-GO HTLs for the design and development of ternary blend systems based PSC technology also.

The main scientific challenges in improving the performance of such 2D materials and ternary-blend based solar cells is, (i) Optimization the Morphology of the active layer for better Charge Dissociation, carrier mobility, and charge transport, (ii) Recombination in the active layer and at the HTL/Active layer interface need to be controlled for enhanced carrier collection, and (iii) Device stability also need to be improved.

Therefore, the motivation of the present thesis work is as follows:

- To elucidate the elementary physical principles prevailing the photovoltaic process in ternary solar cells.; and compare ternary blends with binary blends.
- To explore Carbon based 2D Materials for their utilization in ternary solar cells

The scope of the present thesis is to carry out the in-depth investigations to address the scientific challenges observed in the ternary solar cells. Revealing this knowledge will help in understanding the device physics and improving the performance of ternary solar cells.

1.6 Objectives of the Present Thesis

- The main objectives of the present thesis work are directed towards the following:
  - Development of efficient (D_1:D_2:A)/ (D:A_1:A_2) type of Ternary blends.

- Development of Carbon based 2D Materials such as Graphene Oxide(GO) and Fluorinated Graphene Oxide(FGO) for enhancing performance of solar cells.
- Preparation of (PEDOT:PSS-GO) composites with effective Hole transport properties.
- Improving the performance of Ternary Solar cells fabricated using (D_1:D_2:A) and (D:A_1:A_2) as active layers, using (PEDOT:PSS-GO) composite as HTL.
- In-depth studies related to film morphology, photo-physics, charge carrier dynamics and photostability of the fabricated devices.

The experimental work carried out is as follows:

1. Preparation and optimization of (D_1:D_2:A_1) Ternary blend, [(P3HT (D_1), PTB7-th (D_2), and PCBM (A_1)]. The structural, optical properties and charge transport studies are carried out.
2. Synthesis of GO and FGO have been carryout by Modified Hummer's method. Subsequently, Preparation and optimization of Hole Transport Layers (HTLs): PEDOT:PSS, GO, and PEDOT:PSS-GO composite films (different weight ratios). Analysis of structural, optical and electrical properties are done.
3. Fabrication of Ternary Solar Cells using the [P3HT: PTB7-th: PCBM] blends and studies related to photo-physics and charge carrier dynamics have been carried out.
4. The effect of different HTLs (PEDOT:PSS, GO, and PEDOT:PSS-GO composites) on the Photovoltaic properties of [P3HT: PTB7-th: PCBM] Ternary Solar Cells have been investigated.
5. Preparation and optimization of (D:A_1:A_2) Ternary blends using PTB7-th (D), PCBM (A_1), and F-rGO (A_2). Film morphology and charge carrier dynamics have been studied.
6. Fabrication of [PTB7-th:PCBM:F-rGO] Ternary blend solar cells and photovoltaic performance have been analyzed.

1.7 Thesis outline

The present thesis explores the utilization of carbon 2D materials for improving the performance of (D_1:D_2:A)/ (D:A_1:A_2) type of Ternary blend based solar cells. The studies related to photo-physics and charge carrier dynamics have been investigated in-depth. The current challenges and further prospects on ternary solar cells are also briefly analyzed in the thesis. The thesis comprises of 8 chapters.

★ The present chapter (**chapter 1**) of the thesis is devoted towards the extensive literature survey on past and present research work done on organic solar cells. The working mechanism and various geometry of organic solar cells have been discussed. It summarizes the general review on various strategies for boosting the performance of TSCs (both stability and efficiency) such as different photoactive blends (binary and ternary), hole and electron transport layers (HTL and ETL) and utilization of 2D materials etc. Finally, the objectives and scope of the present work are presented.

★ In **chapter 2** the details of experimental details and characterization techniques used in the present investigations have been mentioned. It includes synthesis of GO and FGO by modified Hummer's method , preparation of Ternary blend active layers [(P3HT (D_1): PTB7-th (D_2): PCBM(A_1), and [PTB7-th (D_1): PCBM (A_1): F-rGO (A_2)], and preparation of PEDOT:PSS, GO, and PEDOT:PSS-GO composite films HTL thin films by spin coating technique. The detailed process for the fabrication of the solar cell devices will be discussed using both the binary and the ternary blends and different PEDOT:PSS/GO/PEDOT:PSS-GO composite films HTLs, in typical planar BHJ device configuration. Further, Equipments require for fabrication process like glove box, thermal evaporation systems and spin coating unit with characterization and PV measurement techniques used in the present work have been discussed in this chapter.

★ **Chapter 3** comprises of structural, optical and electrical characterization of GO and PEDOT:PSS-GO composites films for HTLs. The synthesized GO and FGO sample characterized by XRD, FESEM, HRTEM, AFM, Raman, and FTIR revealing the size of nanosheets 5-10 μm, and thickness of one single sheet ~1.1 nm (indicating the

availability of two or three layers). The chemical composition of the GO sample was investigated by XPS. Further, PEDOT:PSS-GO composite films were deposited by dispersing GO in PEDOT:PSS in different weight ratios i.e., (2:1), (1:1), and (1:2). The effect of GO on the surface morphology of these PEDOT:PSS-GO composite thin films has been revealed by FESEM images and AFM images. Finally, via the optical transmittance, four-point probe resistivity and UPS measurements of the PEDOT:PSS-GO composite thin films carried out in all compositions, it is concluded that PEDOT:PSS-GO(1:1) is the optimum composition as it shows good film morphology, enhanced conductivity, and highest HOMO level (E_{HOMO} = 5.22 eV). Therefore, PEDOT:PSS-GO(1:1) is considered as a potential HTL alternative to PEDOT:PSS, and more ideally suited for effective HTLs in solar cell devices.

★ **Chapter 4** presents the photo-physical properties of [P3HT:PTB7-th:PCBM] (D_1:D_2:A_1) ternary blends for active layer. The ternary blend of P3HT:PTB7-th:PCBM has been investigated in different blend compositions for optimizing the photovoltaic properties. The P3HT:PTB7-th films were deposited on ITO by mixing P3HT and PTB7-th in three different weight propositions i.e., (0.7:0.3), (0.5:0.5) and (0.3:0.7) weight ratios. The absorption spectra confirmed that all three P3HT:PTB7-th films exhibit strong and complementary absorption covering a wider wavelength range from 500-750 nm. Evidently, P3HT:PTB7-th with (0.3:0.7) weight ratio displays more stronger and wider coverage in the entire solar light spectrum as compared to the other two compositions. Further, PL characteristics of pure P3HT, PTB7-th, and P3HT:PTB7-th mixed blends have been recorded to the monitor the PL quenching. Further, when the PCBM acceptor is blended with the donor:donor P3HT:PTB7-th (0.3:0.7) composite, PL at the characteristic peaks of P3HT (650 nm) and PTB7-th (747 nm) have been studied. Further, the TRPL studies were carried out to estimate the photo-exciton lifetime *in P3HT* and *P3HT:PTB7-th:PCBM*, respectively. The significance that both FRET and cascade energy level alignment charge transfer dominated mechanisms on effective exciton dissociation in the ternary blend have been thoroughly investigated and discussed. Hence, the work described in this chapter concludes that P3HT:PTB7-th:PCBM (0.3:0.7:1) is the optimized blend combination for solar cell application.

★ **Chapter 5** describes the photovoltaic performance of [P3HT: PTB7-th: PCBM] ternary solar cells using different HTLs by measuring the *J-V* characteristic under standard AM 1.5G 100 mW cm^{-2} solar illumination. A remarkable enhancement in PCE of [P3HT:PTB7-th:PCBM] (0.3:0.7:1) ternary blend based solar cells (TPSC) from 3.2% to 7.1%, without and with the addition of GO nanosheets in PEDOT:PSS HTL, has been achieved. It has also been described that these TPSCs showed significant improvement in device stability retaining PCE for 500 hours with only a 10 % loss from its initial value. This is due to good photo-stability of GO which significantly improved the overall air-stability of PEDOT:PSS-GO composite HTL based TPSC devices. Hence, PEDOT:PSS-GO composite offers the most desirable hole transport properties over the conventional PEDOT:PSS-only HTLs. In conclusion, [P3HT:PTB7-th:$PC_{71}BM$] (0.3:0.7:1) ternary blend based TPSCs display high performance and good stability when PEDOT:PSS-GO (1:1) is utilized as HTL. These in-depth studies open a new avenue for the potential commercialization of low-cost and solution-processed TPSCs.

★ **Chapter 6** compares the performance of [P3HT:PTB7-th:PCBM] ternary solar cells with binary solar cells. Here, the J-V characteristics of [P3HT:PTB7-th:PCBM] (0.3:0.7:1) ternary blend based TPSCs fabricated is compared with the respective binary devices i.e., P3HT:PCBM and PTB7-th:PCBM binary blends based devices. Here, PEDOT:PSS-GO (1:1) composite HTL is used in all the devices. The enhancement in photovoltaic performance exhibited by P3HT:PTB7-th:PCBM TPSCs attributing to the synergetic effect of P3HT:PCBM and PTB7-th:PCBM binary counterparts was confirmed by absorption studies, EQE measurements, PL quenching and photo-carrier dynamics studies and charge transport studies. The advantageous properties of (P3HT:PTB7-th:$PC_{71}BM$) ternary blend PEDOT:PSS-GO composite HTL collectively boost up the performance of TPSCs. It all makes these devices as a potential candidate to take the TPSCs towards their ultimate goal of envisaged commercialization.

★ **Chapter 7** demonstrates the photovoltaic performance of [PTB7-th:PCBM:F-rGO] ternary blend based solar cells. Here, the F-rGO (reduced FGO) nanosheets are dispersed within polymer PTB7-th matrix as they can be utilized as the electron

acceptor in bulk heterojunction polymer solar cells. The steady-state PL and TRPL studies were made to achieve the optimized weight percentage of F-rGO nanosheets incorporated in PTB7-th. Furthermore, the solar cells, ITO/PEDOT:PSS/PTB7-th:PCBM(1:1)+F-rGO/LiF/Al, and ITO/PEDOT:PSS/PTB7-th:PCBM (1:1)/LiF/Al, were fabricated, and *J-V* characteristic of TPSC devices under standard AM 1.5G 100 mW cm^{-2} solar illumination were measured for further investigations. It has been found that the PCE of TPSC devices with added F-rGO ternary additive (~5 wt%), gets enhanced to 7.36 % compared to the device without F-rGO (PCE ~ 3.54 %). In-depth investigations of charge carrier dynamics studies in support of the enhanced PCE via exciton dissociation in PTB7-th:PCBM matrix have been analyzed and discussed. Also, device stability testing measurements have been examined which showed improved overall air-stability of [PTB7-th:PCBM + F-rGO] ternary compared to [PTB7-th:PCBM] binary blend devices owing to good photo-stability of incorporated F-rGO nanosheets.

★ **Chapter 8** presents the brief summary of the work and the conclusion drawn from major conclusions derived from the present work and the scope of the future study in this field has been suggested.

References

1. Green Martin A. "Silicon Solar Cells Advanced Principles & Practice, Centre for Photovoltaic Devices and Systems University of New South Wales Sydney." NSW 2052 (1995).
2. T. Markvart, and L. Castaner (Eds.), Solar Cells:Materials, Manufacture and Operation, Elsevier, Oxford, UK, 2005.
3. A. Goetzberger, J. Knobloch, and B. Voss (Eds.), Crystalline Silicon Solar Cells, John Wiley & Sons Ltd., England, 1998.
4. Markvart, Tomas. "Light harvesting for quantum solar energy conversion." Progress in quantum electronics 24 (2000) 107-186.
5. Bergmann, R. B. "Crystalline Si thin-film solar cells: a review." Applied physics A 69 (1999) 187-194.
6. Schropp, Ruud EI, and Miro Zeman. Amorphous and microcrystalline silicon solar cells: modeling, materials and device technology. Vol. 8. Boston: Kluwer Academic, 1998.
7. Lee Changyeon, Seungjin Lee, Geon-U. Kim, Wonho Lee, and Bumjoon J. Kim. "Recent advances, design guidelines, and prospects of all-polymer solar cells." Chemical reviews 119 (2019) 8028-8086.

8. Foster Samuel, Florent Deledalle, Akiko Mitani, Toshio Kimura, Ki-Beom Kim, Takayuki Okachi, Thomas Kirchartz et al. "Electron collection as a limit to polymer: PCBM solar cell efficiency: Effect of blend microstructure on carrier mobility and device performance in PTB7: PCBM." Advanced energy materials 4 (2014) 1400311.
9. Wang Gang, Ferdinand S. Melkonyan, Antonio Facchetti, and Tobin J. Marks. "All-polymer solar cells: recent progress, challenges, and prospects." Angewandte Chemie International Edition 58 (2019) 4129-4142.
10. Xu Xiaopeng, Kui Feng, Zhaozhao Bi, Wei Ma, Guangjun Zhang, and Qiang Peng. "Single-junction polymer solar cells with 16.35% efficiency enabled by a platinum (II) complexation strategy." Advanced materials 31 (2019) 1901872.
11. Gurney Robert S., David G. Lidzey, and Tao Wang. "A review of non-fullerene polymer solar cells: from device physics to morphology control." Reports on Progress in Physics 82 (2019) 036601.
12. Karki Akchheta, Joachim Vollbrecht, Alana L. Dixon, Nora Schopp, Max Schrock, GN Manjunatha Reddy, and Thuc-Quyen Nguyen. "Understanding the High Performance of over 15% Efficiency in Single-Junction Bulk Heterojunction Organic Solar Cells." Advanced Materials 31 (2019) 1903868.
13. Lin Yuanbao, Yuliar Firdaus, Mohamad Insan Nugraha, Feng Liu, Safakath Karuthedath, Abdul-Hamid Emwas, Weimin Zhang et al. "17.1% efficient single-junction organic solar cells enabled by n-type doping of the bulk-heterojunction." Advanced Science 7 (2020) 1903419.
14. Yin Hang, Cenqi Yan, Hanlin Hu, Johnny Ka Wai Ho, Xiaowei Zhan, Gang Li, and Shu Kong So. "Recent progress of all-polymer solar cells–From chemical structure and device physics to photovoltaic performance." Materials Science and Engineering: R: Reports 140 (2020) 100542.
15. Chen Hsiu-Cheng, Shu-Wei Lin, Jian-Ming Jiang, Yu-Wei Su, and Kung-Hwa Wei. "Solution-processed zinc oxide/polyethylenimine nanocomposites as tunable electron transport layers for highly efficient bulk heterojunction polymer solar cells." ACS applied materials & interfaces 7 (2015) 6273-6281.
16. Huang Yi-Jiun, Hsiu-Cheng Chen, Hsi-Kuei Lin, and Kung-Hwa Wei. "Doping ZnO electron transport layers with MoS2 nanosheets enhances the efficiency of polymer solar cells." ACS applied materials & interfaces 10 (2018) 20196-20204.
17. Huang Yi-Jiun, Po-Jen Yen, Hao-Cheng Wang, Hsiu-Cheng Chen, and Kung-Hwa Wei. "An universal electron transport layer involving hydrogen plasma–treated tungsten disulfide nanosheets doped zinc oxide layers for polymer donors with fullerene or small molecule acceptor photovoltaics." Organic Electronics 72 (2019) 6-17.
18. Su Yu-Wei, Yu-Che Lin, and Kung-Hwa Wei. "Evolving molecular architectures of donor–acceptor conjugated polymers for photovoltaic applications: from one-dimensional to branched to two-dimensional structures." Journal of Materials Chemistry A 5 (2017) 24051-24075.
19. Ameri Tayebeh, Parisa Khoram, Jie Min, and Christoph J. Brabec. "Organic ternary solar cells: a review." Advanced Materials 25 (2013) 4245-4266.

20. Yang Yang Michael, Wei Chen, Letian Dou, Wei-Hsuan Chang, Hsin-Sheng Duan, Brion Bob, Gang Li, and Yang Yang. "High-performance multiple-donor bulk heterojunction solar cells." Nature photonics 9 (2015) 190-198.
21. Yang Liqiang, Liang Yan, and Wei You. "Organic solar cells beyond one pair of donor–acceptor: ternary blends and more." The journal of physical chemistry letters 4 (2013) 1802-1810.
22. Fan Baobing, Wenkai Zhong, Xiao-Fang Jiang, Qingwu Yin, Lei Ying, Fei Huang, and Yong Cao. "Improved performance of ternary polymer solar cells based on a nonfullerene electron cascade acceptor." Advanced Energy Materials 7 (2017) 1602127.
23. Chen Weichao, Huanxiang Jiang, Gongyue Huang, Jun Zhang, Mian Cai, Xiaobo Wan, and Renqiang Yang. "High-Efficiency Ternary Polymer Solar Cells Based on Intense FRET Energy Transfer Process." Solar RRL 2 (2018) 1800101.
24. Yin Hang, Sin Hang Cheung, Jenner HL Ngai, Carr Hoi Yi Ho, Ka Lok Chiu, Xiaotao Hao, Ho Wa Li, Yuanhang Cheng, Sai Wing Tsang, and Shu Kong So. "Thick-Film High-Performance Bulk-Heterojunction Solar Cells Retaining 90% PCEs of the Optimized Thin Film Cells." Advanced Electronic Materials 3 (2017) 1700007.
25. Mai Jiangquan, Tsz-Ki Lau, Ting Xiao, Chun-Jen Su, U-ser Jeng, Ni Zhao, Xudong Xiao, and Xinhui Lu. "Ternary morphology facilitated thick-film organic solar cell." RSC advances 5 (2015) 88500-88507.
26. Nakano Kyohei, Kaori Suzuki, Yujiao Chen, and Keisuke Tajima. "Roles of energy/charge cascades and intermixed layers at donor/acceptor interfaces in organic solar cells." Scientific reports 6 (2016) 1-11.
27. Khlyabich Petr P., Andrey E. Rudenko, Barry C. Thompson, and Yueh-Lin Loo. "Structural origins for tunable open-circuit voltage in ternary-blend organic solar cells." Advanced Functional Materials 25 (2015) 5557-5563.
28. Huang Jiang, Hanyu Wang, Kangrong Yan, Xiaohua Zhang, Hongzheng Chen, Chang-Zhi Li, and Junsheng Yu. "Highly efficient organic solar cells consisting of double bulk heterojunction layers." Advanced Materials 29 (2017) 1606729.
29. Lu Luyao, Mary Allison Kelly, Wei You, and Luping Yu. "Status and prospects for ternary organic photovoltaics." Nature Photonics 9 (2015) 491-500.
30. Goh Tenghooi, Jing-Shun Huang, Benjamin Bartolome, Matthew Y. Sfeir, Michelle Vaisman, Minjoo L. Lee, and André D. Taylor. "Panchromatic polymer–polymer ternary solar cells enhanced by Förster resonance energy transfer and solvent vapor annealing." Journal of Materials Chemistry A 3 (2015) 18611-18621.
31. Adam Getachew, Battulga Munkhbat, Patrick Denk, Christoph Ulbricht, Calin Hrelescu, and Markus C. Scharber. "Different Device architectures for Bulk-heterojunction solar cells." Frontiers in Materials 3 (2016) 39.
32. Hilal Muhammad, and Jeong In Han. "Significant improvement in the photovoltaic stability of bulk heterojunction organic solar cells by the molecular level interaction of graphene oxide with a PEDOT: PSS composite hole transport layer." Solar Energy 167 (2018) 24-34.
33. Liu Jun, Yuhua Xue, Yunxiang Gao, Dingshan Yu, Michael Durstock, and Liming Dai. "Hole and electron extraction layers based on graphene oxide derivatives for

high-performance bulk heterojunction solar cells." Advanced Materials 24 (2012) 2228-2233.
34. Li Shao-Sian, Kun-Hua Tu, Chih-Cheng Lin, Chun-Wei Chen, and Manish Chhowalla. "Solution-processable graphene oxide as an efficient hole transport layer in polymer solar cells." ACS nano 4 (2010) 3169-3174.
35. Markvart T., and L. Castañer. "Solar Cells: Materials Manufactureand Operation" (2005).
36. Goetzberger, Adolf, Joachim Knobloch, and Bernhard Voss. Crystalline silicon solar cells. Vol. 1. Chichester: Wiley, 1998.
37. Markvart, Tomas. "Light harvesting for quantum solar energy conversion." Progress in quantum electronics 24 (2000) 107-186.
38. R. B. Bergmann, Crystalline Si thin-film solar cells: a review, Applied Physics A (Materials-Science-Processing) 69 (1999) 187.
39. R. Schropp, M. Zeman (Eds.), Amorphous and Microcystalline Silicon Solar Cells: Modelling, Materials and Device Technology" Kluwer, Boston 1998.
40. Sze S. M., and Kwok K. Ng. "Physics of Semiconductor Devices, John Wiley & Sons." New York 68 (1981).
41. Becquerel, Alexandre-Edmond. "Recherches sur les effets de la radiation chimique de la lumiere solaire au moyen des courants electriques." CR Acad. Sci 9 (1839) 1.
42. Ferry D. K., S. M. Goodnick, V. R. Whiteside, and I. R. Sellers. "Challenges, myths, and opportunities in hot carrier solar cells." Journal of Applied Physics 128 (2020) 220903.
43. Nelson, Jenny. "Imperial College Press." The physics of solar cells (2003).
44. Green, Martin A. "Silicon photovoltaic modules: a brief history of the first 50 years." Progress in Photovoltaics: Research and applications 13 (2005) 447-455.
45. Blakers, Andrew, Klaus Weber, and Vernie Everett. "Sliver Solar Cells." Chemistry in Australia 72 (2005) 9-12.
46. Luque, Antonio, and Steven Hegedus, eds. Handbook of photovoltaic science and engineering. John Wiley & Sons 2011.
47. M. A. Green, K. Emery, D. L. King, S. Igari, and W. Warta, Progress in Photovoltaics: Research and Applications 9 (2001) 287.
48. L. C. Rogers, W. C. O'Mara, R. B. Herring, and L. P. Hunt (Ed.), Handbook Semiconductor Silicon Technology: Noyes Publications, New Jersey, USA (1990).
49. W. Wettling, Solar Energy Materials & Solar Cells 38 (1995) 487.
50. Falk, Antony, Christian Durschner, and Karl-Heinz Remmers. Photovoltaics for professionals: solar electric systems marketing, design and installation. Routledge, 2013.
51. Schropp, Ruud EI, and Miro Zeman. Amorphous and microcrystalline silicon solar cells: modeling, materials and device technology. Vol. 8. Boston: Kluwer Academic 1998.
52. Poortmans, Jef, and Vladimir Arkhipov, eds. Thin film solar cells: fabrication, characterization and applications. Vol. 18. John Wiley & Sons, 2006.
53. Brendel, Rolf. Thin-film crystalline silicon solar cells: physics and technology. John Wiley & Sons, 2011.
54. He, Bin, and Wenjun Zhang. "II–VI Semiconductors and their device applications." Handbook of Chalcogen Chemistry: New Perspectives in Sulfur,

Selenium, and Tellurium, 2nd edn. Royal Society of Chemistry, Cambridge (2013) 180-220.
55. Kumar, Vikram, S. C. Jain, Ashok K. Kapoor, Wim Geens, Tom Aernauts, Jef Poortmans, and Robert Mertens. "Carrier transport in conducting polymers with field dependent trap occupancy." Journal of applied physics 92 (2002) 7325-7329.
56. Kapoor, Ashok K., S. C. Jain, Jef Poortmans, Vikram Kumar, and Robert Mertens. "Temperature dependence of carrier transport in conducting polymers: similarity to amorphous inorganic semiconductors." Journal of applied physics 92 (2002) 3835-3838.
57. Günes, Serap, Helmut Neugebauer, and Niyazi Serdar Sariciftci. "Conjugated polymer-based organic solar cells." Chemical reviews 107 (2007) 1324-1338.
58. S. C. Jain, A. K. Kapoor, W. Geens, J. Poortmans, R. Mertens, and M. Willander, Journal of Applied Physics, 92 (2002) 3579.
59. Hoppe, Harald, and Niyazi Serdar Sariciftci. "Organic solar cells: An overview." Journal of materials research 19 (2004) 1924-1945.
60. Kim, Heejoo, Won-Wook So, and Sang-Jin Moon. "The importance of post-annealing process in the device performance of poly (3-hexylthiophene): Methanofullerene polymer solar cell." Solar Energy Materials and Solar Cells 91 (2007) 581-587.
61. Wienk, Martijn M., Martin P. Struijk, and René AJ Janssen. "Low band gap polymer bulk heterojunction solar cells." Chemical Physics Letters 422 (2006) 488-491.
62. Gupta, Bhavana, Minisha Mehta, Ambrose Melvin, R. Kamalakannan, S. Dash, M. Kamruddin, and A. K. Tyagi. "Poly (3, 4-ethylenedioxythiophene)(PEDOT) and poly (3, 4-ethylenedioxythiophene)-few walled carbon nanotube (PEDOT-FWCNT) nanocomposite based thin films for Schottky diode application." Materials Chemistry and Physics 147 (2014) 867-877.
63. Tse, S. C., S. W. Tsang, and S. K. So. "Nearly ohmic injection contacts from PEDOT: PSS to phenylamine compounds with high ionization potentials." In Organic Light Emitting Materials and Devices X, vol. 6333, p. 63331P. International Society for Optics and Photonics, 2006.
64. Kumar, Vikram, S. C. Jain, A. K. Kapoor, Jef Poortmans, and Robert Mertens. "Trap density in conducting organic semiconductors determined from temperature dependence of J− V characteristics." Journal of applied physics 94 (2003)1283-1285.
65. Kumar, Pankaj, Aparna Misra, M. N. Kamalasanan, S. C. Jain, and Vikram Kumar. "Charge transport through conducting organic poly (2-methoxy-5-(2-ethylhexyloxy)-1, 4-phenylenevinylene)." Journal of Physics D: Applied Physics 40 (2007) 561.
66. Ma, Wanli, Cuiying Yang, Xiong Gong, Kwanghee Lee, and Alan J. Heeger. "Thermally stable, efficient polymer solar cells with nanoscale control of the interpenetrating network morphology." Advanced functional materials 15 (2005) 1617-1622.
67. Nelson, Jenny. "Organic photovoltaic films." Current Opinion in Solid State and Materials Science 6 (2002) 87-95.

68. Coakley, Kevin M., and Michael D. McGehee. "Conjugated polymer photovoltaic cells." Chemistry of materials 16 (2004) 4533-4542.
69. Jain, S. C., Wim Geens, Anupama Mehra, Vikram Kumar, Tom Aernouts, Jef Poortmans, Robert Mertens, and M. Willander. "Injection-and space charge limited-currents in doped conducting organic materials." Journal of applied physics 89 (2001) 3804-3810.
70. Spanggaard, Holger, and Frederik C. Krebs. "A brief history of the development of organic and polymeric photovoltaics." Solar Energy Materials and Solar Cells 83 (2004) 125-146.
71. He, Zhicai, Chengmei Zhong, Shijian Su, Miao Xu, Hongbin Wu, and Yong Cao. "Enhanced power-conversion efficiency in polymer solar cells using an inverted device structure." Nature photonics 6 (2012) 591-595.
72. You, Jingbi, Letian Dou, Ken Yoshimura, Takehito Kato, Kenichiro Ohya, Tom Moriarty, Keith Emery et al. "A polymer tandem solar cell with 10.6% power conversion efficiency." Nature communications 4 (2013) 1-10.
73. Nunzi, Jean-Michel. "Organic photovoltaic materials and devices." Comptes Rendus Physique 3, no. 4 (2002): 523-542.
74. Mozer, Attila J., and Niyazi Serdar Sariciftci. "Conjugated polymer photovoltaic devices and materials." Comptes Rendus Chimie 9 (2006) 568-577.
75. Marks, R. N., J. J. M. Halls, D. D. C. Bradley, R. H. Friend, and A. B. Holmes. "The photovoltaic response in poly (p-phenylene vinylene) thin-film devices." Journal of Physics: Condensed Matter 6 (1994) 1379.
76. Günes, Serap, Helmut Neugebauer, and Niyazi Serdar Sariciftci. "Conjugated polymer-based organic solar cells." Chemical reviews 107 (2007) 1324-1338.
77. Hoppe, Harald, and Niyazi Serdar Sariciftci. "Organic solar cells: An overview." Journal of materials research 19, no. 7 (2004) 1924-1945.
78. Jain, S. C., Ashok K. Kapoor, Wim Geens, Jef Poortmans, Robert Mertens, and Magnus Willander. "Trap filled limit of conducting organic materials." Journal of applied physics 92 (2002) 3752-3754.
79. Kumar, Pankaj, Aparna Misra, M. N. Kamalasanan, S. C. Jain, and Vikram Kumar. "Charge transport through conducting organic poly (2-methoxy-5-(2-ethylhexyloxy)-1, 4-phenylenevinylene)." Journal of Physics D: Applied Physics 40 (2007) 561.
80. Nunzi, Jean-Michel. "Organic photovoltaic materials and devices." Comptes Rendus Physique 3 (2002) 523-542.
81. Kapoor, Ashok K., S. Annapoorni, and Vikram Kumar. "Conduction mechanisms in poly (3-hexylthiophene) thin-film sandwiched structures." Semiconductor science and technology 23 (2008) 035008.
82. Nelson, Jenny. "Organic photovoltaic films." Current Opinion in Solid State and Materials Science 6 (2002) 87-95.
83. Wienk, Martijn M., Martin P. Struijk, and René AJ Janssen. "Low band gap polymer bulk heterojunction solar cells." Chemical Physics Letters 422 (2006) 488-491.
84. Mozer, Attila J., and Niyazi Serdar Sariciftci. "Conjugated polymer photovoltaic devices and materials." Comptes Rendus Chimie 9 (2006) 568-577.

85. Ma, Wanli, Cuiying Yang, Xiong Gong, Kwanghee Lee, and Alan J. Heeger. "Thermally stable, efficient polymer solar cells with nanoscale control of the interpenetrating network morphology." Advanced functional materials 15 (2005) 1617-1622.
86. Spanggaard, Holger, and Frederik C. Krebs. "A brief history of the development of organic and polymeric photovoltaics." Solar Energy Materials and Solar Cells 83 (2004) 125-146.
87. Kim, Heejoo, Won-Wook So, and Sang-Jin Moon. "The importance of post-annealing process in the device performance of poly (3-hexylthiophene): Methanofullerene polymer solar cell." Solar Energy Materials and Solar Cells 91(2007) 581-587.
88. Peumans, P., and S. R. Forrest. "Very-high-efficiency double-heterostructure copper phthalocyanine/C 60 photovoltaic cells." Applied Physics Letters 79 (2001) 126-128.
89. Zhou, Qingmei, Qiong Hou, Liping Zheng, Xianyu Deng, Gang Yu, and Yong Cao. "Fluorene-based low band-gap copolymers for high performance photovoltaic devices." Applied Physics Letters 84 (2004) 1653-1655.
90. Xue, Jiangeng, Soichi Uchida, Barry P. Rand, and Stephen R. Forrest. "4.2% efficient organic photovoltaic cells with low series resistances." Applied Physics Letters 84 (2004) 3013-3015.
91. Markov, Denis E., Emiel Amsterdam, Paul WM Blom, Alexander B. Sieval, and Jan C. Hummelen. "Accurate measurement of the exciton diffusion length in a conjugated polymer using a heterostructure with a side-chain cross-linked fullerene layer." The Journal of Physical Chemistry A 109 (2005) 5266-5274.
92. J.-M. Nunzi, C. R. “Organic photovoltaic materials and devices”, Physique 3 (2002) 523–542.
93. Kapoor, Ashok K., S. Annapoorni, and Vikram Kumar. "Conduction mechanisms in poly (3-hexylthiophene) thin-film sandwiched structures." Semiconductor science and technology 23 (2008) 035008.
94. Nelson, Jenny. "Organic photovoltaic films." Current Opinion in Solid State and Materials Science 6 (2002) 87-95.
95. Wienk, Martijn M., Martin P. Struijk, and René AJ Janssen. "Low band gap polymer bulk heterojunction solar cells." Chemical Physics Letters 422 (2006) 488-491.
96. Mozer, Attila J., and Niyazi Serdar Sariciftci. "Conjugated polymer photovoltaic devices and materials." Comptes Rendus Chimie 9 (2006) 568-577.
97. Ma, Wanli, Cuiying Yang, Xiong Gong, Kwanghee Lee, and Alan J. Heeger. "Thermally stable, efficient polymer solar cells with nanoscale control of the interpenetrating network morphology." Advanced functional materials 15 (2005) 1617-1622.
98. Spanggaard, Holger, and Frederik C. Krebs. "A brief history of the development of organic and polymeric photovoltaics." Solar Energy Materials and Solar Cells 83 (2004) 125-146.
99. Kim, Heejoo, Won-Wook So, and Sang-Jin Moon. "The importance of post-annealing process in the device performance of poly (3-hexylthiophene):

Methanofullerene polymer solar cell." Solar Energy Materials and Solar Cells 91 (2007) 581-587.
100. Pientka, M., V. Dyakonov, D. Meissner, A. Rogach, D. Talapin, H. Weller, L. Lutsen, and D. Vanderzande. "Photoinduced charge transfer in composites of conjugated polymers and semiconductor nanocrystals." Nanotechnology 15 (2003) 163.
101. Ha, Na Young, Soon Moon Jeong, Suzushi Nishimura, and Hideo Takezoe. "Color-and reflectance-tunable multiple reflectors assembled from three polymer films." Advanced Materials 22 (2010) 1617-1621.
102. Janssen, René. "Introduction to polymer solar cells (3Y280)." (2007).
103. Xiao, Biao, Hongbin Wu, and Yong Cao. "Solution-processed cathode interfacial layer materials for high-efficiency polymer solar cells." Materials Today 18 (2015) 385-394.
104. J. Nunzi, Molecular Photonics: materials, physics and device, Organic photovoltaic materials and devices, Physics (College. Park. Md) 3 (2002) 523-542.
105. Schlenker, Cody W., and Mark E. Thompson. "The molecular nature of photovoltage losses in organic solar cells." Chemical communications 47 (2011) 3702-3716.
106. R. N. Marks, J.J.M. Halls, D.D.C. Bradley, R.H. Friend, A.B. Holmes, The photovoltaic response in poly(p-phenylene vinylene) thin-film devices, J. Phys. Condens. Matter 6 (1994) 1379-1394.
107. Liu, Feng, Yu Gu, Xiaobo Shen, Sunzida Ferdous, Hsin-Wei Wang, and Thomas P. Russell. "Characterization of the morphology of solution-processed bulk heterojunction organic photovoltaics." Progress in Polymer Science 38 (2013) 1990-2052.
108. Yu, Gang, Jun Gao, Jan C. Hummelen, Fred Wudl, and Alan J. Heeger. "Polymer photovoltaic cells: enhanced efficiencies via a network of internal donor-acceptor heterojunctions." Science 270 (1995) 1789-1791.
109. Blom, Paul WM, Valentin D. Mihailetchi, L. Jan Anton Koster, and Denis E. Markov. "Device physics of polymer: fullerene bulk heterojunction solar cells." Advanced Materials 19 (2007) 1551-1566.
110. Nelson, Jenny, Joe J. Kwiatkowski, James Kirkpatrick, and Jarvist M. Frost. "Modeling charge transport in organic photovoltaic materials." Accounts of chemical research 42 (2009) 1768-1778.
111. http://www.soton.ac.uk/~solar/intro/tech6.htm (JPG images).
112. Benanti, Travis L., and D. Venkataraman. "Organic solar cells: An overview focusing on active layer morphology." Photosynthesis research 87 (2006) 73-81.
113. Gusain, Abhay, Roberto M. Faria, and Paulo B. Miranda. "Polymer solar cells—Interfacial processes related to performance issues." Frontiers in chemistry 7 (2019) 61.
114. An, Qiaoshi, Fujun Zhang, Jian Zhang, Weihua Tang, Zhenbo Deng, and Bin Hu. "Versatile ternary organic solar cells: a critical review." Energy & Environmental Science 9 (2016) 281-322.
115. Shockley, William, and Hans J. Queisser. "Detailed balance limit of efficiency of p-n junction solar cells." Journal of applied physics 32 (1961) 510-519.
116. Beiley, Zach M., M. Greyson Christoforo, Paul Gratia, Andrea R. Bowring, Petra

Eberspacher, George Y. Margulis, Clément Cabanetos, Pierre M. Beaujuge, Alberto Salleo, and Michael D. McGehee "Semi-transparent polymer solar cells with excellent sub-bandgap transmission for third generation photovoltaics." Advanced Materials 25, no. 48 (2013): 7020-7026.
117. Kim, Taehee, Hyeok Kim, Jinjoo Park, Hyungchae Kim, Youngwoon Yoon, Sung-Min Kim, Chonghoon Shin et al. "Triple-junction hybrid tandem solar cells with amorphous silicon and polymer-fullerene blends." Scientific reports 4(2014)1-6.
118. An, Qiaoshi, Fujun Zhang, Jian Zhang, Weihua Tang, Zhenbo Deng, and Bin Hu. "Versatile ternary organic solar cells: a critical review." Energy & Environmental Science 9 (2016) 281-322.
119. An, Qiaoshi, Fujun Zhang, Jian Zhang, Weihua Tang, Zhenbo Deng, and Bin Hu. "Versatile ternary organic solar cells: a critical review." Energy & Environmental Science 9 (2016) 281-322.
120. Ameri, Tayebeh, Gilles Dennler, Christoph Lungenschmied, and Christoph J. Brabec. "Organic tandem solar cells: A review." Energy & Environmental Science (2009) 347-363.
121. D. Zhao, X. Sun, C. Jiang, A. Kyaw, G. Lo and D. Kwong, Efficient tandem organic solar cells with an Al/MoO3 intermediate layer, Appl. Phys. Lett 93 (2008) 083305.
122. Sun, X. W., D. W. Zhao, L. Ke, A. K. K. Kyaw, G. Q. Lo, and D. L. Kwong. "Inverted tandem organic solar cells with a MoO 3/Ag/Al/Ca intermediate layer." Applied Physics Letters 97 (2010) 166.
123. You, Jingbi, Letian Dou, Ziruo Hong, Gang Li, and Yang Yang. "Recent trends in polymer tandem solar cells research." Progress in polymer science 38 (2013) 1909-1928.
124. Ye, Long, Sunsun Li, and Jianhui Hou. "New Polymer Donors for Polymer Solar Cells." Polymer Photovoltaics: Materials, Physics, and Device Engineering (2015)32.
125. Dennler, Gilles, Markus C. Scharber, Tayebeh Ameri, Patrick Denk, Karen Forberich, Christoph Waldauf, and Christoph J. Brabec. "Design Rules for Donors in Bulk-Heterojunction Tandem Solar Cells Towards 15% Energy-Conversion Efficiency." Advanced Materials 20 (2008) 579-583.
126. A. B. Yusoff, D. Kim, H. P. Kim, F. K. Shneider, W. J. da Silva and J. Jang, A high efficiency solution processed polymer inverted triple-junction solar cell exhibiting a power conversion efficiency of 11.83%, Energy Environ. Sci., 8 (2015) 303–316.
127. Chen, Chun-Chao, Wei-Hsuan Chang, Ken Yoshimura, Kenichiro Ohya, Jingbi You, Jing Gao, Zirou Hong, and Yang Yang. "An efficient triple-junction polymer solar cell having a power conversion efficiency exceeding 11%." Advanced materials 26 (2014) 5670-5677.
128. Lu, Luyao, Mary Allison Kelly, Wei You, and Luping Yu, "Status and prospects for ternary organic photovoltaics." Nature Photonics 9 (2015) 491-500.
129. Cheng, Pei, and Xiaowei Zhan. "Versatile third components for efficient and stable organic solar cells." Materials Horizons 2 (2015) 462-485.
130. Z. Hu, S. Tang, A. Ahlvers, S. I. Khondaker and A. J. Gesquiere, Near-infrared photoresponse sensitization of solvent additive processed poly(3-hexylthiophene)/fullerene solar cells by a low band gap polymer, Appl. Phys. Lett.,

(2012) 053308.
131. Zhang, Miao, Fujun Zhang, Qiaoshi An, Qianqian Sun, Jian Wang, Lingliang Li, Wenbin Wang, and Jian Zhang "High efficient ternary polymer solar cells based on absorption complementary materials as electron donor." Solar Energy Materials and Solar Cells 141 (2015) 154-161.
132. Lessard, Benoît H., Jeremy D. Dang, Trevor M. Grant, Dong Gao, Dwight S. Seferos, and Timothy P. Bender. "Bis (tri-n-hexylsilyl oxide) silicon phthalocyanine: a unique additive in ternary bulk heterojunction organic photovoltaic devices." ACS applied materials & interfaces 6 (2014) 15040-15051.
133. Mandoc, M. Magdalena, F. B. Kooistra, Jan C. Hummelen, Bert De Boer, and Paul WM Blom. "Effect of traps on the performance of bulk heterojunction organic solar cells." Applied Physics Letters 91 (2007) 263505.
134. Zhen, Yonggang, Hideyuki Tanaka, Koji Harano, Satoshi Okada, Yutaka Matsuo, and Eiichi Nakamura. "Organic solid solution composed of two structurally similar porphyrins for organic solar cells." Journal of the American Chemical Society 137 (2015) 2247-2252.
135. Chen, Chiu-Hsiang, Chao-Hsiang Hsieh, Martin Dubosc, Yen-Ju Cheng, and Chain-Shu Hsu. "Synthesis and characterization of bridged bithiophene-based conjugated polymers for photovoltaic applications: acceptor strength and ternary blends." Macromolecules 43 (2010) 697-708.
136. Ameri, Tayebeh, Parisa Khoram, Jie Min, and Christoph J. Brabec. "Organic ternary solar cells: a review." Advanced Materials 25, no. 31 (2013): 4245-4266.
137. Yang, Liqiang, Liang Yan, and Wei You. "Organic solar cells beyond one pair of donor–acceptor: ternary blends and more." The journal of physical chemistry letters 4(2013) 1802-1810.
138. Yang, Yang Michael, Wei Chen, Letian Dou, Wei-Hsuan Chang, Hsin-Sheng Duan, Brion Bob, Gang Li, and Yang Yang. "High-performance multiple-donor bulk heterojunction solar cells." Nature photonics 9 (2015) 190-198.
139. Z. S. Wang, X. Ren, X. Xu, Q. Peng, W. E. I. Sha, W. C. H. Choy, A comprehensively theoretical and experimental study of carrier generation and transport for achieving high performance ternary blend organic solar cells, *Nano Energy* 51 (2018) 206.
140. Fan, Baobing, Wenkai Zhong, Xiao-Fang Jiang, Qingwu Yin, Lei Ying, Fei Huang, and Yong Cao. "Improved performance of ternary polymer solar cells based on a nonfullerene electron cascade acceptor." Advanced Energy Materials 7 (2017) 1602127.
141. Chen, Weichao, Huanxiang Jiang, Gongyue Huang, Jun Zhang, Mian Cai, Xiaobo Wan, and Renqiang Yang. "High-Efficiency Ternary Polymer Solar Cells Based on Intense FRET Energy Transfer Process." Solar RRL 2 (2018) 1800101.
142. Yin, Hang, Sin Hang Cheung, Jenner HL Ngai, Carr Hoi Yi Ho, Ka Lok Chiu, Xiaotao Hao, Ho Wa Li, Yuanhang Cheng, Sai Wing Tsang, and Shu Kong So. "Thick-Film High-Performance Bulk-Heterojunction Solar Cells Retaining 90% PCEs of the Optimized Thin Film Cells." Advanced Electronic Materials 3 (2017) 1700007.
143. Gao, Jinhua, Jian Wang, Chunyu Xu, Zhenghao Hu, Xiaoling Ma, Xiaoli Zhang, Lianbin Niu, Jian Zhang, and Fujun Zhang. "A critical review on efficient

thick-film organic solar cells." Solar RRL 4 (2020) 2000364.
144. K. Nakano, K. Suzuki, Y. Chen, K. Tajima, Roles of Energy/Charge Cascades and Intermixed Layers at Donor/Acceptor Interfaces in Organic Solar Cells, *Scientific Reports* 6 (2016) 29529.
145. Khlyabich, Petr P., Andrey E. Rudenko, Barry C. Thompson, and Yueh-Lin Loo. "Structural origins for tunable open-circuit voltage in ternary-blend organic solar cells." Advanced Functional Materials 25 (2015) 5557-5563.
146. Huang, Jiang, Hanyu Wang, Kangrong Yan, Xiaohua Zhang, Hongzheng Chen, Chang-Zhi Li, and Junsheng Yu. "Highly efficient organic solar cells consisting of double bulk heterojunction layers." Advanced Materials 29 (2017) 1606729.
147. Lu, Luyao, Mary Allison Kelly, Wei You, and Luping Yu. "Status and prospects for ternary organic photovoltaics." Nature Photonics 9 (2015) 491-500.
148. R. Yu, H. Yao, J. Hou, Recent Progress in Ternary Organic Solar Cells Based on Nonfullerene Acceptors, Advanced Energy Materials, 1702814 (2018) 1-9.
149. Gupta, Ritesh Kant, Rabindranath Garai, Maimur Hossain, Mohammad Adil Afroz, Dibashmoni Kalita, and Parameswar K. Iyer. "Engineering Polymer Solar Cells: Advancement in Active Layer Thickness and Morphology." Journal of Materials Chemistry C (2021).
150. Liu, S., P. You, J. Li, J. Li, C. S. Lee, B. S. Ong, C. Surya, and F. Yan. "Energy Environ. Sci., 8 1463–1470 (2015)".
151. Zhang, Jianqi, Yajie Zhang, Jin Fang, Kun Lu, Zaiyu Wang, Wei Ma, and Zhixiang Wei. "Conjugated polymer–small molecule alloy leads to high efficient ternary organic solar cells." Journal of the American Chemical Society 137 (2015) 8176-8183.
152. Ameri, Tayebeh, Parisa Khoram, Jie Min, and Christoph J. Brabec. "Organic ternary solar cells: a review." Advanced Materials 25 (2013) 4245-4266.
153. Lu, Luyao, Mary Allison Kelly, Wei You, and Luping Yu. "Status and prospects for ternary organic photovoltaics." Nature Photonics 9 (2015) 491-500.
154. Khlyabich, Petr P., Beate Burkhart, Andrey E. Rudenko, and Barry C. Thompson. "Optimization and simplification of polymer–fullerene solar cells through polymer and active layer design." Polymer 54 (2013) 5267-5298.
155. Chen, Yung-Chung, Chih-Yu Hsu, Ryan Yeh-Yung Lin, Kuo-Chuan Ho, and Jiann T. Lin. "Materials for the active layer of organic photovoltaics: ternary solar cell approach." ChemSusChem 6 (2013) 20-35.
156. Yang, Liqiang, Liang Yan, and Wei You. "Organic solar cells beyond one pair of donor–acceptor: ternary blends and more." The journal of physical chemistry letters 4 (2013) 1802-1810.
157. Cheng, Pei, and Xiaowei Zhan. "Versatile third components for efficient and stable organic solar cells." Materials Horizons 2 (2015) 462-485.
158. Cnops, Kjell, Barry P. Rand, David Cheyns, Bregt Verreet, Max A. Empl, and Paul Heremans. "8.4% efficient fullerene-free organic solar cells exploiting long-range exciton energy transfer." Nature communications 5 (2014) 1-6.
159. Lu, Luyao, Wei Chen, Tao Xu, and Luping Yu. "High-performance ternary blend polymer solar cells involving both energy transfer and hole relay processes." Nature communications 6 (2015) 1-7.
160. Gupta, Vinay, Vishal Bharti, Mahesh Kumar, Suresh Chand, and Alan J. Heeger.

"Polymer–polymer förster resonance energy transfer significantly boosts the power conversion efficiency of bulk-heterojunction solar cells." Advanced Materials 27 (2015) 4398-4404.
161. Cheng, Pei, Cenqi Yan, Yongfang Li, Wei Ma, and Xiaowei Zhan. "Diluting concentrated solution: a general, simple and effective approach to enhance efficiency of polymer solar cells." Energy & Environmental Science 8 (2015) 2357-2364.
162. Yang, Yang Michael, Wei Chen, Letian Dou, Wei-Hsuan Chang, Hsin-Sheng Duan, Brion Bob, Gang Li, and Yang Yang. "High-performance multiple-donor bulk heterojunction solar cells." Nature photonics 9 (2015) 190-198.
163. Zhang, Yajie, Dan Deng, Kun Lu, Jianqi Zhang, Benzheng Xia, Yifan Zhao, Jin Fang, and Zhixiang Wei. "Synergistic effect of polymer and small molecules for high-performance ternary organic solar cells." Advanced materials 27(2015)1071-1076.
164. Lu, Luyao, Tao Xu, Wei Chen, Erik S. Landry, and Luping Yu. "Ternary blend polymer solar cells with enhanced power conversion efficiency." Nature Photonics 8 (2014) 716-722.
165. K. Yao, Y.-X. Xu, F. Li, X. Wang and L. Zhou, A Review of One-dimensional TiO2 Nanostructured Materials for Environmental and Energy Applications, Adv. Opt. Mater 3 (2015) 321–327.
166. An, Qiaoshi, Fujun Zhang, Qianqian Sun, Jian Wang, Lingliang Li, Jian Zhang, Weihua Tang, and Zhenbo Deng. "Efficient small molecular ternary solar cells by synergistically optimized photon harvesting and phase separation." Journal of Materials Chemistry A 3 (2015) 16653-16662.
167. Yang, Liqiang, Huaxing Zhou, Samuel C. Price, and Wei You. "Parallel-like bulk heterojunction polymer solar cells." Journal of the American Chemical Society 134 (2012)5432-5435.
168. Goh, Tenghooi, Jing-Shun Huang, Elizabeth A. Bielinski, Bennett A. Thompson, Stephanie Tomasulo, Minjoo L. Lee, Matthew Y. Sfeir, Nilay Hazari, and André D. Taylor. "Coevaporated bisquaraine inverted solar cells: enhancement due to energy transfer and open circuit voltage control." ACS Photonics 2 (2015) 86-95.
169. Khlyabich, Petr P., Beate Burkhart, and Barry C. Thompson. "Compositional dependence of the open-circuit voltage in ternary blend bulk heterojunction solar cells based on two donor polymers." Journal of the American Chemical Society 134 (2012) 9074-9077.
170. Cha, Hyojung, Dae Sung Chung, Suk Young Bae, Min-Jung Lee, Tae Kyu An, Jihun Hwang, Kyung Hwan Kim, Yun-Hi Kim, Dong Hoon Choi, and Chan Eon Park. "Complementary absorbing star-shaped small molecules for the preparation of ternary cascade energy structures in organic photovoltaic cells." Advanced Functional Materials 23 (2013) 1556-1565.
171. Koppe, Markus, Hans-Joachim Egelhaaf, Gilles Dennler, Markus C. Scharber, Christoph J. Brabec, Pavel Schilinsky, and Claudia N. Hoth. "Near IR sensitization of organic bulk heterojunction solar cells: towards optimization of the spectral response of organic solar cells." Advanced Functional Materials 20 (2010)338-346.
172. Ameri, Tayebeh, Jie Min, Ning Li, Florian Machui, Derya Baran, Michael Forster, Kristina J. Schottler, Daniel Dolfen, Ullrich Scherf, and Christoph J. Brabec.

"Performance enhancement of the P3HT/PCBM solar cells through NIR sensitization using a small-bandgap polymer." Advanced Energy Materials 2 (2012) 1198-1202.
173. Ameri, Tayebeh, Thomas Heumüller, Jie Min, Ning Li, Gebhard Matt, Ullrich Scherf, and Christoph J. Brabec. "IR sensitization of an indene-C60 bisadduct (ICBA) in ternary organic solar cells." Energy & Environmental Science 6 (2013) 1796-1801.
174. Huang, Jing-Shun, Tenghooi Goh, Xiaokai Li, Matthew Y. Sfeir, Elizabeth A. Bielinski, Stephanie Tomasulo, Minjoo L. Lee, Nilay Hazari, and André D. Taylor. "Polymer bulk heterojunction solar cells employing Förster resonance energy transfer." Nature Photonics 7 (2013) 479-485.
175. Honda, Satoshi, Hideo Ohkita, Hiroaki Benten, and Shinzaburo Ito. "Selective dye loading at the heterojunction in polymer/fullerene solar cells." Advanced Energy Materials 1 (2011) 588-598.
176. Kim, Jung Kyu, Myung Jin Park, Sang Jin Kim, Dong Hwan Wang, Sung Pyo Cho, Sukang Bae, Jong Hyeok Park, and Byung Hee Hong. "Balancing light absorptivity and carrier conductivity of graphene quantum dots for high-efficiency bulk heterojunction solar cells." Acs Nano 7 (2013) 7207-7212.
177. Lee, Ju Min, Joonwon Lim, Nayeun Lee, Hyung Il Park, Kyung Eun Lee, Taewoo Jeon, Soo Ah Nam, Jehan Kim, Jonghwa Shin, and Sang Ouk Kim. "Synergistic concurrent enhancement of charge generation, dissociation, and transport in organic solar cells with plasmonic metal–carbon nanotube hybrids." Advanced Materials 27 (2015) 1519-1525.
178. Liu, Yongsheng, Ziruo Hong, Qi Chen, Weihsuan Chang, Huanping Zhou, Tze-Bin Song, Eric Young et al. "Integrated perovskite/bulk-heterojunction toward efficient solar cells." Nano letters 15 (2015) 662-668.
179. Zuo, Chuantian, and Liming Ding. "Bulk heterojunctions push the photoresponse of perovskite solar cells to 970 nm." Journal of Materials Chemistry A 3 (2015) 9063-9066.
180. Liu, Jun, Yuhua Xue, Yunxiang Gao, Dingshan Yu, Michael Durstock, and Liming Dai. "Hole and electron extraction layers based on graphene oxide derivatives for high-performance bulk heterojunction solar cells." Advanced Materials 24 (2012) 2228-2233.
181. Li, Shao-Sian, Kun-Hua Tu, Chih-Cheng Lin, Chun-Wei Chen, and Manish Chhowalla. "Solution-processable graphene oxide as an efficient hole transport layer in polymer solar cells." ACS nano 4 (2010) 3169-3174.
182. Iwan, Agnieszka, Felipe Caballero-Briones, Michal Filapek, Bartosz Boharewicz, Igor Tazbir, Agnieszka Hreniak, and Jesus Guerrero-Contreras. "Electrochemical and photocurrent characterization of polymer solar cells with improved performance after GO addition to the PEDOT: PSS hole transporting layer." Solar Energy 146 (2017) 230-242.
183. Wu, Xinkai, Jun Liu, Dongqing Wu, Yanru Zhao, Xindong Shi, Jing Wang, Saijun Huang, and Gufeng He. "Highly conductive and uniform graphene oxide modified PEDOT: PSS electrodes for ITO-Free organic light emitting diodes." Journal of Materials Chemistry C 2 (2014) 4044-4050.
184. Kymakis, Emmanuel, and Dimitrios Konios. "Graphene oxide-like materials in

organic and perovskite solar cells." In The Future of Semiconductor Oxides in Next-Generation Solar Cells, Elsevier, (2018)357-394.
185. Yu, Jae Choul, Jeong In Jang, Bo Ram Lee, Geon-Woong Lee, Joong Tark Han, and Myoung Hoon Song. "Highly efficient polymer-based optoelectronic devices using PEDOT: PSS and a GO composite layer as a hole transport layer." ACS applied materials & interfaces 6 (2014) 2067-2073.
186. Amollo, Tabitha A., Genene T. Mola, and Vincent O. Nyamori. "High-performance organic solar cells utilizing graphene oxide in the active and hole transport layers." Solar Energy 171 (2018) 83-91.
187. Luceño Sánchez, José Antonio, Rafael Peña Capilla, and Ana Maria Díez-Pascual. "High-Performance PEDOT: PSS/hexamethylene diisocyanate-functionalized graphene oxide nanocomposites: Preparation and properties." Polymers 10 (2018) 1169.
188. Liu, Tao, Xiaonan Xue, Lijun Huo, Xiaobo Sun, Qiaoshi An, Fujun Zhang, Thomas P. Russell, Feng Liu, and Yanming Sun. "Highly efficient parallel-like ternary organic solar cells." Chemistry of Materials 29 (2017) 2914-2920.
189. An, Qiaoshi, Fujun Zhang, Jian Zhang, Weihua Tang, Zhenbo Deng, and Bin Hu. "Versatile ternary organic solar cells: a critical review." Energy & Environmental Science 9 (2016) 281-322.
190. Yang, Liqiang, Huaxing Zhou, Samuel C. Price, and Wei You. "Parallel-like bulk heterojunction polymer solar cells." Journal of the American Chemical Society 134 (2012) 5432-5435.
191. Liu, Zhiyong, Dawei He, Yongsheng Wang, Hongpeng Wu, and Jigang Wang. "Graphene doping of P3HT: PCBM photovoltaic devices." Synthetic Metals 160 (2010) 1036-1039.
192. Yu, Fei, and Vikram K. Kuppa. "Enhancement in the performance of organic photovoltaic devices with pristine graphene." Materials Letters 99 (2013) 72-75.
193. Robaeys, Pieter, Francesco Bonaccorso, Emilie Bourgeois, Jan D'Haen, Wouter Dierckx, Wim Dexters, Donato Spoltore et al. "Enhanced performance of polymer: fullerene bulk heterojunction solar cells upon graphene addition." Applied Physics Letters 105 (2014) 1361.
194. Jun, Gwang Hoon, Sung Hwan Jin, Bin Lee, Bo Hyun Kim, Weon-Sik Chae, Soon Hyung Hong, and Seokwoo Jeon. "Enhanced conduction and charge-selectivity by N-doped graphene flakes in the active layer of bulk-heterojunction organic solar cells." Energy & Environmental Science 6 (2013) 3000-3006.
195. Bonaccorso, Francesco, Nikolaos Balis, Minas M. Stylianakis, Marika Savarese, Carlo Adamo, Mauro Gemmi, Vittorio Pellegrini, Emmanuel Stratakis, and Emmanuel Kymakis. "Functionalized Graphene as an Electron-Cascade Acceptor for Air-Processed Organic Ternary Solar Cells." Advanced Functional Materials 25 (2015) 3870-3880.
196. Stylianakis, M. M., D. Konios, G. Kakavelakis, G. Charalambidis, E. Stratakis, A. G. Coutsolelos, E. Kymakis, and S. H. Anastasiadis. "Efficient ternary organic photovoltaics incorporating a graphene-based porphyrin molecule as a universal electron cascade material." Nanoscale 7 (2015) 17827-17835.
197. Balis, Nikolaos, Dimitrios Konios, Emmanuel Stratakis, and Emmanuel Kymakis. "Ternary organic solar cells with reduced graphene oxide–Sb2S3 hybrid nanosheets

as the cascade material." ChemNanoMat 1 (2015) 346-352.
198. Kim, Jung Kyu, Myung Jin Park, Sang Jin Kim, Dong Hwan Wang, Sung Pyo Cho, Sukang Bae, Jong Hyeok Park, and Byung Hee Hong. "Balancing light absorptivity and carrier conductivity of graphene quantum dots for high-efficiency bulk heterojunction solar cells." Acs Nano 7 (2013) 7207-7212.
199. Li, Fushan, Lijie Kou, Wei Chen, Chaoxing Wu, and Tailiang Guo. "Enhancing the short-circuit current and power conversion efficiency of polymer solar cells with graphene quantum dots derived from double-walled carbon nanotubes." NPG Asia Materials 5 (2013) e60-e60.
200. Sygletou, Maria, Pavlos Tzourmpakis, Costas Petridis, Dimitrios Konios, Costas Fotakis, Emmanuel Kymakis, and Emmanuel Stratakis. "Laser induced nucleation of plasmonic nanoparticles on two-dimensional nanosheets for organic photovoltaics." Journal of Materials Chemistry A 4 (2016) 1020-1027.
201. Kakavelakis, George, Antonio Esau Del Rio Castillo, Vittorio Pellegrini, Alberto Ansaldo, Pavlos Tzourmpakis, Rosaria Brescia, Mirko Prato, Emmanuel Stratakis, Emmanuel Kymakis, and Francesco Bonaccorso. "Size-tuning of WSe2 flakes for high efficiency inverted organic solar cells." ACS nano 11 (2017) 3517-3531.
202. Stylianakis, Minas M., Dimitrios Konios, Constantinos Petridis, George Kakavelakis, Emmanuel Stratakis, and Emmanuel Kymakis. "Ternary solution-processed organic solar cells incorporating 2D materials." 2D Materials 4 (2017) 042005.
203. Yu, Jae Choul, Jeong In Jang, Bo Ram Lee, Geon-Woong Lee, Joong Tark Han, and Myoung Hoon Song. "Highly efficient polymer-based optoelectronic devices using PEDOT: PSS and a GO composite layer as a hole transport layer." ACS applied materials & interfaces 6 (2014) 2067-2073.
204. Díez, Noel, Agata Śliwak, Stanisław Gryglewicz, Bartosz Grzyb, and Grażyna Gryglewicz. "Enhanced reduction of graphene oxide by high-pressure hydrothermal treatment." Rsc Advances 5 (2015) 81831-81837.

CHAPTER 2

EXPERIMENTAL DETAILS: PREPARATION, CHARACTERIZATION AND MEASUREMENTS

2.1 Introduction

In this chapter, experimental details regarding the synthesis of Graphene Oxide (GO) and Fluorinated Graphene Oxide (FGO) by modified Hummer's method **[1,2],** chemical reduction of FGO to form Fluorinated Reduced Graphene Oxide (F-rGO) has been discussed in detail. Subsequently, the preparation of PEDOT:PSS, GO, and PEDOT:PSS-GO composites (different compositions) have been presented which will be utilized as HTLs in polymer solar cell (PSCs) devices. Further, the procedure for the preparation of active layer composed of binary blends [(P3HT:PCBM) or (PTB7-th:PCBM)] and ternary blend [P3HT:PTB7-th:PCBM] for PSCs have been discussed. Finally, the detailed solar cell device fabrication steps have been presented along with the details of the equipments used. Experimental details including various steps involved in device preparation and fabrication equipments like thermal evaporator, spin coating unit, UV ozone cleaner and glove box integrated with vacuum coating unit have been presented.

Fabrication of organic solar cell devices involves many fundamental steps and each step has its own importance. Particularly, processing of device is prompt to changes when different active materials with different interfacial layers are used. Often, even processing of device with the same active material using different HTL can result in different requirements for device processing. In order to obtain the optimal device efficiency from the available materials, much iteration of experiments is essential to establish the best processing conditions for fabrication of OPV devices.

Further, techniques used in the characterization of samples such as, "X-ray diffraction (XRD), Transmission electron microscopy (TEM), atomic force microscopy (AFM), Field emission scanning electron microscope (FESEM), UV-Vis absorption spectroscopy, photo-transmittance, Raman Spectroscopy, X-ray photoelectron

Spectroscopy (XPS), Field-Emission Scanning Electron Microscopy (FESEM), Fourier-transform infrared spectroscopy (FTIR), Ultraviolet Photoelectron Spectroscopy (UPS), Resistivity and conductivity measurements by Four-point probe technique, Photoluminescence (PL), Time-Resolved Photoluminescence (TRPL); and measurement methods such as solar cell Current-Voltage (I-V) measurements, External Quantum Efficiency (EQE) Measurements, and Photostability measurements" are discussed.

2.2 Synthesis of GO, FGO, and F-rGO

2.2.1 Materials Used

Pure grade graphite flakes (Alfa Aesar 99.99%), graphite flakes (Sigma-Aldrich 99.99%), potassium permanganate ($KMnO_4$), Sulfuric acid (H_2SO_4) (98%), Hydrazine monohydrate (80%), and hydrochloric acid (HCl) (35%) were purchased from Merck, Ethanol and hydrogen peroxide (H_2O_2) (30%) was purchased from Rankem. They were used without further purification for experiment. Double deionized water) (DI) was used in the synthesis of GO and FGO.

2.2.2 Synthesis of GO and FGO

(i) Synthesis of GO:

GO was prepared from graphite flakes by using modified Hummer method **[3, 4, 5]**. Briefly, 1.5 g of Graphite flakes (Alfa Aesar 99.99%) Micro wave heating for 10 sec than exfoliated graphite obtained and 250 ml of H_2SO_4 were mixed in a 1000 ml (1 Lt.) volumetric flask kept under at ice bath with stirring continuously. The sample mixture was stirred 300 rpm for 2 hrs at the room temperature and 10.5g of potassium permanganate ($KMnO_4$) was added to the suspension very slowly. The addition rate was controlled carefully to preserve the reaction increases temperature up to 98^0C.The slow addition of 1.5 liter of water. The reaction temperature was increased quickly to 98 ^{0}C.The solution mixture was finally treated with 30 ml H_2O_2 was added to the mix stirring and terminate the reaction, graphene oxide formed yellow color. For purification, the mixture was washed by centrifugation at 4000 rpm, 15 min and Mixture is filtered and washed with 90 mL of HCl + 900 mL of Distilled water, stirring 400 rpm continued

30 min, Solution was centrifuged at 4000 rpm, 15 minutes, removed unexfoliated graphite Oxide. The mixture filtered or washed with only 1 liter of distilled water, stirring 400 rpm continued 1 hr. Again centrifuged at 4000 rpm, 30 min and remove unexfoliated graphite Oxide. After filtration and then it dried in hot air oven, the Graphene Oxide (GO) was obtained as a powder Fig. 2.1.

Figure 2.1 *Schematic diagram showing the steps undertaken for the synthesis of GO by modified Hummer's method.*

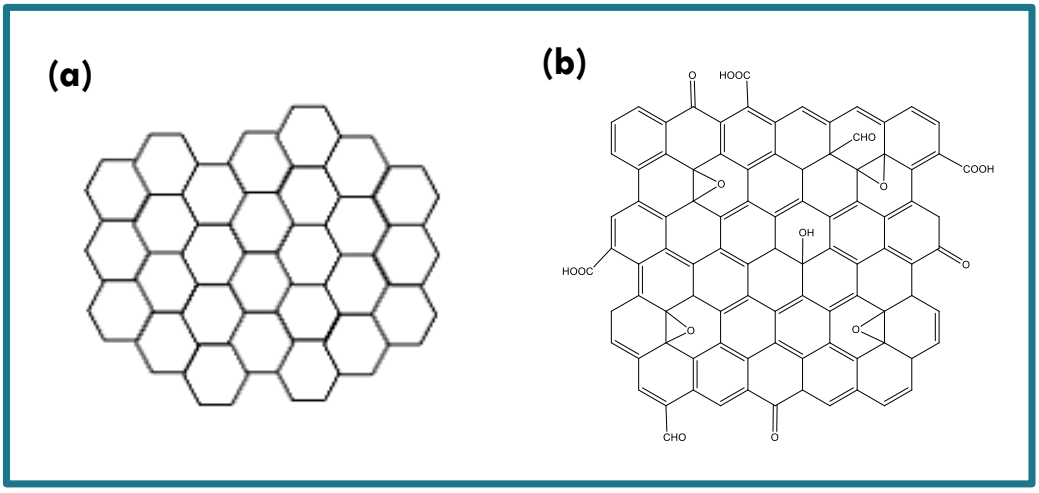

Figure 2.2 *Schematic structure of (a) a single graphene sheet; (b) graphene oxide (GO).*

(ii) Synthesis of FGO:

FGO was prepared by an improved Hummers method **[6, 7, 8].** A fluorinated graphite flake powder (1 g) was dispersed in 100 mL of sulfuric acid. The solution was stirred at 300 rpm for 24 hrs. Then, 7 g of potassium permanganate ($KMnO_4$) was added in small quantities. As the reaction between $KMnO_4$ and the acid is highly exothermic, care must be taken when adding $KMnO_4$. The whole mixture was kept under vigorous stirring continuously for 20 hrs. After the oxidation reaction with $KMnO_4$, ice water added in to the solution continues string 2 hrs. Following this, 5 mL of hydrogen peroxide was added and terminated the reaction. The reaction vessel was kept overnight without disturbance. Layer settling at the bottom and remove the above water. After centrifuged at the rate of 4000 rpm for 30 minutes. Then, the precipitate was washed with hydrochloric acid + DI water (90 ml+900 ml) solution to remove impurities. The layer that settled at the bottom in the acid–water mixture was washed for impurities following the procedure. The filtered product was dried in vacuum oven at 80^0C for 24 hrs. The product obtained is FGO shown below Fig. 2.3.

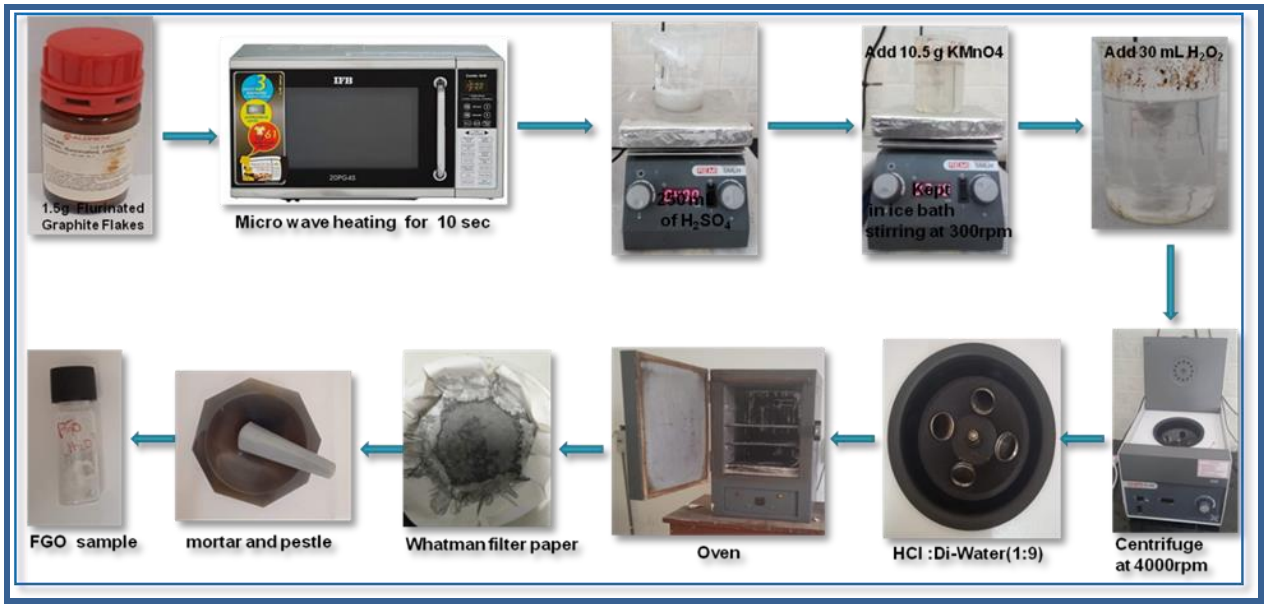

Figure 2.3 *Schematic diagram showing the steps undertaken for the synthesis of FGO by modified Hummer's method.*

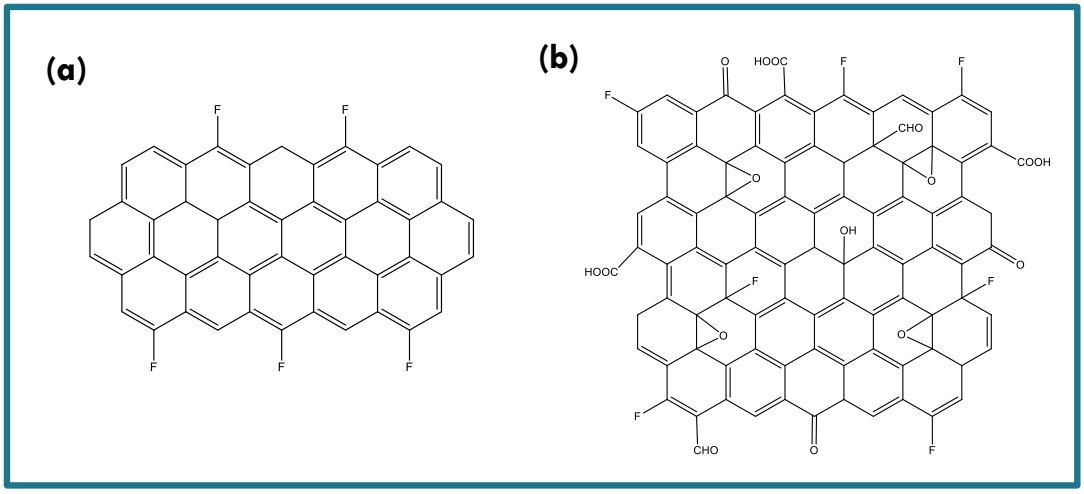

Figure 2.4 *Schematic structure of (a) Fluorinated Graphite (b) Fluorinated Graphene Oxide (FGO).*

(iii) Synthesis of F-rGO:

To get reduced FGO i.e., F-rGO, 50 mg of FGO was dissolved in 100 mL of ethanol and sonicated for 30 min. Subsequently, 5 mL of hydrazine monohydrate was added and sonicated for 60 min. **[8, 9].** A color change from gray to black indicates the reduction process. The product obtained is F-rGO. Dry at 80^{o}C overnight finally F-rGO powder formed.

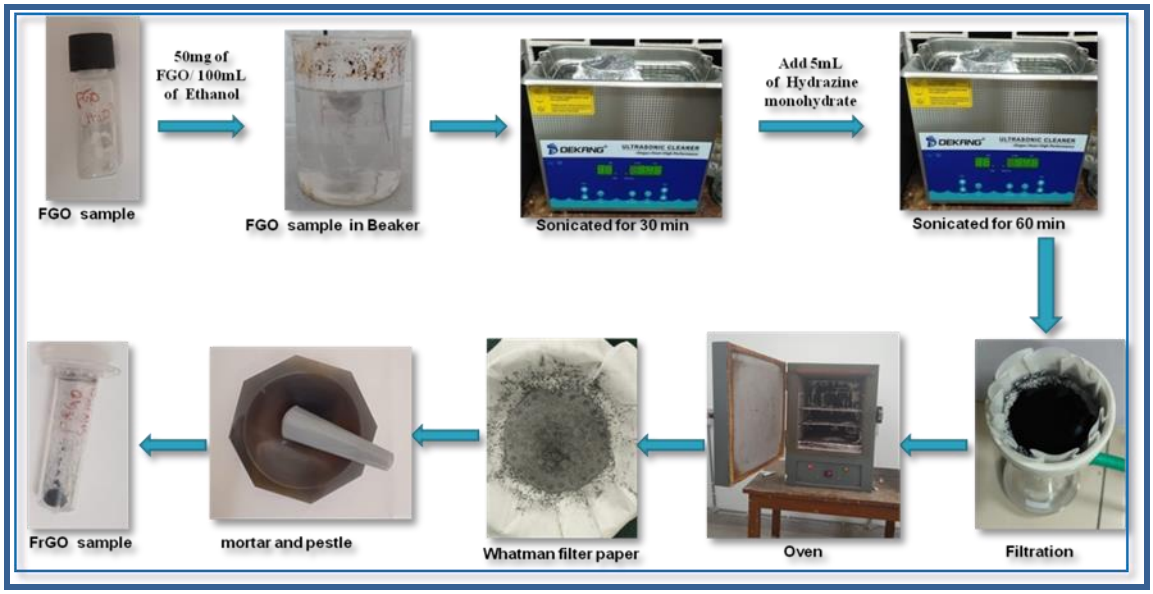

Figure 2.5 *Schematic diagram showing the steps undertaken for the synthesis of F-rGO by Chemical reduction method.*

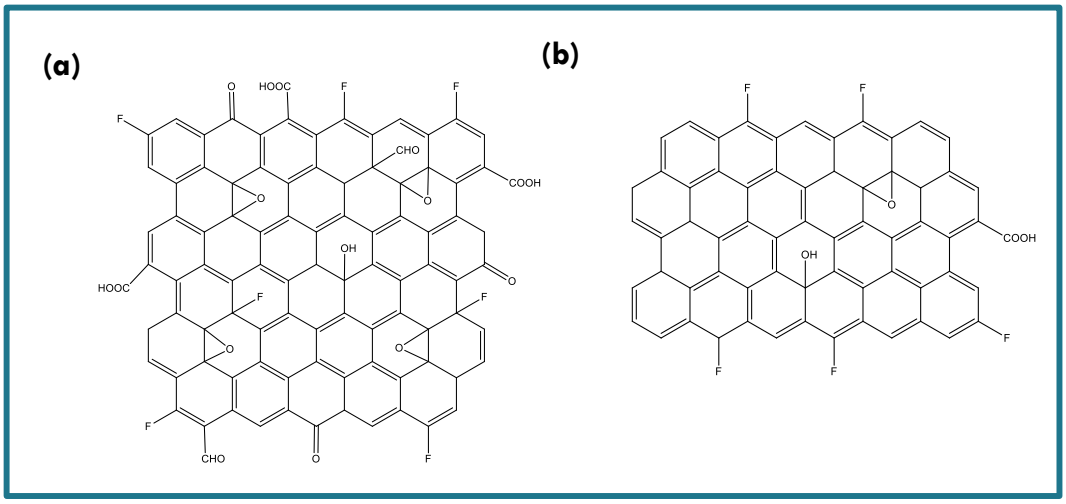

Figure 2.6 *Schematic structure of (a) Fluorinated Graphene Oxide (FGO) (b) Fluorinated Reduced Graphene Oxide (F-rGO)*

2.2.3 Preparation of HTL: PEDOT:PSS, GO and PEDOT:PSS-GO composites

Preparation method: - Volume solutions (100mg in 1 ml) of GO, PEDOT:PSS and PEDOT:PSS-GO composites were prepared. The synthesized GO nanosheets, individually as well as after dispersion in PEDOT:PSS in 2:1, 1:1, and 1:2 weight ratios. The effect of GO nanosheets incorporation in PEDOT:PSS on governing in device performances of PEDOT:PSS-GO HTLs based TPSC devices have been examined systematically. Here, GO, PEDOT:PSS solutions and PEDOT:PSS-GO composites solutions are shown below figure 2.7 by adding GO in PEDOT:PSS in different weight ratios i.e, (2:1), (1:1), and (1:2).

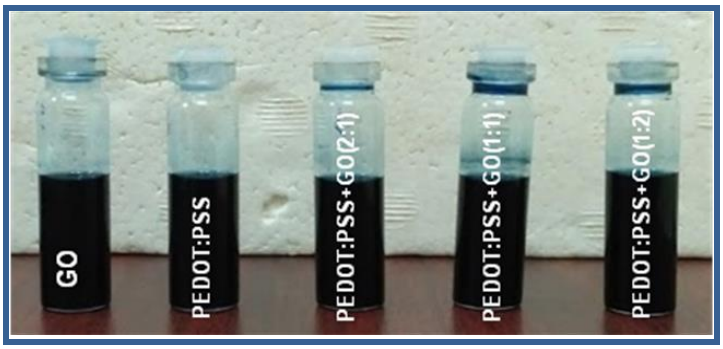

Figure 2.7 *Photograph of GO, PEDOT:PSS and adding GO in PEDOT:PSS in different weight ratios (2:1), (1:1), and (1:2).*

2.2.4 Preparation of Photoactive Layer: Binary and Ternary blends

Preparation of Ternary blend active layers [(P3HT (D_1):PTB7-th (D_2): PCBM (A_1), and [PTB7-th (D_1):PCBM (A_1): F-rGO (A_2)]. 5wt% by volume solutions (chlorobenzene and 1,8-diiodoctane (97:3 vol%)) of P3HT:PTB7-th:PCBM and PTB7-th:PCBM:F-rGO blend were prepared showed Fig. 2.8.

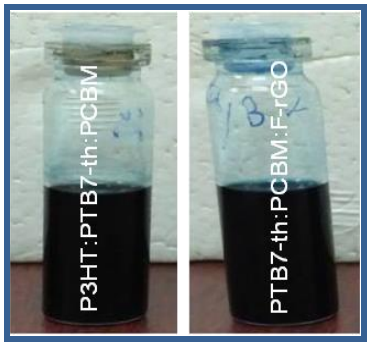

Figure 2.8 *Photograph of solutions of Ternary blends: P3HT:PTB7-th:PCBM and PTB7-th:PCBM:F-rGO.*

2.3 Fabrication of Polymer Solar Cells

The solar cell devices were fabricated in the planar device configuration. The schematic is represented in Fig.2.9.

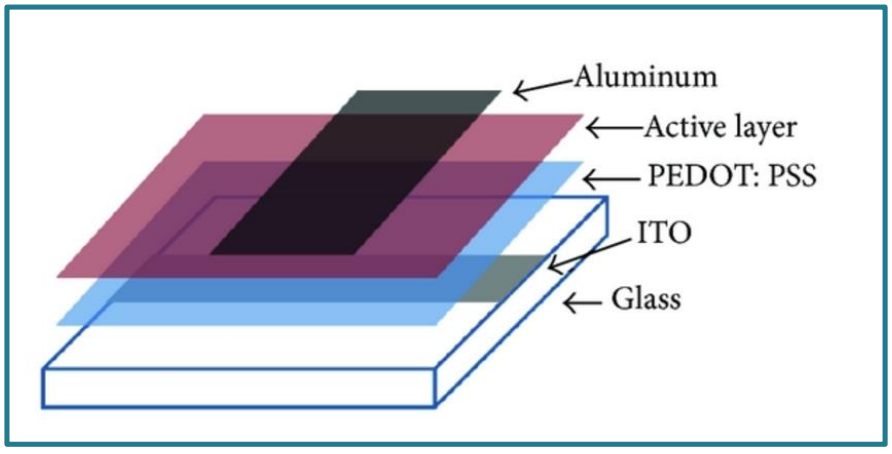

Figure 2.9 *The schematic of the polymer solar cell device showing the respective layers.*

2.3.1 Materials Used

The list of materials used for the preparation of devices is:

- ITO (sheet resistance ~ 15 Ω/□)
- PEDOT:PSS (Sigma Aldrich USA, 99.5%)
- P3HT (Sigma Aldrich USA, 99.5%)
- PTB7-th (Sigma Aldrich USA, 99.2%)
- PCBM (Sigma Aldrich USA, 99.8%)
- GO, FGO nanosheets (self synthesized using Hummer's method)
- F-rGO (self synthesized using chemical method)
- LiF (Sigma Aldrich USA, 99.98%)
- Al (Sigma Aldrich USA, 99.98%)

2.3.2 Steps involved in TSC device fabrication

(i) Patterning of ITO coated glass substrates:

The *ITO* coated glass sheets were cut in 2.5 cm × 2.5 cm dimension substrates. Two strips of 3 mm were masked on these *ITO* substrates using cello tape. The exposed *ITO* was etched using dilute hydrochloric acid solvent and zinc dust powder. The patterned *ITO* strips on glass substrate is shown below. After top electrode deposition, the active area of the device is 3 mm x 3 mm = 0.1 cm^2.

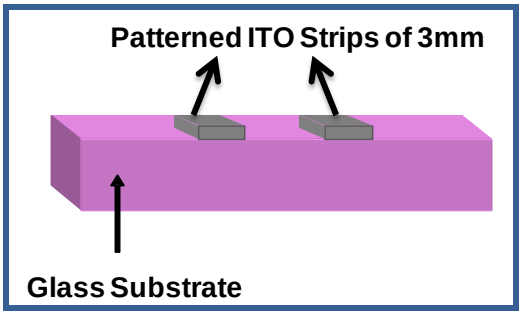

Figure 2.10 *ITO coated glass substrates before and after patterning the strip of 3mm width.*

(ii) Cleaning of patterned ITO glass substrates:

The glass substrates with ITO patterned strips of width 3 mm were cleaned thoroughly following the procedure listed in the flow chart shown below in Fig. 2.11.

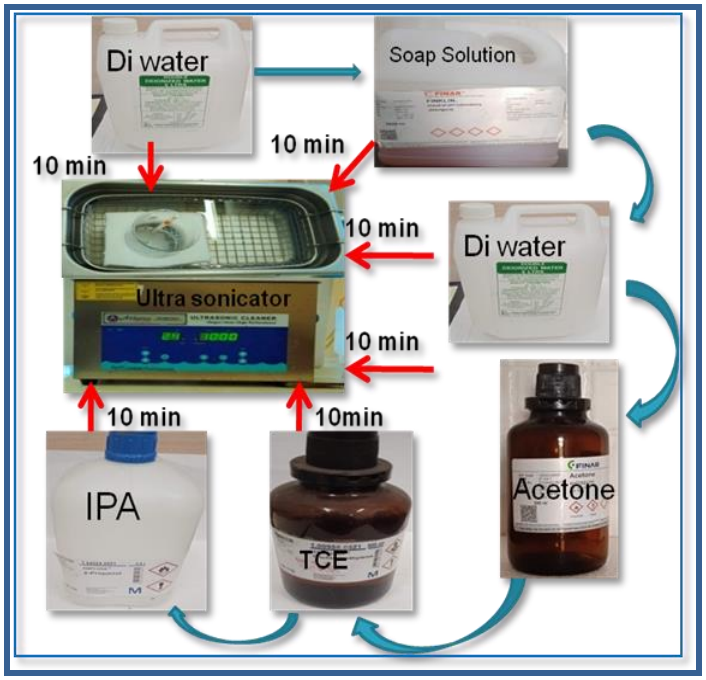

Figure 2.11. *Steps involved in cleaning the patterned ITO glass substrates.*

Vacuum Oven and UV light cleaning of cleaned ITO glass substrates

The ITO coated glass substrates were dried in Vacuum Oven and cleaned using UV light cleaning to remove stain on ITO, which cannot be removed by water and organic solvents. These stains are of nanometre size and form organic contaminants which cannot see through eyes. Hence, these substrates should be further cleaned by treating in UV light cleaner, which also facilitates to reduce the surface pollution created by solvents. The samples exposed to Vacuum Oven and UV light cleaner are shown in Fig. 2.12. UV light cleaner also leads to the supplementary cleaning of these ITO substrates by removing the nano impurities from surface. Moreover, it also increases the adhesiveness of ITO substrates leading to better bonding between anode (ITO) and HTL. Apart from this, it also enhances the work function of ITO which helps holes and electrons to shift toward respective electrodes as high work function anode and low work

function cathode; as in case of conventional structure is the essential obligation for proper running of devices.

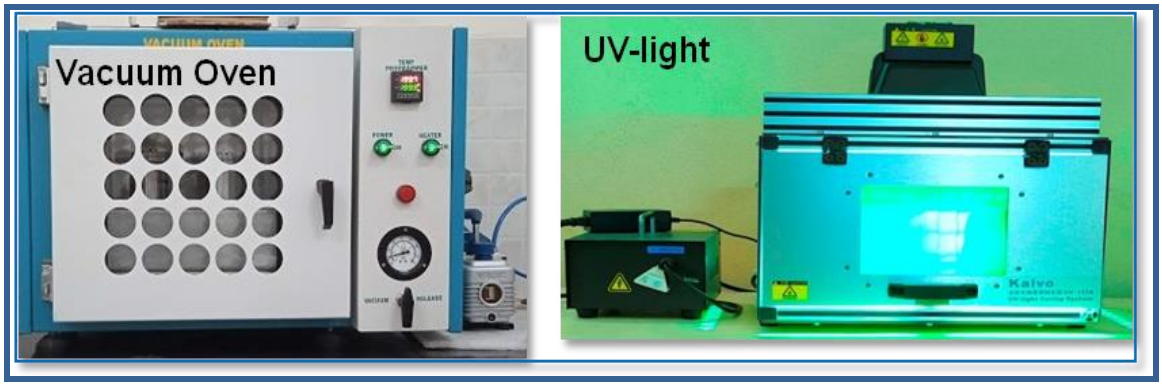

Figure 2.12 *Photograph of Vacuum Oven and UV light cleaning of cleaned ITO glass substrates.*

Plasma Cleaning of Patterned ITO glass Substrates

The ITO coated glass substrates cleaned by above mentioned procedures were further being treated in O_2 plasma for 10 minutes. The samples exposed to O_2 plasma are shown in photograph of Fig. 2.13, plasma further cleans the substrates, removes all the dust particles from the surfaces. Apart from this it also slightly enhances the work function of ITO which makes good suitability for choosing ITO as anode in hole-only devices as high work function anode and low work function cathode is required for the preparation of such devices.

Figure 2.13 *Photograph of ITO coated glass substrates during plasma treatment.*

(iii) Deposition of HTL thin film on plasma treated ITO glass substrates:

A thin film of PEDOT:PSS or PEDOT:PSS-GO (shown below) was spin coated onto pre-cleaned and plasma treated ITO coated glass substrates at 2000 rpm, 50 sec, and cured at 120^0C for 30 min. in vacuum. The spin coater is shown in Fig. 2.14.

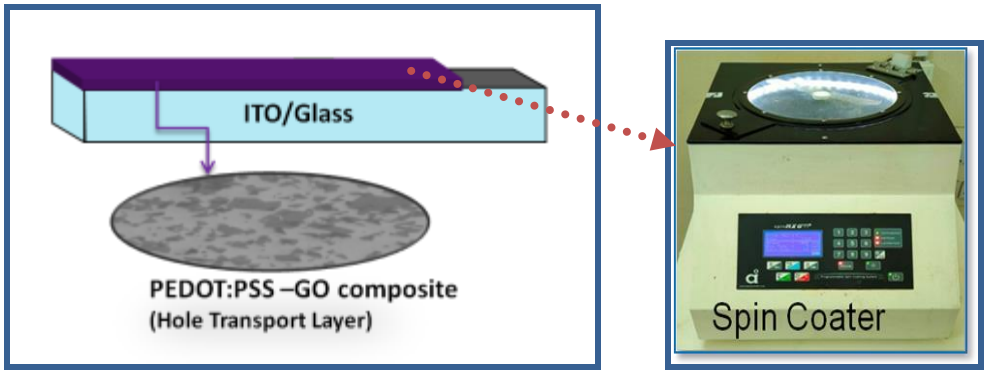

Figure 2.14 *Photograph of Spin Coating Unit used for the deposition of polymer thin films.*

Spin coating is a thin film deposition technique whereby uniform thin films can be deposited onto the flat substrates **[10]**. The deposition conditions needed to be optimized in order to attain controlled deposition of thin film of uniform thickness are choice of solvent, concentration of solution, spin speed and spin time.

(*iv) Deposition of Ternary blends for active layer thin films over the HTL layer:*

For the deposition of polymer thin films, a homogeneous solution of P3HT, PTB7-th, and PCBM has been prepared in (0.3:0.7:1) weight ratio in a mixed solvent of chlorobenzene and 1,8-diiodoctane (1:3 vol%) with a concentration of 20 mg/mL. Then, the polymer blend solution was filtered using a 0.2 µm filter. For all the devices, the ternary blend active layer was spin coated over the HTL coated-ITO substrates at 2000 rpm for 1 min. in a glove box, and finally, cured at 120 °C for 10 min. in the inert (N_2/Ar) glove box. The photograph of the glove box system used for the same is shown in Fig. 2.15.

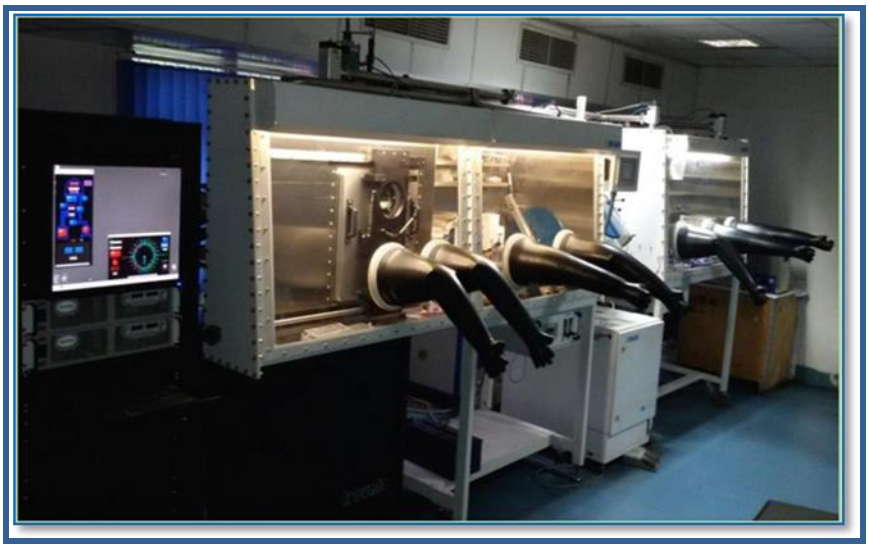

Figure 2.15 *Photograph of Inert Glove Box Coating Unit used for the deposition of Ternary blends for active layer thin films.*

(v) ***Deposition of LiF/Al electrode over the Ternary blends for active layer thin films:***

On top of active layer films, LiF/Al electrodes ~100 nm were deposited by thermal evaporation at a vacuum $5x10^{-6}$ Torr, using mask of aluminum sheet having two 3 mm wide stips. The active area was approx. 0.1 cm^2 for all the devices. The metallic chamber used for the deposition of Al electrode is shown in photograph of Fig. 2.16.

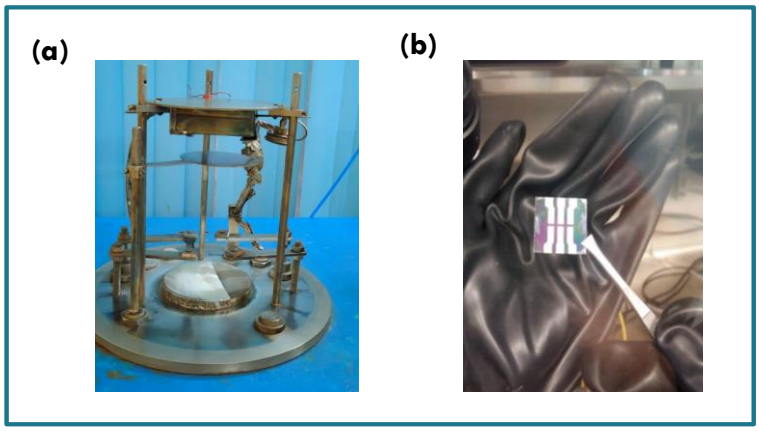

Figure 2.16 *Photograph of (a) Metallic Coating Unit used for the deposition of Lif and Al thin films (b) Fabricated device.*

2.3.3 Device Preparation

The following polymer solar cell devices fabricated in the present thesis work are:

- **Polymer Solar Cells devices with [D_1:A] or [D_2:A] Binary blend & [D_1:D_2:A] Ternary blend** (refer Fig. 2.17)

  I. Effect of different HTL with common ternary blend active layer:

  - ITO/GO/P3HT:PTB7-th:PCBM/LiF/Al
  - ITO/PEDOT:PSS/ P3HT:PTB7-th:PCBM/LiF/Al
  - ITO/PEDOT:PSS-GO(1:2)/ P3HT:PTB7-th:PCBM/LiF/Al
  - ITO/PEDOT:PSS-GO(1:1)/ P3HT:PTB7-th:PCBM/LiF/Al
  - ITO/PEDOT:PSS-GO(2:1)/ P3HT:PTB7-th:PCBM/LiF/Al

  II. Comparison of ternary with binary blend based devices with common HTL:

  - ITO/PEDOT:PSS-GO(1:1)/P3HT:PCBM/LiF/Al
  - ITO/PEDOT:PSS-GO(1:1)/PTB7-th:PCBM/LiF/Al

- **Polymer Solar Cells devices with [D_1:A] Binary blend & [D:A_1:A_2] Ternary blend** (refer Fig. 2.18)

  - ITO/PEDOT:PSS/PTB7-th:PCBM/LiF/Al
  - ITO/PEDOT:PSS/PTB7-th:PCBM:F-rGO/LiF/Al

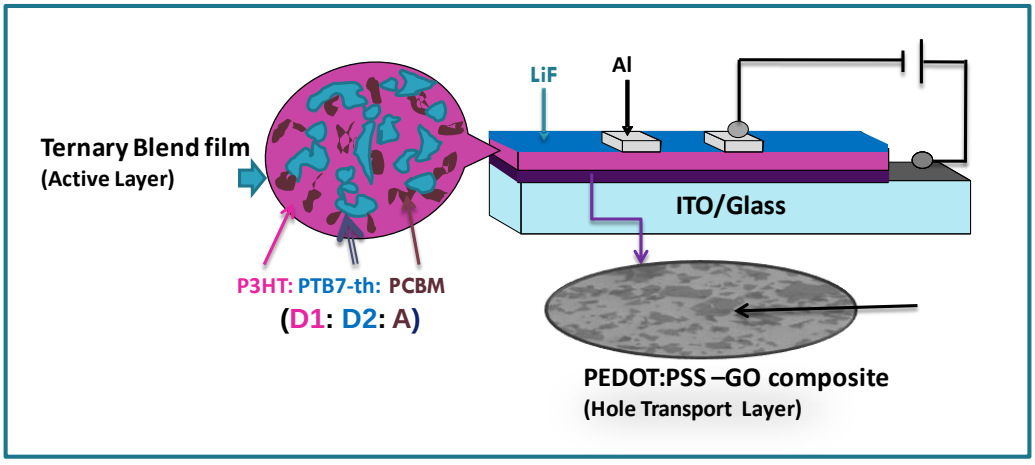

Figure 2.17 *Schematic of the TSC device using (D_1:D_2:A)-type ternary blend active layer [P3HT:PTB7-th:PCBM]*

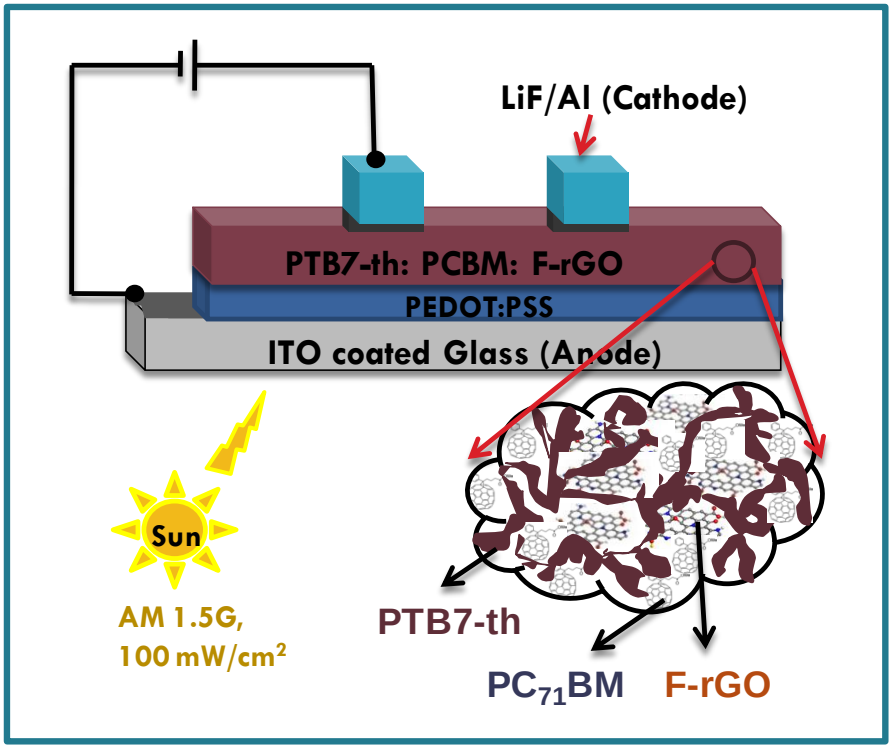

Figure 2.18 *Schematic of the TSC device using (D:A_1:A_2)-type ternary blend active layer [PTB7-th:PCBM:F-rGO]*

2.4 Characterization techniques

2.4.1 Structural Characterization

Structural characterization techniques used in this study include XRD, FESEM, TEM, AFM and FTIR.

2.4.1.1 X-ray Diffraction (XRD)

XRD is one of the most powerful techniques for determining atomic structure of films. In the present work, the X-ray diffraction (Model: PANalytical X'pert Powder) was used where Cu-K_α as the radiation (λ=1.542598 Å) source at a scanning angle ranging between 6°-270° with step size of 9°/per min time.

The X-rays that satisfy Bragg's law: $2d\sin\theta=n\lambda$, interfere constructively forming a bright spot on the detector. Figure 2.19 (a) depicts the essential characteristics of an X-ray diffractometer, whereas Figure 2.19 (b) depicts the setup of a PANalytical powder diffractometer.

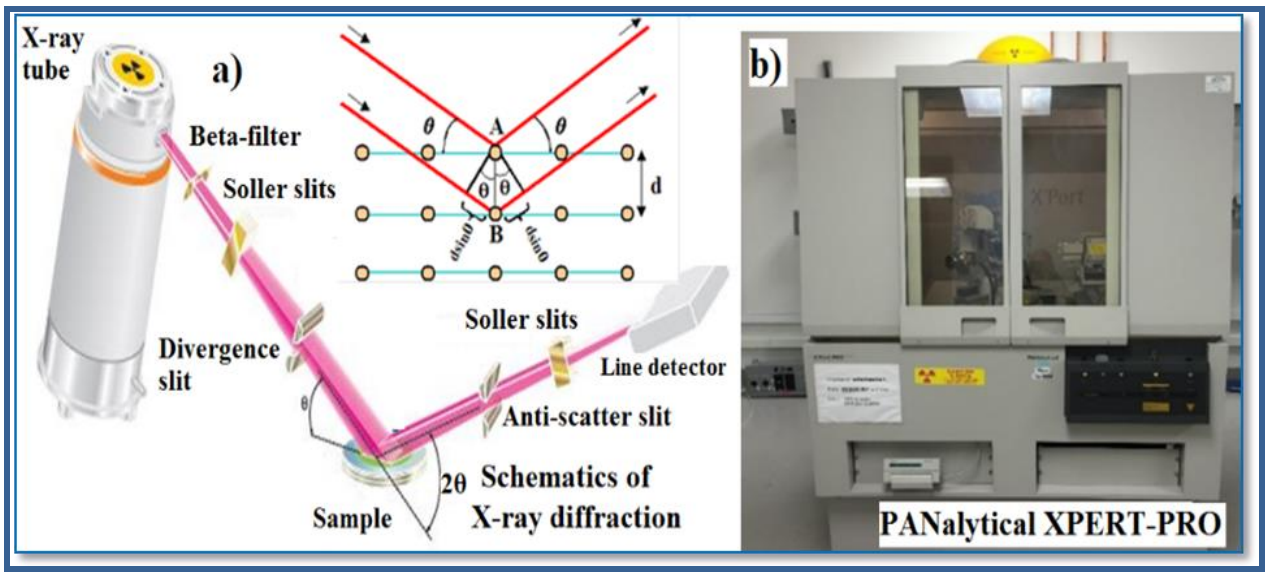

Figure 2.19 *(a) Schematic XRD, showing of Bragg's law, (b)PANalytical XRD diffractometer*

2.4.1.2 Field-Emission Scanning Electron Microscopy (FESEM)

FESEM is one of microscopes which is capable of providing high-resolution images of a sample surface. The schematic of the FESEM equipment used in the present work, is presented in Fig. 2.20.

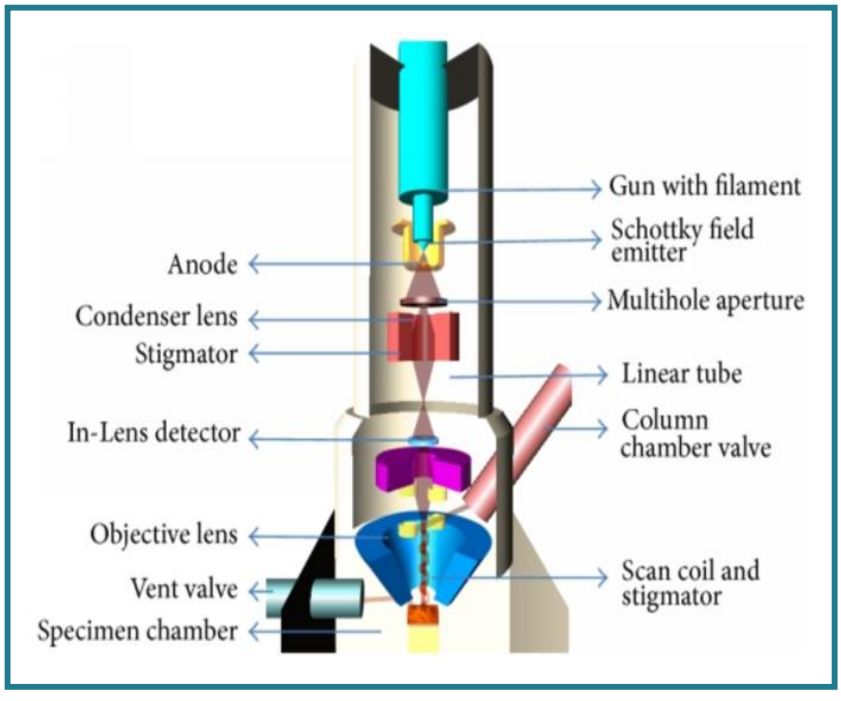

Figure 2.20 *Schematic diagram of FESEM* ***[12].***

Working Principle:

The principle of electron microscope is almost similar to light microscope. In light microscope the light source is visible light whereas in electron microscope the light source is high energetic electrons. The resolution of optical microscope is limited by its wavelength whereas in electron microscope the wavelength of the electrons can be varied with the applied voltage.

$$\lambda = \frac{1.5}{\sqrt{V}} nm$$

Smaller wavelength electrons generated from the field emission gun provide an opportunity to see the atomic structures of the samples. The resolution of any microscope, is determined by the spot size on the surface of the sample, quality of lenses used for focusing and on the performance of the electron gun i.e. brightness. In field emission electron microscope, the spot size is in the range of 1 nm to 25 nm. The sharpness, visibility and Brightness (β) of an image depends on electron probe current (i_p), electron probe convergence angle (α_p),electron probe size (d_p), and electron beam accelerating voltage (V_o). The brightness (β) is defined as the beam current per unit area per unit solid angle. The smaller is the spot size, the higher is the brightness.

Brightness (β) = Current (i_p)/(Area x Solid angle)

where, Area = $[(\pi d^2 p)/4]$ and Solid angle = $[\pi \alpha^2 p]$

Figure 2.21 *Field Emission Scanning Electron Microscope* ***[13].***

The microstructural analysis is carried out on the disc shaped samples coated with palladium and gold. These samples are mounted on to the stub via carbon tape to study their surface features, morphology and texture. The grain size of the samples is determined using "Image J" software. The grain size, morphology and distribution of grains can be estimated through the FESEM microstructure. Any secondary phase segregation can also be detected through microstructural analysis. The prepared samples are characterized using Field Emission Scanning Electron Microscope (Hitachi High-Technologies S-4800) which is shown in Fig. 2.21.

2.4.1.3 Transmission Electron Microscope (TEM)

Transmission electron microscopy (TEM) has been used to study shape, size and distribution of nanoparticles. In the TEM, much smaller wavelength (λ > 1000Å) of electron (0.3 Å) is used to achieve much superior resolution **[14].**

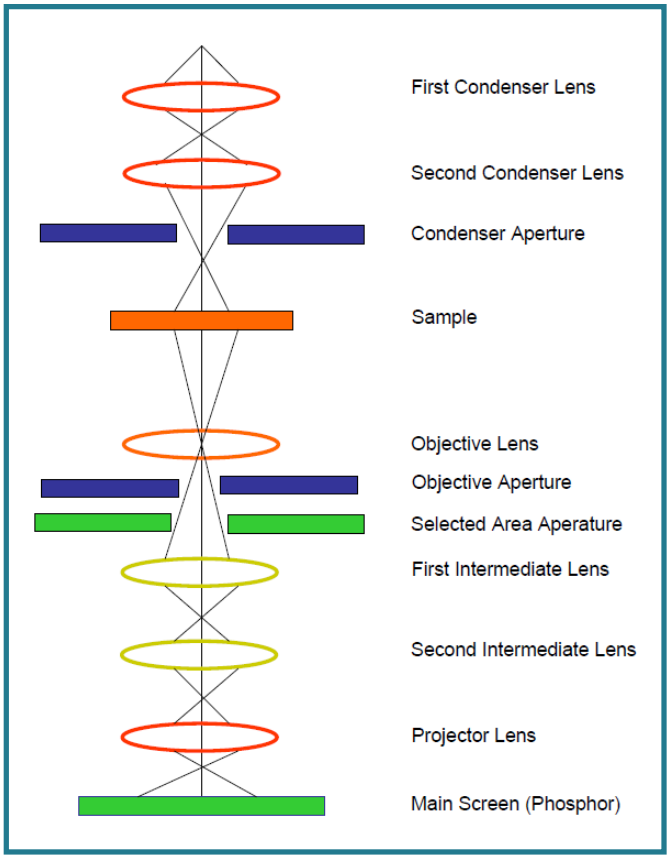

Figure 2.22 *Schematic diagram of a Transmission Electron Microscope.*

Figure 2.22 shows all the component of a TEM **[16].** In TEM, "the transmitted electron beam strikes the phosphor screen and generates an image with varying contrast. The darker areas with higher contrast are those from where fewer electrons are transmitted due to high density or thickness of the sample while the area of lower contrast shows the area of sample, which has less density or thickness, and thus more number of transmitted electrons are present".

In the present study, TEM analysis has been done by depositing a thin film of Graphene Oxide onto the copper grid via drop casting and the film were dried before the measurement. The TEM measurement were done using (JEOL JEM-2100F) electron microscope operating at an accelerating voltage 80kV.

2.4.1.4 Atomic Force Microscope (AFM)

To optimize the surface thin film at nanoscale level, AFM has been proved as one of the powerful tools due to its higher resolution and magnification. The first commercially available AFM was introduced in 1989**[17]**. A 10x10 mm specimen is used for AFM measurements in the tapping mode. During AFM measurement the cantilever (the AFM tip) scans the surface and records the topology in 2D as well as 3D topology information with a colour code for the height scale. To study the magnetic and electric response of surface AFM is found to be useful. The cantilever is usually composed of *Si* or *SiN*, with a very sharp tip (few nanometres). Scratched film is used to measure the thickness and afterwards the step height which is the difference between the averaged heights was measured at one edge of the scratch.

In AFM (shown in Fig. 2.23), "when the tip comes into contact with a sample surface, the cantilever to bend according Hooke's law owing to the forces between the tip and the sample surface" **[18].** AFM modes of operation can be classified into contact mode, non contact mode and tapping mode depending on the purpose of specimen.

In contact mode, the cantilever remains in contact with the surface during scanning. When it encounters variations in the surface it responds by deflecting to follow the contours. In Non-contact mode, there is no direct contact between the tip and surface and the tip remains a few nanometre above the surface of the material vibrating at a little higher frequency little higher than the resonance frequency of tip **[19].** This result into

very small vibrations. In the tapping mode, the cantilever arm resonates at a frequency as it scans the surface. When the tip comes in contact with the surface, a sensor reverses the motion of the cantilever to continue the oscillation. If scanning is processed at a constant height of tip then there is chance of damaging the tip due to non uniformity of film on substrate as the tip can collides with the surface and break. To maintain a consistent force between tip & sample, a feedback system is usually used to adjust the tip and the sample distance.

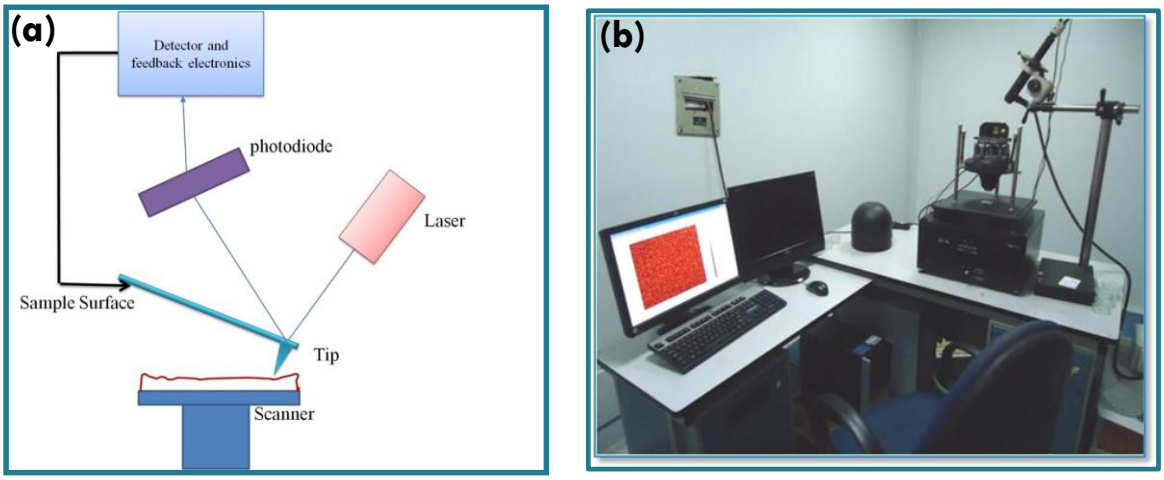

Figure 2.23 *(a)Schematic diagram of AFM, (b)AFM setup used for sample structural characterization.*

2.4.1.5 Fourier-transform infrared spectroscopy (FTIR)

FTIR spectroscopy is a technique for obtaining the infrared spectrum of transmission or solid absorption. It is an important tool used to reveal the presences of various structural groups with carbon bonds are present. The structural properties of graphene oxide, fluorinated graphene oxide, and fluorinated reduced graphene oxide samples were analyzed using Fourier transform infrared spectrometer (FTIR: model S 100; PerkinElmer) as shown in Fig. 2.24. The infrared spectra of the graphene oxide, fluorinated graphene oxide, and fluorinated reduced graphene oxide sample were noted at room temperature in the spectral range "400–4000 cm^{-1} at a resolution of 4 cm^{-1}". The pallets were prepared by mixing sample with KBr (infrared grade-Potassium bromide) in 1:100 ratios by weight and then pressed by hydraulic press. These pellets were immediately used to record FTIR spectra. From each sample, the FTIR spectrum was

normalized with empty KBr pellet. It can be used to analyze organic and inorganic substances. The above studies were done on all graphene oxide, fluorinated graphene oxide, and fluorinated reduced graphene oxide composition before and after completing in vitro studies. Then it helps to determine the chemical bonds or molecular structure of materials in the molecule by producing infrared absorption spectra. Thus the presence of specific functional groups can be monitored by these types of infrared bands, known as group wave number.

Figure 2.24 *Perkin Elmer 100SFTIR Spectrophotometer.*

Working Principle:

The schematic diagram of the Fourier transform infrared spectrophotometer is illustrated in Fig. 2.25**.** FTIR Spectrophotometer has recently replaced the conventional equipment's (dispersing type) due to its superior speed and sensitivity. The FTIR spectrophotometer has consisted of three main basic portions namely infrared source, an interferometer, and a detector. The interferometer again consists of three parts, namely beam splitter, moving mirror, and fixed mirror. The basic part of the instrument is called the Michelson interferometer **[20].**

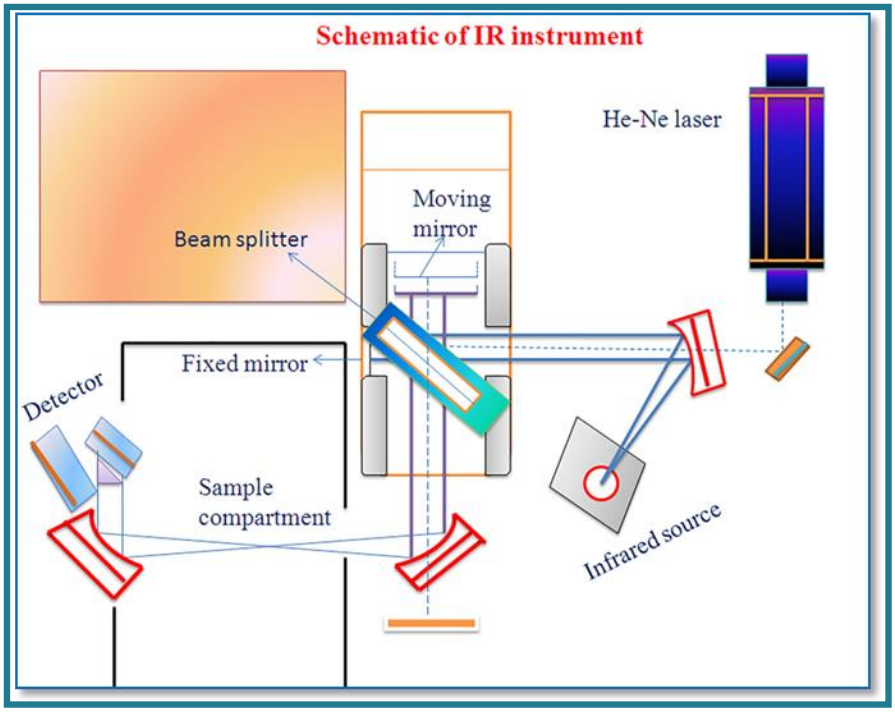

Figure 2.25 *Schematic diagram of Fourier Transform Infrared spectrometer.*

In FTIR, "When the radiation from an IR source is occasion on the beam splitter than half of the radiation is transmitted and half is reflected". The transmitted and reflected beams are made incident on the fixed and moving mirrors respectively from which the beams are reflected rear and incident on the beam splitter. The fixed and moving mirror beams interfere constructively and destructively, depending on the mid-path difference. It is the sinusoidal signal at the beam splitter and affects the pattern and focuses on the detector **[21].**

2.4.2 Optical Characterization

Optical characterization techniques used in this study include UV-Vis absorption Spectroscopy, PL, TRPL, Raman Spectroscopy, XPS and UPS.

2.4.2.1 UV-Vis absorption Spectroscopy

The UV-Vis spectroscopy is very effective technique for the determination of size and optical properties of graphene oxide, polymers materials. This spectrometer gives the spectrum between absorbance (A) versus wavelength (λ). This spectrum corresponds to

degree of absorption at each wavelength. In this spectroscopy the electrons get excited from valence band to conduction band by the absorption of appropriate amount of energy. To determine the nature of charge transition across the optical band gap, variation of optical coefficient with wavelength is calculated. Tauc's expression is used to relate between the absorption and band gap energy as shown in equation **[22-25].**

$(\alpha h\nu) = A\ (h\nu - E_g)^n$

Where 'α' is the absorption coefficient of the nano materials, A is a constant related to the effective masses associated with the bands, E_g is the band gap, hν is the energy of photon and n is the transition.

The block diagram of the computer controlled UV-visible spectrometer JascoV-670 model spectrometer is shown in Fig. 2.26.

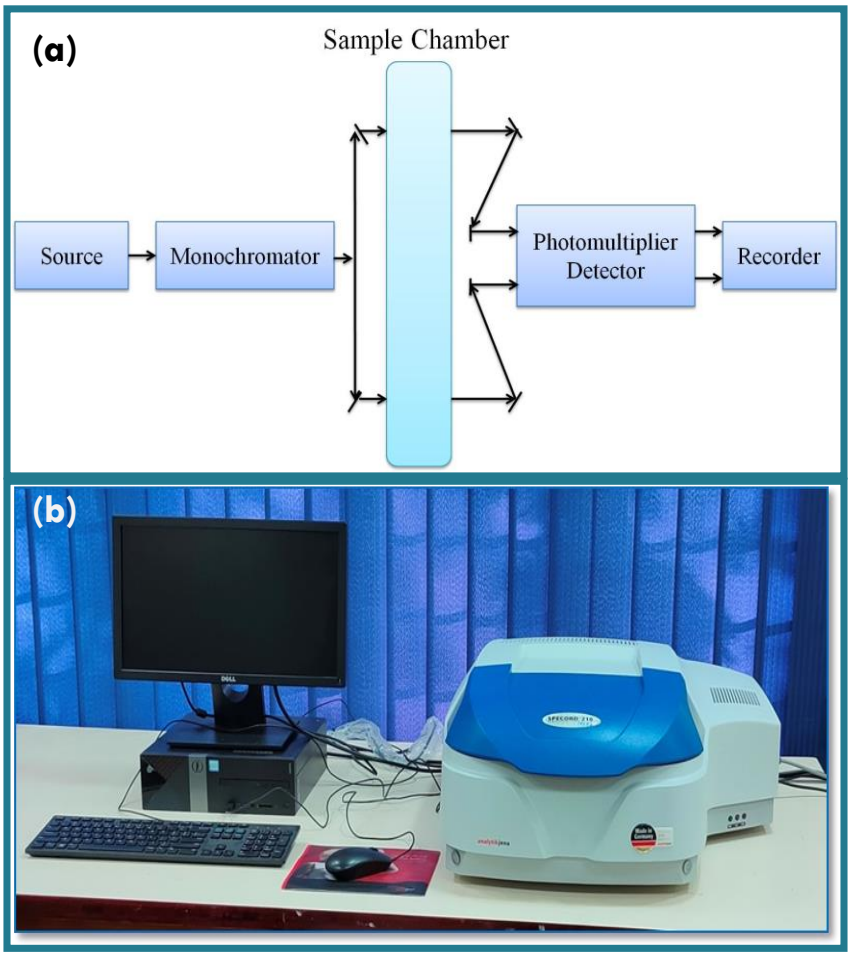

Figure 2.26 ***(a)*** *Schematic diagram of UV-vis absorption spectroscopy* ***[26,*** *(b) UV-Vis absorption spectroscopy.*

The samples measurements were carried out using wavelength in the region 200-850 nm for various measurements like absorbance, transmittance, band gap (E_g) from Tauc plots, and diffuse reflectance measurements. All absorbance spectrophotometers must contain the light source, wavelength selection device, sample holder and photon detector.

2.4.2.2 Photoluminescence Spectroscopy (PL) &Time-Resolved Photoluminescence (TRPL) Photoluminescence Spectroscopy (PL):

PL is simple, versatile, and nondestructive to determine the emission processes dominating in the particular material sample. The PL measurement set-up is shown in Fig. 2.27, which consists of "an laser source, mirror, lenses, optical power meter or spectrophotometer, and a photodetector". In present work, the PL measurements of different samples of pure, binary and ternary blends thin films samples were done using a system consisting of a two stage monochromator, a photomultiplier tube with a lock-in amplifier for PL detection.

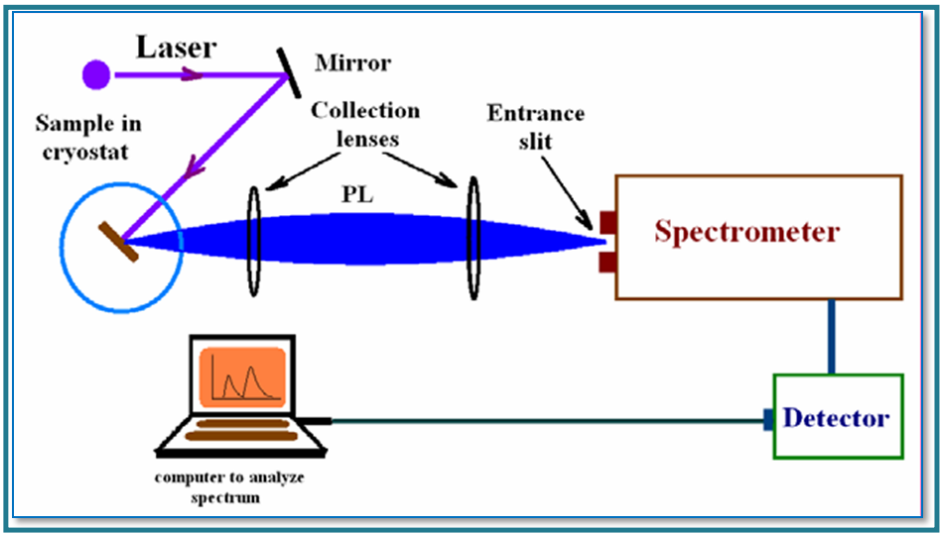

Figure 2.27 *Typical schematic diagram and experimental setup for PL measurements [29].*

Time-Resolved Photoluminescence (TRPL): The PL emission and PL decay profiles of the thin films samples were measured with the "Horiba Jobin-Yvon Fluorolog -3 800

spectrofluorimeter in the wavelength region 450-850 nm at room temperature" (as shown in Fig. 2.28) **[30].**

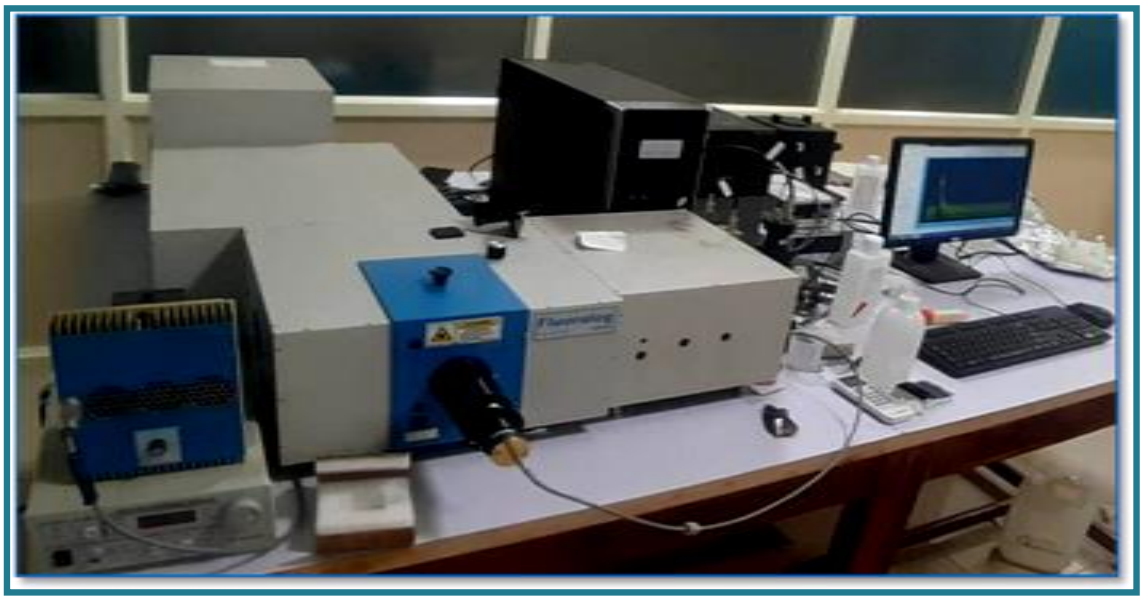

Figure 2.28 *Photograph of spectrofluorimeter for PL mesuerements.*

2.4.2.3 Raman Spectroscopy

Raman spectroscopy first proposed by C. V. Raman in 1928, it is a non-destructive analytical method to identify functional groups present in a variety of samples **[31].** Raman Effect arises due to inelastic scattering of incident light by the atoms/molecules. When atoms/molecules are absorbing the light energy, it is possible to radiate or re-emit the energy through vibration or rotational motion. The energy transition by rotational/vibrational mode depends on the excited energy level. The rotational energy is lesser than the vibrational energy. The atoms/molecules re-emit the same energy as that of incident light energy, indicating no Raman active mode to be present in the system ($\nu_o = \nu$), and this type of transition is called as Rayleigh's elastic scattering. The re-emitted photon energy lower than the incident energy indicate active Raman mode, this mode is generally called as stokes mode ($\nu_o > \nu$). When reemitted photon energy is higher than the incident photon energy, this also indicates the active Raman mode, this mode is called as anti-stokes mode ($\nu_o < \nu$) **[32].** The pictorial representation of Raman modes is shown in Fig. 2.29 (a). The Raman spectroscopic instrument consists of four major components, a laser source, sample illuminator, filter, and detector as shown in Fig. 2.30(b). The

monochromatic laser light source converged with a focal lens is sent via interference filter to obtain the Raman spectrum. Nowadays, Raman spectrometer has more advancement in its instrumentation, in optics, laser, and other features.

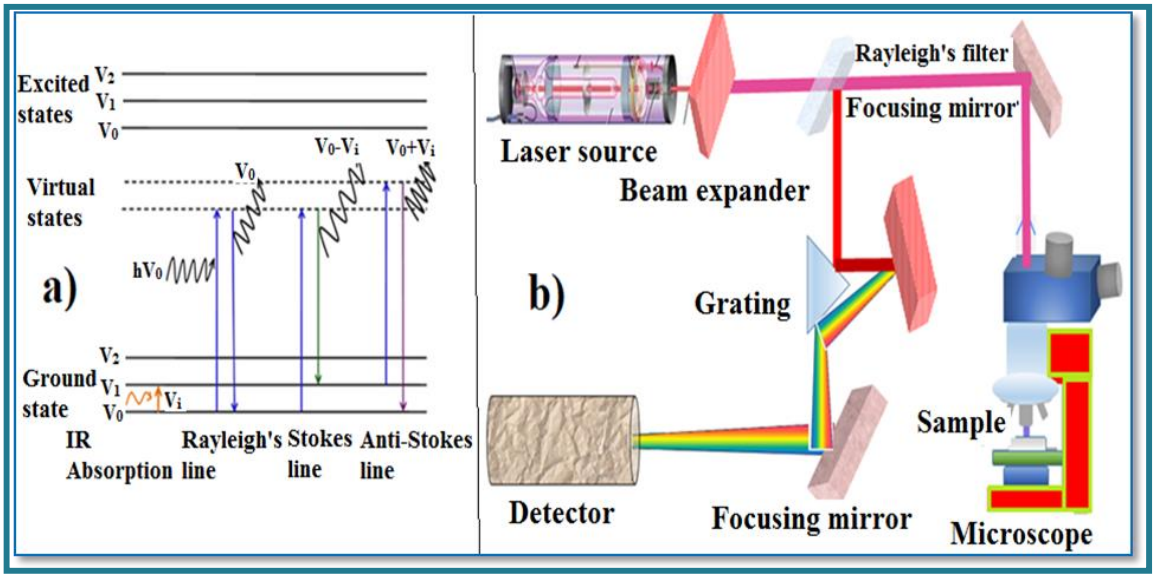

Figure 2.29 *(a) The schematic of Raman scattering effect, and (b). the instrumentation of Raman spectroscopy.*

Raman confocal microscopy is used to investigate the surface homogeneity and uniformity of the sample. In the present research work, Raman analysis was carried out using a Raman spectrometer instrument. Raman spectrometer was used to record Raman spectra with a laser excitation of wavelength 532 nm. Model: WITec alpha300R; Laser options: Integrated internall – 532 nm, high brightness lasers; Spectral range: 100 cm^{-1} to 3500 cm^{-1} minimum; Detector: 1024 x 256 TE air-cooled scientific (shown in Fig. 2.30).

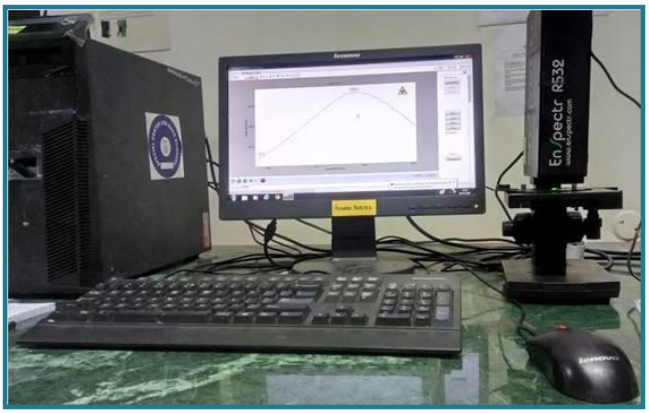

Figure 2.30 *Photograph of confocal Raman spectrometer used for the measurements.*

2.4.2.4 Photoelectron Spectroscopy

Photoelectron spectroscopy employ the kinetic energy distribution of the emitted photoelectrons to study the composition of the sample. Traditionally, surface studies have been subdivided according to the source of exciting radiation into:

(i) X-ray Photoelectron Spectroscopy (XPS) - using soft x-rays (with a photon energy of 200-2000 eV) to examine core-levels.

(ii) Ultraviolet Photoelectron Spectroscopy (UPS) - using vacuum UV radiation (with a photon energy of 10-45 eV) to examine valence levels.

2.4.2.4.1 X-ray photoelectron spectroscopy (XPS)

The XPS is an sophisticated technique to analyze the binding energy and surface oxidation of the elemental constituents of samples **[33].** When the X-ray is focused on the sample, electrons absorb the X-ray energy and escape from the orbital with maximum kinetic energy of $E_k = h\nu - E_B - e\Phi$, where E_B is electron binding energy, ν is the photon frequency, and Φ is work function, which is the minimum energy essential to remove an electron from the surface of the material **[34].** The X-ray radiation is continuously incident on the sample's surface, and the photoelectrons are ejected from the sample surface. The XPS instrument consists of three major parts such as photoelectron production unit, a detector unit and analyzer unit as shown in the Fig. 2.31 (a,b). Model: Theta probe angle-resolved X-ray photoelectron spectrometer (ARXPS) system; Analyzer Type: 180° double focusing hemispherical analyzer with PARXPS detector; X-Ray Source Type: electron spectrometer-Scienta R4000 VG Scienta using a monochromatic, micro-focused Al K-Alpha, X-Ray; Spot Size: 15–400 μm.

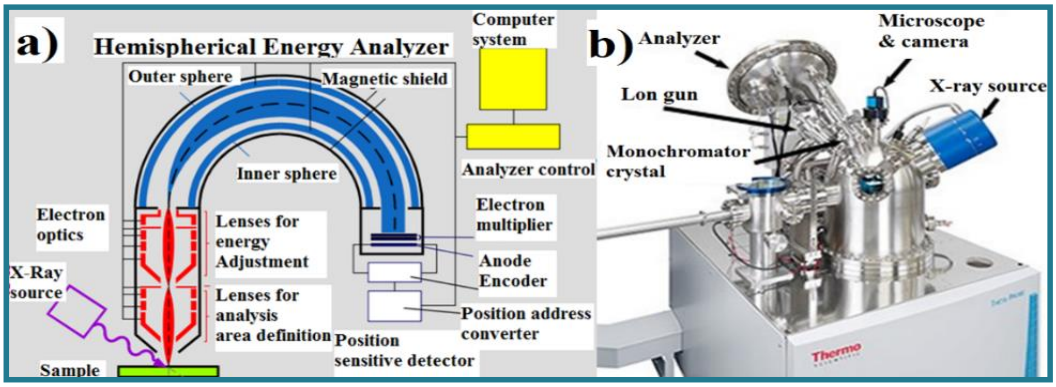

Figure 2.31 *The schematics of (a, b) X-ray photoelectron spectroscopy.*

2.4.2.4.2 Ultraviolet Photoelectron Spectroscopy (UPS)

In UPS, "the photon interacts with valence levels of the molecule or solid, leading to ionization by removal of one of these valence electrons. The kinetic energy distribution of the emitted photoelectrons (i.e. the number of emitted photoelectrons as a function of their kinetic energy) can be measured using any appropriate electron energy analyzer and a photoelectron spectrum can thus be recorded".

2.5 Measurement Techniques

2.5.1 Resistivity and conductivity measurements by Four-point probe technique

The four-probe setup is the commonly used technique to determine the sheet resistance and resistivity of the thin film as at room temperature. In four-probe method, the probes are connected in equal distance, and placed over the surface of the sample. The sheet resistance is estimated by using equation $R_S = F\ (V/I)\ \Omega/\square$, where F = 4.532 is the correction factor, t is the thickness of the sample, V is the voltage drop across any two probes and I is the current applied between the any two probes. The resistivity $(\rho) = R_s \times t$, photograph of home-made four probe unit is shown in Fig. 2.32.

Figure 2.32 *Four probe resistivity measurement setup.*

2.5.2 I-V measurement of Solar Cell Devices in Dark and under Illumination

The J-V characteristics of the solar cell devices were measured /recorded with computer-controlled Keithley 2400 source meter under dark and under illumination. To measure the current density under illumination, the devices were illuminated from the ITO side using shutter controlled Newport Corporation Class AAA solar simulator (as shown in Fig. 2.33) with an air mass 1.5 (AM 1.5) and the light intensity 100 mW/cm². The light intensity was determined by a standard silicon photodiode. Current density can be calculated by dividing the values of current in I-V curve by area of pixel. All measurements were performed at room temperature. After obtaining the values of short circuit current density (J_{sc}) and open circuit voltage (V_{oc}), we can easily calculate the other parameters such as fill factor (FF) and power conversion efficiency (η) of devices.

Figure 2.33 *Solar simulator showing the experimental set-up for J-V characteristics of solar cell devices under illumination with Keithley 2400 source meter.*

2.5.3 External Quantum Efficiency (EQE) Measurements

EQE is defined as " the ratio of the number of collected carriers to the number of all the incident photons on the device active area at a certain wavelength". The J_{SC} can be calculated by integrating EQE over the solar irradiance spectrum. In other words, EQE is defined as "the percentage of photons hitting the device which are converted to electrons and collected by the terminals".

$$\mathbf{EQE(\%)} = \frac{Number\ of\ collected\ electrons}{Number\ of\ incident\ photons}$$

2.5.4 Device Stability Measurements

Although the PCE of solar cells have been increased dramatically, there are still many challenges for this type of solar cell before they can be commercialized. One challenge is the toxic property of the material due to the lead. Another grand challenge is its instability. The water solubility of the organic materials make them instable under atmosphere. Although some capsulations using polymer matrix can prolong the lifetime of the devices, no long-term stability over years have been demonstrated yet.

2.6 Conclusion

This chapter presents the experimental details and characterization techniques used in the present investigations have been mentioned. It includes synthesis of GO and FGO by modified Hummer's method , preparation of Ternary blend active layers [(P3HT (D_1): PTB7-th (D_2): PCBM(A_1), and [PTB7-th (D_1): PCBM (A_1): F-rGO (A_2)], and preparation of PEDOT:PSS, GO, and PEDOT:PSS-GO composite films HTL thin films by spin coating technique. The detailed process for the fabrication of the solar cell devices will be discussed using both the binary and the ternary blends and different PEDOT:PSS/GO/PEDOT:PSS-GO composite films HTLs, in typical planar BHJ device configuration. Further, Equipments require for fabrication process like glove box, thermal evaporation systems and spin coating unit with characterization and PV measurement techniques used in the present work have been discussed in this chapter.

References

1. Han, Joong Tark, Beom Joon Kim, Bo Gyeong Kim, Jun Suk Kim, Bo Hwa Jeong, Seung Yol Jeong, Hee Jin Jeong, Jeong Ho Cho, and Geon-Woong Lee. "Enhanced electrical properties of reduced graphene oxide multilayer films by in-situ insertion of a TiO2 layer." ACS nano 5 (2011) 8884-8891.
2. Yu, Jae Choul, Jeong In Jang, Bo Ram Lee, Geon-Woong Lee, Joong Tark Han, and Myoung Hoon Song. "Highly efficient polymer-based optoelectronic devices using PEDOT: PSS and a GO composite layer as a hole transport layer." ACS applied materials & interfaces 6 (2014) 2067-2073.

3. Park, Yensil, Kyoung Soon Choi, and Soo Young Kim. "Graphene oxide/PEDOT: PSS and reduced graphene oxide/PEDOT: PSS hole extraction layers in organic photovoltaic cells." physica status solidi (a) 209 (2012) 1363-1368.
4. Krishnamoorthy, Karthikeyan, Murugan Veerapandian, Rajneesh Mohan, and Sang-Jae Kim. "Investigation of Raman and photoluminescence studies of reduced graphene oxide sheets." Applied Physics A 106 (2012) 501-506.
5. Aleksandrzak, Malgorzata, Wojciech Kukulka, and Ewa Mijowska. "Graphitic carbon nitride/graphene oxide/reduced graphene oxide nanocomposites for photoluminescence and photocatalysis." Applied Surface Science 398 (2017) 56-62.
6. Marcano, Daniela C., Dmitry V. Kosynkin, Jacob M. Berlin, Alexander Sinitskii, Zhengzong Sun, Alexander Slesarev, Lawrence B. Alemany, Wei Lu, and James M. Tour. "Improved synthesis of graphene oxide." ACS nano 4 (2010) 4806-4814.
7. Mathkar, Akshay, T. N. Narayanan, Lawrence B. Alemany, Paris Cox, Patrick Nguyen, Guanhui Gao, Patricia Chang, Rebeca Romero-Aburto, Sendurai A. Mani, and P. M. Ajayan. "Synthesis of fluorinated graphene oxide and its amphiphobic properties." Particle & Particle Systems Characterization 30 (2013) 266-272.
8. Allen, Matthew J., Vincent C. Tung, and Richard B. Kaner. "Honeycomb carbon: a review of graphene." Chemical reviews 110 (2010) 132-145.
9. Kumar, ET Deva, S. Easwaramoorthi, and J. Raghava Rao. "Fluorinated reduced graphene oxide-encapsulated ZnO hollow sphere composite as an efficient photocatalyst with increased charge-carrier mobility." Langmuir 35 (2019) 8681-8691.
10. Middleman, Stanley, and Arthur K. Hochberg. Process engineering analysis in semiconductor device fabrication. Mcgraw-Hill College, 1993.
11. Bragg, William Henry, and William Lawrence Bragg. "The reflection of X-rays by crystals." Proceedings of the Royal Society of London. Series A, Containing Papers of a Mathematical and Physical Character 88, no. 605 (1913): 428-438.
12. https://images.app.goo.gl/7R5uXQfPL4Pzt4pZ7.Field Emission Scanning Electron Microscope, Jpeg.
13. https://images.app.goo.gl/oiCMHRPGAJk7vJGbA.Field Emission Scanning Electron Microscope, Jpeg.

14. Grundy, Philip James, and Grenville Arthur Jones. Electron microscopy in the study of materials. Vol. 7. Crane Russak, Incorporated, 1976.
15. CARTER, BARRY AUTOR, David Bernard Williams, C. Barry Carter, and David Brian Williams. Transmission Electron Microscopy: A Textbook for Materials Science. Diffraction. II. Vol. 2. Springer Science & Business Media, 1996.
16. http:/www.steve.gb.com/image/science/transmission_electron_mocroscope.png.
17. Binnig, Gerd, Calvin F. Quate, and Ch Gerber. "Atomic force microscope." Physical review letters 56 (1986) 930.
18. Cappella, Brunero, and Giovanni Dietler. "Force-distance curves by atomic force microscopy." Surface science reports 34 (1999) 1-104.
19. Bryant, P. J., R. G. Miller, and R. Yang. "Scanning Tunneling and atomic force microscopy combined." Applied Physics Letters 52 (1988) 2233-2235.
20. Giuliano, Samantha, Ewelina Mistek-Morabito, and Igor K. Lednev. "Forensic Phenotype Profiling Based on the Attenuated Total Reflection Fourier Transform-Infrared Spectroscopy of Blood: Chronological Age of the Donor or Operational manual of Perkin Elmer Spectra-one FTIR Spectrophotometer." ACS omega 5 (2020) 27026-27031.
21. Nafie, L. A., D. W. Vidrine, J. R. Ferraro, and L. J. Basile. "Fourier Transform Infrared Spectroscopy." Fourier Transform Infrared Spectroscopy (1982) 83-123.
22. Cappella, Brunero, and Giovanni Dietler. "Force-distance curves by atomic force microscopy." Surface science reports 34 (1999) 1-104.
23. K. P. Acharya, Ph.D. Thesis, Bowling Green State University, 2009.
24. Rao, B. Srinivasa, B. Rajesh Kumar, V. Rajagopal Reddy, T. Subba Rao, and G. Venkata Chalapathi. "Influence on optical properties of nickel doped cadmium sulfide." Chalcogenide Lett 8 (2011) 39-44.
25. Sadak, Mervat Sh, A. A. A. El-Monem, H. M. S. El-Bassiouny, and Nadia M. Badr. "Physiological response of sunflower (Helianthus annuus L.) to exogenous arginine and putrescine treatments under salinity stress." Journal of Applied Sciences Research October (2012) 4943-4957.
26. Neeraj Chaudhary, Ph.D. Thesis, Delhi Technological University, Bawana Road, Delhi, India, 2017.

27. Albani, Jihad René. Principles and applications of fluorescence spectroscopy. John Wiley & Sons, 2008.
28. Lakowicz, Joseph R., ed. Principles of fluorescence spectroscopy. Springer science & business media, 2013.
29. Kusum Kumari, Ph.D. Thesis, Indian Institute of Technology, Delhi, India, 2011.
30. Gilmore, Adam M. "Water quality measurements with HORIBA Jobin Yvon fluorescence instrumentation Or Operation manual of Fluorolog-3, Horiba Jobin-Yvon, USA " Readout 38 (2011) 90-96.
31. G.F.S., A new radiation, J. Franklin Inst. 206, (1928), 276–277.
32. Hazle, M. A., M. Mehicic, D. J. Gardiner, and P. R. Graves. "Practical Raman Spectroscopy: Springer Verlag, Berlin, 1989 (ISBN 3-540-50254-8). viii+ 157 pp. Price DM 78.00." (1990) 104.
33. Mittal, K. L. "Surface contamination: an overview." Surface contamination (1979) 3-45.
34. Powell, Cedric J., and P. E. Larson. "Quantitative surface analysis by X-ray photoelectron spectroscopy." Applications of Surface Science 1 (1978) 186-201.

CHAPTER 3

HOLE TRANSPORT LAYER: STRUCTURAL, OPTICAL AND ELECTRICAL PROPERTIES OF GO, PEDOT:PSS AND PEDOT:PSS-GO COMPOSITES

3.1 Introduction

In Organic solar cells composed of conjugated polymer donors, poly(3,4-ethylene dioxythiophene):poly(styrenesulfonate) (PEDOT:PSS) is most popularly used as HTL. It also offers high optical transparency in the solar region, high electrical conductivity, and high work function along with easy solution processing in an aqueous medium. However, such Polymer solar cells (PSCs) suffer from several problems such as high hygroscopic, high acidic, poor electrical conductivity [**1-4**], which lead to degradation problems and poor device stability. However, PEDOT:PSS is not an ideal HTL as it exhibits inefficient electron blocking capability, intrinsically hygroscopic and acidic nature which results in instability of the PSC devices. To overcome these shortcomings, recently, 2D carbon materials such as graphene and graphene oxide (GO) have gained much attention as HTL as a cost-effective and easy processing alternative, owing to their attractive optical and electronic properties like excellent optical transparency (>97%), high conductivity, ultrahigh carrier mobilities, large surface to volume ratio, and excellent thermal and chemical stability **[5, 6]**. Their ability to deposit on flexible substrates via a roll-to-roll process using the simple solution and room temperature processing has also been very impressive. Therefore, GO is regarded as a promising candidate and reported to grantee high efficient and high stable PSCs. Generally, despite possessing the favorable high work function well matching with the HOMO of the donor polymers, the high insulating property of GO limits its use as HTL in enhancing the device performances of PSCs. Their application for scalable and reproducible manufacturing of PSCs becomes difficult. Nevertheless, integrating GO with PEDOT:PSS i.e., building the hybrid PEDOT:PSS-GO composite HTL is also a promising strategy with can complement the drawbacks of

single GO and conventional PEDOT:PSS **[7-10]**. Since past few years, both GO and hybrid PEDOT:PSS-GO in the bilayer and composite form has been widely used as HTLS and have shown encouraging results in achieving good interfacial hole extraction properties, high electron blocking, high film optical transparency, surface morphology, and high conductivity, which have significantly improved the PCE and stability of the PSCs devices. However, several groups have reported the use of PEDOT:PSS-GO as HTLs mostly with binary blend BHJ system combinations and reported enhanced PCE as high as 10% **[7]**. This provides a motivational platform to explore the potential use of PEDOT:PSS-GO HTLs for the design and development of ternary blend systems based PSC technology also.

In the present investigations mentioned in this chapter, we present a solution-processed poly(3,4-ethylene dioxythiophene):poly(styrenesulfonate)-graphene oxide (PEDOT:PSS-GO) composite as a novel hole transporting material with excellent hole extraction properties which may boost the performance of ternary blend polymer solar cells (TPSCs). In view of this, firstly we have synthesized GO was prepared by using the modified Hummer's method. Secondly, GO nanosheets are incorporated in PEDOT:PSS in three different weight ratios to form hybrid PEDOT:PSS-GO composite thin films, namely, PEDOT:PSS-GO (2:1), PEDOT:PSS-GO (1:1) and PEDOT:PSS-GO (1:3). These have been investigated systematically for improved hole transport properties in order to improve the performances of TPSCs. To achieve this, the effect of GO on structural and optoelectronic properties of PEDOT:PSS has also been studied in detail via in-depth investigations.

These investigations have resulted in some important findings that the hole transport properties PEDOT:PSS-GO composites get enhanced due to incorporation of GO nanosheets. It is attributed to the fact that the dispersion of GO nanosheets in PEDOT:PSS HTL, (i) improves the film morphology, (ii) tunes the work function making it perfectly matched with the highest occupied molecular orbital (HOMO) of the donor polymer, and (iii) enhances the conductivity of HTL films. These results showed that the PEDOT:PSS-GO composite offers the most desirable hole transport properties over the conventional PEDOT:PSS-only HTLs for accelerating performance of TPSCs. All these studies are discussed in detail in this chapter.

3.2 Results and Discussion

3.2.1 GO: Structural and Optical Properties

GO nanoflakes were synthesized using the modified Hummer's method, as described in Chapter 2, Section 2.2.2. Further these GO nanoflakes were characterized for analyzing their structural and optical properties using various characterization techniques such as XRD, FESEM, HRTEM, XPS, FTIR, UV-Vis absorption, Raman spectroscopy studies etc.

Figure 3.1 (a) and (b) shows the FESEM image of synthesized GO nanosheets deposited on ITO/glass substrate, revealed that the size of GO nanosheets is in the range 5-10 µm. The HRTEM image [Fig. 2 (c)] of GO indicated the corresponding crystalline planes of GO nanosheets. The SAED pattern of GO nanosheets presented in Fig. 3.1 (d)], further confirms the corresponding crystalline planes of GO. The height profile of the white line scan indicated on a single GO nanosheet in the AFM image of the GO sample, as shown in [Fig. 2 (e)], revealed that the thickness of a single nanosheet is approx. 1.1 nm, which is consistent with the thickness of single GO nanosheets shown in previous reports **[8, 11]**.

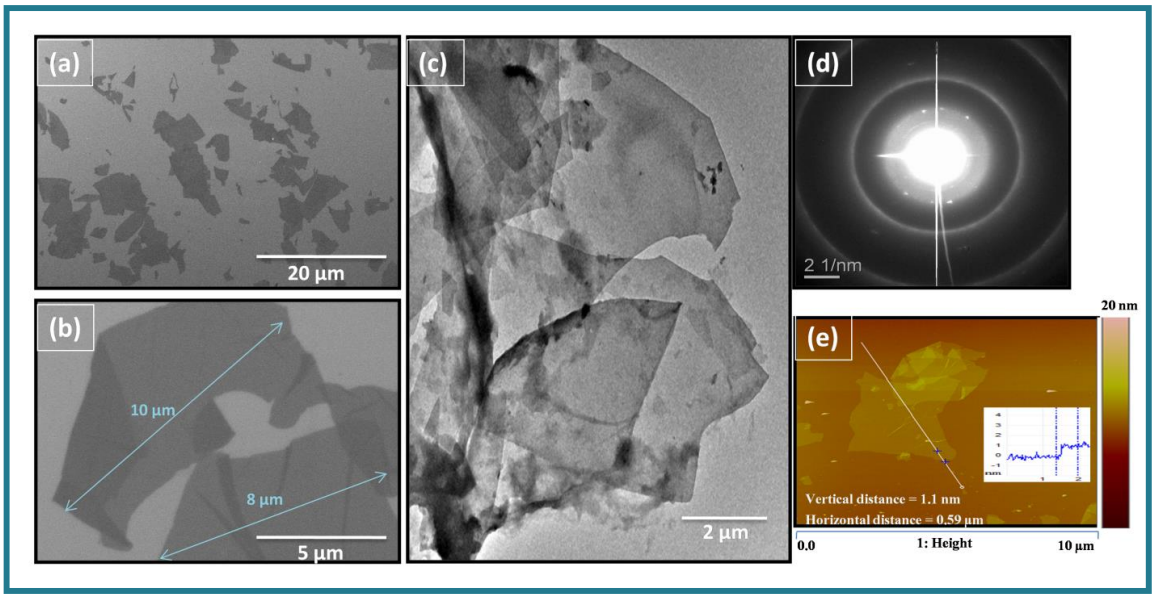

Figure 3.1. *(a) and (b) FESEM of GO Nanosheets on ITO substrate. (c) TEM of GO Nanosheets. (d) SAED pattern of GO nanosheets indicating the spots corresponding to the crystalline planes. (e) AFM image of GO on the ITO substrate. The white line scan in*

the marked region shows the height of a single GO nanosheet is ~ 1.1 nm within the marked portion.

Figure 3.2 (a) shows the XRD pattern of GO. GO sample shows a single peak at 11.3° corresponding to (001) lattice plane, which is the characteristic peak as reported elsewhere **[8, 12].**

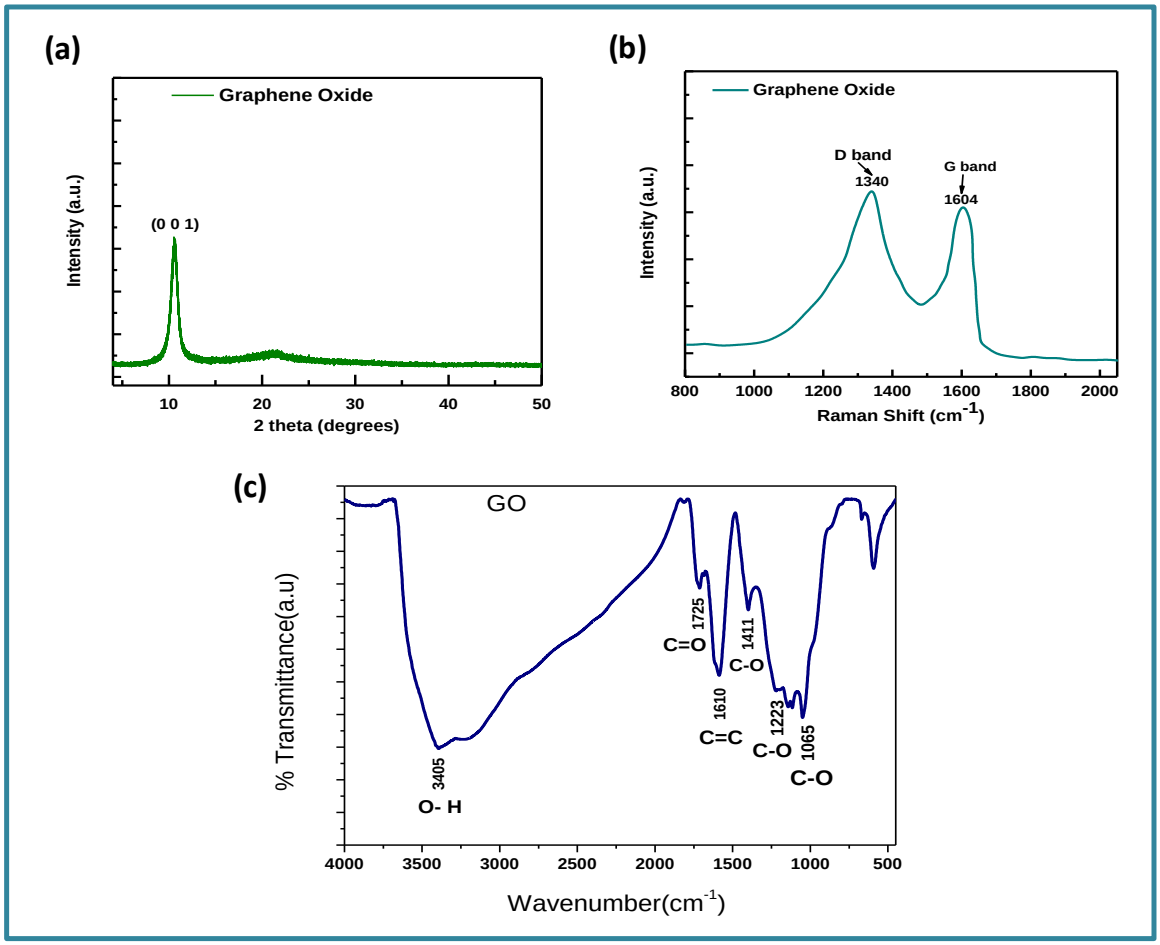

Figure 3.2 *(a) XRD spectra, (b) Raman Spectra of GO and (c) FTIR of GO.*

Raman spectra of GO, as shown in Fig. 3.2 (b), display two dominant peaks at 1340 and 1605 cm^{-1}, associated with the D and G bands, respectively **[12].** The G band is attributed to C_{Sp2}-C_{Sp2} stretching mode in the basal plane of GO sheet, and the D band which corresponds to the degree of functionalization and becomes active in the presence of defects in graphene structure. Higher the intensity of D band more will be the existence of structural defects. This means that the I_D/I_G ratio can be used to measure the degree of the presence of defects in the graphene structure **[11].** The origin of defects could be due to the breaking of a single bond, double bond, or both in the basal plane of

graphene structure. Also, the attachment of oxygen-containing functional groups like hydroxyl, carbonyl, carboxyl and carboxylate groups, etc. to graphene are considered as defects **[11].** Here the I_D/I_G ratio is 1.06 which is consistent with the other reported work **[11].** Further, the FTIR of GO is shown in Fig. 3.2 (c), showing the characteristic peaks associated with all the chemical bonds present in GO nanosheets.

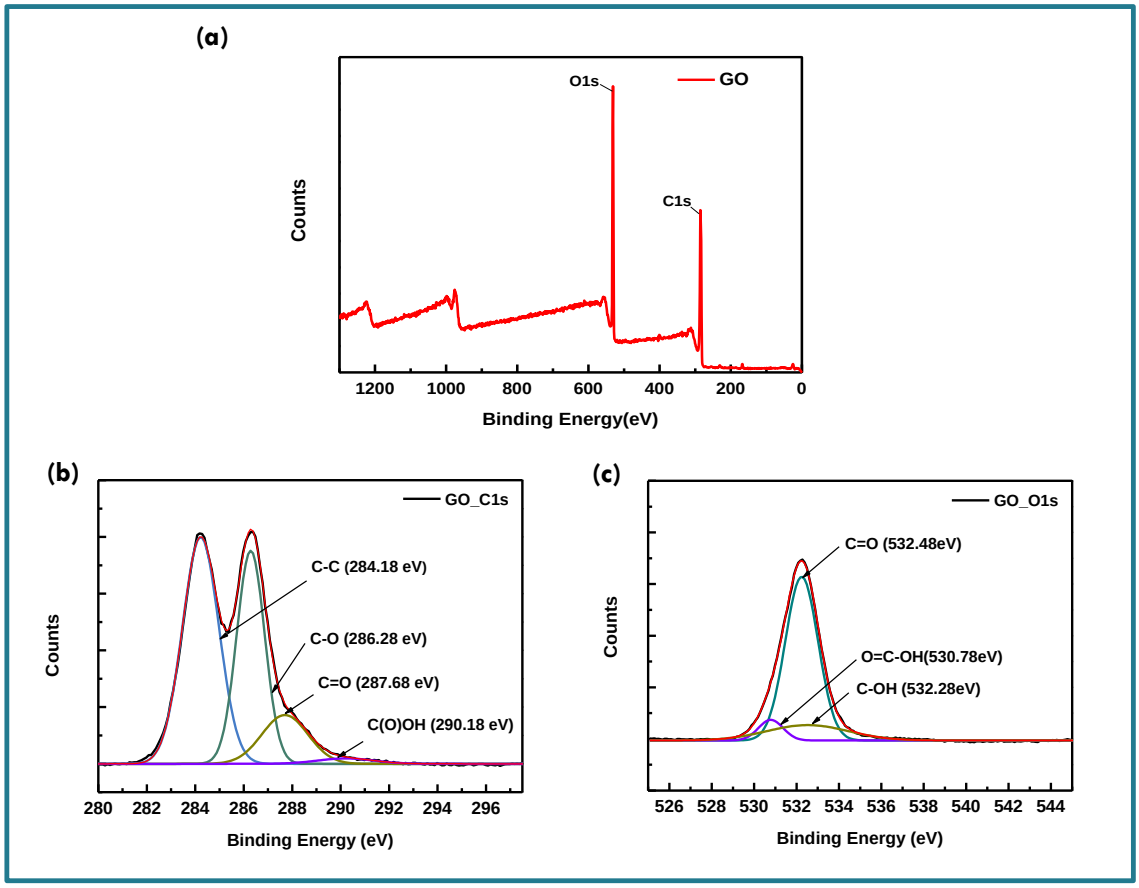

Figure 3.3 *(a) XPS spectra of GO. High resolution deconvoluted XPS spectra (experimental and fitting) of C 1s [(b)] and O 1s [(c)].*

The chemical composition of the GO sample was investigated by XPS. From the XPS spectra of GO on the ITO substrate, as shown in Fig. 3.3 (a), the peaks at binding energy values of 284.60 eV and 532.57 eV are assigned to C 1s and O 1s, respectively. High-resolution XPS deconvoluted spectra corresponding to C 1s and O 1s is shown in Fig. 3.3 (b) and (c), respectively, wherein curve fitting was done using Gaussian and Lorentzian lineshapes. From C 1s spectra, the peaks at 284.18 eV is associated with C-C

(sp^2 bond), and other peaks arising due to oxidation groups such as C-O (286.28 eV), C=O (287.68 eV), and C=O-OH (290.18 eV), match with well-known Lerf–Klinowski model of graphene oxide **[12, 13]**. The deconvoluted spectra of O 1s, show a peak at 532.48 eV, 530.78 eV, and 532.28 eV, attributed to C=O, O=C-OH, and C-OH groups, respectively. Hence, XPS confirmed that the chemical structure of GO consists of chemical functional groups such as carboxyl, hydroxyl, and epoxy groups along with main C–C (sp^2 and sp^3).

3.2.2 FGO: Structural and Optical Properties

FGO nanoflakes were synthesized by modified Hummer's method, as described in Chapter 2, Section 2.2.2, which were further reduced by chemical method to form reduced FGO (F-rGO). The FESEM and AFM confirms the formation of F-rGO nanosheets of size ~ 8-10 nm (Fig. 3.4(a) and (b)). The height profile focused on a single sheet reveal that the nanosheets processing 2 or 3 monolayers.

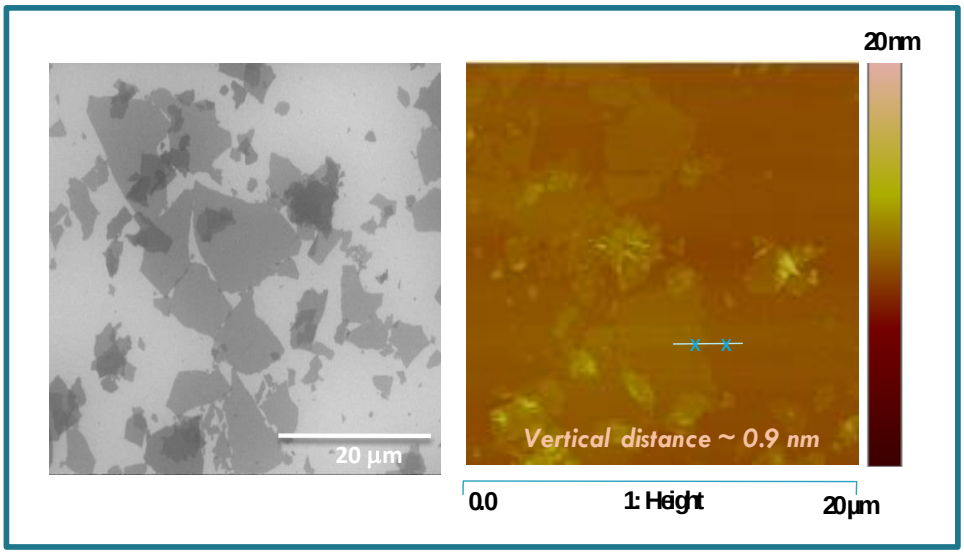

Figure 3.4. *FESEM and AFM images of F-rGO Nanosheets.*

Figure 3.5(a) shows the XRD patterns of FGO and F-rGO, respectively. FGO sample shows a single peak at 11.3° corresponding to (001) lattice plane, which is the characteristic peak as reported elsewhere **[8, 12].** On reduction, the main peak occurs shift to 24.5° indicating that the interplanar space reduces compared to FGO, which confirms the structure is more close to the graphitic phase. Raman spectra of FGO and F-

rGO, respectively, is presented in Fig. 3.5 (b). Both display two dominant peaks at 1340 and 1605 cm^{-1}, associated with the D and G bands, respectively **[12].** The FTIR of FGO is shown in Fig. 3.5(c) which represent the characteristic peaks associated with all the chemical bonds present in FGO nanosheets, the presence of C-F bonds are evident.

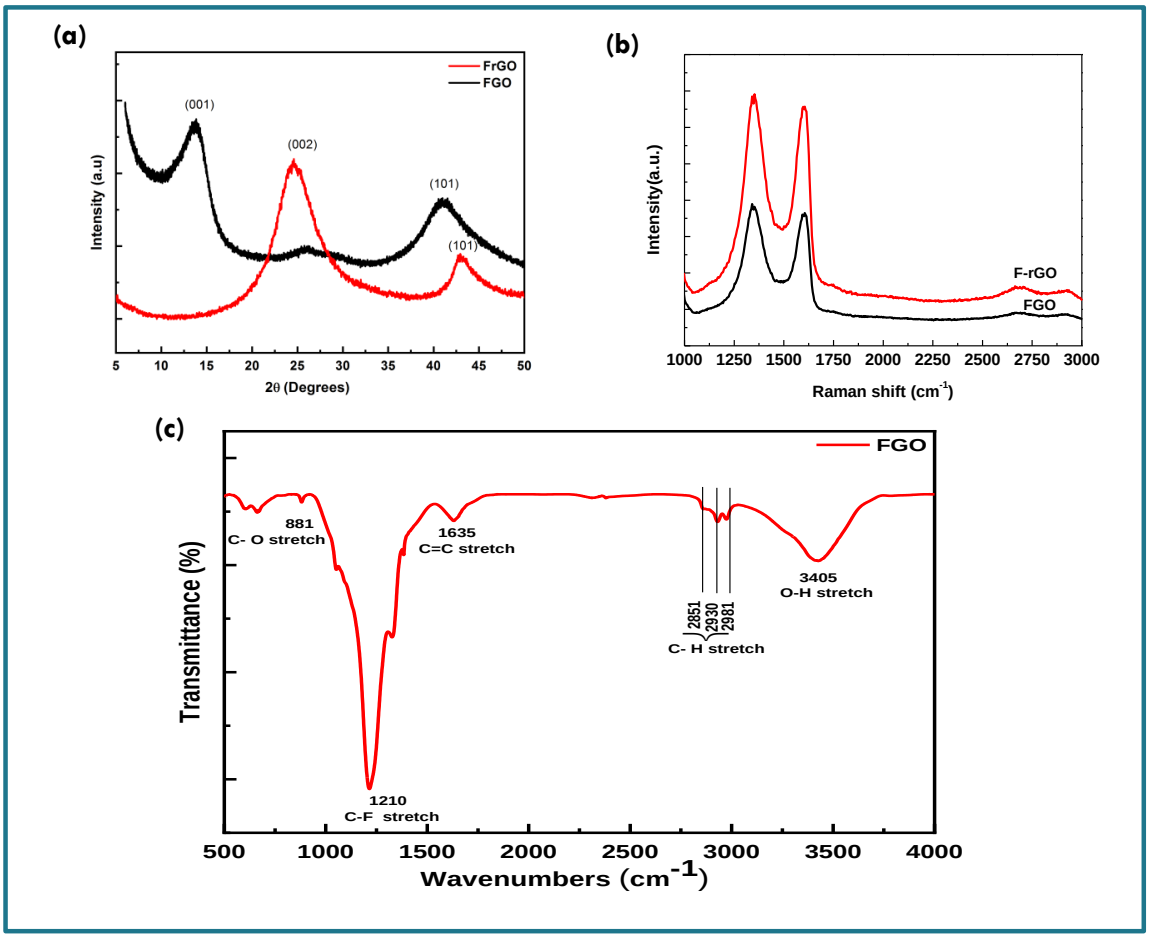

Figure 3.5 *(a) XRD spectra of FGO and F-rGO, (b) Raman Spectra of FGO and F-rGO and (c) FTIR of GO.*

3.2.3 PEDOT:PSS-GO Composites: Structural, Optical and Electrical Properties

Further, to understand the influence of GO on the sheet resistance and the conductivity of PEDOT:PSS, we also studied the surface morphology of these PEDOT:PSS-GO composite thin films (different weight ratios i.e., (2:1), (1:1), and (1:2)) by SEM and AFM. The phase integration and inter-molecular bonding analysis by done

by XRD and Raman spectrum, and compared with that of pure PEDOT:PSS and pristine GO.

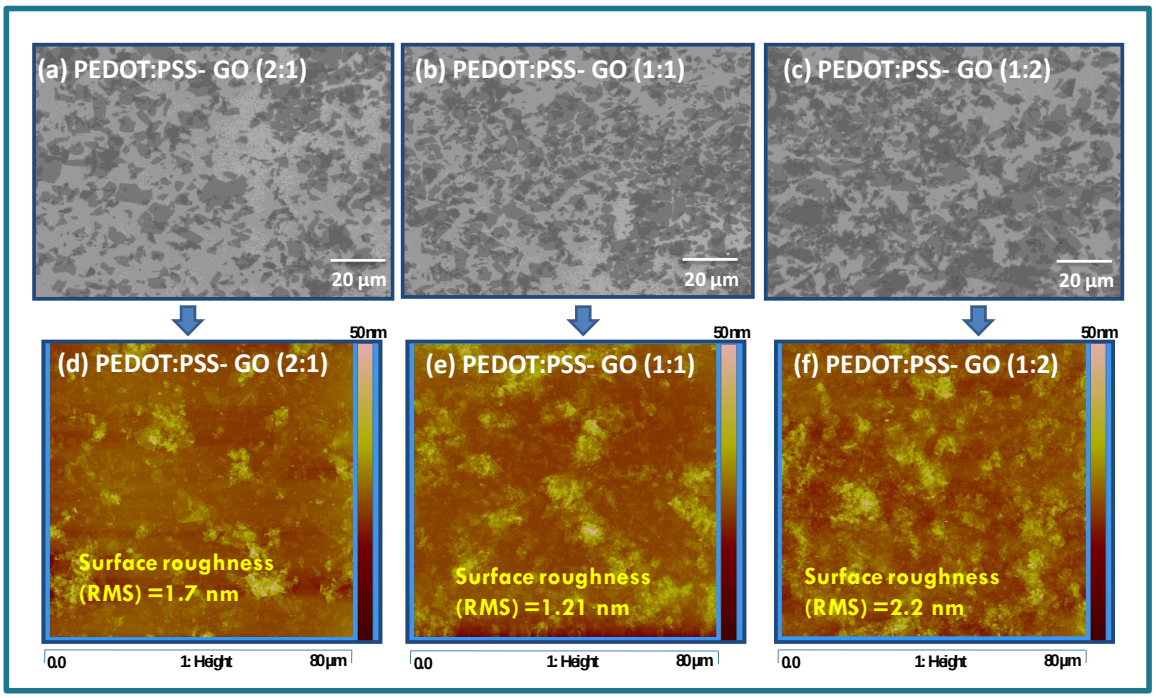

Figure 3.6. *(a-c) FESEM images of PEDOT:PSS-GO (2:1), PEDOT:PSS-GO (1:1), and PEDOT:PSS-GO (1:2) composite film on ITO substrate, respectively. (d-f) AFM images of PEDOT:PSS-GO (2:1), PEDOT:PSS-GO (1:1) and PEDOT:PSS-GO (1:2) composite films deposited over ITO substrates, respectively.*

Figure 3.6 (a-c) depicts the FESEM images of PEDOT:PSS-GO HTL composite films in (2:1), (1:1), and (1:2) weight ratios, respectively. Fig. 3.6 (d-f) represents the respective AFM images of the PEDOT:PSS-GO HTL composite films. These images illustrate that the dispersion of GO of varied sizes (in the range 5-15µm) in PEDOT:PSS forms a homogeneous and smoother film. It is confirmed by the low surface root-mean-square (RMS) roughness values as 1.7 nm, 1.21 nm, and 2.1nm obtained for PEDOT:PSS-GO (2:1) , (1:1), and (1:2) films, respectively. The surface RMS roughness of 1.7 nm of PEDOT:PSS-GO (2:1) films is evident from the fact that GO sheets in PEDOT:PSS-GO (2:1) are evenly distributed in the matrix without agglomeration. Whereas, with little higher GO concentration in PEDOT:PSS-GO (1:1) matrix, surface RMS roughness reduces to 1.21 nm due to the formation of agglomeration-free well-connected GO domains owing to effective steric-stabilization. However, when the

concentration of GO is further increased in PEDOT:PSS-GO (1:2), the surface RMS roughness is increased to value 2.1 nm as there will be a high degree of agglomeration due to dominating van der Waals' interaction amongst the GO sheets. It is concluded that the low RMS roughness (1.21 nm) is precisely the reason for achieving the lowest sheet resistance, better electrical conductivity in the case of PEDOT:PSS-GO (1:1) composite film.

Furthermore, the structure of PEDOT:PSS and PEDOT:PSS-GO films were analyzed based on their degree of crystallanity and phase integration, as determined from XRD measurements. Figure 3.7(a) shows the XRD patterns of GO, PEDOT:PSS and PEDOT:PSS:GO composite films; GO sample shows a peak at 11.3^{o} corresponding to (001) lattice plane, which is the characteristic peak of GO as reported elsewhere **[14].** The PEDOT:PSS film exhibit two characteristic peaks at 17.5^{o} and 25.9^{o} corresponding to the amorphous character of PSS and π–π stacking (020) of the PEDOT thiophene ring, respectively [15, 16]. On the other hand, in XRD spectra of PEDOT:PSS-GO samples, the appearance of small peak at 11.2^{o} corresponds to presence of GO sheets and the other peak at 25.9^{o} is due to PEDOT chain structures. In addition, it is observed that the PSS signature peak at 17.5^{o} gets boarder and lowers in intensity. This signify that there is partial removal of PSS segments from the PEDOT chains when the GO nanosheets are added in PEDOT:PSS, rendering PEDOT as positively charged. Subsequently, the strong molecular in-plane interaction of GO sheets with PEDOT will be developed due to the functional groups induced δ^{+}- δ^{-} dipolar interactions, leading to GO nanosheets physically bonded with the PEDOT molecular chains structures [15]. The increase in the GO peak intensity suggests an increase in over-all crystallanity of the film because of the formation of the highly crystalline GO-bonded PEDOT structures(as also confirmed by previously discussed FESEM and AFM images of these PEDOT:PSS-GO films, as shown in Fig. 5 (a-c) and (d-f)). Almost same is the situation in PEDOT:PSS-GO (1:2) i.e. when the GO concentration is further increased in PEDOT:PSS matrix, with a small difference seen in terms of lowered intensity of peak at 11.2^{o} most likely due to agglomeration of large number, GO nanosheets in PEDOT:PSS matrix disturbing the crystallanity (evident from relatively higher RMS roughness achieved in the PEDOT:PSS-GO composite film).

However, overall it can be understood that the crystallanity of PEDOT:PSS gets improved after incorporation of GO nanosheets.

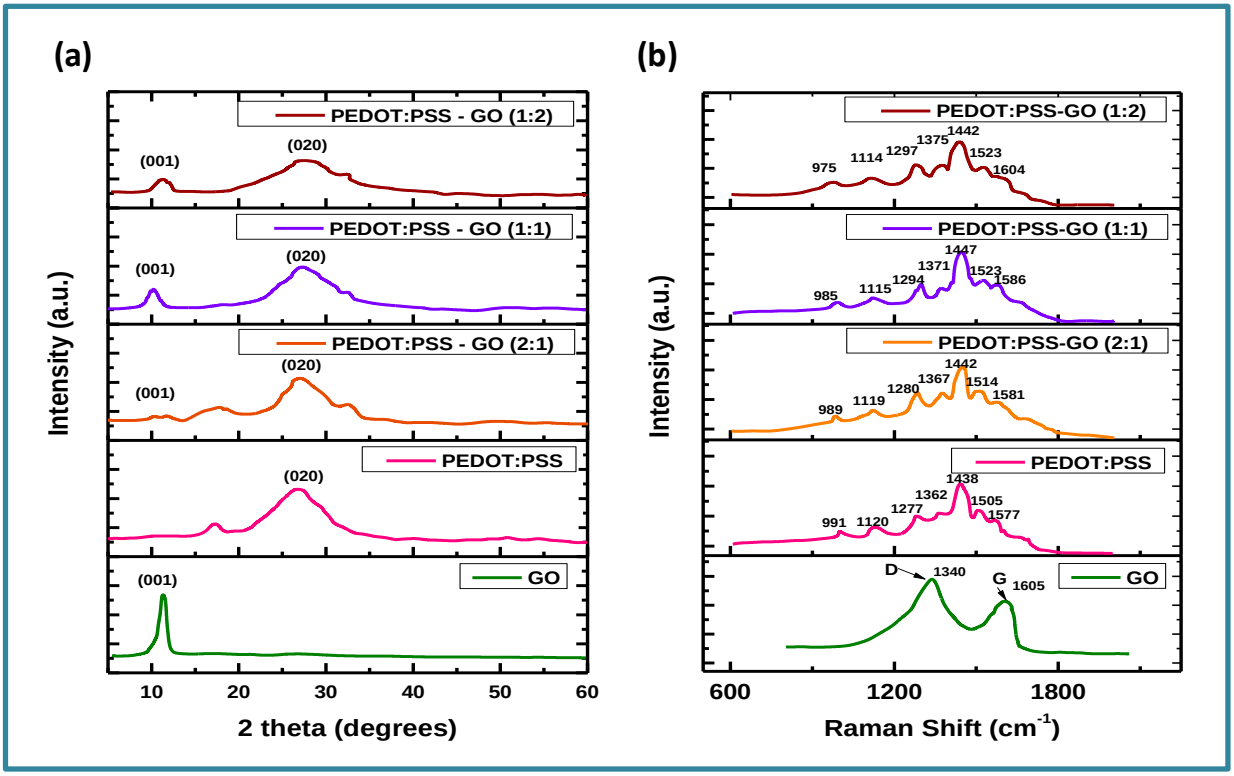

Figure 3.7 *(a) XRD patterns of GO, PEDOT:PSS and PEDOT:PSS:GO composite films, (b) Raman spectra of GO, PEDOT:PSS, PEDOT:PSS:GO composite films.*

The XRD results are correlated with the Raman spectra illustrated in Fig. 3.7 (b). Raman spectroscopy was employed to study the changes that occur at the molecular level during the interaction between PEDOT:PSS and GO. The intermolecular interactions are examined by monitoring the shift in Raman peaks of pristine GO, PEDOT:PSS and PEDOT:PSS-GO composite (2:1, 1:1, and 1:2 weight ratio compositions) films. In Fig. 3.7 (b), GO display two dominant peaks at 1340 cm^{-1} and 1605 cm^{-1}, associated with the D and G bands, respectively [17-19]. The G band is attributed to C_{Sp2}-C_{Sp2} stretching mode in the basal plane of GO sheet, and the D band which corresponds to the degree of structural defects in graphene structure arising due to functional groups. The I_D/I_G ratio measures the degree of the presence of defects in the graphene structure. The origin of defects could be due to breaking of a single bond, double bond, or both in the basal plane of graphene structure. Also, the attachment of oxygen-containing functional groups like

hydroxyl, carbonyl, carboxyl and carboxylate groups, etc. to graphene are considered as defects **[11].** Here the I_D/I_G ratio is 1.23 which is consistent with the other reported work **[11].** In the case of pure PEDOT:PSS film, the Raman active vibrational modes corresponding to both PEDOT and PSS molecular structures are observed. There is a prominent band at 1438 cm^{-1} is assigned to $C_\alpha=C_\beta$ symmetric stretching mode of thiophene rings while other bands observed at 1505 cm^{-1}, 1332 cm^{-1} and 1277 cm^{-1}, are ascribed to $C_\alpha=C_\beta$ asymmetric stretching mode, $C_\beta–C_\beta$ stretching deformations, and $C_\alpha–C_{\alpha'}$ inter-ring stretching vibrations in PEDOT structure, respectively **[7]**. The vibrational modes of PSS structures are located at 1577 cm^{-1}, 1120 $cm^{-1,}$ and 991 cm^{-1}. In the PEDOT:PSS-GO composite spectra, Raman shift of above mentioned prominent bands of PEDOT:PSS and relative change in their intensities have been observed with an increasing concentration ratio of GO in PEDOT:PSS. It suggests that strong molecular interaction occurs between GO nanosheets and PEDOT:PSS. Raman shift of $C_\alpha=C_\beta$ symmetric stretching mode from 1438 cm^{-1} to (1442 cm^{-1} - 1447 cm^{-1}) on the dispersion of GO in PEDOT:PSS, is a consequence of conformation change of benzoid structure (coil conformation) to a quinoid structure (linear conformation) which are the two resonating structures of PEDOT **[9**]. It implies that the GO induces conformational changes in PEDOT structure because of the strong π-π stacking interactions between GO basal plane and aromatic structure of PEDOT chain **[9**], is also due to the coulombic repulsions among themselves [**8**]. A few reports demonstrated that the benzoid-quinoid transition of PEDOT structure after mixing the GO and PEDOT:PSS solution was observed because both the highly oxidized functional groups and the sp^2 conjugation of GO bring about hydrogen bonding and π-π stacking in the previous study [**9**]. Also, the PSS associated Raman band at 1577 cm^{-1} shifts to higher wave number i.e., 1581 cm^{-1}, 1586 cm^{-1}, and 1604 cm^{-1} in case of PEDOT:PSS-GO (2:1), (1:1), and (1:2) weight ratios, respectively, with much increase in intensities, conclude the partial removal of PSS bonds and development of strong molecular in-plane interaction of GO sheets with PEDOT. On the other hand, the partial removal of PSS segments is also observed by the red-shift of the Raman fingerprints bands at 991 cm^{-1} and 1120 cm^{-1} in PEDOT:PSS to 989 cm^{-1} and 1119 cm^{-1} in PEDOT:PSS-GO (2:1), to 985 cm^{-1} and 1115 cm^{-1} in PEDOT:PSS-GO (1:1), and to 975 cm^{-1} and 1119 cm^{-1} in PEDOT:PSS-GO (1:2). Xinkai

Wu *et.al* have reported that the functional groups present in GO nanosheet can effectively separate PSS and PEDOT chains **[8]**. Therefore, the negatively charged PSS chains get dissolve in water, while positively charged insoluble PEDOT chains will bond with GO nanosheets via coulombic attraction as GO sheet are negatively charged due to the carboxyl groups present. Additionally, C_β–C_β stretching deformations (at 1277 cm^{-1}), and C_α–$C_{\alpha'}$ inter-ring stretching vibrations (at 1362 cm^{-1}) of PEDOT structure undergoes a large Raman shift towards higher wave number and increase in intensity bands, is precisely attributed to the structural defect induced vibrational changes in the PEDOT chain. The same is observed in other previously reported studies [**20**]. We can conclude from these results that the bonding of GO nanosheets and PEDOT chain can effectively help to form more conductive pathways. Hence, the carrier transport in the connected PEDOT-GO network becomes almost free. Hence, the conductivity of PEDOT:PSS-GO composite films is increased compared to pure PEDOT:PSS and pristine GO.

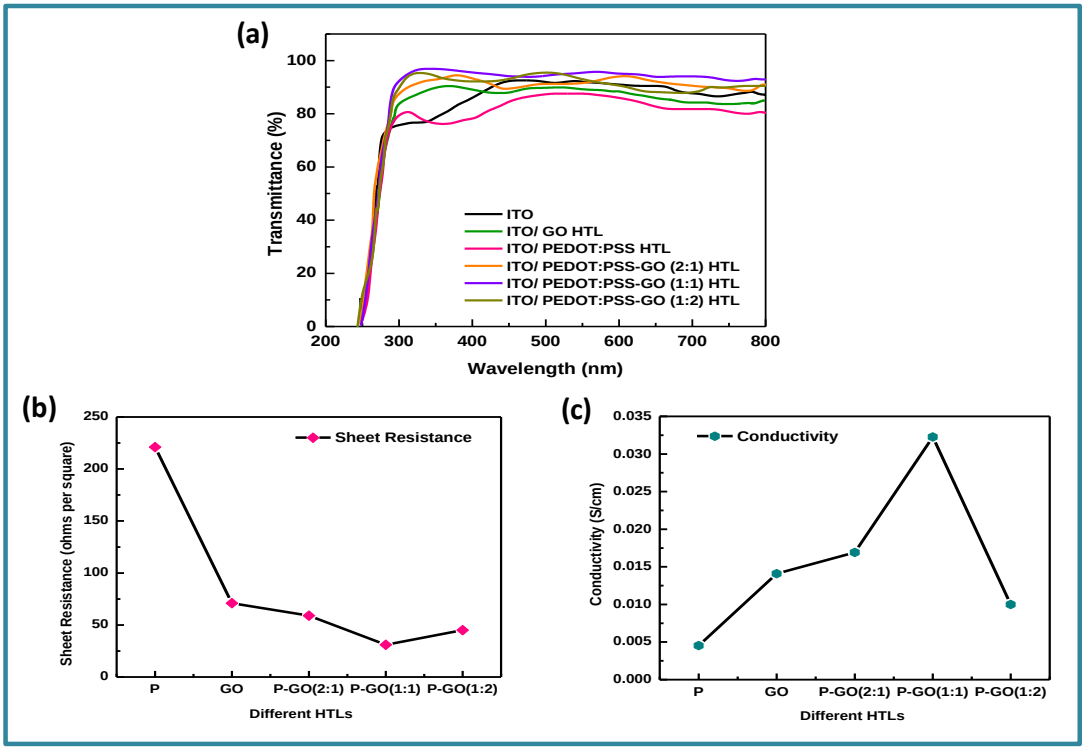

Figure 3.8. *(a) Transmittance spectra of GO, PEDOT:PSS, PEDOT:PSS-GO composite films (different weight ratios); (b) Sheet Resistance (film thickness ~ 40 nm) and (c) Conductivity of pure PEDOT:PSS, GO, and PEDOT:PSS-GO composite films (different weight ratios).*

The transmittance of the anode material and HTLs play a fundamental role in the behavior of TPSC devices because the light is incident from the anode side **[21].** To confirm the transparency of different HTL films, the transmittance spectra of GO, PEDOT:PSS, and PEDOT:PSS-GO HTLs (all with film thicknesses of ~40 nm) were measured, as shown in Fig. 3.8(a). Here, we found that the transmittance of the PEDOT:PSS- GO composite films in all the three different ratios i.e., (2:1), (1:1), and (1:2), is ~90-92% in the wavelength below 550 nm, which is notably higher compared to the 84% transmittance observed in pure PEDOT:PSS and 89% transmittance seen in pristine GO film **[21].** The increase in transmittance on dispersion of GO in PEDOT:PSS is attributed to the synergistic effect of both PEDOT:PSS and GO components present in the composite HTL films. It is confirmed that all of the PEDOT:PSS- GO HTLs are highly transparent in the overall wavelength range with transmittance values up to 90-92% and do not significantly alter the transparency of ITO. Hence, all the three PEDOT:PSS-GO composites prove to be highly beneficial HTLs for achieving efficient TPSC devices. Among all PEDOT:PSS-GO composite films, the one with (1:1) weight ratio is found to be the most suitable composition as it presents the maximum transmittance up to 92% at 550nm. The sheet resistance (R_{sheet}) and electrical conductivity (σ) of pure PEDOT:PSS, pristine GO, and PEDOT:PSS-GO composite films as a function of GO concentration in PEDOT:PSS, determined by four-point probe technique, is plotted in Fig. 4 (b) and (c). Here, GO films show a lower sheet resistance (71 Ω/□) with high conductivity of 14 $x10^{-3}$ S/cm compared to pure PEDOT:PSS films (R_{sheet} = 221 Ω/□, σ = $4x10^{-3}$ S/cm), owing to availability of large number of C-C sp^2 hybridized sigma bonds in the basal plane of GO nanosheets which imparts more conductivity. From the measurements shown in Fig. 4(b) and (c) for all the different PEDOT:PSS-GO composites in increasing weight ratio of GO, it has been found that the dispersion of GO is in PEDOT:PSS not only lowers the sheet resistance but also increases the conductivity significantly because of the available conducting paths provided by GO nanosheets. It is seen that the sheet resistance falls with increasing concentration from 59 Ω/□ obtained for PEDOT:PSS-GO (2:1) to 31 Ω/□ for PEDOT:PSS-GO (1:1) film; and then increase slightly to 45 Ω/□ on a further increase of GO in PEDOT:PSS-GO (1:2) film. Henceforth, the conductivity raises from 16.9 $x10^{-3}$ S/cm for PEDOT:PSS-GO

(2:1) to 32.2 x10^{-3} S/cm for PEDOT:PSS-GO (1:1) film, and which subsequently reduces to 26 x10^{-3} S/cm in PEDOT:PSS-GO (1:2) film i.e., on a further increase of GO concentration in PEDOT:PSS. Finally, it is concluded that the PEDOT:PSS-GO with (1:1) weight ratio shows the lowest sheet resistance and enhanced electrical conductivity.

Finally, it is presented that the all different PEDOT:PSS-GO composites with (2:1), (1:1), and (1:2) ratio show enhanced electrical and optical properties with improved morphologies, and therefore, more ideally suited for effective HTLs in solar cell devices.

Further, we investigated the bandgap (E_g), work function (φ), Highest occupies energy level (E_{HOMO}) and Lowest unoccupied energy level (E_{LUMO}) of these PEDOT:PSS/GO/PEDOT:PSS-GO HTLs, and analyzed to construct the energy level alignment diagram when these HTLs are being used along with the active layer of [P3HT:PTB7-th:PCBM] ternary blend in TPSCs, and comprehend the modulation of hole extraction capability at HTL/active layer interfaces due to the addition of GO in PEDOT:PSS.

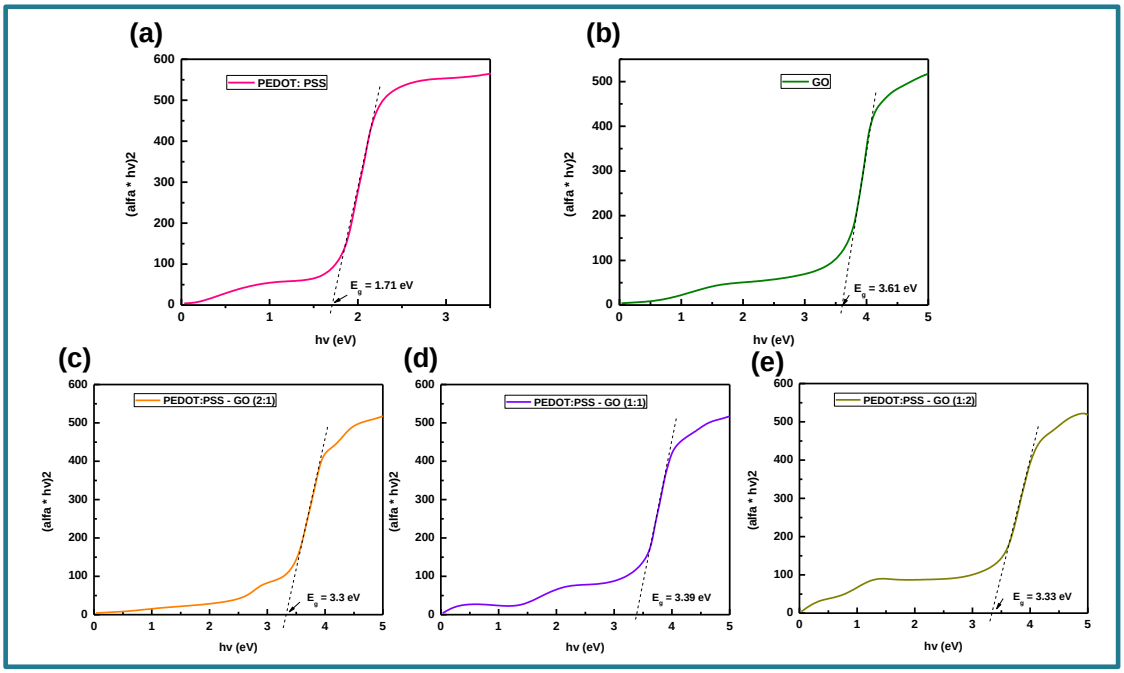

Figure 3.9 *Tauc Plots to estimate the bandgap of GO, PEDOT:PSS, PEDOT:PSS-GO composite films with increasing proportion of GO.*

The band gap can be obtained from the Tauc plots [**22**] from the transmission curves [Fig. 3.8(a)], shown in Fig. 3.9 (a-e), using the relation, $\alpha h\nu = (h\nu - E_g)^{1/2}$ where α is the absorption coefficient and $h\nu$ is the photon energy. The values of E_g obtained are, 3.61 eV for GO, 1.71eV for PEDOT:PSS, 3.3 eV for PEDOT:PSS-GO (2:1), 3.39 eV for PEDOT:PSS-GO (1:1), and 3.33 eV for PEDOT:PSS-GO (2:1) films.

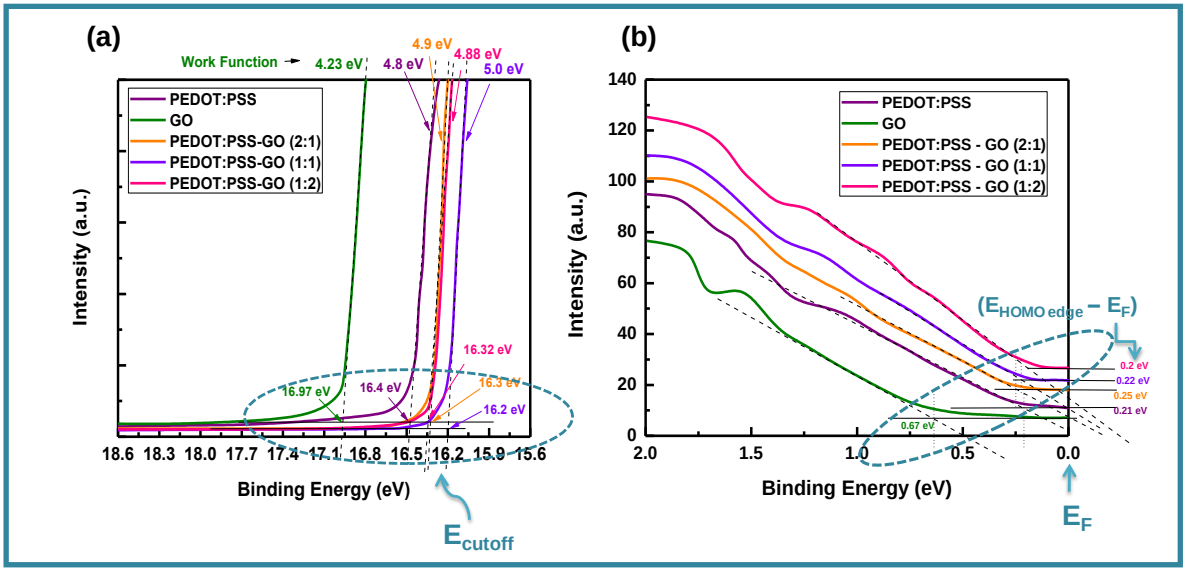

Figure 3.10. *The UPS measurements of GO, PEDOT:PSS and PEDOT:GO composite films (weight ratio of (2:1), (1:1), and (1:2); (a) secondary electron cutoff regions and (b) Fermi edge (valence band edge) regions, respectively, Source (hv = 21.2 eV).*

The UPS measurements were performed to measure ϕ of GO, PEDOT:PSS and PEDOT:GO composite films [weight ratio of (2:1), (1:1), and (1:2)] films, respectively, presented in Fig.3.10, wherein (a) shows the binding energies at secondary electron cutoff regions and (b) represents the Fermi edge (valence band edge) regions. E_{HOMO} and ϕ for all five different HTL samples is calculated from the respective UPS spectra using the formulas, $\phi = h\nu - (E_{cutoff} - E_F)$, and $E_{HOMO} = \phi + (E_{HOMO\ edge} - E_F)$, where, $h\nu$ is excitation energy 21.2 eV, $E_{cutoff} - E_F$ is the binding energy at the secondary electron cutoff, ϕ is the work function, $(E_{HOMO\ edge} - E_F)$ is the binding energy of the HOMO edge relative to the Fermi level obtained by a linear extrapolation of the leading edge of the density of valence band states to zero **[9, 23, 24]**. The values are determined to be ϕ =4.23 eV (E_{HOMO} = 4.9 eV) for pure GO and, ϕ =4.8 eV (E_{HOMO} = 5.01 eV) for pure

PEDOT:PSS; ϕ=4.9 eV (E_{HOMO} = 5.15eV), ϕ =5.0 eV (E_{HOMO} = 5.22 eV), and ϕ = 4.88 eV (E_{HOMO} = 5.10 eV) for PEDOT:PSS-GO composites (2:1), (1:1), and (1:2), respectively, as summarized in Table 1. Based on these values for ϕ and E_{HOMO} of the respective HTLs, the energy band diagram of TPSCs employing different PEDOT:PSS/ GO/ PEDOT:PSS-GO HTLs has been constructed and presented in Fig. 3.11.

Table 3.1: E_{cutoff}, ϕ, E_{HOMO}, E_{LUMO}, and E_g of different HTLs determined from UPS spectra analysis.

HTL films	E_{cutoff} (eV)	$E_{HOMO\ edge} - E_F$ (eV)	ϕ (eV)	$E_{H\ OMO}$ (eV)	E_{LUMO} (eV)	E_g (eV)
PEDOT:PSS	16.4	0.21	4.8	5.01	3.3	1.71
GO	16.97	0.67	4.23	4.9	1.3	3.61
PEDOT:PSS-GO (2:1)	16.3	0.25	4.9	5.15	1.85	3.3
PEDOT:PSS-GO (1:1)	16.2	0.22	5.0	5.22	1.83	3.39
PEDOT:PSS-GO (1:2)	16.32	0.2	4.88	5.1	1.77	3.33

Interestingly, the work function on incorporation GO in PEDOT:PSS increased to 4.9 [PEDOT:PSS-GO (2:1) composite], 5.0 eV [PEDOT:PSS-GO (1:1) composite], and 4.88 eV [PEDOT:PSS-GO (1:2) composite], compared to 4.23 eV obtained for pristine GO and 4.8 eV calculated for pure PEDOT:PSS. Here, the increase of work function of PEDOT:PSS-GO is a consequence of the benzoid-quinoid transition of PEDOT:PSS originating by the addition of GO in PEDOT:PSS **[11]**, as confirmed from earlier discussed Raman analysis. It is seen in Fig. 8 that the hole injection barrier at the anode/active layer interface decreases in case of PEDOT:PSS-GO (2:1) and (1:2) composite ie., by 0.05 eV and 0.1 eV, compared to existing hole injection barrier when pure PEDOT:PSS (0.19 eV) and pristine GO (0.3 eV) HTL are used, due to increase in respective E_{HOMO}. It is more pronounced for PEDOT:PSS-GO (1:1), reaching to maximum enhancement in E_{HOMO} such that it matches well with the E_{HOMO} of both the polymer donors, thereby, forming a perfect contact at the interface with almost no interface barrier. Hence, it is confirmed that from the increase of ϕ and E_{HOMO} that the

presence of GO in PEDOT:PSS contribute to enhance the hole injection/extraction at the HTL/Active layer interface.

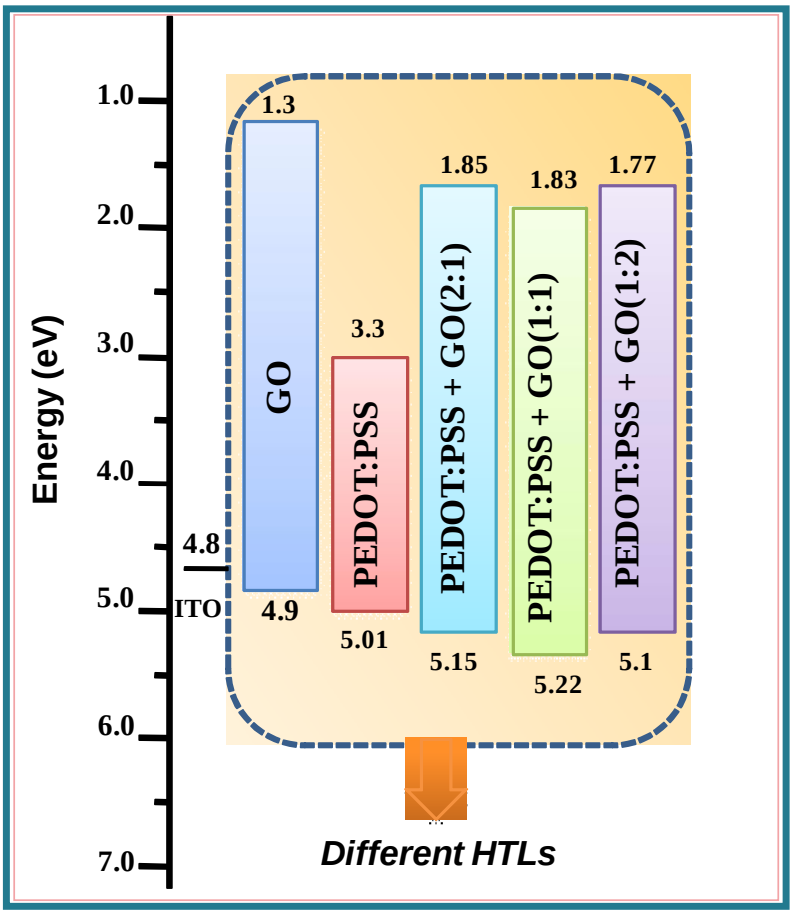

Figure 3.11. *The energy level diagram of different HTLs based on HOMO,LUMO and work function of the respective layers.*

3.3 Conclusions

The 3rd chapter comprises of structural, optical and electrical characterization of GO and PEDOT:PSS-GO composites films for HTLs. The synthesized GO and FGO sample characterized by FESEM, TEM, AFM, revealing the size of nanosheets 5-10μm, and thickness of one single sheet ~1.1nm indicating the availability of two or three layers. XRD, Raman, and FTIR revealed the (001) main graphitic peak, D and G bands(1340 and 1605 cm^{-1}) and all the oxygenated functional groups present on the basal plane of the graphene sheet, respectively, which is consistent with the previous reports [11,12]. The

chemical composition of the GO sample was investigated by XPS where the peaks at binding energy values of 284.60 eV and 532.57 eV are assigned to C 1s and O 1s, respectively. Hence, XPS confirmed that the chemical structure of GO consists of chemical functional groups such as carboxyl, hydroxyl, and epoxy groups along with main C–C (sp2 and sp3). Further, PEDOT:PSS-GO composite films were deposited by dispersing GO in PEDOT:PSS in different weight ratios i.e., (2:1), (1:1), and (1:2). Surface morphology of these PEDOT:PSS-GO composite thin films revealed by FESEM images and AFM images, the low surface roughness (RMS) = 1.21 nm obtained in (1:1) weight ratio signify that GO is dispersed homogeneously in PEDOT:PSS after acheiving good steric stabilization in the matrix. Also, it is found that the dispersion of GO is in PEDOT:PSS not only lowers the sheet resistance but also increases the conductivity significantly because of the available conducting paths provided by GO nanosheets. Henceforth, the conductivity raises from 16.9 $x10^{-3}$ S/cm for PEDOT:PSS-GO (2:1) to 32.2 $x10^{-3}$ S/cm for PEDOT:PSS-GO (1:1) film, and which subsequently reduces to 26 $x10^{-3}$ S/cm in PEDOT:PSS-GO (1:2) film i.e., on a further increase of GO concentration in PEDOT:PSS. Finally, it is concluded that the PEDOT:PSS-GO with (1:1) weight ratio shows the lowest sheet resistance and enhanced electrical conductivity. The transmittance of PEDOT:PSS-GO films [all three different ratios i.e., (2:1), (1:1), and (1:2)] ~ 88-90% at wavelength 550 nm, which is relatively higher compared to the transmittance shown by its two individual components is GO (89%) and PEDOT:PSS (84%). Grom, UPS measurements, the work function on incorporation GO in PEDOT:PSS increased to 4.9 eV [PEDOT:PSS-GO (2:1) composite], 5.0 eV [PEDOT:PSS-GO (1:1) composite], and 4.88 eV [PEDOT:PSS-GO (1:2) composite], compared to 4.23 eV obtained for pristine GO and 4.8 eV calculated for pure PEDOT:PSS. Here, the increase of work function of PEDOT:PSS-GO is a consequence of the benzoid-quinoid transition of PEDOT:PSS originating by the addition of GO in PEDOT:PSS **[9]**. It is concluded that PEDOT:PSS-GO(1:1) is the optimum composition as it shows good film morphology, enhanced conductivity, and highest HOMO level (E_{HOMO} = 5.22 eV). Therefore, PEDOT:PSS-GO(1:1) is considered as a potential HTL alternative to PEDOT:PSS, and more ideally suited for effective HTLs in solar cell devices.

References

1. Lu, Luyao, Mary Allison Kelly, Wei You, and Luping Yu. "Status and prospects for ternary organic photovoltaics." Nature Photonics 9 (2015) 491-500.
2. Goh, Tenghooi, Jing-Shun Huang, Benjamin Bartolome, Matthew Y. Sfeir, Michelle Vaisman, Minjoo L. Lee, and André D. Taylor. "Panchromatic polymer–polymer ternary solar cells enhanced by Förster resonance energy transfer and solvent vapor annealing." Journal of Materials Chemistry A 3 (2015) 18611-18621.
3. Adam, Getachew, Battulga Munkhbat, Patrick Denk, Christoph Ulbricht, Calin Hrelescu, and Markus C. Scharber. "Different Device architectures for Bulk-heterojunction solar cells." Frontiers in Materials 3 (2016) 39.
4. Hilal, Muhammad, and Jeong In Han. "Significant improvement in the photovoltaic stability of bulk heterojunction organic solar cells by the molecular level interaction of graphene oxide with a PEDOT: PSS composite hole transport layer." Solar Energy 167 (2018) 24-34.
5. Wu, Xinkai, Jun Liu, Dongqing Wu, Yanru Zhao, Xindong Shi, Jing Wang, Saijun Huang, and Gufeng He. "Highly conductive and uniform graphene oxide modified PEDOT: PSS electrodes for ITO-Free organic light emitting diodes." Journal of Materials Chemistry C 2 (2014) 4044-4050.
6. Iwan, Agnieszka, Felipe Caballero-Briones, Michal Filapek, Bartosz Boharewicz, Igor Tazbir, Agnieszka Hreniak, and Jesus Guerrero-Contreras. "Electrochemical and photocurrent characterization of polymer solar cells with improved performance after GO addition to the PEDOT: PSS hole transporting layer." Solar Energy 146 (2017) 230-242.
7. Iwan, Agnieszka, Felipe Caballero-Briones, Michal Filapek, Bartosz Boharewicz, Igor Tazbir, Agnieszka Hreniak, and Jesus Guerrero-Contreras. "Electrochemical and photocurrent characterization of polymer solar cells with improved performance after GO addition to the PEDOT: PSS hole transporting layer." Solar Energy 146 (2017) 230-242.
8. Wu, Xinkai, Jun Liu, Dongqing Wu, Yanru Zhao, Xindong Shi, Jing Wang, Saijun Huang, and Gufeng He. "Highly conductive and uniform graphene oxide modified

PEDOT: PSS electrodes for ITO-Free organic light emitting diodes." Journal of Materials Chemistry C 2 (2014) 4044-4050.

9. Yu, Jae Choul, Ji A. Hong, Eui Dae Jung, Da Bin Kim, Soo-Min Baek, Sukbin Lee, Shinuk Cho, Sung Soo Park, Kyoung Jin Choi, and Myoung Hoon Song. "Highly efficient and stable inverted perovskite solar cell employing PEDOT: GO composite layer as a hole transport layer." Scientific reports 8 (2018) 1-9.
10. Liu, Yue-Feng, Jing Feng, Yi-Fan Zhang, Hai-Feng Cui, Da Yin, Yan-Gang Bi, Jun-Feng Song, Qi-Dai Chen, and Hong-Bo Sun. "Improved efficiency of indium-tin-oxide-free organic light-emitting devices using PEDOT: PSS/graphene oxide composite anode." Organic Electronics 26 (2015) 81-85.
11. Díez, Noel, Agata Śliwak, Stanisław Gryglewicz, Bartosz Grzyb, and Grażyna Gryglewicz. "Enhanced reduction of graphene oxide by high-pressure hydrothermal treatment." Rsc Advances 5 (2015) 81831-81837.
12. Johra, Fatima Tuz, Jee-Wook Lee, and Woo-Gwang Jung. "Facile and safe graphene preparation on solution based platform." Journal of Industrial and Engineering Chemistry 20 (2014) 2883-2887.
13. de Moraes, Ana Carolina Mazarin, Bruna Araujo Lima, Andreia Fonseca de Faria, Marcelo Brocchi, and Oswaldo Luiz Alves. "Graphene oxide-silver nanocomposite as a promising biocidal agent against methicillin-resistant Staphylococcus aureus." International journal of nanomedicine 10 (2015) 6847.
14. Amollo, Tabitha A., Genene T. Mola, and Vincent O. Nyamori. "High-performance organic solar cells utilizing graphene oxide in the active and hole transport layers." Solar Energy 171 (2018) 83-91.
15. Luo, Hui, Xuanhuai Lin, Xian Hou, Likun Pan, Sumei Huang, and Xiaohong Chen. "Efficient and air-stable planar perovskite solar cells formed on graphene-oxide-modified PEDOT: PSS hole transport layer." Nano-micro letters 9 (2017) 39.
16. Yu, Runnan, Huifeng Yao, and Jianhui Hou. "Recent progress in ternary organic solar cells based on nonfullerene acceptors." Advanced Energy Materials 8 (2018) 1702814.
17. Borges, Bruno G. AL, Soheila Holakoei, Mathues FF das Neves, Luana CW de Menezes, Carolina F. de Matos, Aldo JG Zarbin, Lucimara S. Roman, and Maria

Luiza M. Rocco. "Molecular orientation and femtosecond charge transfer dynamics in transparent and conductive electrodes based on graphene oxide and PEDOT: PSS composites." Physical Chemistry Chemical Physics 21 (2019) 736-743.

18. Lee, Hongjoo, Youngno Kim, Hangyeol Cho, Jin-geun Lee, and Jung Hyun Kim. "Improvement of PEDOT: PSS linearity via controlled addition process." RSC advances 9 (2019) 17318-17324.
19. Yoo, Dohyuk, Jeonghun Kim, and Jung Hyun Kim. "Direct synthesis of highly conductive poly (3, 4-ethylenedioxythiophene): poly (4-styrenesulfonate)(PEDOT: PSS)/graphene composites and their applications in energy harvesting systems." Nano Research 7 (2014) 717-730.
20. Huang, Xu, Heng Guo, Jian Yang, Kai Wang, Xiaobin Niu, and Xiaobo Liu. "Moderately reduced graphene oxide/PEDOT: PSS as hole transport layer to fabricate efficient perovskite hybrid solar cells." Organic Electronics 39 (2016) 288-295.
21. Hilal, Muhammad, and Jeong In Han. "Significant improvement in the photovoltaic stability of bulk heterojunction organic solar cells by the molecular level interaction of graphene oxide with a PEDOT: PSS composite hole transport layer." Solar Energy 167 (2018) 24-34.
22. Amollo, Tabitha A., Genene T. Mola, and Vincent O. Nyamori. "High-performance organic solar cells utilizing graphene oxide in the active and hole transport layers." Solar Energy 171 (2018) 83-91.
23. Wang, Fei, Xiao-Yu Yang, Meng-Si Niu, Lin Feng, and Xiao-Tao Hao. "Förster resonance energy transfer and morphology optimization for high-performance ternary organic photodetectors." Organic Electronics 67 (2019) 146-152.
24. Chauhan, A. K., Abhay Gusain, P. Jha, S. P. Koiry, Vibha Saxena, P. Veerender, D. K. Aswal, and S. K. Gupta. "Graphene composite for improvement in the conversion efficiency of flexible poly 3-hexyl-thiophene:[6, 6]-phenyl C71 butyric acid methyl ester polymer solar cells." Applied Physics Letters 104 (2014) 133901.

CHAPTER 4

PHOTO-PHYSICAL PRPERTIES OF (D_1:D_2:A_1) - [P3HT: PTB7-th: PCBM] TERNARY BLENDS FOR ACTIVE LAYER

4.1 Introduction

Significant efforts in improvements of binary blend polymer BHJs based PSC devices, the main limitation is associated with the narrow absorption window (≈100–200 nm) of polymers thin films (typically ~100nm) compared to inorganic semiconductors such as silicon **[1-3].** To overcome such absorption limitations linked with binary blend polymer BHJ, tandem PSCs have emerged. In tandem configuration, there is vertical stacking of multiple active layers with complementary absorption connected together by an interfacial buffer layer. Such a tandem configuration not only improves the light-harvesting due to complementary absorption but also reduces the thermalization losses as each active layer independently absorbs a specific portion of the solar spectrum. However, the complexity of the fabrication process involved in tandem PSC significantly increases its manufacturing cost **[2, 3].** On the other hand, recently, a ternary blend based PSC has attracted tremendous interest employing a blend of three absorption complementary components, comprising of either two-electron donors and one electron acceptor (D_1:D_2:A)systems, offering enhanced light-harvesting ability of the photoactive layer **[4-6].** The exceptional advantage of the ternary blend is attributed to the simplicity of the processing steps used which make them more attractive than the complex tandem cells. Also, the third ternary additive in ternary blend acting either as a secondary donor or acceptor material forms a charge cascade structure offering an extra interface for exciton dissociation and charge transfer **[7-10].** As a result, ternary blend PSCs have demonstrated better performances compared to many binary system PSCs showing state-of-the-art PCE approaching ~10-12% **[2-10].**

Many reports on ternary blends present enhanced exciton dissociation probability as supported by Förster resonance energy transfer (FRET) between donor-donor, and charge transfer (CT) at donor/acceptor interface due to cascade energy alignment, in

different ternary blend systems **[6,11,12].** Besides, suitable microstructure, solution-processing, and easy fabrication are some of the added advantages over the widely used tandem solar cell technology **[6-13].** Currently, TPSCs have PCE exceeded 12% **[4-11].** Nevertheless, for improving the performance of TPSCs, it is mandatory to control the blend morphology, and optimize the PV processes such as exciton generation, dissociation, carrier generation, charge transport, and collection. However, the understanding of underlying mechanisms is not straightforward and required extensive studies. A detailed and in-depth studies on the morphology, photo charge carrier dynamics, charge carrier transport (trap-limited and recombination-limited), etc. of the ternary system are very limited.

Keeping this in view in the present work, we have investigated the blend of P3HT and PTB7-th along with PCBM for utilizing as active layer in TPSCs. The detailed and in-depth studies on the morphology, photo-carrier dynamics, charge transport (via traps/ trap-free), and recombination dynamics of the (P3HT:PTB7-th:PCBM) ternary blend are presented. The effect of different weight compositions of the ternary additive have been investigated and compare with that of the respective binary blend constituents. It has been found that the ternary blend of (P3HT:PTB7-th:PCBM) offers broad and strong solar light absorption due to complementary absorption, ranging from visible to NIR region. This chapter deals with some interesting and important results that we have obtained based on the above mentioned study.

4.2 Results and Discussion

The ternary blend of P3HT:PTB7-th:PCBM has been investigated in different blend compositions for optimizing the photovoltaic properties. The P3HT:PTB7-th films were deposited on ITO by mixing P3HT and PTB7-th in three different weight propositions i.e., (0.7:0.3), (0.5:0.5) and (0.3:0.7) weight ratios. The schematic of Ternary blend of (P3HT:PTB7-th:PCBM) has been represented in Fig. 4.1. Here, pure P3HT (a wide bandgap ~2eV conjugated polymer) exhibit high absorption coefficient over the blue-green region (480 - 640 nm), whereas pure PTB7-th (a low bandgap ~1.61 eV conjugated polymer) absorbs primarily in yellow-red (650 - 750 nm) part of the solar spectrum.

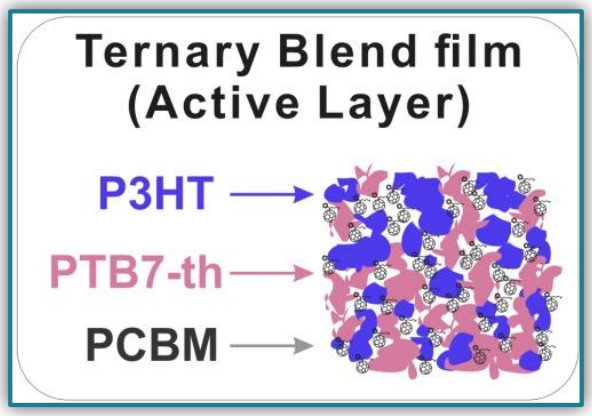

Figure 4.1 *Schematic of Ternary blend of (P3HT:PTB7-th:PCBM) for active layer.*

4.2.1 UV-Vis Absorption Spectra of ternary blend

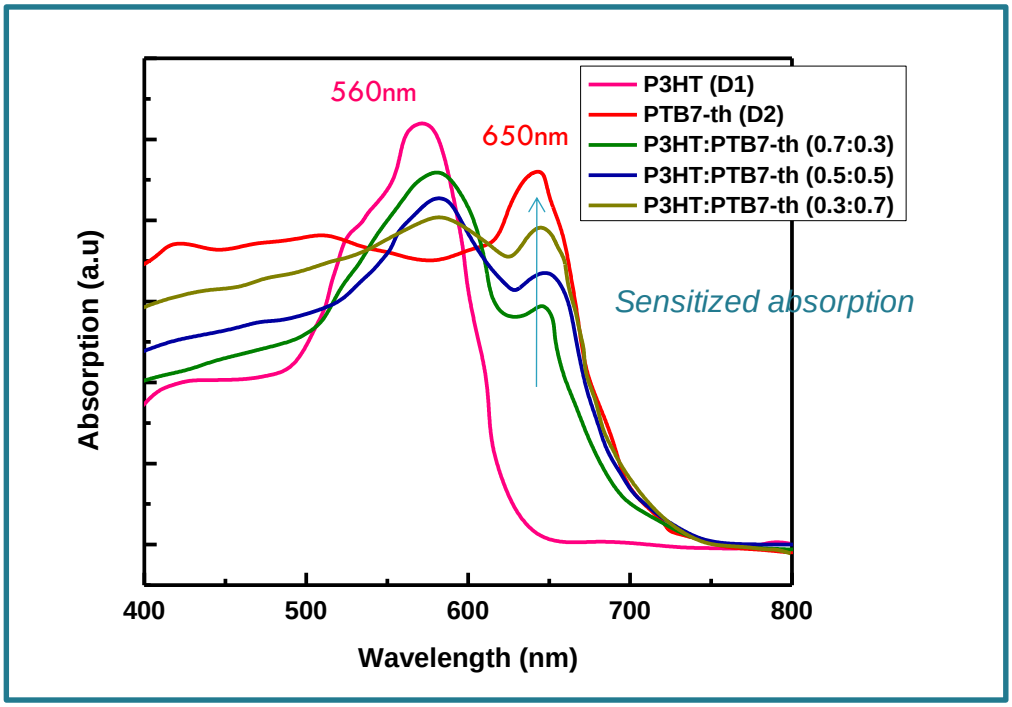

Figure 4.2 *Absorption spectra of P3HT (D_1) and PTB7-th (D_2), and P3HT: PTB7-th showing complementary absorption.*

The recorded absorption spectra, depicted in Fig. 4.2, confirm that all three P3HT:PTB7-th films with (0.7:0.3), (0.5:0.5), and (0.3:0.7) exhibit strong and complementary absorption covering a wider wavelength range from 500-750nm. This

widening of the absorption window is due to the contribution of both P3HT in 480-640nm, and PTB7-th in 650-750nm region of the solar spectrum. Evidently, P3HT:PTB7-th with (0.3:0.7) weight ratio displays more stronger and wider coverage in the entire solar light spectrum as compared to the other two compositions, enabling P3HT:PTB7-th (0.3:0.7) blending composition a promising combination for solar cell application.

4.2.2 Photo-excited carrier dynamics of ternary blend

Further, it is noteworthy that these ternary blends systems [(D_1:D_2:A)/ (D:A_1:A_2)] offer cascade energy alignment depending on the HOMO and LUMO energy levels of respective donors and acceptors these systems are composed of. Depending on their respective band-gaps, the formation of three different cascade structures are reported in the literature. The schematic representation of three different types of cascade structures particularly in (D_1:D_2:A) ternary blends are presented in Fig. 4.3. The possible excitons dissociation mechanisms via FRET between the two donors and CT at donor/acceptor interfaces, and their probabilities are governed by the type of cascade formation **[2, 9].** As seen in Fig. 4.3. (a-c), the first category is A-Type [D_1: D_2 (low E_g): A] blend system wherein both FRET & CT is possible. B-type [D_1: D_2 (low E_g): A] blend also represents the same yet with different energy alignment. However, the third category, C-Type [D_1: D_2 (high E_g): A] blend system, demonstrate that only CT with no possibility of FRET **[2, 26]**. So far all these three categories of cascade ternary blends have been reported worldwide for TPSCs, achieved a noticeable increase in PCEs up to 30-50 % owing to sensitized emission, and strong PL quenching due to FRET/charge transfer assisted enhanced exciton dissociation within the ternary blend **[2, 13].** However, very few reports are available on the dynamics of excitons dissociation in these (D_1:D_2:A) systems and its effect on device performance. Particularly, the P3HT:PTB7-th: PCBM blend, which falls under the type-A category of ternary systems, is a new ternary blend combination with only a few reports available till now, and the detailed studies focusing device physics and excited state carrier dynamics is less explored. We aim at revealing precisely the same in the ternary blend of (P3HT:PTB7-th:PCBM). Here, in this type of A-ternary blend also, the cascade structure expectedly known to trigger both FRET and CT at donor/donor intermixed phases and donor/acceptor interfaces in the blend film (as shown in Fig. 4.3).

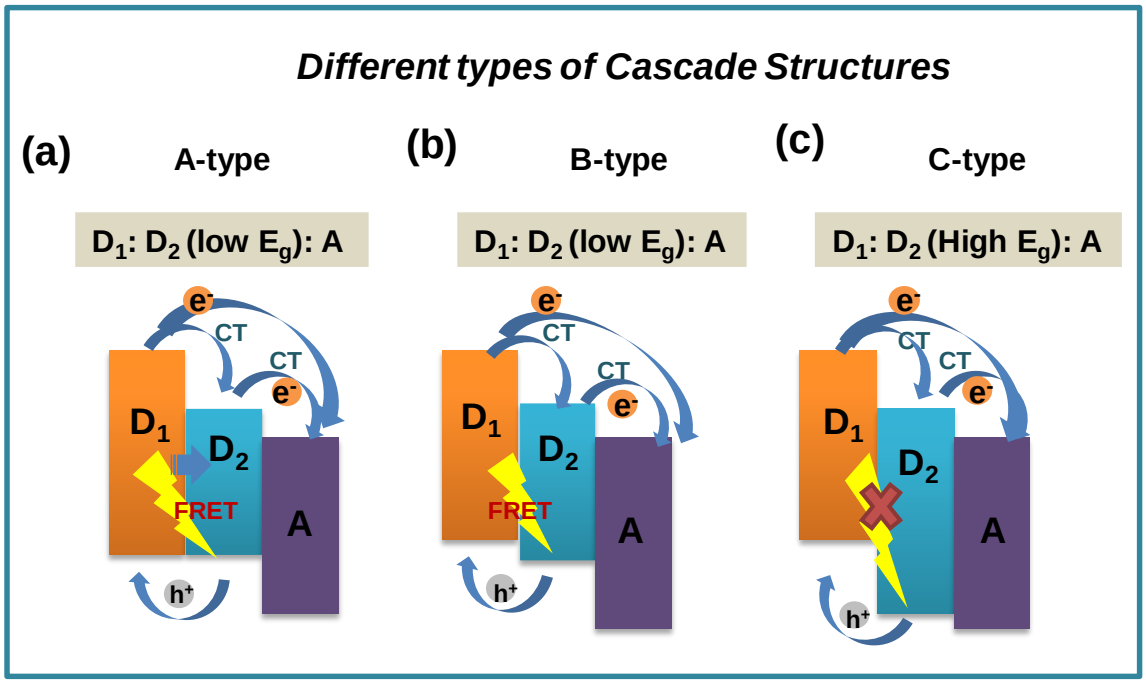

Figure 4.3 *Schematic energy diagrams of different cascades of dual donor and acceptor interfaces; (a) (A-Type) [D_1: D_2 (low E_g): A] blend system: both FRET & CT processes possible; (b) (B-Type) [D_1: D_2 (low E_g): A] blend system: both FRET & CT processes possible; (c) (C-Type) [D_1: D_2 (high E_g): A] blend system: only CT possible and FRET prohibited.*

The probabilities of FRET and CT are investigated via steady-state PL characteristics of pure P3HT, PTB7-th, and P3HT:PTB7-th mixed blends in different weight ratios at 465 nm excitation wavelength [Fig. 4.4]. The two major effects observed in PL spectra with increasing concentration of PTB7-th in P3HT polymer are, (i) PL quenching due to considerable decrease of characteristic PL peaks of P3HT at 650 nm (corresponding to (0-0) π*-π transition), (ii) origin of PL peak at 738 nm in P3HT:PTB7-th (0.7:0.3) films which further shifts to 747 nm and increases in intensity, in both P3HT:PTB7-th (0.5:0.5) and P3HT:PTB7-th (0.3:0.7) films, respectively, indicating the sensitized emission channelized towards the PTB7-th polymer. Both this PL quenching (in P3HT) and sensitized emission (towards PTB7-th) are due to dominating energy transfer as well as electron transfer processes from P3HT (D_1) to PTB7-th (D_2) **[6, 12, 13].**

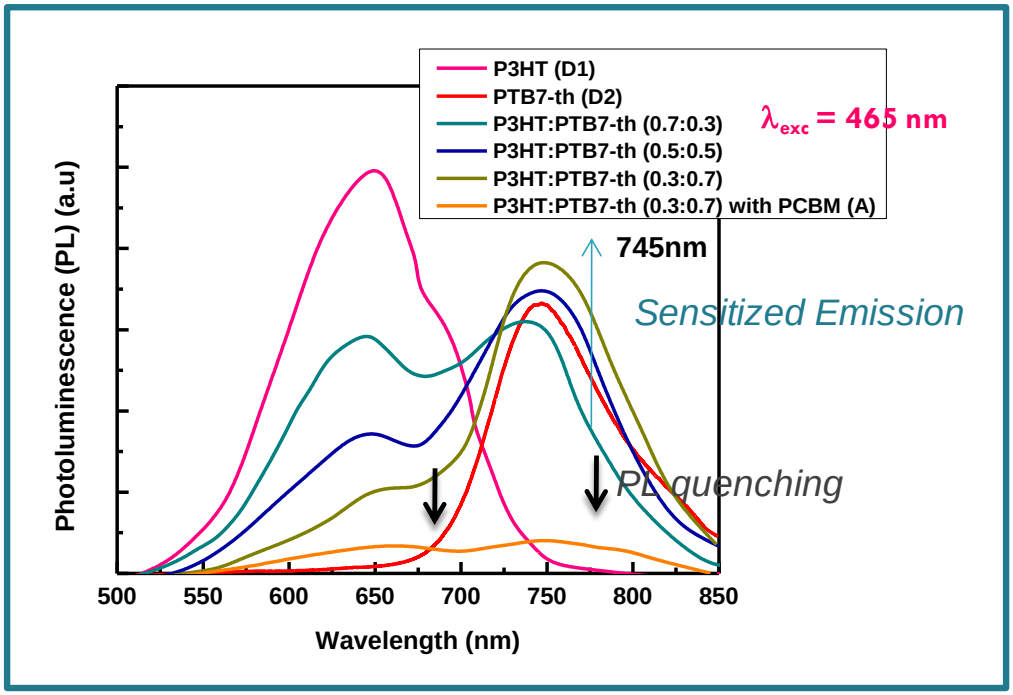

Figure 4.4 *Steady-state PL spectra of P3HT, PTB7-th, P3HT:PTB7-th:$PC_{71}BM$ films at the excitation wavelength of 465 nm. PL curves show sensitized PL and PL quenching in the mixed blends without and with PCBM.*

To verify the PL quenching of P3HT PL_{peak} at 650 nm via energy transfer, we checked for the overlap of PL emission spectra of P3HT with the absorption spectra of PTB7-th by plotting together in Fig. 4.5. It is seen that the absorption edge of PTB7-th is lying exactly at the PL_{peak} of P3HT, satisfies the criterion for FRET occurrence. This confirms that FRET is taking place from one donor i.e., P3HT to the other donor i.e., PTB7-th **[26, 27].** Apparently, P3HT molecules transfer the non-radiative de-excitation exciton energy to PTB7-th via FRET. the ground state PTB7-th molecules thereby absorb this energy and move to the excited state leading to generation of excitons in PTB7-th, which subsequently may or may not recombine radiatively, depending on the donor/acceptor interface it forms with PCBM.

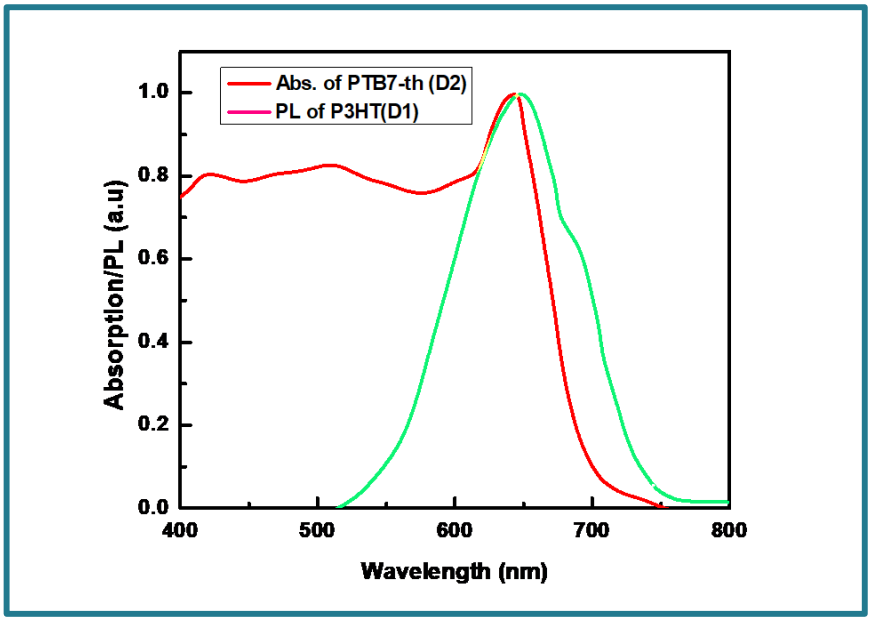

Figure 4.5 *Overlap of PL spectra of P3HT and absorption of PTB7-th, indicating non-radiative FRET is occurring dominantly between P3HT and PTB7-th in P3HT:PTB7-th blends causing PL quenching.*

The parameter which is important in any FRET process is the Forster radius (R_0) which reveals the distance for 50% of FRET efficiency, is calculated as ~5.7 nm, as per the equation **[31, 32]:**

$$R_0 = \frac{9000(\ln 10)Q_D k^2}{128\pi^5 n^4 N_A} J$$

where, k represents the relative orientation of the donor and acceptor dipoles, Q_D defines the photoluminescence quantum efficiency of donor, N_A is Avogadro's number, and n is the implication of refractivity. In P3HT:PTB7-th system, the P3HT is donor and PTB7-th is acting as energy acceptor, so we assume k=2/3, Q_D=1%, and n=1.4, as reported **[32].** Here, J is a definition of the spectral overlap, which is given by the following formula;

$$J = \frac{\int F_D(\lambda)\varepsilon_A(\lambda)\lambda^4 d\lambda}{\int F_D(\lambda) d\lambda}$$

where, $F_D(\lambda)$ is the normalized donor emission spectrum, and ε_A is the acceptor molar extinction coefficient.

Apart from FRET, another possibility of PL quenching of P3HT peak is electron transfer which probably may occur at P3HT/PTB7-th interface due to the energy cascade alignment of P3HT and PTB7-th polymer donors. Further, when the PCBM acceptor is blended with the donor:donor P3HT:PTB7-th (0.3:0.7) composite, PL at both the characteristic peaks of P3HT (650nm) and PTB7-th (747nm) gets completely quenched, shown in Fig. 4.4. This PL quenching due to non-radiative exciton de-excitation confirms markedly enhanced charge transfer at the donor-acceptor, i.e., P3HT/PCBM and PTB7-th /PCBM interfaces due to providing the energy cascade structure leading to efficient exciton dissociation [refer Fig. 4.3 (a)].

To provide the evidence of FRET and CT processes, we probe the fluorescence decay dynamics in P3HT:PTB7-th: blends without and with PCBM ternary additive by time-resolved PL (TRPL) measurements via a time-correlated single-photon count (TCSPC) and estimated the photo-excited carrier lifetime.

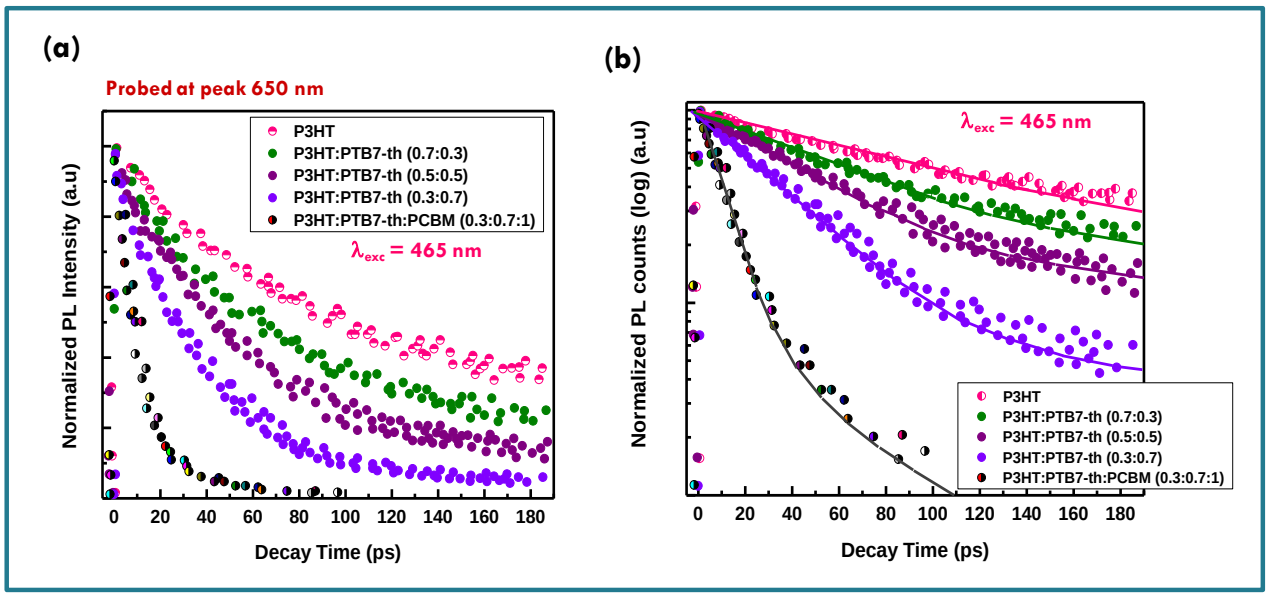

Figure 4.6 *(a) The TRPL decay curve corresponding to pure P3HT and dual donor P3HT:PTB7-th blends in different compositions (without and with PCBM). (b) fitting of PL decay curve (solid lines) using bi-exponential and tri-exponential decay equation where τ represents is the photon-exciton lifetime and the χ2 value is ~1.1 in the numerical fitting parameter.*

Figure 4.6 (a) exhibit the PL decay spectra of pure P3HT, and P3HT: PTB7-th dual donor system in three different compositions, and also by adding PCBM acceptor, at the excitation wavelength (λ_{exc}) at 550nm and emission wavelength (λ_{em}) at 650 nm (PL_{peak}), respectively. It helps in understanding that the exact origin of non-radiative fluorescence, ie., whether PL quenching is occurring via the charge transfer or by FRET. All the PL decay profiles were fitted with well-known multi-exponential function describe elsewhere [Fig. 4.6 (b)] **[31-33,35],** as

$$I = Io + A_1 e^{-\left(\frac{t}{\tau_1}\right)} + A_2 e^{-\left(\frac{t}{\tau_2}\right)} + A_3 e^{-\left(\frac{t}{\tau_3}\right)}$$

where, three components of lifetimes of the photo-excited state are assigned as fast component (τ_1) of non-radiative recombination time; medium component (τ_2) and slowest component (τ_3) to radiative recombination time owing to recombination from interface surface states/traps, with respectively A_1, A_2, and A_3 amplitude constants. The PL decay profiles 1 of Pure P3HT, and P3HT: PTB7-th blends fit reasonably with a bi-exponential decay function. However, for PL decay of the ternary blend of P3HT: PTB7-th:PCBM, tri-exponential decay fit is adopted. The corresponding lifetimes τ_1, τ_2, τ_3, and τ_{avg} (average lifetime) and amplitude components are listed/summarized in Table 1.

Table 4.1: *Fitting parameter of PL decay curves by multi-exponential decay equation.*

Active layer blends	A_1	τ_1(ps)	A_2	τ_2(ps)	A_3	τ_3(ps)	τ_{avg}(ps)	Efficiency of FRET $E_{eff} = 1 - (\tau_{DA}/\tau_D)$
P3HT	0.11	129	0.89	590	-	-	360	-
P3HT:PTB7-Th (0.7:0.3)	0.25	80	0.75	419	-	-	329	E_{FRET} = 37.9 %
P3HT:PTB7-Th (0.5:0.5)	0.38	61	0.62	315	-	-	188	E_{FRET} = 52.7 %
P3HT:PTB7-Th (0.3:0.7)	0.43	47	0.57	206	-	-	126	E_{FRET} = 63.5%
P3HT:PTB7-Th:PCBM (0.3:0.7:1)	0.46	17	0.28	42	0.26	109	54	$E_{FRET\ \&\ CT}$ =86.8 %

Here, a closer look into the time-resolved decay parameters reveals that the lifetimes for non-radiative and radiative transitions change individually on the addition of PTB7-th in P3HT in different compositions, respectively, and also when PCBM acceptor

is added in this P3HT: PTB7-th dual donor blend. The decay of the pristine P3HT film is bi-exponential with τ_1 = 129 ps (A_1 = *0.89)* and τ_2 = 560 ps (A_2 = 0.11). This indicates that 89 % of the PL quenching takes place at decay time τ_1 = 129 ps, while ~ 11 % of PL intensity prevails due to radiative recombination (τ_2 = 560 ps) within the existing traps in the bulk polymer and surface states at the polymer crystallite boundaries apparently due highly disordered conducting polymers molecular chains. The blending of donor P3HT with another donor PTB7-th strongly quench the P3HT PL emission making the short lived photo-excitons τ_1 decrease from 129 ps (A_1 = 0.89) to 80 ps (A_1 = 0.75), 61 ps (A_1 = 0.62), and 47 ps (A_1 = 0.57), respectively, achieved for P3HT: PTB7-th (0.7:0.3), (0.5:0.5), and (0.3:0.7) blend compositions. This decrease in the photo-exciton lifetime in donor P3HT strongly imply that the non-radiative relaxation of these photo-excited excitons is initiated and relaxation energies are transferred to ground state donor PTB7-th molecules by dipole-dipole interaction-based FRET, causing excitation process in PTB7-th molecules followed radiative de-excitation process dominantly. The later process is confirmed through the coincident increase seen in the slow A_2 or longer-lived τ_2 component i.e., from 590 ps (A_2 = 0.11) to 419 ps (A_2 = 0.25), 315 ps (A_2 = 0.38), and 206 ps (A_2 = 0.43) in these respective P3HT:PTB7-th (0.7:0.3), (0.5:0.5), and (0.3:0.7) blends i.e., with increasing compositions of PTB7-th in P3HT. The increased percentage of A_2 amplitudes also confirm that higher the PTB7-th concentration in P3HT, more prominent is the FRET-governed PL quenching, and thereby more and more generation of excitons in PTB7-th molecules. This effect is further quantified by calculating the FRET efficiency (E_{FRET}). The E_{FRET} from donor P3HT to donor PTB7-th (which act as energy acceptor in the present case) can be quantified by the formula: $E_{FRET} = 1 - \tau_{D\text{-}A}/\tau_D$. In the formula, τ_D and $\tau_{D\text{-}A}$ are the PL lifetime of excited exciton in single donor P3HT in the absence and presence of acceptor (PTB7-th), respectively. The E_{FRET} *in* P3HT: PTB7-th blends increases from 37.9 % obtained in P3HT: PTB7-th (0.7:0.3)] to 52.7 % and 63.5 %, obtained for P3HT: PTB7-th (0.5:0.5)] and P3HT: PTB7-th (0.3:0.7) blends, respectively. Furthermore, upon addition of PCBM in P3HT: PTB7-th (0.3:0.7) blend, the exciton lifetime further decreases drastically from τ_1 = 47 ps (A_1 = *0.57)* to τ_1 = 17 ps (A_1 = 0.46) is a direct experimental evidence of additional charge transfer process at donor/acceptor i.e., P3HT/PCBM and PTB7-th/PCBM interfaces in the ternary blend,

besides FRET, as the cascade energy alignment favors charge separation/dissociation with the total efficiency (FRET and CT) reported maximum 86.8%. Wang *et al.* reported that this simultaneous energy transfer and charge transfer processes among the dual donors and donor-acceptor species **[32,35],** however, dominated mainly by CT, is a significant pathway to generate higher photocurrents. Also note that, the other long-lived $\tau_2 = 42$ ps and $\tau_3 = 109$ ps lifetime components are probably attributed to the non-radiative recombination conquered by defects and impurities and bimolecular recombination **[33, 34].** These results conclude that the enhanced energy and charge transfer efficiency achieved in the ternary blend may improve the overall characteristic performance of TPSCs using such a P3HT: PTB7-th:PCBM (0.3:0.7:1) ternary blend as active layers.

4.3 Conclusion

Chapter 4 presents the Photo-Physical properties of [P3HT: PTB7-th: PCBM] (D_1:D_2:A_1) ternary blends for active layer. The ternary blend of P3HT:PTB7-th:PCBM has been investigated in different blend compositions for optimizing the photovoltaic properties. The P3HT:PTB7-th films were deposited on ITO by mixing P3HT and PTB7-th in three different weight propositions i.e., (0.7:0.3), (0.5:0.5) and (0.3:0.7) weight ratios. The absorption spectra confirmed that all three P3HT:PTB7-th films exhibit strong and complementary absorption covering a wider wavelength range from 500-750nm. This widening of the absorption window is due to the contribution of both P3HT in 480-640nm, and PTB7-th in 650-750nm region of the solar spectrum. Evidently, P3HT:PTB7-th with (0.3:0.7) weight ratio displays more stronger and wider coverage in the entire solar light spectrum as compared to the other two compositions. Further, the recorded PL characteristics of pure P3HT, PTB7-th, and P3HT:PTB7-th mixed blends, show sensitized emission leading to an additional peak at 747nm compared (due to the incorporation of PTB7-th) to the quenching of regular PL emission at 650nm due to P3HT component. Both this PL quenching (in P3HT) and sensitized emission (towards PTB7-th) are due to dominating energy transfer as well as electron transfer processes from P3HT (D_1) to PTB7-th (D_2). It is seen that the absorption edge of PTB7-th is lying exactly at the PLpeak of P3HT, satisfies the criterion for Förster resonance energy

transfer (FRET) occurrence. This confirms that FRET is taking place from one donor i.e., P3HT to the other donor i.e., PTB7-th **[26-30].** The parameter which is important in any FRET process is the Forster radius (R_0) which reveals the distance for 50% of FRET efficiency, is calculated as ~5.7 nm. Further, when the PCBM acceptor is blended with the donor:donor P3HT:PTB7-th (0.3:0.7) composite, PL at both the characteristic peaks of P3HT (650nm) and PTB7-th (747nm) gets completely quenched. This PL quenching due to non-radiative exciton de-excitation confirms markedly enhanced charge transfer at the donor-acceptor, i.e., P3HT/PCBM and PTB7-th /PCBM interfaces due to providing the energy cascade structure leading to efficient exciton dissociation. The TRPL studies demonstrated the reduction in photo-exciton lifetime drastically from τ_1 = 129ps (*in P3HT)* and τ_1 = 17ps (*in P3HT:PTB7-th:PCBM*), which signify that both FRET and cascade energy level alignment charge transfer dominated mechanisms lead to effective exciton dissociation in the ternary blend. Hence, it is concluded that P3HT:PTB7-th:PCBM (0.3:0.7:1) is the optimized blend combination for solar cell application.

References

1. Ameri, Tayebeh, Parisa Khoram, Jie Min, and Christoph J. Brabec. "Organic ternary solar cells: a review." Advanced Materials 25 (2013) 4245-4266.
2. Yang, Yang Michael, Wei Chen, Letian Dou, Wei-Hsuan Chang, Hsin-Sheng Duan, Brion Bob, Gang Li, and Yang Yang. "High-performance multiple-donor bulk heterojunction solar cells." Nature photonics 9 (2015) 190-198.
3. Yang, Liqiang, Liang Yan, and Wei You. "Organic solar cells beyond one pair of donor–acceptor: ternary blends and more." The journal of physical chemistry letters 4 (2013) 1802-1810.
4. Fan, Baobing, Wenkai Zhong, Xiao-Fang Jiang, Qingwu Yin, Lei Ying, Fei Huang, and Yong Cao. "Improved performance of ternary polymer solar cells based on a nonfullerene electron cascade acceptor." Advanced Energy Materials 7 (2017) 1602127.

5. Chen, Weichao, Huanxiang Jiang, Gongyue Huang, Jun Zhang, Mian Cai, Xiaobo Wan, and Renqiang Yang. "High-Efficiency Ternary Polymer Solar Cells Based on Intense FRET Energy Transfer Process." Solar RRL 2 (2018) 1800101.
6. Yin, Hang, Sin Hang Cheung, Jenner HL Ngai, Carr Hoi Yi Ho, Ka Lok Chiu, Xiaotao Hao, Ho Wa Li, Yuanhang Cheng, Sai Wing Tsang, and Shu Kong So. "Thick-Film High-Performance Bulk-Heterojunction Solar Cells Retaining 90% PCEs of the Optimized Thin Film Cells." Advanced Electronic Materials 3 (2017) 1700007.
7. Mai, Jiangquan, Tsz-Ki Lau, Ting Xiao, Chun-Jen Su, U-ser Jeng, Ni Zhao, Xudong Xiao, and Xinhui Lu. "Ternary morphology facilitated thick-film organic solar cell." RSC advances 5 (2015) 88500-88507.
8. Nakano, Kyohei, Kaori Suzuki, Yujiao Chen, and Keisuke Tajima. "Roles of energy/charge cascades and intermixed layers at donor/acceptor interfaces in organic solar cells." Scientific reports 6 (2016) 1-11.
9. Khlyabich, Petr P., Andrey E. Rudenko, Barry C. Thompson, and Yueh-Lin Loo. "Structural origins for tunable open-circuit voltage in ternary-blend organic solar cells." Advanced Functional Materials 25 (2015) 5557-5563.
10. Huang, Jiang, Hanyu Wang, Kangrong Yan, Xiaohua Zhang, Hongzheng Chen, Chang-Zhi Li, and Junsheng Yu. "Highly efficient organic solar cells consisting of double bulk heterojunction layers." Advanced Materials 29 (2017) 1606729.
11. Lu, Luyao, Mary Allison Kelly, Wei You, and Luping Yu. "Status and prospects for ternary organic photovoltaics." Nature Photonics 9 (2015) 491-500.
12. Goh, Tenghooi, Jing-Shun Huang, Benjamin Bartolome, Matthew Y. Sfeir, Michelle Vaisman, Minjoo L. Lee, and André D. Taylor. "Panchromatic polymer–polymer ternary solar cells enhanced by Förster resonance energy transfer and solvent vapor annealing." Journal of Materials Chemistry A 3 (2015) 18611-18621.
13. Adam, Getachew, Battulga Munkhbat, Patrick Denk, Christoph Ulbricht, Calin Hrelescu, and Markus C. Scharber. "Different Device architectures for Bulk-heterojunction solar cells." Frontiers in Materials 3 (2016) 39.
14. Hilal, Muhammad, and Jeong In Han. "Significant improvement in the photovoltaic stability of bulk heterojunction organic solar cells by the molecular level interaction

of graphene oxide with a PEDOT: PSS composite hole transport layer." Solar Energy 167 (2018) 24-34.

15. Liu, Jun, Yuhua Xue, Yunxiang Gao, Dingshan Yu, Michael Durstock, and Liming Dai. "Hole and electron extraction layers based on graphene oxide derivatives for high-performance bulk heterojunction solar cells." Advanced Materials 24 (2012) 2228-2233.
16. Li, Shao-Sian, Kun-Hua Tu, Chih-Cheng Lin, Chun-Wei Chen, and Manish Chhowalla. "Solution-processable graphene oxide as an efficient hole transport layer in polymer solar cells." ACS nano 4 (2010) 3169-3174.
17. Iwan, Agnieszka, Felipe Caballero-Briones, Michal Filapek, Bartosz Boharewicz, Igor Tazbir, Agnieszka Hreniak, and Jesus Guerrero-Contreras. "Electrochemical and photocurrent characterization of polymer solar cells with improved performance after GO addition to the PEDOT: PSS hole transporting layer." Solar Energy 146 (2017) 230-242.
18. Wu, Xinkai, Jun Liu, Dongqing Wu, Yanru Zhao, Xindong Shi, Jing Wang, Saijun Huang, and Gufeng He. "Highly conductive and uniform graphene oxide modified PEDOT: PSS electrodes for ITO-Free organic light emitting diodes." Journal of Materials Chemistry C 2 (2014) 4044-4050.
19. J. C. Yu, J. A. Hong, E. D. Jung, D. B. Kim, S.-M. Baek, S. Lee, S. Cho, S. S. Park, K. J. Choi, M. H. Song, Highly efficient and stable inverted perovskite solar cell employing PEDOT:GO composite layer as a hole transport layer, Scientific Reports 8 (2018) 1070.
20. Liu, Yue-Feng, Jing Feng, Yi-Fan Zhang, Hai-Feng Cui, Da Yin, Yan-Gang Bi, Jun-Feng Song, Qi-Dai Chen, and Hong-Bo Sun. "Improved efficiency of indium-tin-oxide-free organic light-emitting devices using PEDOT: PSS/graphene oxide composite anode." Organic Electronics 26 (2015) 81-85.
21. Han, Joong Tark, Beom Joon Kim, Bo Gyeong Kim, Jun Suk Kim, Bo Hwa Jeong, Seung Yol Jeong, Hee Jin Jeong, Jeong Ho Cho, and Geon-Woong Lee. "Enhanced electrical properties of reduced graphene oxide multilayer films by in-situ insertion of a TiO2 layer." ACS nano 5 (2011) 8884-8891.

22. Yu, Jae Choul, Jeong In Jang, Bo Ram Lee, Geon-Woong Lee, Joong Tark Han, and Myoung Hoon Song. "Highly efficient polymer-based optoelectronic devices using PEDOT: PSS and a GO composite layer as a hole transport layer." ACS applied materials & interfaces 6 (2014) 2067-2073.
23. Díez, Noel, Agata Śliwak, Stanisław Gryglewicz, Bartosz Grzyb, and Grażyna Gryglewicz. "Enhanced reduction of graphene oxide by high-pressure hydrothermal treatment." Rsc Advances 5 (2015) 81831-81837.
24. Johra, Fatima Tuz, Jee-Wook Lee, and Woo-Gwang Jung. "Facile and safe graphene preparation on solution based platform." Journal of Industrial and Engineering Chemistry 20 (2014) 2883-2887.
25. de Moraes, Ana Carolina Mazarin, Bruna Araujo Lima, Andreia Fonseca de Faria, Marcelo Brocchi, and Oswaldo Luiz Alves. "Graphene oxide-silver nanocomposite as a promising biocidal agent against methicillin-resistant Staphylococcus aureus." International journal of nanomedicine 10 (2015) 6847-6861.
26. Amollo, Tabitha A., Genene T. Mola, and Vincent O. Nyamori. "High-performance organic solar cells utilizing graphene oxide in the active and hole transport layers." Solar Energy 171 (2018) 83-91.
27. Luceño Sánchez, José Antonio, Rafael Peña Capilla, and Ana Maria Díez-Pascual. "High-Performance PEDOT: PSS/hexamethylene diisocyanate-functionalized graphene oxide nanocomposites: Preparation and properties." Polymers 10 (2018) 1169.
28. Borges, Bruno G. AL, Soheila Holakoei, Mathues FF das Neves, Luana CW de Menezes, Carolina F. de Matos, Aldo JG Zarbin, Lucimara S. Roman, and Maria Luiza M. Rocco. "Molecular orientation and femtosecond charge transfer dynamics in transparent and conductive electrodes based on graphene oxide and PEDOT: PSS composites." Physical Chemistry Chemical Physics 21 (2019) 736-743.
29. Lee Hongjoo, Youngno Kim, Hangyeol Cho, Jin-geun Lee, and Jung Hyun Kim. "Improvement of PEDOT: PSS linearity via controlled addition process." RSC advances 9 (2019) 17318-17324.
30. Yoo Dohyuk, Jeonghun Kim, and Jung Hyun Kim. "Direct synthesis of highly conductive poly (3, 4-ethylenedioxythiophene): poly (4-styrenesulfonate)(PEDOT:

PSS)/graphene composites and their applications in energy harvesting systems." Nano Research 7 (2014) 717-730.

31. Yu Runnan, Huifeng Yao, and Jianhui Hou. "Recent progress in ternary organic solar cells based on nonfullerene acceptors." Advanced Energy Materials 8 (2018) 1702814.
32. Wang Fei, Xiao-Yu Yang, Meng-Si Niu, Lin Feng, and Xiao-Tao Hao. "Förster resonance energy transfer and morphology optimization for high-performance ternary organic photodetectors." Organic Electronics 67 (2019) 146-152.
33. Hwang In-Wook, Jaemin Kong, Hyung Keun Yoo, and Kwanghee Lee. "Improved Carrier Dynamics and High Solar Cell Performance in Postadditive-Soaked PTB7: $PC_{71}BM$ Bulk Heterojunction Materials." The Journal of Physical Chemistry C 119 (2015) 12896-12903.
34. Kusum Kumari, S. Chand, P. Kumar, S. N. Sharma, V. D. Vankar, V. Kumar, "Effect of CdSe quantum dots on hole transport in poly (3-hexylthiophene) thin films", *Applied Physics Letters,* 92 (2008) 263504.
35. Guguloth Lalsingh, Kuldeep Singh, VS Reddy Channu, and Kusum Kumari. "Improved performance of ternary blend polymer solar cells via work function tuning and suppressed interface recombination using hybrid PEDOT: PSS-graphene oxide hole transport layer." Applied Surface Science 540 (2021) 148266.

CHAPTER 5

PHOTOVOLTAIC PERFORMANCE OF [P3HT: PTB7-th: PCBM] TERNARY SOLAR CELLS USING DIFFERENT HTLs

5.1 Introduction

Single junction bulk-heterojunction(BHJ) polymer solar cells (PSCs) based on a binary blend of donor and acceptor have proved to be promising photovoltaic technology since the extensive research in the past few decades **[1-6].** It is emerging as a novel approach owing to the low cost, lightweight, flexibility, easy processing, and tunable electrical and optical properties **[7-10].** Such binary blends composed of conjugated polymers such as poly(3-hexyl)thiophene) (P3HT) **[4],** poly[N-9′ -heptadecanyl-2,7-carbazole-alt-5,5-(4′ ,7′ -di-2-thienyl-2′ ,1′ ,3′-benzothiadiazole)] (PCDTBT) [10], poly[2,6-(4,4-bis(2-ethylhexyl)-4H-cyclopenta [2,1-b;3,4-b′]dithiophene)-alt-4,7(2,1,3-benzothiadiazole)] (PCPDTBT) **[11],** poly[(ethylhexyloxy)-benzodithiophene-(ethylhexyl)-thienothiophene] (PTB7) **[12,13],** Poly[4,8-bis(5-(2-ethylhexyl)thiophen-2-yl)benzo[1,2-b;4,5-b']dithiophene-2,6-diyl-alt-(4-(2-ethylhexyl)-3-fluorothieno[3,4-b]thiophene-)-2-carboxylate-2-6-diyl)] (PBDTTT-EFT or PTB7-th) **[13],** Poly[(4,8-bis-(2-ethylhexyloxy)-benzo(1,2-b:4,5-b′)dithiophene)-2,6-diyl-alt-(4-(2-ethylhexanoyl)-thieno[3,4-b]thiophene-)-2-6-diyl)] (PBDTTT-C) **[14],** and Poly[(5,6-dihydro-5-octyl-4,6-dioxo-4H-thieno[3,4-c]pyrrole-1,3-diyl)[4,8-bis[(2-ethylhexyl)oxy]benzo[1,2-b:4,5-b′]dithiophene-2,6-diyl] (PBDTTPD) **[10]** as electron donors, and [6,6]-phenyl C71-butyric acid methyl ester ($PC_{71}BM$), Indene-C60 bisadduct (ICBA) as electron acceptors, demonstrate state-of-the-art PCE approaching ~15-17% **[6-9].** Unfortunately, these binary blends exhibit poor solar light harvesting, due to the intrinsically narrow absorption bands of most of these polymer donors, and week absorption of PCBM acceptor (only in UV region), wasting a significant fraction of available solar light **[15-17]**. However their poor stability is also a matter of concern. To address all these issues, more recently, a new morphological strategy of ternary blends have been adopted by

adding a third ternary component into the binary blend which could either be a donor or an acceptor resulting in (D_1:D_2:A) and (D_1:A_1:A_2) ternary systems, respectively **[18-20].** This technology, popularly known as ternary blend solar cells (TPSCs), has drawn a great interest as they not only provide an advantage of strong light harvesting by complementary absorption, but also effectively improve charge generation and carrier collection properties **[15-25].** Many reports on ternary blends present enhanced exciton dissociation probability as supported by Förster resonance energy transfer (FRET) between donor-donor, and charge transfer (CT) at donor/acceptor interface due to cascade energy alignment, in different ternary blend systems **[20,25,26].** Besides, suitable microstructure, solution-processing, and easy fabrication are some of the added advantages over the widely used tandem solar cell technology **[20-26].** Currently, TPSCs have PCE exceeded 12% **[19-25].** Nevertheless, for improving the performance of TPSCs, it is mandatory to control the blend morphology, and optimize the PV processes such as exciton generation, dissociation, carrier generation, charge transport, and collection.

On the other hand, since past few years, both GO and hybrid PEDOT:PSS-GO in the bilayer and composite form has been widely used as HTLS and have shown encouraging results in achieving good interfacial hole extraction properties, high electron blocking, high film optical transparency, surface morphology, and high conductivity, which have significantly improved the PCE and stability of the PSCs devices. However, several groups have reported the use of PEDOT:PSS-GO as HTLs mostly with binary blend BHJ system combinations and reported enhanced PCE as high as 10% **[27, 28]**. This provides a motivational platform to explore the potential use of PEDOT:PSS-GO HTLs for the design and development of ternary blend systems based PSC technology as well.

Here, we fabricated TPSC devices composed of a ternary blend of dual donor polymers namely, P3HT (a high bandgap polymer donor) and poly[4,8-bis(5-(2-ethylhexyl)thiophen-2-yl)benzo[1,2-b;4,5-b0]dithiophene-2,6-diyl-alt-(4-(2-ethylhexyl)-3 fluorothieno[3,4-b]thiophene-)-2-carboxylate-2-6-diyl)] commonly known as PTB7-Th (low bandgap polymer donor), and fullerene acceptor PCBM as active layer; and employing solution-processable hybrid PEDOT:PSS-GO composite as HTL. In this

work, both addition of GO nanosheets in PEDOT:PSS HTLs (in different compositions) have been investigated systematically to improve the performances of TPSCs. Their solar cell behavior is compared with PEDOT:PSS-only and GO-only HTLs based TPSC devices. Interestingly, it has been found that the PCE of TPSC devices with PEDOT:PSS-GO composite HTLs gets enhanced to 7.1 % (especially in (1:1) weight ratio composition) compared to GO-only (PCE= 2.3 %) and PEDOT:PSS-only (PCE= 3.2 %). The improvement in performance of TPSCs with PEDOT:PSS-GO HTLs is predominantly attributed to the better charge extraction and carrier collection owing to significantly reduced photo-generated exciton lifetime, tuned work function, reduced HTL/active layer interface potential barrier, remarkably improved film morphology, and increased conductivity of PEDOT:PSS-GO films. Therefore, PEDOT:PSS-GO HTLs significantly boost the performance and lifetime stability of (P3HT:PTB7-th:$PC_{71}BM$) ternary blend-based TPSCs. Our work demonstrates the superior hole transport properties of PEDOT:PSS-GO over conventional PEDOT:PSS HTLs for the accelerating development of TPSCs. The fundamental and applied facets revealed from these investigations are discussed in this chapter.

5.2 Results and Discussion

TPSCs fabricated using a ternary blend composed of P3HT (D_1), PTB7 (D_2) and PCBM acceptor (A) have been shown through a schematic representation in Fig. 5.1. TPSCs using [*P3HT:PTB7-th:PCBM] (0.3:0.7:1)* ternary blend were fabricated in the following device configuration,

- Device 1: Indium tin oxide (*ITO)/ GO-only HTL / ternary blend/ LiF/Al*,
- Device 2: *ITO/ PEDOT:PSS-only HTL/ternary blend/LiF/Al*,
- Device 3: *ITO/ PEDOT:PSS-GO (2:1) HTL/ ternary blend /LiF/Al*,
- Device 4: *ITO/ PEDOT:PSS-GO (1:1) HTL/ ternary blend /LiF/Al*, *and*
- Device 5: *ITO/ PEDOT:PSS-GO (1:2) HTL/ ternary blend /LiF/Al.*

The ternary blend active layer [P3HT:PTB7-th:PCBM] and PEDOT:PSS-GO composite HTL have been optimized separately for efficient photovoltaic performances.

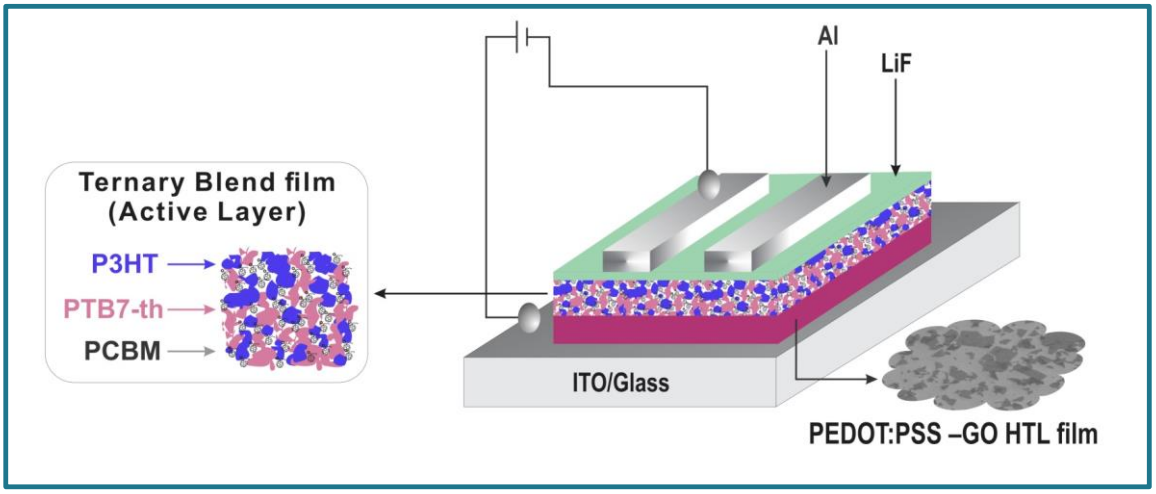

Figure 5.1. *Schematic of the device configuration of (P3HT:PTB7-th:PCBM) ternary blend TPSC employing PEDOT:PSS-GO composite HTL.*

5.2.1 Photovoltaic performance of TPSCs

The *J-V* characteristic curves of the fabricated TPSC devices using P3HT:PTB7-th:PCBM (0.3:0.7:1) ternary blend, and PEDOT:PSS/GO/PEDOT:PSS-GO HTLs i.e., Devices (1-5) under standard AM 1.5G 100 mW cm^{-2} solar illumination are shown in Fig. 5.2(a). The photovoltaic device parameters obtained for all the devices are summarized in Table 1.

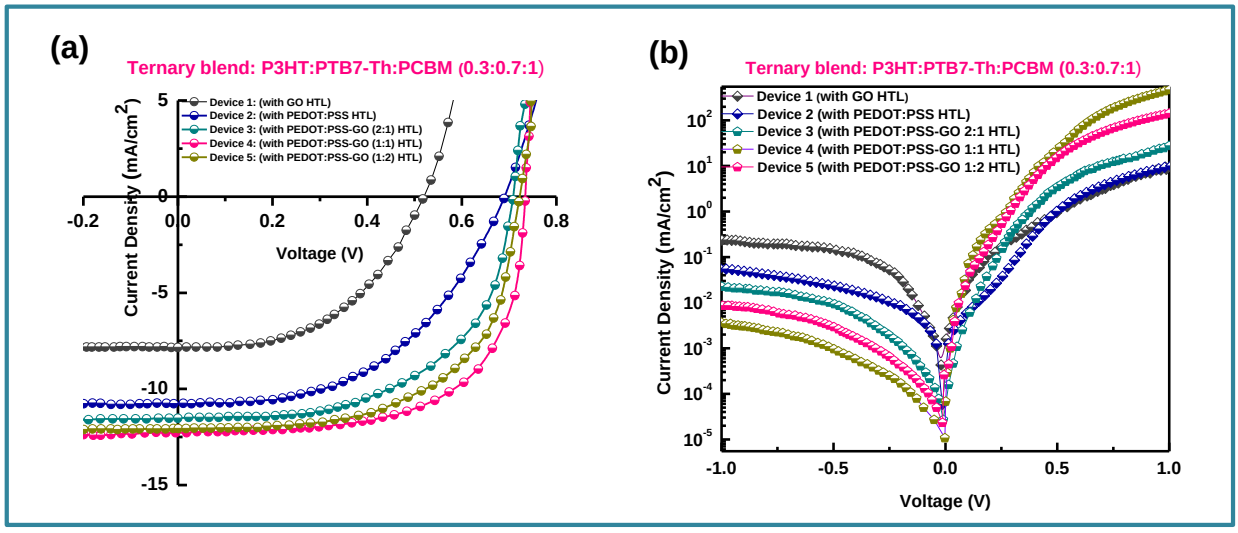

Figure 5.2. *(a) J-V characteristics of TPSCs without and with HTLs: GO, PEDOT:PSS, PEDOT:PSS-GO composite films with various compositions under Air Mass 1.5 Solar illumination (P_{in} =100 mW/cm^2). (b) J-V curves in dark.*

Table 5.1: *Photovoltaic parameters P3HT:PTB7-th:PCBM (0.3:0.7:1) based TPSCs fabricated using different HTLs.*

	Device Structure	J_{sc} (mA /cm^2)	V_{oc} (V)	FF	PCE (%)	R_S (Ω cm^2)	R_{SH} (Ω cm^2)
Device 1	**ITO / GO / Ternary blend/ LiF / Al**	7.9	0.52	0.55	**2.3**	12	2469
Device 2	**ITO / PEDOT:PSS /Ternary blend / LiF / Al**	10.7	0.69	0.43	**3.2**	17	977
Device 3	**ITO / PEDOT:PSS -GO (2:1) / Ternary blend/ LiF / Al**	11.52	0.7	0.71	**5.71**	11	3646
Device 4	**ITO / PEDOT:PSS - GO (1:1) / Ternary blend/ LiF / Al**	12.3	0.74	0.78	**7.1**	5	4111
Device 5	**ITO / PEDOT:PSS -GO (1:2) /Ternary blend/ LiF / Al**	12.11	0.73	0.72	**6.4**	9	3921

The effect of different HTLs on solar cell parameters i.e., PCE, J_{sc}, *FF*, and V_{oc} of TPSC devices (1-5) is demonstrated in Fig. 5.3 (a-d) as shown in the supplementary information.

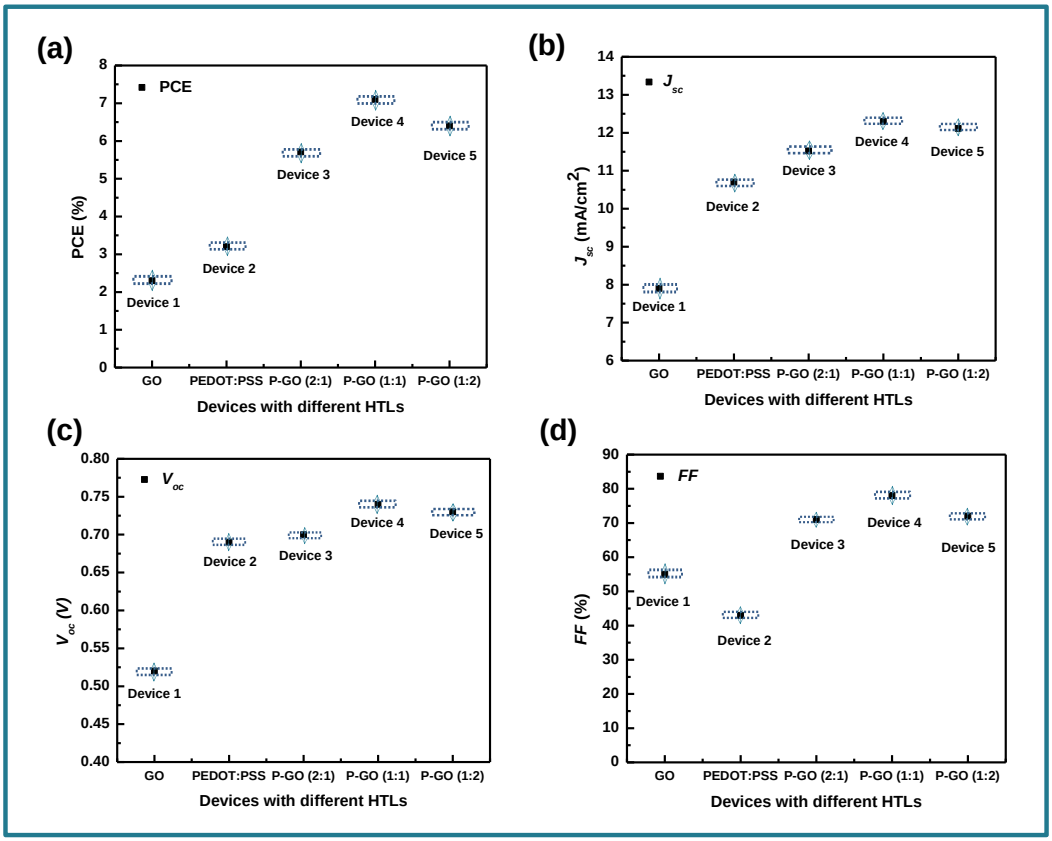

Figure 5.3. *(a-d) Effect of different HTLs on PCE, J_{sc}, FF, and V_{oc}, respectively for Device 1-5; The corresponding PCE J_{sc}, FF, and V_{oc} statistics is based on 10 devices.*

In Table 1, the modulation of solar cell parameters can be understood with the help of the energy band diagram shown in Fig. 5.4.

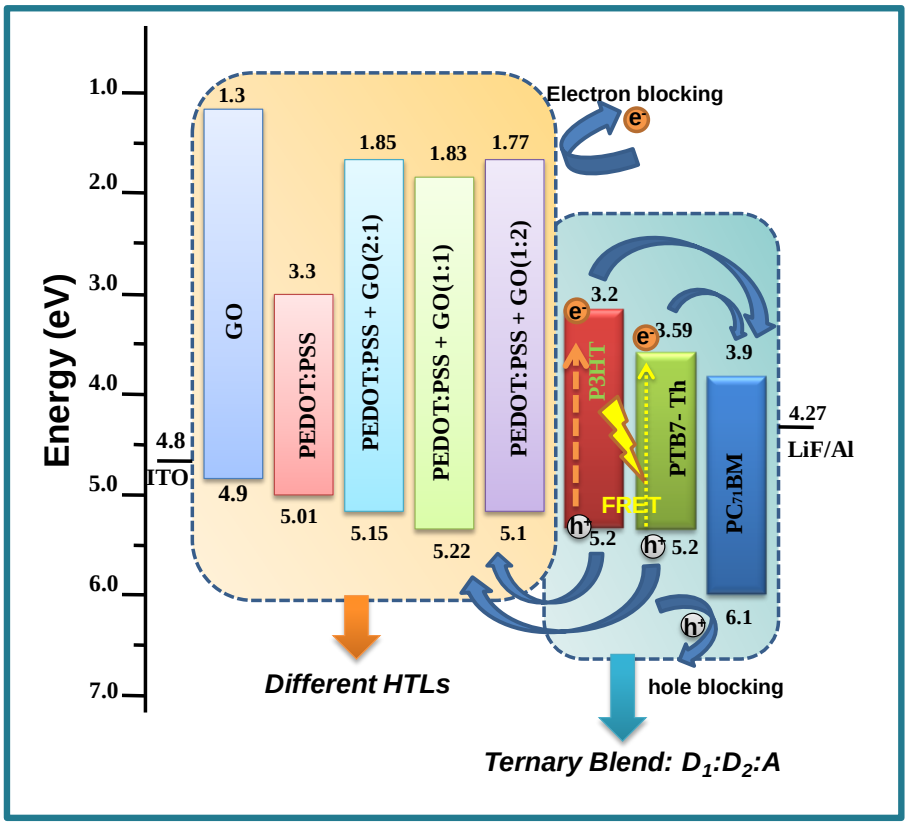

Figure 5.4. *Energy level diagram of TPSCs using ternary blend P3HT:PTB7-th:PCBM with different HTLs [PEDOT:PSS/GO/PEDOT:PSS-GO].*

Here, Device 2 (with PEDOT:PSS-only HTL) has shown slightly better PCE ~3.2% compared to Device 1 (with GO-only HTL) PCE ~2.3%, owing to increase in J_{sc} from 7.9 mA/cm^2 to 10.7 mA/cm^2, V_{oc} from 0.52 V to 0.69 V. However, *FF* (~43%) in case of Device 2 is relatively less compared to 55% observed in Device 1, due to relatively high R_S and low R_{SH} of Device 2. However, it is found that in Devices 3-5, wherein PEDOT:PSS-GO composite HTLs are used in different composition, the solar cell parameters get drastically enhanced to 60-68% and 44-55% in comparison to Device 1 (with GO-only HTL) and Device 2 (with PEDOT:PSS-only HTL), respectively. Incorporating GO nanosheets in PEDOT:PSS HTLs lead to significant increase in PCEs for Device 3 [PCE ~5.71%,], Device 4 [PCE ~7.1%,], Device 5 [PCE ~6.4%,]. It is owed to enhanced values of J_{sc}, V_{oc}, and *FF* achieved in these PEDOT:PSS-GO HTL based

devices (with all (2:1), (1:1) and (1:2) compositions). Interestingly, the maximum increase in the PCE approach to ~7.1 % in PEDOT:PSS-GO (1:1) HTL based Device 4, with the highest enhancement in J_{sc}, V_{oc}, FF value to 12.3 mA/cm^2, 0.74 V, and 78 %, respectively.

5.2.2 Exciton Dissociation, Carrier Generation and Charge Extraction Properties

In order to understand the role of PEDOT:PSS-GO composite based HTL on the enhanced performance of TPSCs [Devices (3-5)], in-depth and detailed investigations on exciton dissociation, carrier generation, and charge extraction properties were carried out. It is well known that in BHJ solar cells, three optimizations are required for efficient generation of the photocurrent, (i) efficient excitons dissociation into free charge carriers at the donor-acceptor interface, (ii) efficient carrier extraction i.e., holes at the HTL/active layer interface and electrons at the active layer/ETL interface, and finally (iii) efficient collection of the separated charges at the respective electrodes **[29]**.

The significant improvement in the performance of Devices (3-5) is due to, firstly, high photo-exciton generation owing to strong and extended light absorption as shown by ternary blend, and secondly, efficient exciton dissociation at donor/acceptor interface via FRET and CT due to cascade energy alignment of the ternary blend (as discussed earlier. Besides, the exciton dissociation at HTL/active layer interfaces is boosted by the addition of GO nanosheets in PEDOT:PSS HTL films, on comparison with only-PEDOT:PSS based HTLs since HOMO level of PEDOT:PSS gets considerably lowered on the addition of GO enabling it to match perfectly with the HOMO level of active layer donor polymers (as depicted in Fig. 5.4). To authenticate such an effect of GO nanosheets on PEDOT:PSS HTLs, we additionally performed the charge carrier dynamics studies by TRPL measurements, and examined the charge extraction and recombination processes at HTL/Active layer interface. Fig. 5.5 (a) is the steady-state PL of (P3HT:PTB7-th) mixed blend film deposited on HTL coated-ITO/glass substrates. Herein, the PL intensity is recorded as a function of different HTLs (GO-only/ PEDOT:PSS-only/ PEDOT:PSS-GO). The PL intensity of the P3HT:PTB7-th (0.3:0.7)blends deposited on the PEDOT:PSS-only and GO-only decreased about 40% and 73%, respectively, compared to PL intensity recorded without any HTL. However, the PL intensity of P3HT:PTB7-th

(0.3:0.7) blends film deposited on PEDOT:PSS-GO HTLs get quenched to 83 % for (2:1), 87 % for (1:1) and 92 % for (1:2) compositions, respectively. Strong quenching in PL peak at 740nm is observed as the HTL is changed from PEDOT:PSS-only to PEDOT:PSS-GO composite film, signify that the presence of GO in PEDOT:PSS significantly could able to extract the photogenerated excitons at the HTL/Active layer interface before their radiative recombination within the active layer itself. Hence, PEDOT:PSS-GO composite films are more efficient in charge extraction/dissociation as compared to PEDOT:PSS-only and GO-only cases.

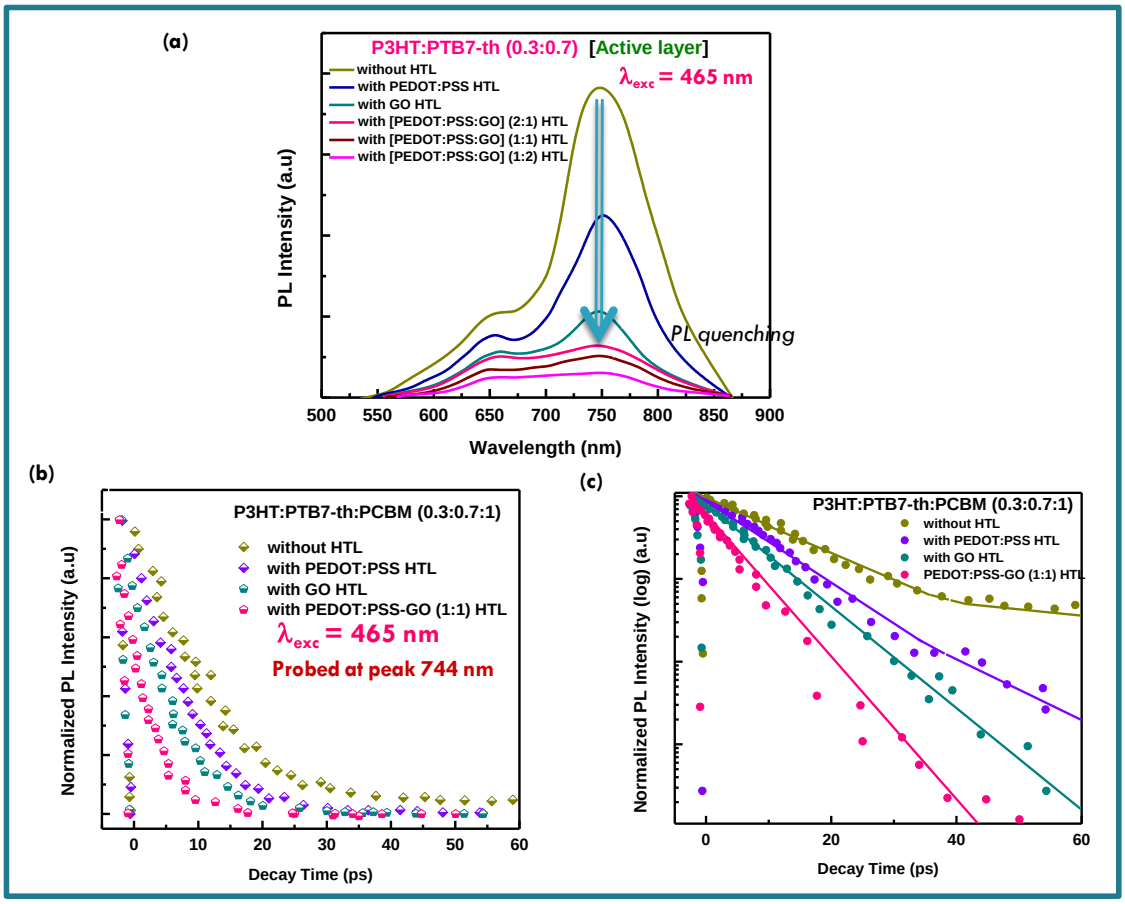

Figure 5.5. *(a) Steady-state PL spectra of P3HT:PTB7-th (0.3:0.7)blends with different HTLs (excitation wavelength = 465 nm). PL quenching in the mixed blends without and with different HTLs is monitored. (b) The PL decay curve P3HT:PTB7-th:PCBM (0.3:0.7:1) blends probed at peak 744 nm, without and with different HTLs. (c) fitting of PL decay curve (solid lines) using bi-exponential and single-exponential decay equation.*

Further, we analyzed the TRPL spectra of P3HT:PTB7-th (0.3:0.7) blend films deposited on PEDOT:PSS-only/ GO-only/ PEDOT:PSS-GO HTLs, respectively, illustrated in Fig. 5.5 (b). The PL decay profiles are shown in Fig. 5.5 (c) were fitted with single, bi- and tri-exponential function describe elsewhere **[29-31]**, as

$$I = \sum_i A_i \exp\left[-\left(\frac{t-t_0}{\tau_i}\right)\right]$$

where three components of lifetimes of the photo-excited state are assigned as, fast component (τ_1) of non-radiative recombination time; medium component (τ_2) and slowest component (τ_3) to radiative recombination time owing to recombination from interface surface states/traps, with respectively A_1, A_2, and A_3 amplitude constants. The decay profile of PL decay profiles of [P3HT:PTB7-th:PCBM] ternary blend without HTL fit with tri-exponential decay function, whereas decay profiles corresponding to ternary blend onto PEDOT:PSS-only HTL fit with a bi-exponential decay function. However, for PL decay of the ternary blend onto GO-only and PEDOT:PSS-GO HTL, a single exponential function fitting is adopted, respectively. The consequent lifetimes τ_1, τ_2, τ_3, and τ_{avg} (average lifetime) and amplitude components are listed/summarized in Table 2.

Table 5.2. *TRPL fitting parameters corresponding to the PL decay curves of the ternary blend active layer without and with PEDOT:PSS/GO/PEDOT:PSS-GO HTLs.*

Active layer P3HT:PTB7-th:PCBM (0.3:0.7:1)	**A_1**	**τ_1 (ps)**	**A_2**	**τ_2 (ps)**	**A_3**	**τ_3 (ps)**	**τ_{avg} (ps)**
Pure (without HTL)	0.46	17	0.28	42	0.26	109	54
with PEDOT:PSS HTL	0.89	12	0.11	35	-	-	23.5
with GO HTL	1	9	-	-	-	-	9
with PEDOT:PSS-GO (1:1) HTL	1	5	-	-	-	-	5

Here, the faster decay component τ_1 originated from the non-radiative recombination is accountable for the PL quenching effect, suggesting that the photo-generated excitons get effectively dissociated into free charge carriers and get transported to the respective electrodes. On the other side, the slow component τ_2 is attributed to the radiative recombination photo-generated excitons and does not get dissociated and

collected at the electrodes. More explicitly, in case of ternary blend without HTL, show τ_{avg} = 54 ps, wherein more contribution is radiative recombination component leading to high values of τ_2 = 42 ps and τ_3 = 109 ps. For ternary blend film deposited on PEDOT:PSS-only HTL display fast decay lifetime (τ_1 = 12 ps) with an amplitude A_1 ~ 0.89 fraction and slow decay lifetime (τ_2 = 35 ps) with an amplitude A_1 ~ 0.11 fraction, suggesting that 89 % of PL decay is responsible due to the PL quenching i.e., depopulation of photo-generated carriers via non-radiative recombination, and only 11 % is PL originating from non-radiative recombination due to the traps and other defects present in the HTL layer. However, it is interesting to note here that when the blend is deposited on GO-only and PEDOT:PSS-GO HTLs, there is a single fast decay component τ_1 as 9 ps and 5 ps, respectively, with 100 % dominated by non-radiative recombination of photo-generated carriers symptomatic of the efficient dissociation occurring via fast hole extraction at HTL/ternary blend interface. It implied that the extraction of holes at the HTL/active layer interface occurs more efficiently using a PEDOT:PSS-GO composite HTLs in the TPSC devices. It should also be noted that GO not only acts in improving the hole extraction at HTL/active layer interface but also significantly contribute in blocking the electrons at the interface. It reduces the possibility of recombination losses of the separated charges at the HTL/active layer interfaces. Hence, the majority of charge-separated carriers are swept to the respective electrodes with minimum recombination in the case of PEDOT:PSS-GO HTLs, while the recombination process still takes place in some degree of fraction in PEDOT:PSS-only HTL **[32].** The fast charge transfer and collection (shown by PEDOT:PSS-GO HTLs based devices compared to PEDOT:PSS-only and GO-only HTL based devices) along with high conductivity, the high work function, better-aligned energy-levels, and the improved morphology of PEDOT:PSS-GO HTL composites (as discussed above), thus contributing to the enhancement of the solar cell parameters under the working conditions.

The dark *J-V* characteristics of the devices were also examined to investigating the role of GO in PEDOT:PSS HTL and on device performance, depicted in Fig. 5.2 (b). Current rectification ratios ~ 34.5, ~211.5, ~1373.8, ~172566.7, and ~18212.5 has been obtained at ±1 V bias, respectively, for Devices (1-5). The current rectification ratio of

Devices (3-5) with PEDOT:PSS-GO HTL is very high compared to devices with PEDOT:PSS-only and GO-only HTLs, suggesting that the leakage current was effectively suppressed in the former **[33- 35]**. These results indicate that the incorporation of GO in PEDOT:PSS improves the performance of TPSCs. For further probing the recombination processes/rates, we calculated the series resistance (R_S) and the shunt resistance (R_{SH}) from the *J-V* curves, listed in Table 1. R_S is related to the interfacial resistance and R_{SH} represents the current leakage in the system **[34, 35]**. From these values, it is proved that the improvement of *FF* (55%) in Device 1 (with GO-only HTL) compared to PEDOT:PSS-only HTL based Device 2 (*FF* ~ 43%), is due to reduction in R_S from 27 Ω cm^2 to 17 Ω cm^2 and improvement in R_{SH} from 977 Ω cm^2 to 2469 Ω cm^2 which is responsible for less dark reverse leakage current. We also observed a further reduced R_S of 11 Ω cm^2, 5 Ω cm^2, and 9 Ω cm^2 in the PEDOT:PSS-GO composite HTLs based Devices (3-5) implying a superior charge transport ability of GO, which was probably due to a higher conductivity (0.032 S/cm) and enhance charge extraction probability due to a higher ϕ than those of PEDOT:PSS-only and GO-only HTLs. More importantly, an abrupt shunt resistance of 3646 Ω cm^2, 4111 Ω cm^2, and 3921 Ω cm^2 in the PEDOT:PSS-GO composite HTLs based Devices (3-5) compared to the PEDOT:PSS-only based Device 2 (977 Ω cm^2) and GO-only based Device 3 (2469 Ω cm^2), suggesting that carrier recombination could be more efficiently reduced through the PEDOT:PSS-GO/ternary blend heterojunction than through the PEDOT:PSS/ternary blend and GO/ternary blend, probably due to the higher LUMO of GO/PEDOT:PSS-GO based HTLs which is known to block electrons.

In general, to produce photocurrent, the dissociated photo-generated excitons into separate free charge carriers, should get collected at the respective electrodes before getting lost by recombination processes **[36]**. The increment in J_{sc} observed in the ternary blend is elucidated in terms of EQE curves shown in Fig. 5.6. It confirmed the enhanced photocurrent in the overall wavelength range for all the P3HT:PTB7-th:PCBM TPSC devices. Also, the J_{sc} values calculated using EQE data were within a 2% error corresponding to J_{sc} values obtained in the *J–V* measurements.

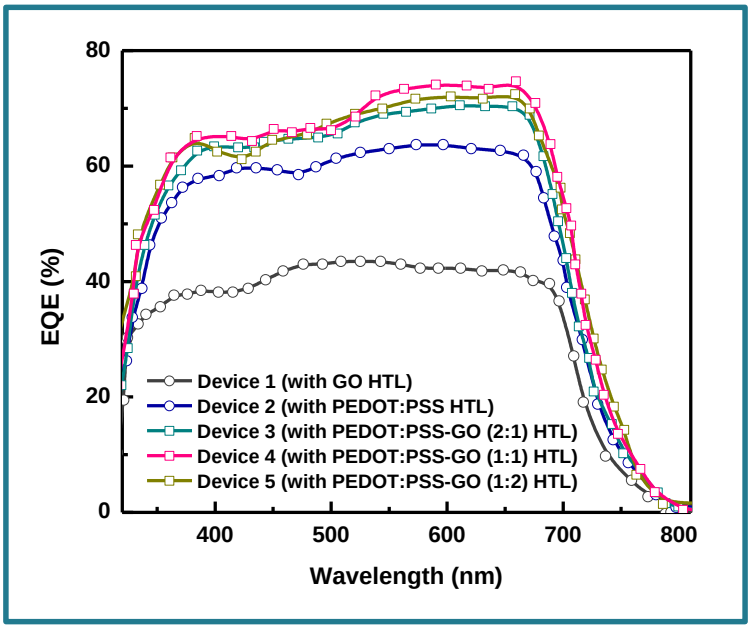

Figure 5.6. *EQE spectra of devices with P3HT:PTB7-th:PCBM (0.3:0.7:1) TPSCs with different HTLs.*

It is seen that the all the TPSC devices (1-5) composed of different HTLs have showed a high and broad spectral response in the wavelength range from 300 nm to 800 nm with a maximum peak approaching 65% at 400 nm and 74% at 700nm of EQE, which is divided into two regions; low wavelength region from 380-510nm with 65-67%, while in the high wavelength region from 540-700nm with 73-74%. It is essentially as per the absorption spectra [refer Fig. 4.2 of Chapter 4]. It is attributed to the combined and complementary absorption bands of P3HT and PTB7-th molecules. Overall, the enhanced EQE indicates that the efficiency of photon-to-electron conversion was superior in the PEDOT:PSS-GO HTL devices than PEDOT:PSS-only device and GO-only device. Such an improvement is highly beneficial for photovoltaics for achieving high J_{sc}.

Further, to have a more clear vision of the exciton dissociation and carrier collection capabilities of PEDOT:PSS-GO HTLs on photovoltaic behavior of the ternary blends, we analyzed the photocurrent density (J_{ph}) as a function of effective voltage (V_{eff}) for TPSC devices (1-5), respectively. Figure 5.7 illustrates the dependence of the measured J_{ph} on V_{eff} in the three devices. Here, $J_{ph} = J_L - J_D$, where J_L and J_D are the current densities under illumination and in dark, respectively. $V_{eff} = V_0 - V_{app}$, where, V_0 is the voltage at which J_{ph}=0, and V_{app} is the applied voltage **[36].** The purpose of plotting J_{ph}

versus V_{eff} is to study the photocurrent generation as a function of electric field in the device. It is noteworthy that V_{oc} is the voltage at which J_L =0. At V_{oc} the electric field will be extremely small, however, the electric field is zero only at voltage V_0. Therefore, V_{eff} = V_0-V_{app} is calculated using V_0 but not V_{oc}.

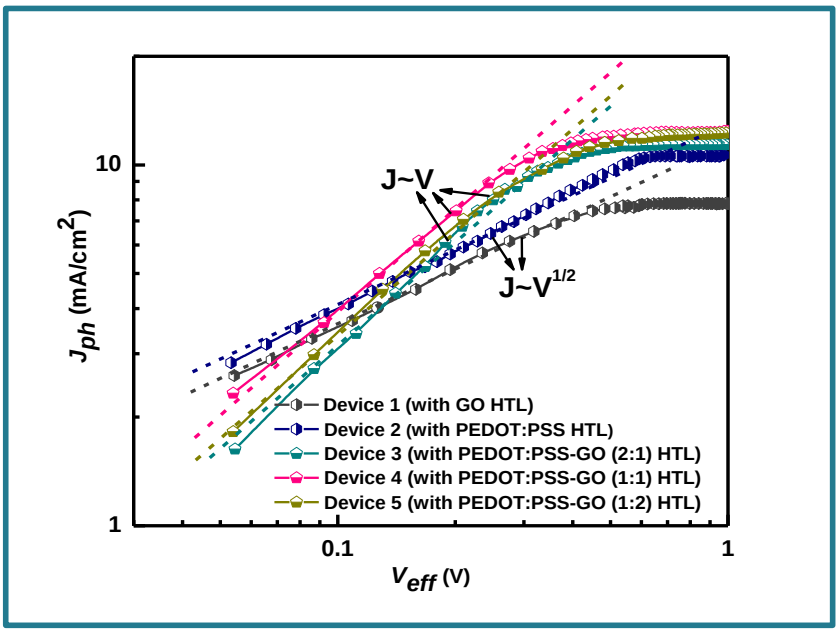

Figure 5.7 *The photocurrent density (J_{ph}) as a function of the effective voltage for TPSC devices with different HTLs.*

In Device 1 and Device 2, J_{ph} is proportional to $V^{1/2}$ at low voltages finally saturates at high voltages. At high voltages, the internal field is large enough to sweep out all the dissociated carriers from the device for collection, and current becomes independent of voltage, as described by V_{sat} in all the devices. However, the dependence of J_{ph} on V_{eff} in low voltage regime imply explicitly the probability of exciton dissociation into free carriers, and how ease they transport to the respective electrodes. $J_{ph} \sim V_{eff}^{1/2}$ is observed in Device 1 (with GO-only HTL) and Device 2 (with PEDOT:PSS-only HTL) shows that the J_{ph} through the cell is limited by charge recombination via interface surface traps prevailing at the respective GO (HTL)/active layer and PEDOT:PSS (HTL)/active layer in these devices. Hence, strong interface recombination losses occur in Device 1 (with GO-only HTL) and Device 2 (with PEDOT:PSS-only HTL). Note that,

a linear dependence of J_{ph} on V_{eff} is observed in Devices 3-5, respectively, which confirm that interface recombination is extremely less and charge transport thereby becomes almost trap-free. It could be understood as the incorporation of GO in PEDOT:PSS HTL smoothened the film, as consistent with low RMS roughness value obtained in these composite films compared to pure PEDOT:PSS films (as discussed in Fig. 3.6 of Chapter 3) reducing the number of surface states/traps at the interface of HTL/active layer. Such a significant effect was seen in PEDOT:PSS-GO HTLs based TPSCs Devices 3-5, becomes the basis for obtaining high J_{sc}, and better *FF*, as compared to devices with GO-only (Device 1) and PEDOT:PSS-only (Device 2) HTLs.

Other essential parameters to look at is V_{sat}. The V_{sat} values are 0.57V (Device 1), 0.59V (Device 2), 0.41V (Device 3), 0.39V (Device 4), and 0.4V (Device 5). Here, it should be noted that V_{sat} occurs at lower internal fields in Devices 3-5 (with PEDOT:PSS-GO HTL), compared to Device 2 (with PEDOT:PSS-only HTL) and Device 1 (with GO-only HTL). The reduction of V_{sat} in devices with PEDOT:PSS-GO as HTLs imply that the electron and hole separation into free charge carrier occurs at much low voltages and much more efficient compared to devices having PEDOT:PSS-only or GO-only HTLs. It is on account of, (i) the reduction in the potential barrier that existed at the interfaces between HTL and active layer due to the perfectly matched HOMO of the HTL with the HOMO of the active layer polymer donors in case of PEDOT:PSS-GO based HTLs, (ii) improved morphology of PEDOT:PSS-GO films owing to low RMS surface roughness. More Insight into the effect PEDOT:PSS-GO HTLs on charge dissociation, generation and collection process can be gained by determining the saturation current density (J_{sat}), exciton dissociation efficiency [$P_{diss}(E, T)$], maximum exciton generation rate (G_{max}) and charge collection efficiency [$P_{coll}(E, T)$], for all the TPSC devices with different HTLs. In general, it is believed that all the photogenerated electron and hole carriers get collected at high V_{eff} which is 1V in all the devices, and then J_{sat} is limited only by the number of photons that come in and absorbed by the active layer. At this point, the rate of charge extraction and collection is determined by the rate of the photons coming in. Consequently, $J_{sat} = qLG_{max}$, where L is film thickness. Measuring J_{sat} will enable the determination of the number of generated charge carriers. G_{max} values (as calculated from J_{sat}) are 4×10^{27} m^{-3} s^{-1} for Device 3, 4.3×10^{27} m^{-3} s^{-1} for Device 4, and 4.2×10^{27} m^{-3} s^{-1}

for Device 5, which are much higher than 2.74×10^{27} m^{-3} s^{-1} for Device 1, and 3.6×10^{27} m^{-3} s^{-1} for Device 2. Such an enhancement is expected from the devices having PEDOT:PSS-GO HTLs as GO enables high solar light optical transmission leading to enhanced light absorption by the ternary blend, thereby more charge carriers will be generated. Among all PEDOT:PSS-GO HTLs, (1:1) weight ratio composition is the optimum one presenting the highest capability of generation rate owing to maximum G_{max} value obtained. The exciton dissociation efficiency *P(E, T)* which depends on electric field and temperature, is calculated as [**35, 37**], $P_{diss}(E, T)=J_{ph}^{(SC)}/J_{sat}$, and the charge collection efficiency is $P_{coll}(E, T)= J_{ph}^{(MPP)}/J_{sat}$ where $J_{ph}^{(SC)}$ and $J_{ph}^{(MPP)}$ are the J_{ph} values at short circuit condition and maximum power point, respectively. Higher P_{diss} = 92.6%, and P_{coll} = 84.3% obtained for Device 4 [PEDOT:PSS-GO (1:1) HTL] compared to P_{diss} = 81.7%, and P_{coll} = 74.1% for Device 1 (GO-only HTL), and P_{diss} = 83.5%, and P_{coll} = 79.7% for Device 2 (PEDOT:PSS-only HTL) indicate the most efficient carrier generation and charge collection processes in PEDOT:PSS-GO (1:1) HTL based TPSCs. All these parameters are summarized in Table 3. Hence, high J_{sc} and *FF* obtained in these devices is well justified.

Table 5.3. *J_{sat}, $P_{diss}(E, T)$, G_{max} and $P_{coll}(E, T)$ for the TPSC devices (1-3) with different HTLs.*

Devices	V_{sat}	J_{sat} ($J_{sat} = qLG_{max}$)	Max. exciton generation rate (G_{max})	Exciton dissociation efficiency $P_{diss} = J_{ph}^{(SC)}/J_{sat}$	Charge Collection efficiency $P_{coll}= J_{ph}^{(MPP)}/J_{sat}$
Device 1 (with GO HTL)	0.57V	7.8 mA/cm^2	2.74×10^{27} m^{-3} s^{-1}	81.7%	74.1%
Device 2 (with PEDOT:PSS HTL)	0.59V	10.5 mA/cm^2	3.6×10^{27} m^{-3} s^{-1}	83.5%	79.7%
Device 4 [with PEDOT:PSS-GO(1:1)]	0.39V	12.5 mA/cm^2	4.3×10^{27} m^{-3} s^{-1}	92.6%	84.3%

5.2.3 Stability Tests of TPSCs

The stability of the fabricated devices was also carried out to examine the degradation Studies [**37**]. After every 50-100 hrs of storage, the solar cell measurements

were taken for the best TPSC Device 4 (with PEDOT:PSS-GO (1:1) HTL) and is compared with Device 1 (GO-only HTL) and Device 2 (PEDOT:PSS-only HTL). The stability characteristics of all the devices are shown in Fig. 5.8 (a-d) demonstrating the normalized PCE, normalized J_{sc}, normalized V_{oc}, and normalized *FF*. It has been found that there is a 30% loss in PCE in Device 1 and 26% loss in Device 2 whereas Device 4 retained its PCE for 500 hrs with only 10% reduction from its initial value. Therefore, Device 4 exhibit a better life as compared to Device 1 and Device 2. It is because pure PEDOT:PSS film is highly hygroscopic known to absorb more moisture and water molecules that diffuse towards the active layers and degrade the film quality. Hence, PEDOT:PSS-only HTLs always lead to poor stability of devices. On the other hand, PEDOT:PSS-GO films show less degradation because of good thermal and photo-stability of the incorporated GO nanosheets, and therefore, the devices with PEDOT:PSS-GO HTLs showed better long-term stability.

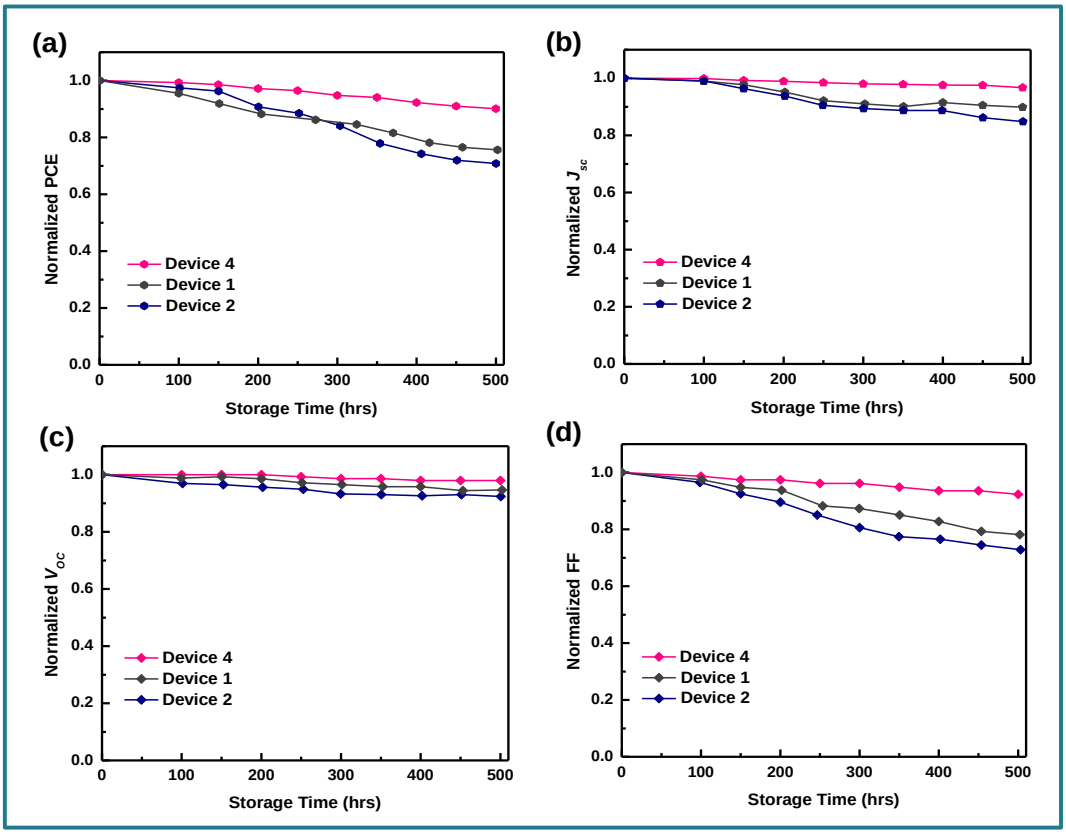

Figure 5.8. *Stability characteristics of Device 4, Device 1, Device 2. (a) Normalized PCE; (b) Normalized J_{sc}; (c) Normalized V_{oc}; (d) Normalized FF.*

5.3 Conclusion

Chapter 5 describes the photovoltaic performance of [P3HT: PTB7-th: PCBM] Ternary solar cells using different HTLs by measuring the *J-V* characteristic under standard AM 1.5G 100 mW cm^{-2} solar illumination. A remarkable enhancement in PCE of [P3HT:PTB7-th:PCBM] (0.3:0.7:1) ternary blend based solar cells (TSC) from 3.2% to 7.1% without and with the addition of GO nanosheets in PEDOT:PSS HTL has been achieved. Such an enhancement in PCE of TPSC devices when PEDOT:PSS-GO (1:1) composite is used as HTL is attributed to the fact that the dispersion of GO nanosheets in PEDOT:PSS HTL, (i) reduced HTL/active layer interface barrier via tuning the work function making it perfectly matched with the highest occupied molecular orbital (HOMO) of the donor polymer, (ii) enhanced σ of HTL films, and (iii) improved morphology of PEDOT:PSS-GO films owing to low RMS surface roughness enabling the trap-free carrier transport, (iv) better electron blocking capability of PEDOT:PSS-GO, promoting the carrier collection at the anode without interface-state recombination at the HTL/active layer interface. It has also been found that these TSCs showed significant improvement in device stability retaining PCE for 500 hours with only a 10 % loss from its initial value. This is due to good photo-stability of GO which significantly improved the overall air-stability of PEDOT:PSS-GO composite HTL based TSC devices. Hence, PEDOT:PSS-GO composite offers the most desirable hole transport properties over the conventional PEDOT:PSS-only HTLs. In conclusion, [P3HT:PTB7-th:$PC_{71}BM$] (0.3:0.7:1) ternary blend based TSCs display high performance and good stability when PEDOT:PSS-GO (1:1) is utilized as HTL. These in-depth studies open a new avenue for the potential commercialization of low-cost and solution-processed TSCs.

References

1. Scharber, Markus Clark, and Niyazi Serdar Sariciftci. "Efficiency of bulk-heterojunction organic solar cells." Progress in polymer science 38 (2013) 1929-1940.
2. Foster, Samuel, Florent Deledalle, Akiko Mitani, Toshio Kimura, Ki-Beom Kim, Takayuki Okachi, Thomas Kirchartz et al. "Electron collection as a limit to polymer: PCBM solar cell efficiency: Effect of blend microstructure on carrier mobility and device performance in PTB7: PCBM." Advanced energy materials 4 (2014) 1400311.

3. Huang, Ye, Edward J. Kramer, Alan J. Heeger, and Guillermo C. Bazan. "Bulk heterojunction solar cells: morphology and performance relationships." Chemical reviews 114 (2014) 7006-7043.
4. Wang, Gang, Ferdinand S. Melkonyan, Antonio Facchetti, and Tobin J. Marks. "All-polymer solar cells: recent progress, challenges, and prospects." Angewandte Chemie International Edition 58 (2019) 4129-4142.
5. Lee, Changyeon, Seungjin Lee, Geon-U. Kim, Wonho Lee, and Bumjoon J. Kim. "Recent advances, design guidelines, and prospects of all-polymer solar cells." Chemical reviews 119 (2019) 8028-8086.
6. Xu, Xiaopeng, Kui Feng, Zhaozhao Bi, Wei Ma, Guangjun Zhang, and Qiang Peng. "Single-junction polymer solar cells with 16.35% efficiency enabled by a platinum (II) complexation strategy." Advanced materials 31 (2019) 1901872.
7. Gurney, Robert S., David G. Lidzey, and Tao Wang. "A review of non-fullerene polymer solar cells: from device physics to morphology control." Reports on Progress in Physics 82 (2019) 036601.
8. Karki, Akchheta, Joachim Vollbrecht, Alana L. Dixon, Nora Schopp, Max Schrock, GN Manjunatha Reddy, and Thuc-Quyen Nguyen. "Understanding the High Performance of over 15% Efficiency in Single-Junction Bulk Heterojunction Organic Solar Cells." Advanced Materials 31 (2019) 1903868.
9. Lin, Yuanbao, Yuliar Firdaus, Mohamad Insan Nugraha, Feng Liu, Safakath Karuthedath, Abdul-Hamid Emwas, Weimin Zhang et al. "17.1% efficient single-junction organic solar cells enabled by n-type doping of the bulk-heterojunction." Advanced Science 7 (2020) 1903419.
10. Yin, Hang, Cenqi Yan, Hanlin Hu, Johnny Ka Wai Ho, Xiaowei Zhan, Gang Li, and Shu Kong So. "Recent progress of all-polymer solar cells–From chemical structure and device physics to photovoltaic performance." Materials Science and Engineering: R: Reports 140 (2020) 100542.
11. Park, Sung Heum, Anshuman Roy, Serge Beaupre, Shinuk Cho, Nelson Coates, Ji Sun Moon, Daniel Moses, Mario Leclerc, Kwanghee Lee, and Alan J. Heeger. "Bulk heterojunction solar cells with internal quantum efficiency approaching 100%." Nature photonics 3 (2009) 297-302.
12. Huang, Di, Yang Li, Zheng Xu, Suling Zhao, Ling Zhao, and Jiao Zhao. "Enhanced performance and morphological evolution of PTB7: PC 71 BM polymer solar cells by using solvent mixtures with different additives." Physical Chemistry Chemical Physics 17 (2015) 8053-8060.
13. Fernandes, Liliana, Hugo Gaspar, João PC Tomé, Flávio Figueira, and Gabriel Bernardo. "Thermal stability of low-bandgap copolymers PTB7 and PTB7-Th and their bulk heterojunction composites." Polymer Bulletin 75 (2018) 515-532.

14. Chen, Hsiang-Yu, Jianhui Hou, Shaoqing Zhang, Yongye Liang, Guanwen Yang, Yang Yang, Luping Yu, Yue Wu, and Gang Li. "Polymer solar cells with enhanced open-circuit voltage and efficiency." Nature photonics 3 (2009) 649-653.
15. Ameri, Tayebeh, Parisa Khoram, Jie Min, and Christoph J. Brabec. "Organic ternary solar cells: a review." Advanced Materials 25 (2013) 4245-4266.
16. Yang, Liqiang, Liang Yan, and Wei You. "Organic solar cells beyond one pair of donor–acceptor: ternary blends and more." The journal of physical chemistry letters 4 (2013) 1802-1810.
17. Yang, Yang Michael, Wei Chen, Letian Dou, Wei-Hsuan Chang, Hsin-Sheng Duan, Brion Bob, Gang Li, and Yang Yang. "High-performance multiple-donor bulk heterojunction solar cells." Nature photonics 9 (2015) 190-198.
18. Wang, Zi Shuai, Xingang Ren, Xiaopeng Xu, Qiang Peng, E. I. Wei, and Wallace CH Choy. "A comprehensively theoretical and experimental study of carrier generation and transport for achieving high performance ternary blend organic solar cells." Nano Energy 51 (2018) 206-215.
19. Fan, Baobing, Wenkai Zhong, Xiao-Fang Jiang, Qingwu Yin, Lei Ying, Fei Huang, and Yong Cao. "Improved performance of ternary polymer solar cells based on a nonfullerene electron cascade acceptor." *Advanced Energy Materials* 7 (2017) 1602127.
20. Chen, Weichao, Huanxiang Jiang, Gongyue Huang, Jun Zhang, Mian Cai, Xiaobo Wan, and Renqiang Yang. "High-Efficiency Ternary Polymer Solar Cells Based on Intense FRET Energy Transfer Process." Solar RRL 2 (2018) 1800101.
21. Yin, Hang, Sin Hang Cheung, Jenner HL Ngai, Carr Hoi Yi Ho, Ka Lok Chiu, Xiaotao Hao, Ho Wa Li, Yuanhang Cheng, Sai Wing Tsang, and Shu Kong So. "Thick-Film High-Performance Bulk-Heterojunction Solar Cells Retaining 90% PCEs of the Optimized Thin Film Cells." Advanced Electronic Materials 3 (2017) 1700007.
22. Mai, Jiangquan, Tsz-Ki Lau, Ting Xiao, Chun-Jen Su, U-ser Jeng, Ni Zhao, Xudong Xiao, and Xinhui Lu. "Ternary morphology facilitated thick-film organic solar cell." RSC advances 5 (2015) 88500-88507.
23. Nakano, Kyohei, Kaori Suzuki, Yujiao Chen, and Keisuke Tajima. "Roles of energy/charge cascades and intermixed layers at donor/acceptor interfaces in organic solar cells." Scientific reports 6 (2016) 1-11.
24. Khlyabich, Petr P., Andrey E. Rudenko, Barry C. Thompson, and Yueh-Lin Loo. "Structural origins for tunable open-circuit voltage in ternary-blend organic solar cells." Advanced Functional Materials 25 (2015) 5557-5563.
25. Huang, Jiang, Hanyu Wang, Kangrong Yan, Xiaohua Zhang, Hongzheng Chen, Chang-Zhi Li, and Junsheng Yu. "Highly efficient organic solar cells consisting of double bulk heterojunction layers." Advanced Materials 29 (2017) 1606729.

26. Lu, Luyao, Mary Allison Kelly, Wei You, and Luping Yu. "Status and prospects for ternary organic photovoltaics." Nature Photonics 9 (2015) 491-500.
27. An, Qiaoshi, Fujun Zhang, Jian Zhang, Weihua Tang, Zhenbo Deng, and Bin Hu. "Versatile ternary organic solar cells: a critical review." Energy & Environmental Science 9 (2016) 281-322.
28. Stylianakis, Minas M., Dimitrios Konios, Constantinos Petridis, George Kakavelakis, Emmanuel Stratakis, and Emmanuel Kymakis. "Ternary solution-processed organic solar cells incorporating 2D materials." 2D Materials 4 (2017) 042005.
29. Chauhan, A. K., Abhay Gusain, P. Jha, S. P. Koiry, Vibha Saxena, P. Veerender, D. K. Aswal, and S. K. Gupta. "Graphene composite for improvement in the conversion efficiency of flexible poly 3-hexyl-thiophene:[6, 6]-phenyl C71 butyric acid methyl ester polymer solar cells." Applied Physics Letters 104 (2014) 133901.
30. Wang, Fei, Xiao-Yu Yang, Meng-Si Niu, Lin Feng, and Xiao-Tao Hao. "Förster resonance energy transfer and morphology optimization for high-performance ternary organic photodetectors." Organic Electronics 67 (2019) 146-152.
31. Hwang, In-Wook, Jaemin Kong, Hyung Keun Yoo, and Kwanghee Lee. "Improved Carrier Dynamics and High Solar Cell Performance in Postadditive-Soaked PTB7: $PC_{71}BM$ Bulk Heterojunction Materials." The Journal of Physical Chemistry C 119 (2015) 12896-12903.
32. Yeo, Jun-Seok, Rira Kang, Sehyun Lee, Ye-Jin Jeon, NoSoung Myoung, Chang-Lyoul Lee, Dong-Yu Kim et al. "Highly efficient and stable planar perovskite solar cells with reduced graphene oxide nanosheets as electrode interlayer." Nano Energy 12 (2015) 96-104.
33. Amollo, Tabitha A., Genene T. Mola, and Vincent O. Nyamori. "High-performance organic solar cells utilizing graphene oxide in the active and hole transport layers." Solar Energy 171 (2018) 83-91.
34. Li, Ping, Bo Wu, You Chang Yang, Hai Shen Huang, Xiu De Yang, Guang Dong Zhou, and Qun Liang Song. "Improved charge transport ability of polymer solar cells by using NPB/MoO3 as anode buffer layer." Solar Energy 170 (2018) 212-216.
35. Wang, Hanyu, Jiang Huang, Shen Xing, and Junsheng Yu. "Improved mobility and lifetime of carrier for highly efficient ternary polymer solar cells based on TIPS-pentacene in PTB7: $PC_{71}BM$." Organic Electronics 28 (2016) 11-19.
36. Lu, Luyao, Wei Chen, Tao Xu, and Luping Yu. "High-performance ternary blend polymer solar cells involving both energy transfer and hole relay processes." Nature communications 6 (2015) 1-7.
37. Liu, Yu, Benlin He, Jialong Duan, Yuanyuan Zhao, Yang Ding, Mixue Tang, Haiyan Chen, and Qunwei Tang. "Poly (3-hexylthiophene)/zinc phthalocyanine composites for advanced interface engineering of 10.03%-efficiency CsPbBr 3 perovskite solar cells." Journal of Materials Chemistry A 7 (2019) 12635-12644.

CHAPTER 6

A COMPARISION OF [P3HT: PTB7-th: PCBM] TERNARY SOLAR CELL WITH BINARY SOLAR CELLS

6.1 Introduction

We fabricated [P3HT:PTB7-th:PCBM] (0.3:0.7:1) ternary blend based TPSCs using PEDOT:PSS-GO (1:1) composite HTL. In order to illustrate the advantages of ternary blends, the J-V characteristics of these TPSCs are compared with the respective binary counterparts i.e., devices with P3HT:PCBM and PTB7-th:PCBM binary blends. Also, to understand the effect of GO in PEDOT:PSS HTL, we have done the comparison with the TPSCs fabricated using only-PEDOT:PSS HTL **[1,2].** It has been found that these TPSCs showed significant improvement in performances and stability with PCE ~ 7.1% and retained for 500 hours with only a 10 % loss from its initial value. The enhancement in photovoltaic performance exhibited by P3HT:PTB7-th:PCBM TPSCs, attributed to the synergetic effect of P3HT:PCBM and PTB7-th:PCBM binary counterparts is owing to, (i) strong and complementary absorption by P3HT and PTB7-th molecules leading to broad spectral response with photon-to-electron conversion approaching up to 67-75% in extended wavelength range 350-780nm, as confirmed by EQE spectra; (ii) PL quenching and photo-carrier dynamics studies demonstrate that photo-exciton lifetime decreases drastically from τ_1 = 129 ps (in P3HT) and τ_1 = 17 ps (in P3HT:PTB7-th:PCBM) blends which is a consequence of both FRET and CT owing to cascade energy level alignment, resulting in effective exciton dissociation in ternary blend; (iii) improved quality of P3HT:PTB7-th:PCBM active layer thin films as compared to P3HT:PCBM and PTB7-th:PCBM binary blend films. These findings display that P3HT:PTB7-th:PCBM and PEDOT:PSS-GO composite can be a promising ternary blend active layer and hole transporting material, respectively, toward high performance PSC. This work provides a new platform for the development of ternary blend approach of PSC technology **[3, 4].**

The fundamental and applied facets revealed from these investigations are discussed in this chapter.

6.2 Results and Discussion

Solar cell devices were fabricated in device configuration,

Ternary Solar Cells:

Device 1 : *ITO/PEDOT:PSS-GO (1:1)(~40nm)/P3HT:PTB7-th:PCBM (0.3:0.7:1) (~200nm)/LiF/Al*

Binary Solar Cells:

Device 2 : *ITO/ PEDOT:PSS-GO (1:1) (~40nm) / P3HT:PCBM (1:1) (~200nm)/ LiF/Al*

Device 3 : *ITO/ PEDOT:PSS-GO (1:1) (~40nm) / PTB7-th:PCBM (1:1) (~200nm)/ LiF/Al*

6.2.1 Photovoltaic performance

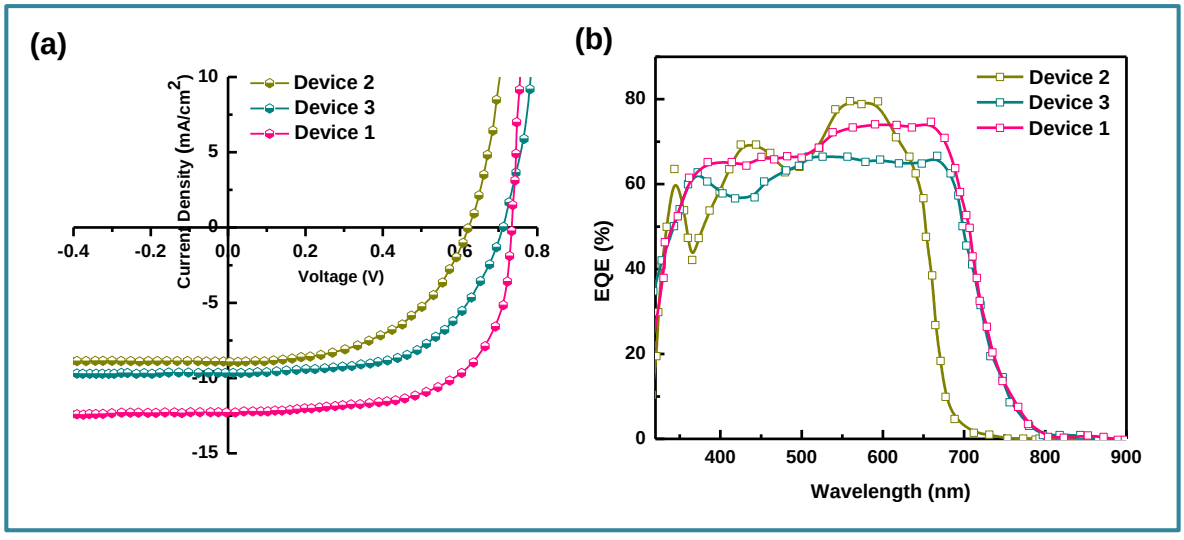

Figure 6.1 *(a) J-V characteristics of TPSC (Device 1) : ITO/ PEDOT:PSS-GO(1:1)/ P3HT:PTB7-th:PCBM (0.3:0.7:1)/ LiF/Al, under Air Mass 1.5 Solar illumination (P_{in} =100 mW/cm^2), and comparison with Device 2: ITO/ PEDOT:PSS-GO(1:1)/ P3HT:PCBM (1:1)/ LiF/Al, and Device 3: ITO/ PEDOT:PSS-GO(1:1)/ PTB7-th:PCBM (1:1)/ LiF/Al . (b) EQE spectra of Device 1, Device 2 and Device 3.*

The TPSCs are fabricated using ternary blend i.e., P3HT:PTB7-th:PCBM (0.3:0.7:1) (best composition) and HTL as PEDOT:PSS-GO (1:1) composite films. The

J-V characteristics of TPSC of Device 1 [*ITO/ PEDOT:PSS-GO(1:1)/ P3HT:PTB7-th:PCBM (0.3:0.7:1)/ LiF/Al*] under Air Mass 1.5 Solar illumination is presented in Fig. 6.1(a), and is compared with Device 2 [*ITO/ PEDOT:PSS-GO(1:1)/ P3HT:PCBM (1:1)/ LiF/Al*] and Device 3 [*ITO/ PEDOT:PSS-GO(1:1)/ PTB7-th:PCBM (1:1)/ LiF/Al*]. The device parameters for all the three devices are summarized in Table 1.

Table 6.1: ***Photovoltaic parameters for Device 1, Device 2, and Devices 3.***

Devices	Device Structure	J_{sc} (mA/cm^2)	V_{oc} (V)	FF	PCE (%)	R_s (Ω cm^2)	R_{sh} (Ω cm^2)
Device 1	**ITO / PEDOT:PSS + GO (1:1) HTL / P3HT:PTB7-Th:PCBM (0.3:0.7:1)/ LiF / Al**	**12.3**	**0.74**	**0.78**	**7.1**	**5**	**4111**
Device 2	**ITO / PEDOT:PSS + GO (1:1) HTL / P3HT:PCBM (1:1) / LiF / Al**	**8.9**	**0.62**	**0.67**	**3.7**	**21**	**2761**
Device 3	**ITO / PEDOT:PSS + GO (1:1) HTL / PTB7-Th:PCBM (1:1) / LiF / Al**	**9.6**	**0.71**	**0.58**	**4**	**19**	**2897**

The performance of Device 1 with P3HT:PTB7-th:PCBM, is superior compared to binary blend based Device 2 (P3HT:PCBM) and Device 3 (PTB7-th:PCBM), which shows a huge enhancement in PEC ~7.1% seen in Device compared to PCE= 3.7% (Device 2) and PCE= 4% (Device 3). Hence, there is an increment of 45-48% in ternary blend based device, apparently attributed to significantly high J_{sc}, V_{oc} and FF as compared to values obtained for binary blend based Device 2 and Device 3, respectively. The improvement in J_{sc} is ascribed to the reduction of series resistance (R_s) to 5 Ω cm^2 and increase of shunt resistance (R_{sh}) to 4111 Ω cm^2 in Device 1, compared to Device 2 (R_s = 21 Ω cm^2; R_{sh}= 2761 Ω cm^2) and Device 3 (R_s = 19 Ω cm^2; R_{sh}= 2897 Ω cm^2) (refer Table 2). On the other hand, the significant improvement in the performance of Device 1 is due to (i) high exciton generation due to strong and extended light absorption as shown by ternary blend, (ii) efficient exciton dissociation at donor/acceptor interface via FRET and CT due to cascade energy alignment of the ternary blend, as proved by TRPL studies in the ternary blend **[5, 6].** And, this exciton dissociation at HTL/active layer, as already discussed earlier, was further get accelerated by the use of PEDOT:PSS-GO composite HTL, due to well-matched HOMO levels of HTL and polymer donors.

To understand further the enhanced performance shown by Device 1 the detailed and comparative investigations were made ahead focusing the exciton dissociation, carrier generation, and carrier transport properties in the P3HT:PTB7-th:PCBM (0.3:0.7:1) ternary blend.

6.2.2 Charge Extraction and Carrier Generation

In General, to get photocurrent, the bound electron-hole pair (excitons) should dissociate and generate free charge carriers, which should get collected at the respective electrodes before getting lost by recombination processes.

This step-up of J_{sc} in the ternary blend is elucidated by the results of EQE spectra shown in Fig. 6.1 (b). The enhanced EQE in an overall broader wavelength range for all is clearly seen for the ternary blend Device 1. Also, the J_{sc} values calculated using EQE data were within a 2% error corresponding to J_{sc} values obtained in the *J–V* measurements. The binary devices with P3HT:PCBM (Device 2) show a narrow absorption range, however, with high conversion percentages of 69% at 432 nm and 79% at 573 nm. On the other hand, PTB7-th:PCBM based Device 3 covers comparatively broad spectra absorption however with little less conversion percentages i.e., 61% at 370 nm and 56% at 432 nm, 66% at 541nm, maintaining same 66 % up to 674 nm. Therefore, it is seen that the TPSCs with P3HT:PTB7-th:PCBM ternary blend (Device 1) showed a high and broad spectral response in the wavelength range from 300 nm to 800 nm with a maximum peak approaching 65% at 400 nm and 74 % at 700 nm of EQE, which is divided into two regions; low wavelength region from 380-510 nm with 65-67 %, while in the high wavelength region from 540-700 nm with 73-74 %. This is essentially in agreement with the absorption spectra; and attributed to the combined and complementary absorption effect from P3HT and PTB7-th molecules, which is reflected in their blends with all three different weight ratios. This improvement is highly beneficial for photovoltaics for achieving high J_{sc}.

The improvement of P3HT:PTB7-th:PCBM ternary blend (Device 1) can be understood via the energy level diagram, shown in Fig. 6.2. It is evident (as discussed in chapter 4), (i) efficient exciton dissociation at donor/acceptor interface via FRET and CT due to cascade energy alignment of the ternary blend, (ii) As PEDOT:PSS-GO is used as

HTL, energy barrier at HTL/Active layer is reduced compared to only-PEDOT:PSS. Therefore, better Charge transfer occurs at HTL/Active layer Interface

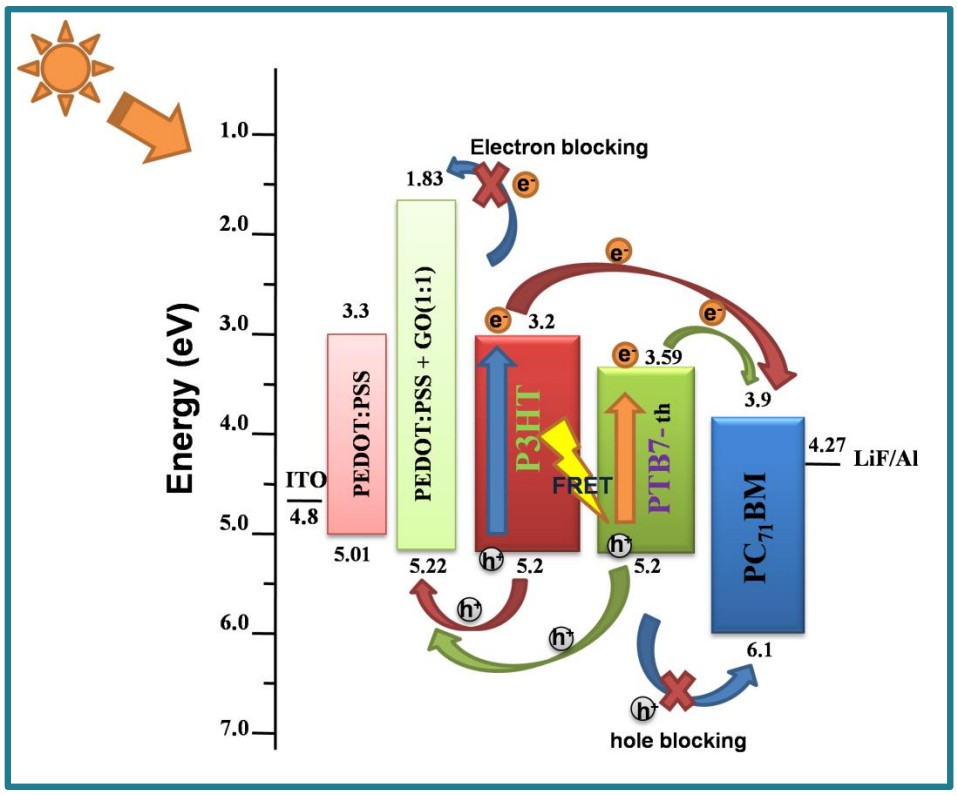

Figure 6.2 *Energy level alignment of P3HT:PTB7-th:PCBM ternary blend and the respective PEDOT:PSS and PEDOT:PSS-GO HTL.*

6.2.3 Photocurrent Recombination dynamics

Further, to understand the recombination dynamics after exciton dissociation and carrier collection and its correlation with the charge transport properties of the ternary blend, we calculated the exciton dissociation efficiency $P_{diss}(E,T)$, charge collection efficiency $P_{coll}(E,T)$ and exciton generation rate (G_{max}) by analyzing the photocurrent density (J_{ph}) as a function of effective voltage (V_{eff}) for the P3HT:PTB7-th:PCBM based TPSCs and compared with that of P3HT:PCBM and PTB7-th:PCBM binary blend devices, respectively **[7, 8].** Figure 6.3 (a) depicts the dependence of the measured J_{ph} on V_{eff} in the three devices. Here, $J_{ph} = J_L - J_D$, where J_L and J_D are the current densities under illumination and in dark, respectively. $V_{eff} = V_0 - V_{app}$, where, V_0 is the voltage at which $J_{ph}=0$ and V_{app} is the applied voltage.

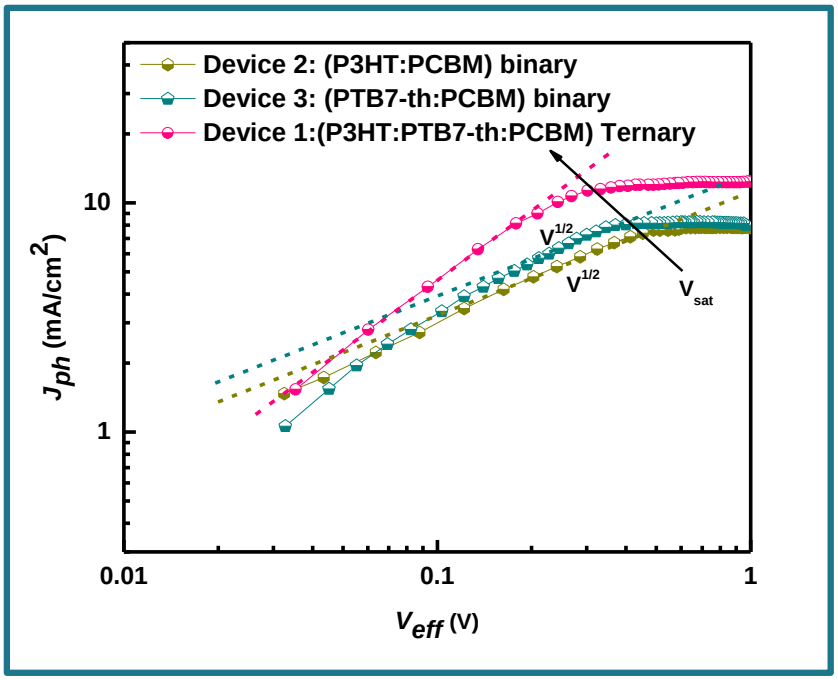

Figure 6.3 *photocurrent density (J_{ph}) as a function of effective voltage for the devices with binary and ternary blends.*

Apparently, J_{ph} increases linearly at very low voltages in Device 2 and Device 3, but J_{ph} is proportional to $V^{1/2}$, at intermediate voltages and finally tends to saturate at high V_{eff} voltages. This means that at high voltages, the internal field is sufficiently large to sweep out all the dissociated carriers from the device. At comparatively intermediate voltages, a large $V^{1/2}$ regime is observed in Device 2 and Device 3, where as J_{ph} is proportional to V_{eff}, implying that the photocurrent is recombination limited due to presence of defect traps and surface traps in case of binary blend devices; and less recombination and photocurrent is trap-free in case of ternary blend devices.

This is further supports better charge transport in ternary blends as compared to binary blends. This is further investigated by via structural analysis by AFM studies. Morphology of the active layer also plays a major role in governing the carrier transport properties. The morphology of the binary blends, P3HT:PCBM and PTB7-th:PCBM, and P3HT:PTB7-th:PCBM ternary blend have been investigated by AFM [shown in Fig. 6.4 (a-c)], yielding the RMS roughness values as 2.87 nm, 1.92 nm and 1.05 nm, respectively. This means that the blending of P3HT with PTB7-th, markedly improves

the morphology by producing less aggregations and reducing the RMS roughness. This improved morphology justifies trap-free charge transport observed in P3HT:PTB7-th:PCBM ternary blends. This supports the enhancement in J_{sc} of TPSC devices.

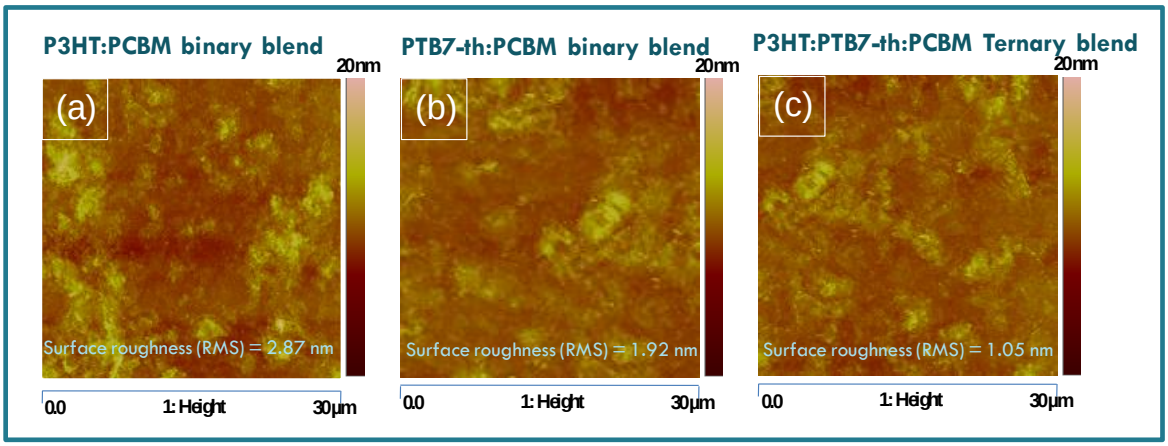

Figure 6.4 (a-c). *AFM of P3HT:PCBM binary blend, PTB7-th:PCBM binary blend, and P3HT:PTB7-th:PCBM ternary blend, respectively.*

Another effect observed is V_{sat} shifts to lower voltages 0.3V in Device 1, compared to V_{sat} = 0.46V (Device 2) to V_{sat} = 0.34V (Device 3). This could be understood in regard to dielectric constant. The P3HT:PTB7-th (0.3:0.7) blend includes a higher dielectric constant polymer (ε_r=3.5) in blended with low dielectric constant polymer (ε_r=3), hence, making effective ε_r=3.35 for the ternary blend. As we know that the exciton binding energies are inversely proportional to the dielectric constant of the materials, therefore, we can say that the excitonic energies decrease in PTB7-th and P3HT:PTB7-th (0.3:0.7) blend compared to P3HT. Hence, making the all the photo-generated excitons to dissociate into free charge carriers easily and effectively at relatively lower field. On the other hand J_{sat} which is limited by the number of photons absorbed by the active layer, is given by $J_{sat} = qLG_{max}$, where L is film thickness, and G_{max} is the maximum generation rate. J_{sat} increases from 7.7 mA/cm^2 in P3HT:PCBM device 2 to 8.16 mA/cm^2 in PTB7-th:PCBM device 3, which increases further to 12.1 mA/cm^2 in P3HT:PTB7-th (0.3:0.7) ternary blend device 1. G_{max} calculated from the J_{sat}, is 2.62×10^{27} m^{-3} s^{-1} for Device 1, is much higher to values 1.67×10^{27} m^{-3} s^{-1} for Device 2 and 1.77×10^{27} m^{-3} s^{-1} for Device 3. The enhancement in G_{max} is attributed to the enhanced

light absorption band of the ternary blend obtained in UV-Vis absorption spectra whereas both the binary blend exhibit a narrow absorption band. The exciton dissociation efficiency *P(E,T)* which depends on electric field and temperature, is calculated as [45, 47], $P_{diss}(E,T)=J_{ph}^{(SC)}/J_{sat}$, and the charge collection efficiency is $P_{coll}(E,T)= J_{ph}^{(MPP)}/J_{sat}$ where $J_{ph}^{(SC)}$ and $J_{ph}^{(MPP)}$ are the J_{ph} values at short circuit condition and maximum power point, respectively. As calculated, P_{diss} = 92.6%, and P_{coll} = 84.3% for P3HT:PTB7-th:PCBM (0.3:0.7:1) ternary blend device 1, is much higher compared to that of binary devices, ie., P_{diss} = 80.7%, and P_{coll} = 76.3% for P3HT:PCBM and P_{diss} = 81.5%, and P_{coll} = 78.9% for PTB7-th:PCBM. All these parameters are summarized in Table 2.

Table 6.2. *J_{sat}, $P_{diss}(E, T)$, G_{max} and $P_{coll}(E, T)$ for the TPSC devices (1-3) with different HTLs.*

Devices	V_{sat}	J_{sat} ($J_{sat} = qLG_{max}$)	Max. exciton generation rate (G_{max})	Exciton dissociation efficiency $P_{diss} = J_{ph}^{(SC)}/J_{sat}$	Charge Collection efficiency $P_{coll} = J_{ph}^{(MPP)}/J_{sat}$
Device 1 (P3HT:PTB7-th:PCBM)	0.3V	12.1 mA/cm^2	2.62x10^{27} m^{-3} s^{-1}	92.6%	84.3%
Device 2 (P3HT: PCBM)	0.46V	7.7 mA/cm^2	1.67x10^{27} m^{-3} s^{-1}	80.7%	76.3%
Device 3 (PTB7-th:PCBM)	0.34V	8.16 mA/cm^2	1.77x10^{27} m^{-3} s^{-1}	81.5%	78.9%

These results confirm that the exciton dissociation, carrier generation, charge transport, and charge collection processes are indeed more efficient in the P3HT:PTB7-th:PCBM ternary blend with (0.3:0.7:1) composition. This is in coherence with the high J_{sc} and *FF* obtained in these devices.

To build more understanding for the increase of J_{sc} and *FF* in ternary blends, we probe the recombination kinetics, by studying the J_{sc} and V_{oc} the under illumination with different intensities, shown in Figure 6.5 (a) and (b). It is well known J_{sc} and Light Intensity (I_L) obeys power-law i.e., $J_{sc} \propto I_L^a$ where exponent *a* describes the bimolecular loss **[9-11].** If *a* is close to unity, then bimolecular losses are very weak. A deviation from $a \approx 1$ suggests strong bimolecular losses.

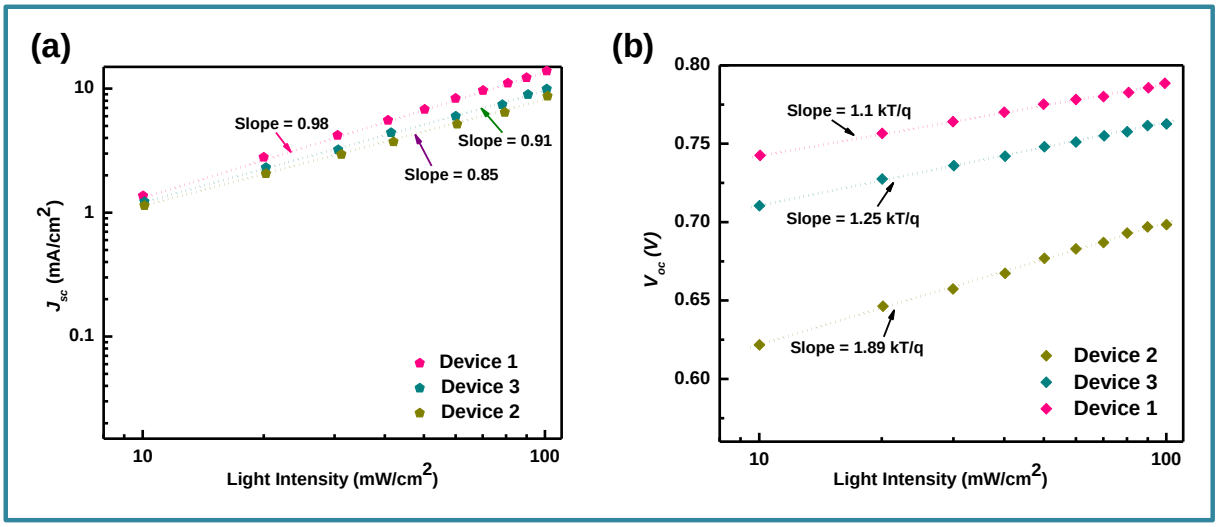

Figure 6.5 *(a) J_{ph} vs Light Intensity, (b) V_{oc} vs Light Intensity.*

Figure 6.5 (a) shows J_{sc} vs. I_L on a log-log scale for Device 1, Device 2, and Device 3. The values are fitted with the power-law as described above. a = 0.85 and a = 0.91 were obtained for binary blend based Devices 2 and 3, suggesting that photo-carriers are not swept away from the active layer blend easily under short circuit conditions. They get slow down due to strong bimolecular recombination in P3HT:PCBM blend, which relatively weakens in PTB7-th:PCBM blends, owing to the high density of traps present in P3HT:PCBM blend and less trap density in PTB7-th:PCBM matrices (as discussed earlier). Such bimolecular recombination limits the exciton dissociation after charge transfer (interface CT entities) and greatly deteriorates the charge separation and transport, and hence low J_{sc} and *FF* observed in these binary blend devices. On the other hand, a increases to 0.98, which is close to unity, imply that almost no bimolecular recombination or very weak recombination occurs in ternary blends, confirming further the trap-free charge transport owing to large charge carrier mobilities, high R_{sh} (table 2), and hence, justifies the enhanced J_{sc}, and *FF* obtained in TPSCs.

Furthermore, the dependence of V_{oc} on I_L tells about the nature of recombination in these binary and ternary blends. The V_{oc} follows the relation, $V_{oc} = nk_BT/q\ [ln(I_L)]$, where q is the elementary charge, k_B is Boltzmann constant, T the absolute temperature, and n the ideality factor **[9].** Here, the slope of V_{oc} vs. $ln(I_L)$ is equal to kT/q mean the bimolecular recombination losses, and $2kT/q$ signify trap assisted-Shockley Read-Hall

(SRH) recombination losses. The plot of V_{oc} vs. I_L is shown in Fig. 6.5 (b). The slope = 1.89kT/q for Device 2, suggest that only trap assisted-SRH recombination exist in P3HT:PCBM blend. Whereas in PTB7-th:PCBM blend, slope = 1.25kT/q, signify that both bimolecular and trap assisted-SRH recombination coexist yet the effect is weak. However in P3HT:PTB7-th:PCBM ternary blend, slope close to 1.1kT/q prove that very weak recombination losses exclusively due to bimolecular recombination accounting the fast charge transport observed in these ternary blends.

6.2.4 Stability of TPSCs

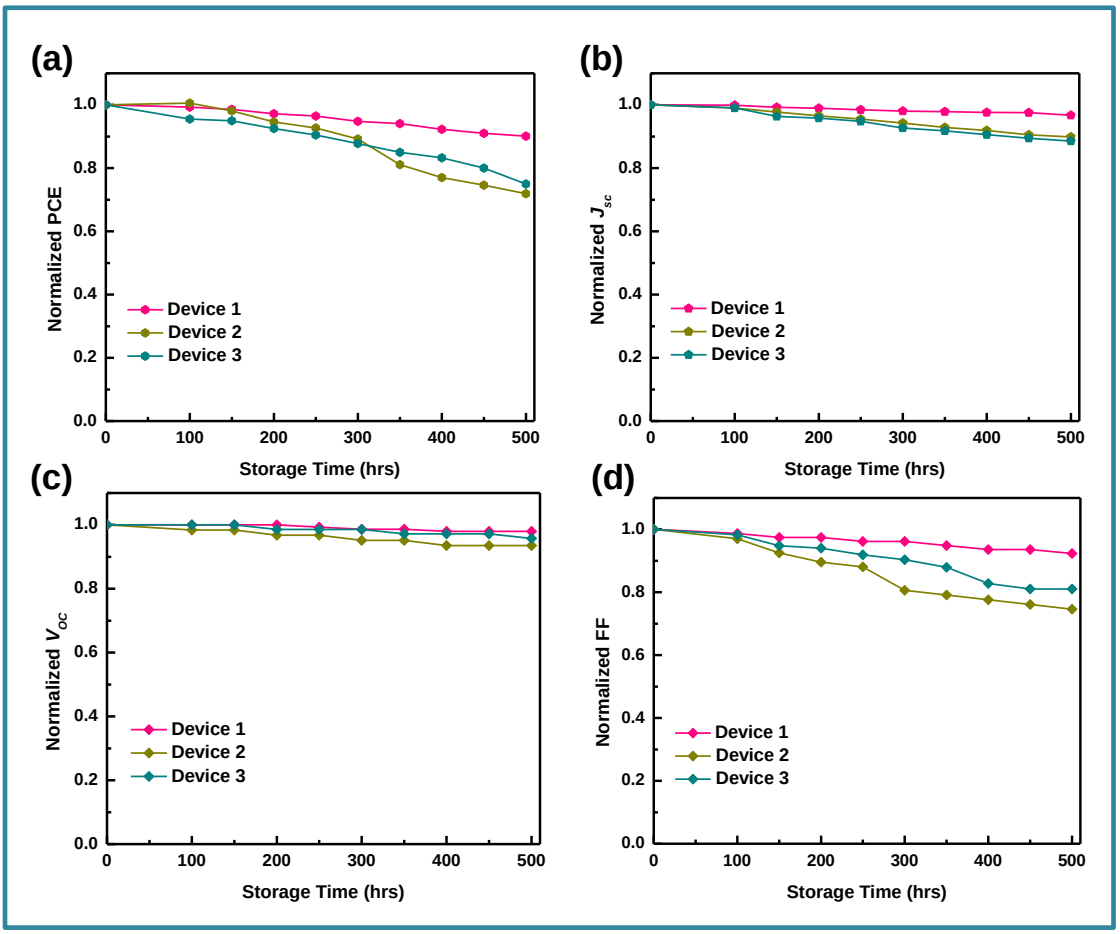

Figure 6.6 *Stability characteristics of Device 1, Device 2 and Device 3. (a) Normalized PCE. (b) Normalized J_{sc}. (c) Normalized V_{oc}. (d) Normalized FF*

The fabricated devices were tested for degradation, the studies were extended to examine the stability of the fabricated TPSC devices, as described elsewhere **[12].** For stability studies, the measurements were taken every 50-100 hrs of storage. The stability

characteristics of TPSC Device 1 is compared with binary blend Device 2 (P3HT:PCBM) and Device 3 (PTB7-th:PCBM), and also with TPSC Device 4 (with only-PDOT:PSS HTL). Figure 6.6 (a-d) shows the stability characteristics of all the Devices representing the normalized PCE, normalized J_{sc}, normalized V_{oc}, and normalized *FF*. On comparing data of Device 1 with Device 2 and Device 3, we observed that the devices with P3HT:PTB7-th:PCBM (0.3:0.7:1) ternary blend showed better stability compared to (P3HT:PCBM) and (PTB7-th:PCBM) binary blend devices, where PCE is retained for 500 hrs with only 10% reduction from its initial value. Hence, [P3HT:PTB7-th:$PC_{71}BM$] (0.3:0.7:1) ternary blend based TPSCs using PEDOT:PSS-GO (1:1) display good performance and stability.

6.3 Conclusions

In this chapter, TPSCs employing P3HT:PTB7-th:$PC_{71}BM$ (0.3:0.7:1) ternary blend and PEDOT:PSS-GO (1:1) composite HTL have been reported. These TPSCs showed PCE ~7.1%, which signify that there is an enhancement of 48% and 45% compared to P3HT:$PC_{71}BM$ (PCE ~3.7%) and PTB7-th: $PC_{71}BM$ (PCE ~4%) binary BHJ solar cells. This is primarily due to an increase of short circuit current (J_{sc}) to 12.3 mA/cm^2, open circuit voltage (V_{oc}) to 0.74V , and Fill factor (*FF*) to 0.78 in case of ternary solar cells. When compared with the TPSC device with only-PEDOT:PSS HTL, an enhancement of 55% in PCE has been observed in devices in which GO nanosheets is added in PEDOT:PSS HTL. Besides, these devices showed long-term photostability. We present a detailed analysis and a closer look at the underlying photovoltaic processes and corresponding prevailing mechanisms accounting for the improvement of the performance of the TPSCs. We found that the improvement in the performance of the P3HT:PTB7-th:$PC_{71}BM$ (0.3:0.7:1) ternary blend based TPSC devices with PEDOT:PSS-GO (1:1) composite HTL, is attributed to (i) broad spectral coverage of solar light harvesting owing to strong and complementary absorption; (ii) Efficient exciton dissociation into free charge carriers via FRET and CT at the D_1/D_2 and D/A interfaces; (iii) High charge extraction ability at HTL/active layer interface due to well-matched HOMO level of PEDOT:PSS-GO with HOMO of polymer donors; (iv) efficient electron blocking capability of PEDOT:PSS-GO reduces the probability of HTL/active

layer interface states induced-recombination losses, facilitating carrier collection. This work unveils the device physics which is fundamentally important for the design and development of better stable and efficient TPSCs.

References

1. Tang, Ching W. "Two-layer organic photovoltaic cell." Applied physics letters 48 (1986) 183-185.

2. Yu, Gang, Jun Gao, Jan C. Hummelen, Fred Wudl, and Alan J. Heeger. "Polymer photovoltaic cells: enhanced efficiencies via a network of internal donor-acceptor heterojunctions." Science 270 (1995) 1789-1791.
3. Thompson, Barry C., and Jean MJ Fréchet. "Polymer–fullerene composite solar cells." Angewandte chemie international edition 47 (2008) 58-77.
4. Lu, Heng, Xinjun Xu, and Zhishan Bo. "Perspective of a new trend in organic photovoltaic: ternary blend polymer solar cells." Science China Materials 59 (2016) 444-458.
5. Scharber, Markus Clark, and Niyazi Serdar Sariciftci. "Efficiency of bulk-heterojunction organic solar cells." Progress in polymer science 38 (2013) 1929-1940.
6. Huang, Ye, Edward J. Kramer, Alan J. Heeger, and Guillermo C. Bazan. "Bulk heterojunction solar cells: morphology and performance relationships." Chemical reviews 114 (2014) 7006-7043.

7. Lee, Changyeon, Seungjin Lee, Geon-U. Kim, Wonho Lee, and Bumjoon J. Kim. "Recent advances, design guidelines, and prospects of all-polymer solar cells." Chemical reviews 119 (2019) 8028-8086.

8. Foster, Samuel, Florent Deledalle, Akiko Mitani, Toshio Kimura, Ki-Beom Kim, Takayuki Okachi, Thomas Kirchartz et al. "Electron collection as a limit to polymer: PCBM solar cell efficiency: Effect of blend microstructure on carrier mobility and device performance in PTB7: PCBM." Advanced energy materials 4 (2014) 1400311.

9. Liu, Yu, Benlin He, Jialong Duan, Yuanyuan Zhao, Yang Ding, Mixue Tang, Haiyan Chen, and Qunwei Tang. "Poly (3-hexylthiophene)/zinc phthalocyanine composites for advanced interface engineering of 10.03%-efficiency CsPbBr 3 perovskite solar cells." Journal of Materials Chemistry A 7 (2019) 12635-12644.

10. Sung, Sae Jin, Jae Ho Kim, Se Hoon Gihm, Jisoo Park, Young Shik Cho, Seung Jae Yang, and Chong Rae Park. "Revisiting the Role of Graphene Quantum Dots in Ternary Organic Solar Cells: Insights into the Nanostructure Reconstruction and Effective Förster Resonance Energy Transfer." ACS Applied Energy Materials 2 (2019) 8826-8835.

11. Wang, Hanyu, Jiang Huang, Shen Xing, and Junsheng Yu. "Improved mobility and lifetime of carrier for highly efficient ternary polymer solar cells based on TIPS-pentacene in PTB7: $PC_{71}BM$." Organic Electronics 28 (2016) 11-19.

12. Hilal, Muhammad, and Jeong In Han. "Significant improvement in the photovoltaic stability of bulk heterojunction organic solar cells by the molecular level interaction of graphene oxide with a PEDOT: PSS composite hole transport layer." Solar Energy 167 (2018) 24-34.

CHAPTER 7

PHOTOVOLTAIC PERFORMANCE OF (D_1:A_1:A_2) -[PTB7-th:PCBM:F-rGO] TERNARY SOLAR CELLS

7.1 Introduction

In the past few years, research on 2D materials such as graphene oxide (GO) and reduced-graphene oxide (rGO) have been intensely growing as hole transport layer (HTL) exclusively for high-performance organic photovoltaics (OPV), owing to their extraordinary carrier transporting abilities, high conductivity, excellent chemical and thermal stability, and a well-matched work function [1-4]. On the other hand, several groups have reported that GO/rGO can significantly improve the efficiency and stability of PSCs when incorporated in BHJ as a ternary acceptor additive [5-9] by inducing balanced hole and electron mobilities, increased charge dissociation ability via energy level alignment, and decreased recombination via effective interface modification. Recently, the versatile functionalization of graphene has demonstrated the controllability of the electronic properties of graphene which enable to achieve high performance PSCs, and leads to the widespread use as HTL as well as ternary additive in the active layer of PSCs [9-13]. Tunable open circuit voltage is also one of the added advantage of these graphene based acceptor additives. Various functionalized derivatives of graphene are reported till now such as GO functionalized with butyl amine [14], nitrogen [11], chlorine [15], fluorine [16-18] atoms etc, have been demonstrated as the most promising interfacial material which has lead to the achievement of enhanced performances of OPVs. Among all these, mainly the fluorinated graphene has shown significant improvement rendering most proficient hole transporting properties because fluorine could successfully modify electronic and chemical properties of graphene [16-19]. Besides, fluorinated graphene show many excellent properties such as wide band gap of 3.1eV, high conductivity, good thermal stability below 400 ^{o}C, and high hydrophobicity

[20,21]. Considering these properties highly beneficial, several groups have utilized fluorinated graphene and demonstrated the Maximum PCE ~7-8% in PSCs [22].

Above reports have sufficiently revealed the application of F-rGO as efficient HTL for enhancing the performance the OPV devices [9-12]. However it is noteworthy that the feasible use of F-rGO in the active layer ternary additive has not yet been explored and addressed so far. In this chapter, we successfully demonstrated the use of novel solution-processable F-rGO, as an electron acceptor ternary additive in the active layer donor-acceptor blend of PTB7-th:PCBM BHJs, opening up a new avenue for the improvement of device performance. It was established that PTB7-th:PCBM:F-rGO ternary blend based PSCs (with 5 wt.% of F-rGO) exhibited an enhanced PCE ~ 7.36%. There is an significant enhancement of 107% in the ternary solar cell compared with the binary reference cell based on PTB7-th:PCBM without F-rGO. Results revealed that F-rGO nanosheets simultaneously enhance the charge transfer from the donor (PTB7-th) to acceptor (PCBM), facilitate the exciton dissociation after charge transfer, and also promote the charge transport though the active layer ternary blended films.

7.2 Results and Discussion

The F-rGO nanosheets are dispersed within polymer PTB7-th matrix as the electron acceptor in polymer solar cells in different weight percentages. Subsequently, ternary blend of PTB7-th:PCBM:F-rGO was optimized for active layer with improved photovoltaic properties. In-depth morphology, charge carrier dynamics and charge transport properties of PTB7-th:PCBM:F-rGO ternary blends were examined and compared with that of constituent binary bland based solar cell.

7.2.1 Photo-excited carrier dynamics of ternary blend

In view of above, firstly, F-rGO nanosheets were incorporated in PTB7-th in increasing weight percentages i.e., 2 wt.%, 5 wt.%, and 10 wt.%, and corresponding steady-state Photoluminescence(PL) were investigated (as shown in Fig. 7.1 (a)). It is evident that [PTB7-th:F-rGO] with 5 wt % shows maximum PL quenching of π^*-π transition peak of PTB7-th (~744nm). It is also shown that when PCBM is mixed in

[PTB7-th:F-rGO(5wt%)], PL gets further more quenched drastically making it ideally suited for solar cell application.

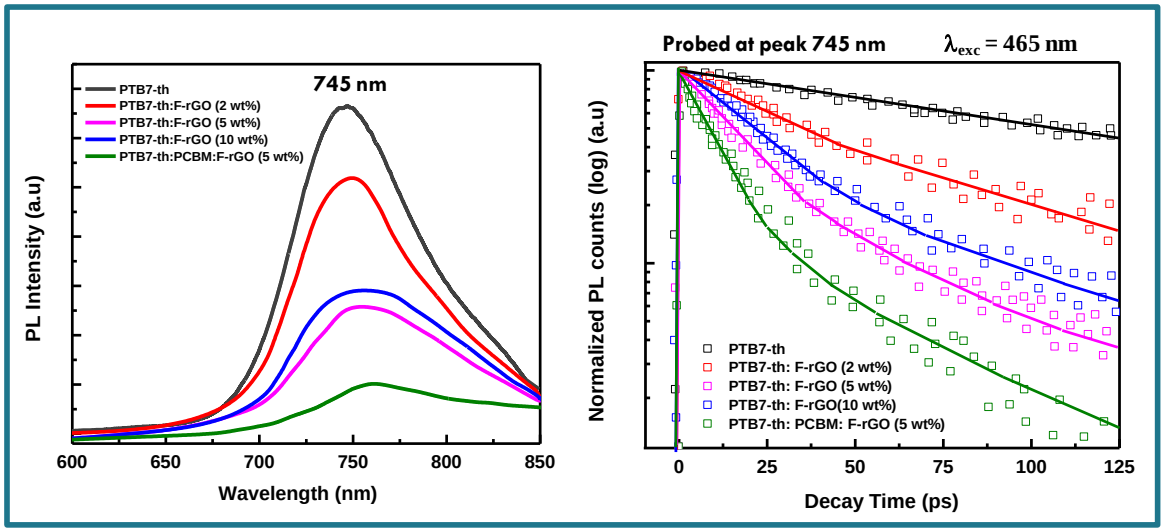

Figure 7.1 (*a) Steady state PL spectra of PTB7-th films without and with incorporation of F-rGO nanosheets in different composition at the excitation wavelength of 465 nm. PL emission quenching is observed with increasing wt. % of F-rGO in PTB7-th. (b) The TRPL curves for PTB7-th blends without and with addition of F-rGO nanosheets in different composition (without and with acceptor PCBM). Fitting of PL decay curve is shown by solid lines using bi-exponential and decay equation where τ represents is the photon-exciton life time and the χ2 value is found to be ~1.1 in the numerical fitting parameter.*

Furthermore, to probe into the photo-excited carrier dynamics in the respective blend samples, we recorded the time-resolved PL spectra of PTB7-th, and PTB7-th:F-rGO without and with PCBM, represented in Fig. 7.1 (b), at excitation wavelength ~465 nm. The PL decay profiles were fitted with well-known bi-exponential and tri-exponential decay equation reported elsewhere [ref.] as,

$$I = A_1 e^{-\left(\frac{t}{\tau_1}\right)} + A_2 e^{-\left(\frac{t}{\tau_2}\right)} + A_3 e^{-\left(\frac{t}{\tau_3}\right)}$$

where, τ_1, τ_2, and τ_3 represent the PL decay time assigned to faster non-radiative recombination time, medium radiative recombination time, and slowest radiative recombination time owing to recombination from interface surface states/traps, respectively. A_1, A_2, and A_3 are the respective amplitude constants. The PL decay profiles

of pure PTB7-th, and PTB7-th:F-rGO blends fit reasonably well with a bi-exponential decay function. However, PL decay of the ternary blend [PTB7-th:PCBM:F-rGO] fit with tri-exponential decay function. The corresponding lifetimes τ_1, τ_2, τ_3, and τ_{avg} (average lifetime) and amplitude components are listed/summarized in Table 7.1.

Table 7.1. *PL decay lifetime obtained for different active layer blend combinations on adding F-rGO in different weight percentages.*

Active layer blends	**A_1**	**τ_1 (ps)**	**A_2**	**τ_2 (ps)**	**A_3**	**τ_3 (ps)**	**τ_{avg} (ps)**
PTB7-th	0.10	101	0.90	431			398
PTB7-th: F-rGO (2 wt. %)	0.37	87	0.63	379			271
PTB7-th: F-rGO (5 wt. %)	0.68	52	0.32	275			123
PTB7-th: F-rGO (10 wt. %)	0.54	61	0.46	288			165
PTB7-th: PCBM: F-rGO (5 wt. %)	0.77	29	0.14	96	0.09	117	46

The faster non-radiative component τ_1 dominate the PL decay. It reduces from τ_1= 129 ps in PTB7-th polymer to τ_1 = 87 ps when F-rGO is added into the polymer in 2 wt. %, and further decreased to τ_1 = 52 ps when F-rGO is in 5 wt. %, indicating that the photogenerated excitons are transferred to the acceptor more promptly in the later. However, when the F-rGO concentration is increased to 10 wt. %, τ_1 increases to 61 ps ascertain relatively more contribution due to radiative recombination (τ_2 = 560 ps) within the F-rGO induced surface states interfaces and the existing traps within the bulk polymer. Further, when PCBM is added in the PTB7-th:F-rGO (5 wt.%) blend to make ternary blend, the recombination life time drastically drops down to 29 ps, which is an evidence that the charge transfer at the donor-acceptor interface has been initiated leading effective PL quenching, Hence, [PTB7-th:PCBM:F-rGO (5 wt. %)] ternary blend is more favorable for photovoltaics devices.

7.2.2 Photovoltaic performance

[PTB7-th:PCBM:F-rGO (5 wt. %)] ternary blend solar cell devices were fabricated in device configuration,

Binary Solar Cells:

Device 1 : *ITO/ PEDOT:PSS(~40 nm)/ PTB7-th:PCBM:F-rGO (5 wt. %) (~180 nm) / LiF/ Al]*

Ternary Solar Cells:

Device 2 : *ITO(ϕ ~4.8 eV) / PEDOT:PSS (~40 nm)/ PTB7-th:PCBM (~180 nm) / LiF/ Al (ϕ ~4.3 eV)]*

The *J-V* characteristics of Device 1 and Device 2 under Air Mass 1.5 Solar illumination are presented in Fig. 7.2 (a), and the device parameters are summarized in Table 7.2. Here, it is evident that on incorporation of F-rGO nanosheets in PTB7-th:PCBM, significantly enhance the J_{SC} from 9.6 mA/cm^2 to 12.1 mA/cm^2, V_{OC} from 0.71 V to 0.77 V, and *FF* from 0.58 to 0.79.

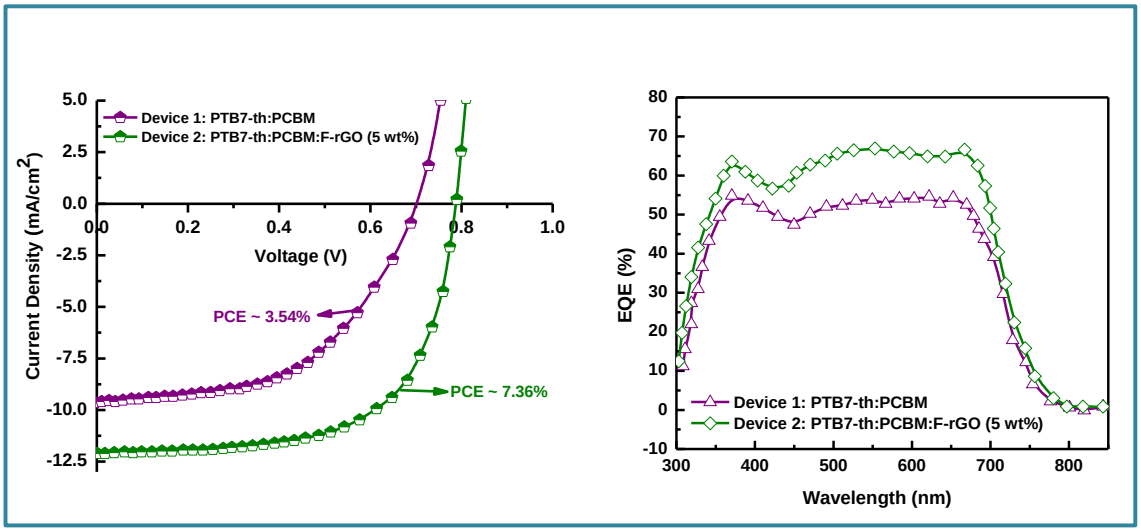

Figure 7.2 *(a) J-V characteristics of TPSC (Device 1) : ITO/ PEDOT:PSS/ PTB7-th:PCBM (1:1)/ LiF/Al, and Device 2:ITO/ PEDOT:PSS/ PTB7-th:PCBM:F-rGO (5wt. %)/ LiF/Al, under Air Mass 1.5 Solar illumination (P_{in} =100 mW/cm^2). (b) Comparison of EQE spectra of Device 1 and Device 2.*

Table 7.2. Photovoltaic device parameters obtained for Device 1 and Device 2.

	J_{sc} (mA/cm^2)	V_{oc} (V)	FF	PCE (%)	R_s (Ω cm^2)	R_{sh} (Ω cm^2)
Device 1 (with PTB7-th:PCBM)	9.6	0.71	0.58	3.54	31	2307
Device 2 [with PTB7-th:PCBM:F-rGO (5wt%)]	12.1	0.77	0.79	7.36	14	3971

In order to understand the exact effect of F-rGO nanosheets on the photovoltaic performances, we examined the hole mobilities in pure PTB7-th without and with addition of F-rGO nanosheets, in hole-only device configuration, ITO/ PEDOT:PSS/ polymer/ Au, and The *J-V* characteristics of electron-only devices in the dark for $PC_{71}BM$ (Al/ $PC_{71}BM$/Al) is presented in Fig. 7.3 (a) and (b), respectively. The *J-V* characteristics are measured at room temperature (~288K).

7.2.3 Charge Transport mechanism in ternary blend

In order to understand the exact effect of F-rGO nanosheets on the photovoltaic performances, we examined the hole mobilities in pure PTB7-th without and with addition of F-rGO nanosheets, in hole-only device configuration, ITO/ PEDOT:PSS/ polymer/ Au, and The *J-V* characteristics of electron-only devices in the dark for $PC_{71}BM$ (Al/ $PC_{71}BM$/Al) is presented in Fig. 7.3 (a) and (b), respectively. The *J-V* characteristics are measured at room temperature (~288K).

Earlier studies in organic materials have suggested that the charge transport is governed by strong power-law dependence, $J \sim V^m$ in dark. Based on exponent *m* of *J-V* curve, transport could either be trap-free ($m = 2$) of trap-limited transport($m > 2$) **[23].** Assuming $P_i < P_o$, charge transport follows Mott-Gurney law **[22-25],**

$$J = \frac{9}{8}\varepsilon_0\varepsilon_r\mu\frac{V^2}{d^3}$$

where, J is the current density, V is applied voltage, ε_o is the permittivity of free space, ε_r is the relative permittivity of the materials, μ is the carrier mobility, d is the film thickness.

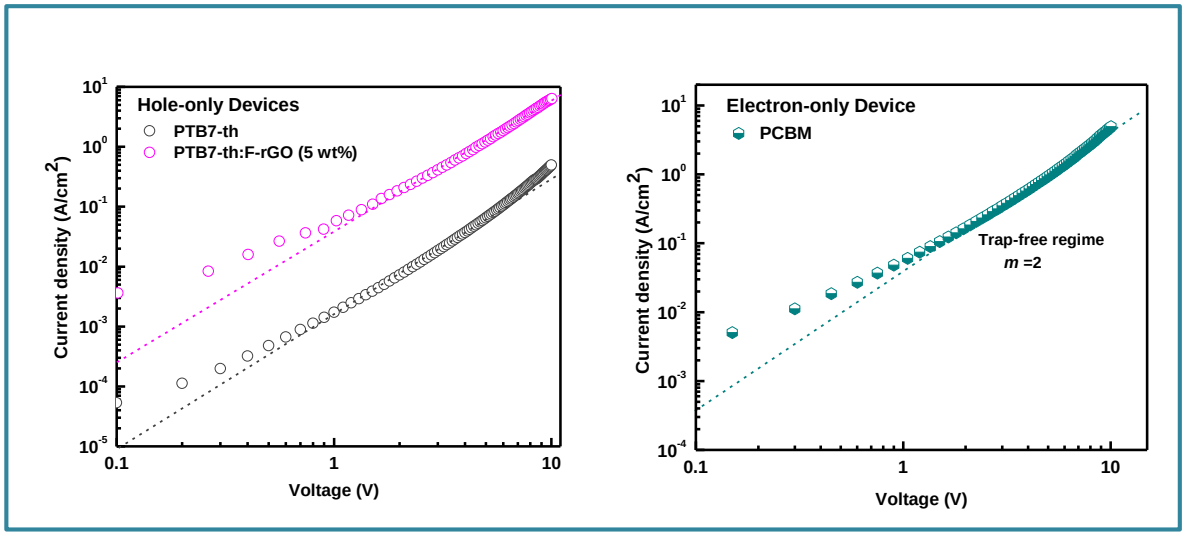

Figure 7.3 *(a) J-V characteristics in the dark for PTB7-th, and PTB7-th:F-rGO (5wt.%) in hole-only device configuration, ITO/ PEDOT:PSS/ polymer/ Au, (b) J-V characteristics of electron-only devices in the dark for $PC_{71}BM$, Al/ $PC_{71}BM$/Al. The measurements are taken at room temperature (288 K).*

In Fig. 7.3 (a), the *J-V* characteristic of PTB7-th film and of PTB7-th:F-rGO (5wt.%) blend film show m = 2 regime at high electric fields indicating a trap-free transport of holes in both the films. The experimental curves are fitted with the theoretical curves generated by Eq. (2) (Mott-Gurney Child's law), result in μ_h=8×10^{-4} cm^{2}V^{-1}s^{-1} in PTB7-th films (using ε_r=3.5 and d=180 nm), and μ_h=7×10^{-3} cm^{2}V^{-1}s^{-1} in PTB7-th:F-rGO (5wt.%) blend films (using ε_r=3.5 and d=180 nm). Importantly, there is a remarkable increase in hole mobility from 8×10^{-4} cm^{2}V^{-1}s^{-1} to 7×10^{-3} cm^{2}V^{-1}s^{-1} without and with incorporation of F-rGO nanosheets in PTB7-th films. The hole trap density N_t is calculated by the equation [49],

$$V_{TFL} = \frac{qN_t d^2}{2\varepsilon_0 \varepsilon_r}$$

where V_{TFL} is the trap-filled limit voltage, q is the elementary, charge of an electron, d is the thickness of the film, ε_r is the dielectric constant of the material, ε_o is the permittivity

of the free space. The calculated N_t for PTB7-th, PTB7-th:F-rGO films is 0.91×10^{17} cm^{-3} and 0.15×10^{17} cm^{-3}, respectively. On the other hand, the *J-V* characteristic of $PC_{71}BM$ thin film in the electron-only device configuration shown in Fig. 7.3 (b), also show trap-free electron transport due to m = 2 at high electric fields. The fitting with Mott-Gurney Child's law as Eq. (2), yield electron mobility, $\mu_e=2\times10^{-3}$ $cm^2V^{-1}s^{-1}$ obtained by using $\varepsilon_r=4$ and $d=180$ nm. From the V_{TFL} = 8.1V, $N_t = 1.08\times10^{17}$ cm^{-3} is derived. The decrease in trap density is supported by the improved morphology with low surface roughness (RMS) ~0.71 obtained in PTB7-th:PCBM:F-rGO (5 wt.%) films as compared to ~ 2.1nm obtained in PTB7-th:PCBM films, as revealed in AFM images of these respective films (refer Fig. 7.4). Hence, hole mobility get enhanced in PTB7-th:F-rGO compared to pure PTB7-th.

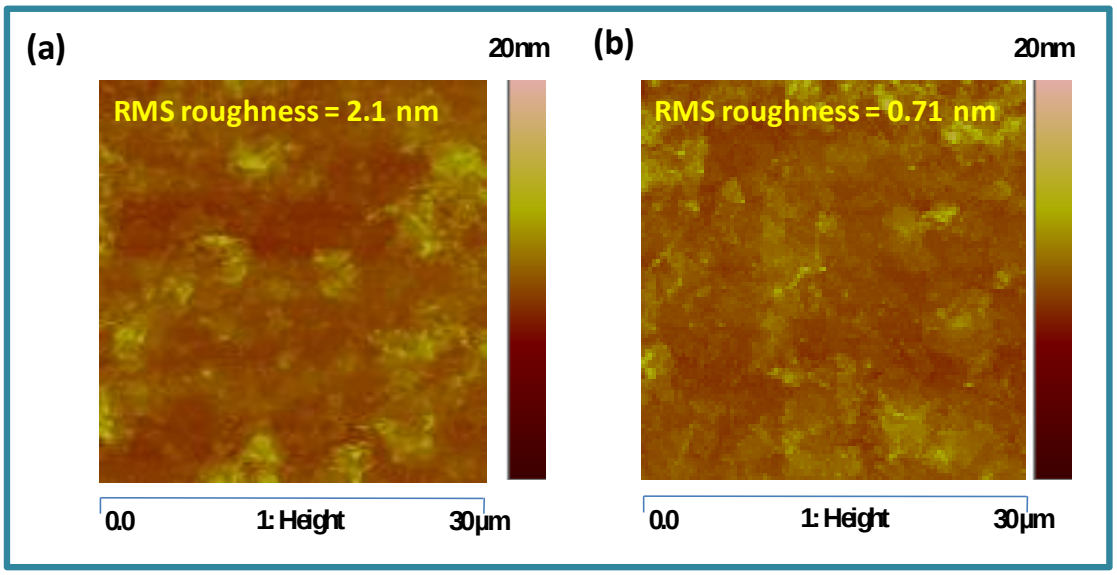

Figure 7.4 *AFM of (a) PTB7-th:PCBM binary blend (b) PTB7-th:PCBM:F-rGO (5 wt. %) ternary blend.*

It is noteworthy that a balanced hole and electron mobilities (μ_e/μ_h =0.28) have been achieved in PTB7-th:PCBM:F-rGO (5 wt. %) ternary blend as compared to (μ_e/μ_h =2.5) PTB7-th:PCBM binary blend. Hence, the charge transport is facilitated in the ternary blend which is governed by the trap-free limited current with weak bimolecular recombination. Better charge transport and markedly improved film morphology in turn

supports the enhancement in J_{sc} and decreases R_s observed in TOSC device 2. In addition, the energy level alignment of PTB7-th:PCBM:F-rGO ternary blend, as shown in Fig. 7.5, reveal that the incorporation of F-rGO in PTB7-th:PCBM promote the exciton dissociation owing to high work function (ϕ ~5.1 eV) [16,20] (i.e., high accepting properties of F-rGO nanosheets due to available C-F high polar bonds) leading to increase in J_{SC} obtained in case of F-rGO based ternary blend devices compared to binary blend devices.

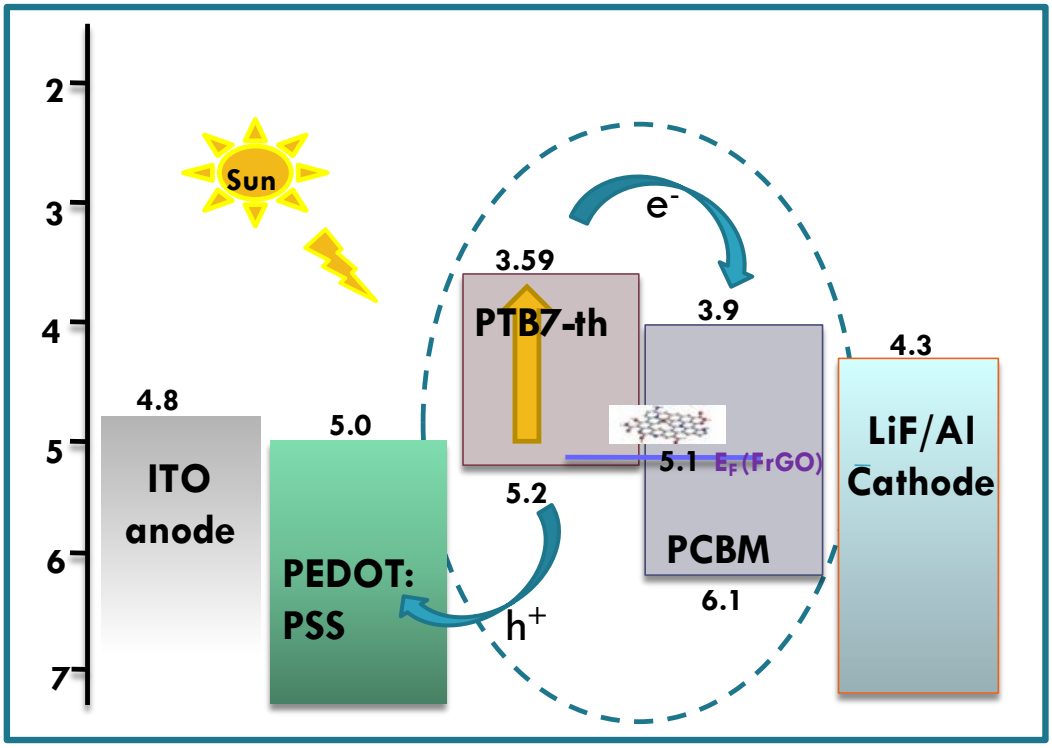

Figure 7.5 *The Energy level alignment of (PTB7-th:PCBM:F-rGO) TPSC.*

7.3 Conclusion

In conclusion, we report high-performance TOSC by blending the F-rGO nanosheets in PTB7-th: $PC_{71}BM$ bulk-heterojunction binary blend. The optimized device based on PTB7-th:PCBM:F-rGO with 5wt% F-rGO, achieved a higher PCE of 7.36 % with an open-circuit voltage (V_{OC}) of 0.77V, a short-circuit current density (J_{SC}) of 12.1 mA/cm^2 and a fill factor (*FF*) of 79%. The enhancement in PCE compared to the

reference binary blend PTB7-th:PCBM cell (~3.54%) attributed to, (i) F-rGO induced enhanced exciton dissociation at F-rGO/PTB7-th interfaces owing to high work function and electron accepting property (p-type doing effect) resulting in better carrier generation, (ii) enhanced charge transport from donor to acceptor via balance electron and hole mobility and availability of more efficient exciton dissociation pathways throughout the active layer blend, over all resulting in high charge extraction time, and (iii) good morphology of PTB7-th:PCBM:F-rGO ternary blend resulting in suppressed carrier recombination rates. Hence, the work demonstrate F-rGO as a promising acceptor ternary additive for realizing efficient TOSCs.

.

References

1. Das Sonali, Deepak Pandey, Jayan Thomas, and Tania Roy. "The role of graphene and other 2D materials in solar photovoltaics." Advanced Materials 31 (2019) 1802722.
2. Mahmoudi Tahmineh, Yousheng Wang, and Yoon-Bong Hahn. "Graphene and its derivatives for solar cells application." Nano Energy 47 (2018) 51-65.
3. Singh Eric, and Hari Singh Nalwa. "Stability of graphene-based heterojunction solar cells." Rsc Advances 5 (2015) 73575-73600.
4. Díez-Pascual Ana Maria, José Antonio Luceño Sánchez, Rafael Peña Capilla, and Pilar García Díaz. "Recent developments in graphene/polymer nanocomposites for application in polymer solar cells." Polymers 10 (2018) 217.
5. Gao Yan, Hin-Lap Yip, Kung-Shih Chen, Kevin M. O'Malley, Orb Acton, Ying Sun, Guy Ting, Hongzheng Chen, and Alex K-Y. Jen. "Surface doping of conjugated polymers by graphene oxide and its application for organic electronic devices." Advanced Materials 23 (2011) 1903-1908.
6. Chauhan A. K., Abhay Gusain, P. Jha, S. P. Koiry, Vibha Saxena, P. Veerender, D. K. Aswal, and S. K. Gupta. "Graphene composite for improvement in the conversion efficiency of flexible poly 3-hexyl-thiophene:[6, 6]-phenyl C71 butyric acid methyl ester polymer solar cells." Applied Physics Letters 104 (2014) 133901.

7. Robaeys Pieter, Francesco Bonaccorso, Emilie Bourgeois, Jan D'Haen, Wouter Dierckx, Wim Dexters, Donato Spoltore et al. "Enhanced performance of polymer: fullerene bulk heterojunction solar cells upon graphene addition." Applied Physics Letters 105 (2014) 083306.
8. Stylianakis Minas M., Dimitrios M. Kosmidis, Katerina Anagnostou, Christos Polyzoidis, Miron Krassas, George Kenanakis, George Viskadouros, Nikolaos Kornilios, Konstantinos Petridis, and Emmanuel Kymakis. "Emphasizing the operational role of a novel graphene-based ink into high performance ternary organic solar cells." Nanomaterials 10 (2020) 89.
9. Lyu Cheng-Kun, Fei Zheng, B. Hari Babu, Meng-Si Niu, Lin Feng, Jun-Liang Yang, Wei Qin, and Xiao-Tao Hao. "Functionalized graphene oxide enables a high-performance bulk heterojunction organic solar cell with a thick active layer." The journal of physical chemistry letters 9 (2018) 6238-6248.
10. Liu Qian, Zunfeng Liu, Xiaoyan Zhang, Nan Zhang, Liying Yang, Shougen Yin, and Yongsheng Chen. "Organic photovoltaic cells based on an acceptor of soluble graphene." Applied Physics Letters 92 (2008) 195.
11. Jung Seungon, Junghyun Lee, Jihyung Seo, Ungsoo Kim, Yunseong Choi, and Hyesung Park. "Development of annealing-free, solution-processable inverted organic solar cells with n-doped graphene electrodes using zinc oxide nanoparticles." Nano letters 18 (2018) 1337-1343.
12. Zheng Fei, Xiao-Yu Yang, Peng-Qing Bi, Meng-Si Niu, Cheng-Kun Lv, Lin Feng, Wei Qin, Yu-Zhu Wang, Xiao-Tao Hao, and Kenneth P. Ghiggino. "Poly (3-hexylthiophene) coated graphene oxide for improved performance of bulk heterojunction polymer solar cells." Organic Electronics 44 (2017) 149-158.
13. Wang Jigang, Yongsheng Wang, Dawei He, Zhiyong Liu, Hongpeng Wu, Haiteng Wang, Pan Zhou, and Ming Fu. "Polymer bulk heterojunction photovoltaic devices based on complex donors and solution-processable functionalized graphene oxide." Solar Energy Materials and Solar Cells 96 (2012) 58-65.
14. Valentini, Luca, Marta Cardinali, Silvia Bittolo Bon, Diego Bagnis, Raquel Verdejo, Miguel Angel Lopez-Manchado, and Josè M. Kenny. "Use of

butylamine modified graphene sheets in polymer solar cells." Journal of Materials Chemistry 20 (2010) 995-1000.

15. Yang Dong, Lingyu Zhou, Wei Yu, Jian Zhang, and Can Li. "Work-Function-Tunable Chlorinated Graphene Oxide as an Anode Interface Layer in High-Efficiency Polymer Solar Cells." Advanced Energy Materials 4 (2014) 1400591.
16. Kim Su-Hyeon, Cheol-Ho Lee, Jin-Mun Yun, Yong-Jin Noh, Seok-Soon Kim, Sungho Lee, Seung Mu Jo, Han-Ik Joh, and Seok-In Na. "Fluorine-functionalized and simultaneously reduced graphene oxide as a novel hole transporting layer for highly efficient and stable organic photovoltaic cells." Nanoscale 6 (2014) 7183-7187.
17. Cheng Xiaofang, Juan Long, Rui Wu, Liqiang Huang, Licheng Tan, Lie Chen, and Yiwang Chen. "Fluorinated reduced graphene oxide as an efficient hole-transport layer for efficient and stable polymer solar cells." ACS omega 2 (2017) 2010-2016.
18. Yu Youn-Yeol, Byung Hyun Kang, Yang Doo Lee, Sang Bin Lee, and Byeong-Kwon Ju. "Effect of fluorine plasma treatment with chemically reduced graphene oxide thin films as hole transport layer in organic solar cells." Applied Surface Science 287 (2013) 91-96.
19. Nicasio-Collazo Juan, Jose-Luis Maldonado, Julio Salinas-Cruz, Denisse Barreiro-Argüelles, Irving Caballero-Quintana, Carlos Vazquez-Espinosa, and Daniel Romero-Borja. "Functionalized and reduced graphene oxide as hole transport layer and for use in ternary organic solar cell." Optical Materials 98 (2019) 109434.
20. Kim Yeon Hoo, Ji Soo Park, You-Rim Choi, Seo Yun Park, Seon Yong Lee, Woonbae Sohn, Young-Seok Shim et al. "Chemically fluorinated graphene oxide for room temperature ammonia detection at ppb levels." Journal of Materials Chemistry A 5 (2017) 19116-19125.

21. Feng Wei, Peng Long, Yiyu Feng, and Yu Li. "Two-dimensional fluorinated graphene: synthesis, structures, properties and applications." Advanced Science 3 (2016) 1500413.
22. Stylianakis Minas M., Dimitrios Konios, Constantinos Petridis, George Kakavelakis, Emmanuel Stratakis, and Emmanuel Kymakis. "Ternary solution-processed organic solar cells incorporating 2D materials." 2D Materials 4 (2017) 042005.
23. Han, Joong Tark, Beom Joon Kim, Bo Gyeong Kim, Jun Suk Kim, Bo Hwa Jeong, Seung Yol Jeong, Hee Jin Jeong, Jeong Ho Cho, and Geon-Woong Lee. "Enhanced electrical properties of reduced graphene oxide multilayer films by in-situ insertion of a TiO2 layer." ACS nano 5 (2011) 8884-8891.
24. Yu Jae Choul, Jeong In Jang, Bo Ram Lee, Geon-Woong Lee, Joong Tark Han, and Myoung Hoon Song. "Highly efficient polymer-based optoelectronic devices using PEDOT: PSS and a GO composite layer as a hole transport layer." ACS applied materials & interfaces 6 (2014) 2067-2073.
25. Guguloth Lalsingh, Kuldeep Singh, VS Reddy Channu, and Kusum Kumari. "Enhancement in performance of ternary blend-polymer solar cells using a PEDOT: PSS–graphene oxide hole transport layer via Förster resonance energy transfer and balanced charge transport." Materials Advances 1 (2020) 2872-2887.

CHAPTER 8

SUMMARY, CONCLUSIONS AND SCOPE FOR FUTURE WORK

This chapter presents the summary and the conclusion drawn from the investigations carried out in the present thesis on the study of photophysics, charge carrier dynamics, and device stability of the ternary blend based solar cells (TPSCs). The scope for future work is also discussed in this chapter.

8.1 Summary

The present thesis work explores the fundamental device physics of ternary blends which is the bottleneck and crucial for the design and development of TPSCs.

The brief summary of the thesis work is as follows:

1. (P3HT:PTB7-th:PCBM)Ternary Blends have been optimized for solar cell applications. (P3HT:PTB7-th:PCBM) (0.3:0.7:1) composition offer good photovoltaic properties and hence showed potential to use as active layer.
2. GO and F-rGO nanosheets have been successfully utilized for improving the properties of HTL and active layer, respectively.
3. PEDOT:PSS-GO(1:1) composite provides beneficial hole transport properties over PEDOT:PSS. Hence, it is an potential alternative HTL.
4. Ternary solar cells composed of (P3HT:PTB7-th:PCBM) (0.3:0.7:1) ternary blends, and PEDOT:PSS-GO(1:1) HTL have showed the best and enhanced performance (PSC ~7.1%) and stability~only10% loss after 500 hours) compared to other binary blend and other HTLs based devices.
5. The utilization of F-rGO as the electron acceptor material in PTB7-th:PCBM bulk heterojunction photovoltaic devices has been demonstrated, yielding in a PCE enhancement (~7.36%) compared to PTB7-th:PCBM (~3.54%) based devices with good device stability.

8.2 Conclusions

The conclusions derived from the present work based on exploring the utilization of carbon 2D materials for improving the performance of (D_1:D_2:A)/ (D:A_1:A_2) type of TPSCs; and the studies related to photophysics and charge carrier dynamics of the ternary blend and photovoltaic performance of TPSCs, are given below:

- The synthesized GO and FGO sample characterized by FESEM, TEM, AFM, revealing the size of nanosheets 5-10μm, and thickness of one single sheet ~1.1nm indicating the availability of two or three layers.
- XRD, Raman, and FTIR revealed the (001) main graphitic peak, D and G bands(1340 and 1605 cm^{-1}) and all the oxygenated functional groups present on the basal plane of the graphene sheet, respectively, which is consistent with the previous reports.
- The chemical composition of the GO sample was investigated by XPS where the peaks at binding energy values of 284.60 eV and 532.57 eV are assigned to C 1s and O 1s, respectively. Hence, XPS confirmed that the chemical structure of GO consists of chemical functional groups such as carboxyl, hydroxyl, and epoxy groups along with main C–C (sp^2 and sp^3) bond.
- Further, PEDOT:PSS-GO composite films were deposited by dispersing GO in PEDOT:PSS in different weight ratios i.e., (2:1), (1:1), and (1:2). Surface morphology of these PEDOT:PSS-GO composite thin films revealed by FESEM images and AFM images, the low surface roughness (RMS) = 1.21 nm obtained in (1:1) weight ratio signify that GO is dispersed homogeneously in PEDOT:PSS after acheiving good steric stabilization in the matrix.
- Also, it is found that the dispersion of GO is in PEDOT:PSS not only lowers the sheet resistance but also increases the conductivity significantly because of the available conducting paths provided by GO nanosheets. Henceforth, the conductivity raises from 16.9 $x10^{-3}$ S/cm for PEDOT:PSS-GO (2:1) to 32.2 $x10^{-3}$ S/cm for PEDOT:PSS-GO (1:1) film, and which subsequently reduces to 26 $x10^{-3}$ S/cm in PEDOT:PSS-GO (1:2) film i.e., on a further increase of GO concentration in PEDOT:PSS. Finally, it is concluded that the PEDOT:PSS-GO with (1:1) weight ratio shows the lowest sheet resistance and enhanced electrical conductivity.

- The transmittance of PEDOT:PSS-GO films [all three different ratios i.e., (2:1), (1:1), and (1:2)] ~ 88-90% at wavelength 550 nm, which is relatively higher compared to the transmittance shown by its two individual components is GO (89%) and PEDOT:PSS (84%).
- From, UPS measurements, the work function on incorporation GO in PEDOT:PSS increased to 4.9 eV [PEDOT:PSS-GO (2:1) composite], 5.0 eV [PEDOT:PSS-GO (1:1) composite], and 4.88 eV [PEDOT:PSS-GO (1:2) composite], compared to 4.23 eV obtained for pristine GO and 4.8 eV calculated for pure PEDOT:PSS. Here, the increase of work function of PEDOT:PSS-GO is a consequence of the benzoid-quinoid transition of PEDOT:PSS originating by the addition of GO in PEDOT:PSS.
- It is concluded that PEDOT:PSS-GO(1:1) is the optimum composition as it shows good film morphology, enhanced conductivity, and highest HOMO level (E_{HOMO} = 5.22 eV). Therefore, PEDOT:PSS-GO(1:1) is considered as a potential HTL alternative to PEDOT:PSS, and more ideally suited for effective HTLs in solar cell devices.
- The absorption spectra confirmed that all three P3HT:PTB7-th films (in three different weight propositions i.e., (0.7:0.3), (0.5:0.5) and (0.3:0.7) weight ratios) exhibit strong and complementary absorption covering a wider wavelength range from 500-750nm. This widening of the absorption window is due to the contribution of both P3HT in 480-640nm, and PTB7-th in 650-750nm region of the solar spectrum. Evidently, P3HT:PTB7-th with (0.3:0.7) weight ratio displays more stronger and wider coverage in the entire solar light spectrum as compared to the other two compositions.
- Further, the recorded PL characteristics of pure P3HT, PTB7-th, and P3HT:PTB7-th mixed blends, show sensitized emission leading to an additional peak at 747nm compared (due to the incorporation of PTB7-th) to the quenching of regular PL emission at 650nm due to P3HT component. Both this PL quenching (in P3HT) and sensitized emission (towards PTB7-th) are due to dominating energy transfer as well as electron transfer processes from P3HT (D_1) to PTB7-th (D_2).
- It is found that the absorption edge of PTB7-th is lying exactly at the PLpeak of P3HT, satisfies the criterion for Förster resonance energy transfer (FRET)

occurrence. This confirms that FRET is taking place from one donor i.e., P3HT to the other donor i.e., PTB7-th [26, 27]. The parameter which is important in any FRET process is the Forster radius (R_0) which reveals the distance for 50% of FRET efficiency, is calculated as ~5.7 nm. Further, when the PCBM acceptor is blended with the donor:donor P3HT:PTB7-th (0.3:0.7) composite, PL at both the characteristic peaks of P3HT (650nm) and PTB7-th (747nm) gets completely quenched. This PL quenching due to non-radiative exciton de-excitation confirms markedly enhanced charge transfer at the donor-acceptor, i.e., P3HT/PCBM and PTB7-th /PCBM interfaces due to providing the energy cascade structure leading to efficient exciton dissociation.

- The TRPL studies demonstrated the reduction in photo-exciton lifetime drastically from τ_1 = 129ps (*in P3HT)* and τ_1 = 17ps (*in P3HT:PTB7-th:PCBM*), which signify that both FRET and cascade energy level alignment charge transfer dominated mechanisms lead to effective exciton dissociation in the ternary blend. Hence, it is concluded that P3HT:PTB7-th:PCBM (0.3:0.7:1) is the optimized blend combination for solar cell application.
- A remarkable enhancement in PCE of [P3HT:PTB7-th:PCBM] (0.3:0.7:1) ternary blend based solar cells (TSC) from 3.2% to 7.1% without and with the addition of GO nanosheets in PEDOT:PSS HTL has been achieved. Such an enhancement in PCE of TPSC devices when PEDOT:PSS-GO (1:1) composite is used as HTL is attributed to the fact that the dispersion of GO nanosheets in PEDOT:PSS HTL, (i) reduced HTL/active layer interface barrier via tuning the work function making it perfectly matched with the highest occupied molecular orbital (HOMO) of the donor polymer, (ii) enhanced σ of HTL films, and (iii) improved morphology of PEDOT:PSS-GO films owing to low RMS surface roughness enabling the trap-free carrier transport, (iv) better electron blocking capability of PEDOT:PSS-GO, promoting the carrier collection at the anode without interface-state recombination at the HTL/active layer interface.
- It has also been found that these TSCs showed significant improvement in device stability retaining PCE for 500 hours with only a 10 % loss from its initial value. This is due to good photo-stability of GO which significantly improved the overall

air-stability of PEDOT:PSS-GO composite HTL based TSC devices. Hence, PEDOT:PSS-GO composite offers the most desirable hole transport properties over the conventional PEDOT:PSS-only HTLs. In conclusion, [P3HT:PTB7-th:$PC_{71}BM$] (0.3:0.7:1) ternary blend based TSCs display high performance and good stability when PEDOT:PSS-GO (1:1) is utilized as HTL.

- Furthermore, the J-V characteristics of [P3HT:PTB7-th:PCBM] (0.3:0.7:1) ternary blend based TSCs fabricated is compared with the respective binary devices i.e., P3HT:PCBM and PTB7-th:PCBM binary blends based devices. TPSCs with [P3HT:PTB7-th:PCBM] (0.3:0.7:1) ternary blend showed PCE ~7.1%, which signify that there is an enhancement of 48% and 45% compared to P3HT:$PC_{71}BM$ (PCE ~3.7%) and PTB7-th: $PC_{71}BM$ (PCE ~4%) binary BHJ solar cells. This is primarily due to an increase of short circuit current (Jsc) to 12.3 mA/cm2, open circuit voltage (Voc) to 0.74V, and Fill factor (FF) to 0.78 in case of ternary solar cells.
- We found that the improvement in the performance of the P3HT:PTB7-th:$PC_{71}BM$ (0.3:0.7:1) ternary blend based TPSC devices with PEDOT:PSS-GO (1:1) composite HTL, is attributed to (i) broad spectral coverage of solar light harvesting owing to strong and complementary absorption; (ii) Efficient exciton dissociation into free charge carriers via FRET and CT at the D_1/D_2 and D/A interfaces; (iii) High charge extraction ability at HTL/active layer interface due to well- matched HOMO level of PEDOT:PSS-GO with HOMO of polymer donors; (iv) efficient electron blocking capability of PEDOT:PSS-GO reduces the probability of HTL/active layer interface states induced-recombination losses, facilitating carrier collection.
- It is concluded that the devices with P3HT:PTB7-th:PCBM (0.3:0.7:1) ternary blend showed better stability compared to (P3HT:PCBM) and (PTB7-th:PCBM) binary blend devices, where PCE is retained for 500 hrs with only 10% reduction from its initial value. Hence, [P3HT:PTB7-th:$PC_{71}BM$] (0.3:0.7:1) ternary blend based TPSCs using PEDOT:PSS-GO (1:1) display good performance and stability.
- The optimized device based on PTB7-th:PCBM:F-rGO with 5wt% F-rGO, achieved a higher PCE of 7.36 % with an open-circuit voltage (V_{OC}) of 0.77V, a short-circuit current density (J_{SC}) of 12.1 mA/cm^2 and a fill factor (FF) of 79%.

- The enhancement in PCE compared to the reference binary blend PTB7-th:PCBM cell (~3.54%) attributed to, (i) F-rGO induced enhanced exciton dissociation at F-rGO/PTB7-th interfaces owing to high work function and electron accepting property (p-type doing effect) resulting in better carrier generation, (ii) enhanced charge transport from donor to acceptor via balance electron and hole mobility and availability of more efficient exciton dissociation pathways throughout the active layer blend, over all resulting in high charge extraction time, and (iii) good morphology of PTB7-th:PCBM:F-rGO ternary blend resulting in suppressed carrier recombination rates. Hence, the work demonstrate F-rGO as a promising acceptor ternary additive for realizing efficient TPSCs.

8.3 Scope for Future Work

In the present work some important fundamental and applied facets of *Graphene oxide, binary blend and ternary blend* have been addressed via studying in detail and systematic way their synthesis, structural, optical and photophysics and charge carrier dynamics properties. The knowledge generated through this work would prove beneficial for future researchers in this important and potential area of ternary blend solar cells. Other 2D materials such as WSe_2, MoS_2, $MoSe_2$ etc., along with other polymer donor and acceptors can be explored and utilized in the ternary blend solar cells, and in-depth studies can be carried out. The work revealed the device physics which is fundamentally important for the design and development of better stable and efficient ternary solar cells. More importantly, the in-depth studies carried out in the thesis open a new avenue for the potential commercialization of low-cost and solution-processed TSCs.

LIST OF PUBLICATIONS

Publications in International Journals (SCI):

1. **Lalsingh Guguloth**, Kuldeep Singh, V.S.R. Channu, Kusum Kumari, "Improved performance of ternary blend polymer solar cells via work function tuning and suppressed interface recombination using hybrid PEDOT:PSS-graphene oxide hole transport layer", Applied Surface Science 540 (2021) 148266.
2. **Lalsingh Guguloth**, Kuldeep Singh, V.S.R. Channu, Kusum Kumari, "Enhancement in performance of ternary blend-polymer solar cells using a PEDOT:PSS–graphene oxide hole transport layer via Förster resonance energy transfer and balanced charge transport", Materials Advances 1 (2020) 2872-2887.
3. **Lalsingh Guguloth**, P. V. Shekar, V S Reddy Channu, and Kusum Kumari, "Effect of fluorinated reduced graphene oxide ternary additive component on synergistically boosting the photovoltaic performance of polymer bulk-heterojunction solar cells", Solar Energy 225 (2021) 259-265.

Papers contributed in International Conferences:

1. **Lalsingh Guguloth**, Kuldeep Singh, and Kusum Kumari, and Poster Presentation on " Excited state carrier dynamics of ternary blend polymer solar cells" presented at "International Conference on Advanced Functional materials and Devices [ICAFMD 2019]" organized by Department of Physics, National Institute of Technology Warangal, Telangana, India. During 26^{th} -28^{th} February 2019.
2. **Lalsingh Guguloth**, Kuldeep Singh, and Kusum Kumari, and Poster Presentation on "Polymer Solar Cells using Graphene/Transition Metal Dichalcogenite 2D Materials as Ternary additives " presented at "National Conference on Luminescence & its Applications [NCLA-2020]" is being organized by Department of Physics, National Institute of Technology, Warangal 506004, jointly with Luminescence Society of India, Warangal, Telangana, India, during 10^{th} - 12^{th} February 2020.

3. **Lalsingh Guguloth**, Kuldeep Singh, V S Reddy Channu, Satyendra Singh and Kusum Kumari, and Poster Presentation on "Optical Properties Study of (PEDOT:PSS):Graphene Oxide Nano-composite" presented at "5th International Conference on Emerging Electronics. Hosted by- Indian Institute of Technology Delhi, India. During 26^{th} -28^{th} Nov 2020.
4. **Lalsingh Guguloth**, Kuldeep Singh, V S Reddy Channu, and Kusum Kumari, and Poster Presentation on "Performance of Ternary Blend Polymer Solar Cells using PEDOT:PSS, graphene oxide and reduced graphene oxide as Hole Transport Layer" presented at "6th International Conference on Nanoscience and Nanotechnology (ICONN 2021)", hosted by Department of Physics & Nanotechnology SRM Institute of Science and Technology, Kattankulanthur, Chennai, Tamil Nadu, India. During 1^{st} -3^{rd} February 2021.
5. **Lalsingh Guguloth**, Nagaraju Macherla, Kuldeep Singh, and Kusum Kumari, and Poster Presentation on "TERNARY POLYMER SOLAR CELLS USING PEDOT:PSS-GO HOLE TRANSPORT LAYER via FöRSTER RESONANCE ENERGY TRANSFER AND BALANCED CHARGE TRANSPORT" presented at "International Conference on Optoelectronics and Advanced Materials (ICOAM-2021)" (Virtual Conference), hosted by Department of Physics, SRI VENKATESWARA UNIVERSITY, TIRUPATI -517 502, ANDHRA PRADESH, INDIA, March 26-27, 2021.

BIO-DATA

I was born on 20th August 1986, at Venkatathanda, Anepuram, Maripeda, Mahabubabad, Telangana, India. I have had a throughout brilliant academic career. I obtained B.Sc (M.P.Cs) degree (3-year course) from Kakatiya University, Warangal, Telangana, India, in 2007. M.Sc. (2-year course) degree in Physics Kakatiya University, Warangal, Telangana, India, in 2009. Subsequently in 2010, I completed B.Ed. degree (1-year course) from Osmania University, Hyderabad, Telangana, India. Thereafter, I did M.Tech (2-year course), in Solid State Technology in 2012, from Indian Institute of Technology Madras, Chennai, India, with a C.G.P.A. of 6.71 (at point scale of 10). Since 2015. I am pursuing Ph.D. work in the research area entitled "Studies on Photophysics and Charge Carrier Dynamics of Graphene Oxide and Ternary Blend based Polymer Solar Cells", from National Institute of Technology Warangal, Telangana, which is submitted in the present thesis.